UNIVERSITY OF SÃO PAULO
SÃO CARLOS SCHOOL OF ENGINEERING

Antonio Rodrigues Neto

Numerical formulations based on the Isogeometric Boundary Element Method for the mechanical analysis of three-dimensional reinforced nonhomogeneous solids

Formulações numéricas baseadas no Método dos Elementos de Contorno Isogeométrico para a análise mecânica de sólidos não-homogêneos reforçados tridimensionais

São Carlos

2023

Antonio Rodrigues Neto

Numerical formulations based on the Isogeometric Boundary Element Method for the mechanical analysis of three-dimensional reinforced nonhomogeneous solids

PhD Thesis presented to the Graduate Program in Structural Engineering at the São Carlos School of Engineering, University of São Paulo, Brazil to obtain the degree of Doctor of Science.

Concentration area: Structural Engineering

Advisor: Prof. Edson Denner Leonel

Corrected version

(Original version is available at São Carlos School of Engineering)

São Carlos

2023

Ficha catalográfica elaborada pela Biblioteca Prof. Dr. Sérgio Rodrigues Fontes da EESC/USP com os dados inseridos pelo(a) autor(a).

Rodrigues Neto, Antonio
R696f Formulações numéricas baseadas no Método dos Elementos de Contorno Isogeométrico para a análise mecânica de sólidos não-homogêneos reforçados tridimensionais / Antonio Rodrigues Neto; orientador Edson Denner Leonel. São Carlos, 2023.

Tese (Doutorado) - Programa de Pós-Graduação em Engenharia Civil (Engenharia de Estruturas) e Área de Concentração em Estruturas -- Escola de Engenharia de São Carlos da Universidade de São Paulo, 2023.

1. Método dos elementos de Contorno. 2. IGABEM não linear. 3. Análise isogeométrica. 4. Materiais enrijecidos. 5. Refinamento adaptativo. I. Título.

Eduardo Graziosi Silva - CRB - 8/8907

FOLHA DE JULGAMENTO

Candidato: Engenheiro **ANTONIO RODRIGUES NETO.**

Título da tese: "Formulações numéricas baseadas no Método dos Elementos de Contorno Isogeométrico para a análise mecânica de sólidos não-homogêneos reforçados tridimensionais".

Data da defesa: 28/02/2023.

Comissão Julgadora	**Resultado**
Prof. Associado **Edson Dener Leonel (Orientador)** (Escola de Engenharia de São Carlos – EESC/USP)	APROVADO
Prof. Dr. **Eder Lima de Albuquerque** (Universidade de Brasília – UnB)	APROVADO
Prof. Titular **Osvaldo Luís Manzoli** (Universidade Estadual Paulista "Júlio de Mesquita Filho"/UNESP)	APROVADO
Prof. Associado **Rodrigo Ribeiro Paccola** (Universidade Federal do Rio de Janeiro/UFRJ)	APROVADO
Prof. Dr. **Lucas Silveira Campos** (Universidade Federal do Espírito Santo/UFES)	APROVADO

Coordenador do Programa de Pós-Graduação em Engenharia Civil (Engenharia de Estruturas):
Prof. Associado **Vladimir Guilherme Haach**

Presidente da Comissão de Pós-Graduação:
Prof. Titular **Murilo Araujo Romero**

Acknowledgements

The following research project would not be possible without the sponsorship from the São Paulo State Foundation for Research (FAPESP), grant 2018/20253-4, and their support is greatly appreciated. This study was also financed in part by the Coordenação de Aperfeiçoamento de Pessoal de Nível Superior - Brasil (CAPES) - Finance Code 001.

I am deeply grateful to my family for their unconditional support and incentive over the course of these intense years, specially my mother Luzia Donizeti dos Santos Rodrigues and father José Aparecido Rodrigues. Special thanks go to my lovely wife Rafaela Santos da Silva, who has been by my side all my higher education academic journey.

I gratefully acknowledge my advisor Prof. Edson Leonel for the supervision, guidance, partnership and friendship built over these years. Our partnership has completed more than six years and has definitely had a great impact in my personal and professional achievements.

I would like to thank all my friends from São Carlos for the enjoyable times spent together. Special thanks for my research group colleagues Matheus Rocha, Heider de Castro e Andrade, Sérgio Gustavo Ferreira Cordeiro and Hugo Luiz Oliveira. Also for my doctorate colleagues Henrique Barbosa Soares, Caio Silva Ramos, Murilo Henrique Campana Bento, Péricles Rafael Pavão Carvalho and Marcela Bassoli.

Last but not least, I acknowledge the staff at the Department of Structural Engineering (SET) for their support, cordiality and solicitude throughout my doctoral years.

ABSTRACT

RODRIGUES NETO, A. **Numerical formulations based on the Isogeometric Boundary Element Method for the mechanical analysis of three-dimensional reinforced nonhomogeneous solids**. 2023. 242p. Thesis (Doctorate) - São Carlos School of Engineering, University of São Paulo, São Carlos, 2023.

The main objective of this doctoral thesis is the development of numerical formulations based on the Isogeometric Boundary Element Method (IGABEM) for the three-dimensional mechanical analysis of reinforced and nonhomogeneous structural systems. BEM's lack of domain mesh is advantageous in both contexts: the integration with IGA frameworks and the representation of reinforcements embedded into 3D bodies. This study takes advantage of those by working in reinforced IGABEM formulations. The sub-region technique applied to the 3D IGABEM allows for representing non-homogeneous bodies. The 1DBEM/IGABEM coupling formulation is extended to 3D domains, with the modelling of crossings between fibres and IGABEM boundaries via the connection element. That approach does not require remeshing in the NURBS surfaces and makes possible to represent reinforcements crossing crack surfaces modelled by either the Dual IGABEM or at interfaces. Nonlinear formulations are presented via elastoplastic reinforcements and bond-slip. Such formulations allow to accurately model the pull-out phenomenon in 3D numerical models. Besides, this study works with the cohesive crack approach to represent nonlinear fractures at the 3D body, via different cohesive laws. With that, nonlinearities can be represented in both matrix or reinforcements. This study also works with time-dependent behaviour of reinforced bodies by both the viscoelasticity at matrix or reinforcements and the viscous response of cohesive interfaces to different loading rates. Numerical applications show the accuracy of the proposed formulations to represent various mechanical behaviours, using both numerical or experimental results as reference. The IGABEM models to lead to accurate results with good performance with fewer degrees of freedom necessary when comparing against pure FEM or Lagrangian BEM models. The convergence of the proposed formulations is also studied. In this context, adaptive refinement strategies are proposed, making possible to use CAD geometrical models as basis for the mechanical analysis. Such models are refined via knot insertion, having the adaptive refinement guided by a posteriori error estimator. Innovative error estimators are proposed for both the IGABEM and its reinforced version. The last approach is able to identify the refinement required at the most critical fibre's regions, minimising the mechanical fields oscillations usually observed. The developed adaptive strategies present excellent convergence rates, which show better results when compared against global uniform refinement in several complex numerical applications.

Keywords: Boundary element method. Nonlinear IGABEM. Isogeometric analysis. Reinforced materials. Adaptive refinement.

RESUMO

RODRIGUES NETO, A. **Formulações numéricas baseadas no Método dos Elementos de Contorno Isogeométrico para a análise mecânica de solídos não-homogêneos reforçados tridimensionais**. 2022. 242p. Tese (Doutorado) - Escola de Engenharia de São Carlos, Universidade de São Paulo, São Carlos, 2022.

O objetivo principal desta tese de doutorado é o desenvolvimento de formulações numéricas baseadas no Método dos elementos de contorno Isogeométrico (IGABEM) para a análise mecânica tridimensional de sistemas estruturais enrijecidos e não homogêneos. A não necessidade de malha de domínio do BEM é uma grande vantagem em ambos os contextos isogeométrico e a representação de domínios 3D enrijecidos. A técnica de sub-regiões permite a representação de domínios não homogêneos. A formulação do acoplamento 1DBEM/IGABEM é estendida para domínios 3D, com a modelagem de cruzamentos entre fibras e contornos do IGABEM via o elemento de conexão. A abordagem não requer remalhamento nas superfícies NURBS e possibilita a representação de enrijecedores cruzando superfícies de fissuras modeladas pelo Dual IGABEM ou em interfaces. Formulações não lineares são apresentadas via enrijecedores elastoplásticos e escorregamento. Tais formulações permitem modelar com precisão o fenômeno pull-out em modelos 3D. Além disso, este estudo trabalha com a abordagem de fissura coesiva para representar fraturas não lineares no domínio 3D, via diferentes leis coesivas. Com isso, as não linearidades podem ser representadas tanto na matriz quanto nos enrijecedores. O comportamento dependente do tempo também é estudado em domínios enrijecidos tanto pela viscoelasticidade quanto pela resposta viscosa de fissuras coesivas a diferentes taxas de carregamento. Aplicações numéricas mostram a precisão das formulações propostas para representar vários comportamentos mecânicos, usando resultados numéricos ou experimentais como referência. Os modelos IGABEM levam mostram bom desempenho com menos graus de liberdade necessários quando comparados com modelos de FEM puros ou BEM lagrangiano. A convergência das formulações propostas também é estudada. Estratégias de refinamento adaptativo são propostas, possibilitando o uso de modelos geométricos CAD como base para a análise mecânica. Os modelos são refinados via "knot insertion", de forma adaptativa guiada por um estimador de erro a posteriori. Estimadores de erro são propostos tanto para o IGABEM quanto para sua versão enrijecida. A última abordagem é capaz de identificar o refinamento necessário nas regiões mais críticas dos enrijecedores, minimizando as oscilações dos campos mecânicos normalmente observadas. As estratégias adaptativas apresentam excelentes taxas de convergência, com melhores resultados quando comparadas com o refinamento uniforme global em diversas aplicações complexas.

Palavras-chave: Método dos elementos de Contorno. IGABEM não linear. Análise isogeométrica. Materiais enrijecidos. Refinamento adaptativo.

List of Figures

Contents

1

Introduction

Foreseeing the correct mechanical behaviour of materials and structures is essential in any engineering project, being in aeronautics, automotive or any construction field. With that, the engineers can properly evaluate all of the project variables in a realistic and reliable way during the analysis phase. Thus, the project's costs, geometry, materials, design and manufacturing may be more efficient and adequate to each scenario. Besides, the project's safety is directly affected once the most probable failure scenarios are identified in the analysis phase, such as stress concentrations, critical loads and weak points. Then, the probability of occurring a failure during posterior project phases is minimised. The cost of failures or modifications at those phases is significantly higher than at the analysis phase. Hence, one highlights the importance of carefully analysing the projects beforehand.

Engineers usually deal with these analyses through two different approaches. The first is the analytical solving of mathematical problems related to engineering projects and structures, which can be assisted by experimental tests or scale models. The second approach is the numerical solving of such mathematical problems. Nevertheless, the advent of accessible and efficient numerical processing tools has brought a true revolution in this area, making the numerical approach more common nowadays. With that, engineers have more robust, efficient and fast tools to model and analyse the projects. Especially in structural engineering, the numerical analyses are now fundamental tools in basically every single design, rather than the classical approaches.

The mechanical collapse and its correct prediction is a primary concerning in engineering. The collapse in many situations is a result of crack growth, that means, discontinuities propagation into the continuous medium. Figure 1 illustrates the crack process in different structural components, such as gears, fibre reinforced composite materials, short fibre reinforced concrete and aircraft panels. Hence, it is clear that this phenomenon is observed in several engineering areas.

Figure 1 – Illustration of the mechanical collapse process in different reinforced structural systems.

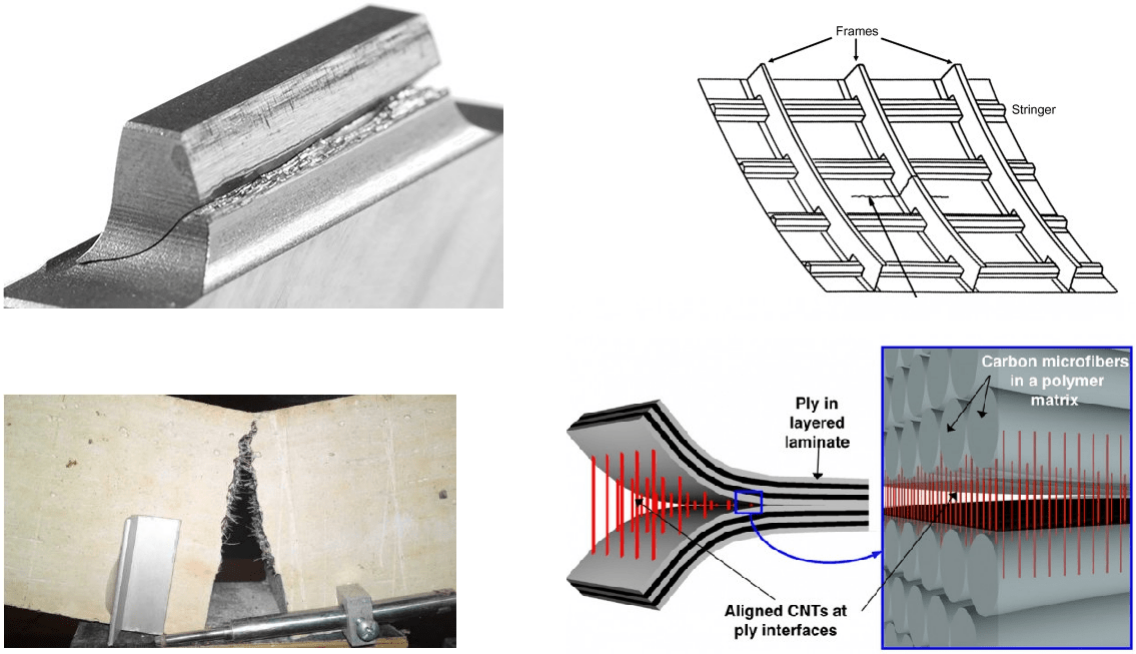

Source: (3, 4, 5, 6), adapted.

The classical continuous mechanics is not exactly efficient in representing the complex cracking process. On the other hand, the fracture mechanics field contains a set of tools that allow the precise representation of the mechanical behaviour of cracked deformable solids. Besides, it provides adequate parameters that allow the correct evaluation of the crack growth process as a function of the applied loads. Then, the analytical solutions in the context of fracture mechanics are restricted to a few simple problems, such as infinite media and elastic materials. In addition, the experimental approach of this phenomenon is usually expensive and limited. This approach could require, for instance, several experimental tests for a single engineering project. Therefore, the best course of action herein would be coupling the numerical methods to the fracture mechanics framework.

This study is inserted in this context, which has been receiving special attention from several renowned research centres worldwide. Both the proposition of robust numerical approaches to handle real-world engineering problems and the development of adequate methodologies to represent different mechanical phenomena are priorities in the engineering context. Those represent research lines currently in evidence. One may highlight the representation of the mechanical degradation of solids composed by materials of complex behaviour. Among the most common numerical methods applied for those purposes, two main groups stand out: the methods based on domain discretization, such as the Finite Element Method (FEM) and the methods in which such procedure is not necessary, such as the Boundary Element Method (BEM) and meshless/mesh-reduced methods.

Figure 2 illustrates a comparison between the main idea behind the discretisation proposed by the FEM and the BEM for 2D elastostatic homogeneous problems. In that case, the BEM only requires the discretization of the contour of the solid, thus one observes a dimensionality reduction in the discretization. This feature is not only an advantage for several particular problems, but also results in a reduced number of variables associated with the numerical model, which leads to in smaller algebraic systems. Despite that fact, the algebraic system obtained by the BEM is non-symmetric and non-sparse, in opposition to the FEM. Hence, the BEM system requires more complex and demanding solution procedures, which might be seen as unfavourable. In the end, there is a balance between the disadvantage of the system's complexity and the advantage of its smaller dimensions regarding the system solver procedures.

Figure 2 – Direct comparison between the discretization of the FEM and BEM. 2D representation.

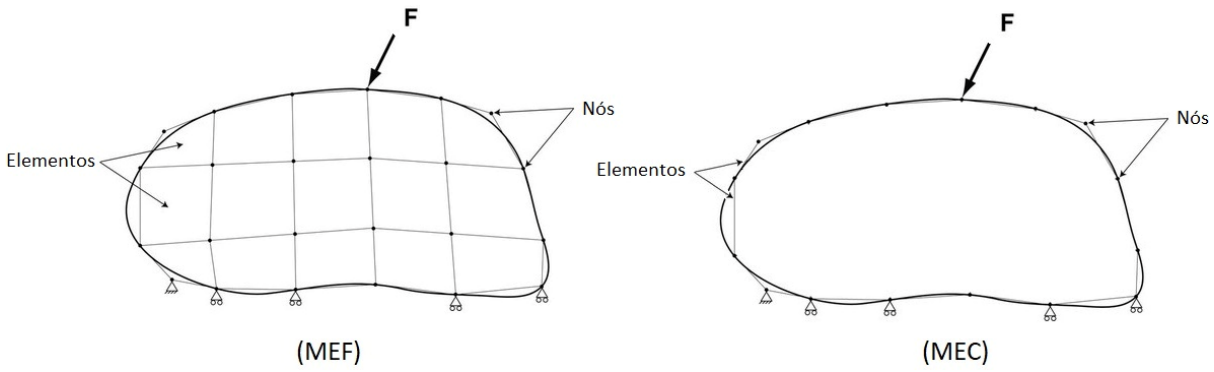

Source: (7), adapted.

In fact, particularities of the BEM make it an excellent technique to approach specific engineering problems, which are related to the representation of high gradients in the mechanical fields. Due to the mesh's dimensionality reduction, the BEM naturally and precisely represents stress concentrations present in the domain related to the existence of physical discontinuities, such as cracks or reinforcements. This aspect makes the method adequate and effective to solve fracture mechanics problems, leading to more efficient and accurate models when compared against FEM models. Besides, the mesh's dimensionality reduction leads to a easy representation of cracks and remeshing, which may be required for numerous modelling problems.

In the context of the BEM, a different approach has been standing out recently: the Isogeometric approach known as IGABEM (Isogeometric Boundary Element Method). The IGABEM is specially interesting for the straightforward connection between the mechanical analysis and the geometry model design. That is because engineering projects often carry out the geometry design using CAD (Computer Aided Design) software, which represent solids through Splines and NURBS (Non Uniform Rational Basis Spline) surfaces positioned at the solids' contours. The IGABEM adopts these same functions to

approximate both geometry and mechanical fields at the boundary. Thus, one completely eliminates the need for creating a mesh specially for the mechanical analysis from the CAD model. For complex structures, this process could demand a huge computational time, which may even exceed the mechanical analysis time itself (8). Besides, it also creates a source of error in the geometry input of the analysis process.

The IGA approaches use the exact geometry model provided by the CAD, which completely eliminates the errors regarding the creating of a polynomial mesh. In addition, the use of NURBS functions allows for the exact description of complex shapes, such as spheres, cylinders, propellers and torus. Then, the number of elements and nodes necessary to describe such geometries is smaller when compared against polynomial approximations. It is worth mentioning that the IGABEM is particularly interesting, since both the numerical method and the CAD designs only require the discretization of the boundaries. IGA approaches of the FEM, on the other hand, still require the construction of an isogeometric domain mesh from the CAD design. These features contribute for the good performance and accuracy of the IGABEM in the mechanical analysis of 3D structures.

Furthermore, the BEM allows for an efficient modelling of reinforced domains. The absence of domain mesh favours the simple representation of embedded reinforcements. In this context, one highlights the importance of the coupled domain/reinforcement formulations based on the technique firstly proposed by Zienkiewicz (9). That study presented the FEM/BEM coupling technique, in which the FEM represents the reinforcing substructures and the BEM represents the matrix/domain. On one hand, the FEM is well-known for the modelling of reticulated structures, such as trusses, beams and shells. On the other hand, the BEM is particularly efficient to handle two and three dimensional domains due to the mesh's dimensionality reduction. Then, the proposed FEM/BEM coupling takes advantage from the strong points of both methods, which results in effective and accurate models. The application of this type of coupling for 3D reinforced structures allows for the efficient representation of complex engineering structures, such as the ones illustrated in Fig. 3.

In the context of reinforced structures (as illustrated in Fig. 3), it is worth highlighting that its application has become essential in several engineering areas. This concept allows the design of efficient components, i.e., with high stiffness and low weight. It is well-known that these components are extremely important in mechanical and aeronautic engineering (12), in addition to civil engineering, in which many projects apply reinforced concrete and reinforced soils. Furthermore, nowadays one cannot neglect the fibre-reinforced materials, such as the polymers reinforced by steel, carbon or glass fibres, which can be oriented in different ways (aligned, continuous or random). Different material matrices can be found as well, such as ceramic, polymeric, metallic or thermoplastic. Thus, these materials present a huge variety and are excellent to achieve high-stiffness and low-weight designs.

Figure 3 – Application of reinforcements in engineering: ship hull (a) and aircraft fuselage (b).

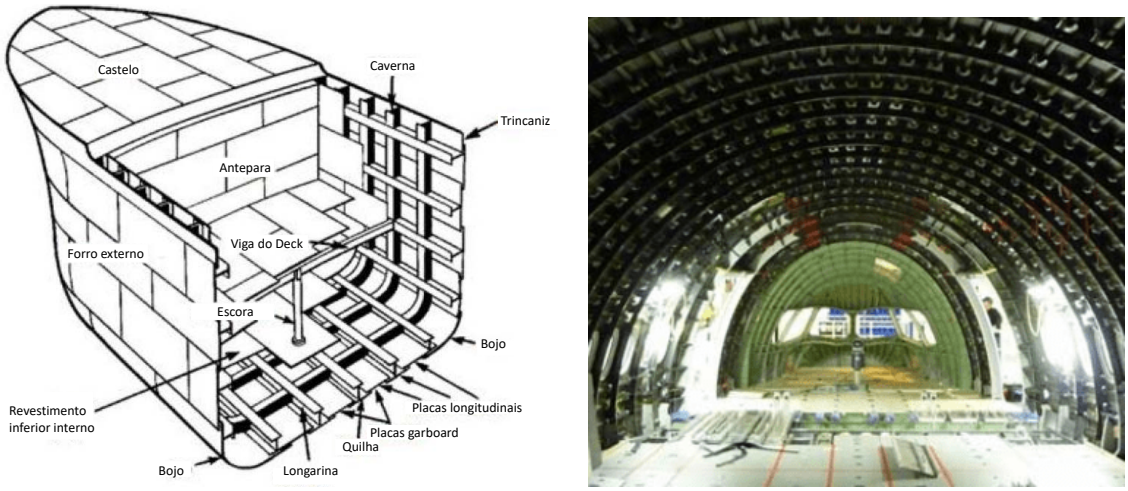

(a) (b)

Source: (10), adapted and (11).

In this context, the mechanical analysis of such materials requires numerical techniques, since their mechanical behaviour is usually quite complex and challenging. Therefore, it is clear how the proposition of numerical approaches, particularly the numerical coupling approaches, to adequately handle such structures and materials is of high importance in the engineering field.

Above all, it is clear that the accurate representation of complex mechanical behaviours considering the mechanical-material degradation is a significantly relevant topic. In this regard, the knowledge produced in this area must increase throughout time in order to keep up with the increasing complexity of engineering projects and materials. Hence, there is a vast motivation to develop and propose new formulations and approaches to handle more complex structural systems effective and accurate ways. This is the main motivation for the development of this PhD thesis, which will deeply contribute to the study of the representation of reinforced structures and materials in different situations and considering various mechanical behaviours.

1.1 Objectives and innovative aspects

The main objective of this work is proposing IGABEM formulations to properly represent reinforced media and fracture behaviour of 3D solids. For that, concepts from the linear and nonlinear fracture mechanics should be applied to adequately represent cracked reinforced bodies. The use of the Isogeometric approach in the proposed formulation is remarkable, since it allows the exact representation of a vast amount of geometries and shapes frequently used in engineering projects. Besides, it enables a straightforward integration between the mechanical analysis tool and the geometric model construction

from any CAD software.

Initially, the 1DBEM/BEM coupling technique (13) is applied for nonhomogeneous 3D domains using a Lagrangian approach of the BEM. Using this mechanical model, nonlinear formulations are developed to represent the mechanical degradation at the fibres, characterised by yielding and bond-slip modelling. The reinforced formulations developed are then coupled with a Isogeometric approach of the 3D BEM, originating the 1DBEM/IGABEM coupling. This Reinforced IGABEM formulation should be able to effectively represent complex 3D reinforced solids and structures. The nonlinear formulations regarding the reinforcements mechanical behaviour are applied to the 1DBEM/IGABEM coupling, leading to a innovative nonlinear approach of the 3D IGABEM.

Based on the Reinforced IGABEM formulation developed, the fracture analysis of 3D bodies is carried out considering linear and nonlinear fracture mechanics. The linear fracture mechanics (LEFM) approach applies the Dual BEM technique (14) to properly represent the presence of cracks. Furthermore, nonlinear cracks analysis and propagation are assessed by considering the cohesive behaviour at interfaces. The existence of fibres that cross crack surfaces can also be represented by the proposed connection element strategy, which is another novel aspect of this study.

The analysis of viscoelastic reinforced bodies is another mechanical behaviour modelling objective of this study. Time-dependent behaviours of both matrix and reinforcements are proposed based on rheological models of Kelvin-Voigt and Boltzmann. The nonlinear behaviour of the reinforcements can be coupled with the viscoleastic behaviour of the solid, which leads to the modelling of nonlinear and time-dependent structures. This formulation will be able to properly represent real-life engineering structures and materials, such as polymeric composites reinforced by steel fibres. This point is also a relevant contribution of this work, since such formulations based on the IGABEM are not vastly exploited in the available literature.

A pre-processing computational tool is built to receive IGA models directly from CAD software as the numerical models' mesh. For that, the library "pyiges" (15) based on Python language provides intrinsic functions to read information from IGES files. This type of file is commonly used for most CAD tools. With that, the exact geometry from the CAD design can be used as the mesh itself for the mechanical analysis. However, the mechanical fields representation usually demands finer meshes than the geometry representation, which leads to the necessity to refine the IGA models from the CAD. The strategy of knot insertion (16) is applied herein to refine the meshes of NURBS surfaces.

In order to properly evaluate the refinement necessity of meshes obtained directly from CAD models, mesh adaptativity strategies are studied. Those strategies are based on the procedure presented by Zienkiewicz (17) and are initially based on the hypersingular error estimator available in the literature (18). Afterwards, different error estimators

are proposed for homogeneous or reinforced media, in order to produce more effective mesh adaptativity strategies. Thus, a fully integration between CAD and the mechanical modelling via the IGABEM can be achieved.

1.2 Organisation of the text

The remainder of this thesis is structured as follows: Chapter 2 describes the applied 3D formulation of the BEM (including IGABEM and the Dual approach). Chapter 3 describes the coupling formulation technique for linear applications. Chapter 4 presents the developed nonlinear reinforced formulations, regarding yielding and bond-slip, that may be applied to both the 1DBEM/BEM and the 1DBEM/IGABEM. Chapter 5 presents the developed time-dependent formulations regarding the viscoelastic behaviour of both matrix and reinforcement. Chapter 6 presents the developed cohesive fracture formulation implemented for cracks at interfaces of the IGABEM, also considering the crack viscous behaviour. With the mechanical models covered, Chapter 7 presents the mesh refinement adaptivity strategies studies and developments. All chapters present, in the beginning, the extensive literature review made for each topic and, in the ending, the numerical applications executed with the implemented formulations. Finally, Chapter 7 draws some conclusions obtained from the present research and offers some recommendations for future work.

2

Fundamentals of the Boundary Element Method

This chapter presents the numerical method utilized to represent the mechanical behaviour of structures in this study. The method presented herein is the basis for all of the developments of the work. Appendix A presents the essential points of the theory of elasticity that are necessary for this chapter, thus its previous reading is recommended.

2.1 The BEM: Literature Review

The BEM has been applied to mathematical problems originated from physical models in several contexts. For this, the governing equations of the problem must be written in a integral form, which is the reason why the method was initially called the integral equations' method. Thus, the process of transforming differential equation into integration equations is essential. In this regard, the study of Abel in 1823 (19) can be considered a starting point for the integral representation of physical models. Abel applied integral equations to obtain the solution of a classic problem called "isochronous pendulum", which initiated the main ideas that would eventually culminate in the BEM as known today.

In that early period in the history of the method, it is worth mentioning the studies that concern potential problems. These problems apply Green's theorem to obtain the integral representation. The technique has been firstly presented for acoustics, by (20) and for elasticity, by (21, 22). Still in 1848, Lord Kelvin demonstrated the fundamental problem's solutions for isotropic materials, which represent the displacements integral equation until today (23). From these solutions, Somigliana developed an equation that correspond to Green's theorem for elasticity problems, also known as Somigliana's identity

(24).

After that period, there was a rapid development of electronic computers, which affected the research studies in the area. The use of computational methods in researches has been encouraged and significantly increased. The integral equations' method was then applied for wave propagation (25), acoustics (26), elasticity (27), among many other areas. It is worth mentioning the study of Kupradze (28), which discussed the application of a functional equations' method for potential problems. This approach can be considered the origin of the fundamental solutions' method (29).

The studies mentioned so far deal with indirect methods, i.e., with variables without physical meaning. Rizzo (30) firstly presented a method to solve Somigiliana's Identity in a direct way. Two-dimensional problems of elasticity have been solved considering variable with physical meaning, such as displacements and tractions. Rizzo utilised straight elements with constant displacements and force approximations, which was applied to study the correspondency between potential and elastic problems. In another study (31), the sub-region technique was presented to properly represent nonhomogeneous problems, which is applied in BEM formulations until today. Furthermore, this author also proposed a formulation to deal with non-isotropic linear elasticity (32), which preceded a two-dimensional formulation for materials with general anisotropy (33). In that period, there was a significant increase in the use of the integral equation's method, which has been encouraged by the important studies recently published and the rise of computers.

In that same decade, Brebbia (34) demonstrated that the integral formulation for elasticity problems can be achieved through the method of mean weighted residuals. That made clear the common root between the integral formulations and other numerical methods such as the FEM, which favored exploring couplings between such methods. Brebbia was also one of the creators of the name "Boundary Element Method", which was firstly mentioned in 1977 in (35), (36) and (37). With that, the BEM gets relevance in a context in which other numerical methods were previously dominant, as mentioned in (9). Particularly, Zienkiewicz (9) was pioneer when introduced the coupled formulation between the BEM and the FEM, which is recurrently mentioned in the literature for several applications. This coupling technique takes advantages of the positive sides of each numerical method and has been applied in numerous studies such as (38, 39, 40, 41), among many others.

The fracture mechanics is an important field in which the BEM stands out. It presents several advantages over other numerical methods for dealing with cracked bodies. The fracture mechanics' theories are based on the work of Griffith (42), which presented an energy formulation for crack growth inside continuous bodies. In another study (43), the Westergaard solutions for infinite media with a central crack were presented, which would be further developed in (44) e (45). The first studies to apply the BEM in fracture

mechanics problems were published in the 70's (46, 47). At first, the formulations were limited due to singularities present in the elements over the crack, which was overcome by the Dual BEM formulation. This approach utilises a displacements integral equation for one side of the crack and a tractions integral equation for the other side. Such approach was firstly published by (14, 48) and rapidly became relevant in the literature (49, 50, 51). Thus, the Dual BEM became a consolidated and effective tool to treat fracture mechanics problems. Besides, the SET/EESC research group have produced several studies in this field: (52, 53, 54) and (55).

Therefore, the BEM has received the attributes and characteristics that we know today. It has also established itself as a well-consolidated tool to treat several problems, such as: infinite media, fracture mechanics, soil mechanics, soil-structure interaction, reinforced domains, among others.

2.2 Integral equations in elastostatics

Consider a linear-elastic Boundary Value Problem (BVP) with domain Ω and contour Γ. The dynamic effects can be neglected. As demonstrated in the Appendix A, its governing equation is as follows:

$$\sigma_{ij,j} + b_i = 0 \tag{2.1}$$

The integral BEM equations can be obtained by the weighted residual technique (56, 57). The error obtained in the approximate evaluation of Eq. 2.1 throughout the domain Ω is weighted by the fundamental solution of displacements U^*_{ki}, as follows:

$$\int_\Omega (\sigma_{ij,j} + b_i) U^*_{ki} d\Omega = 0 \tag{2.2}$$

Applying partial integration in the first term of Eq. 2.2, one writes:

$$\int_\Gamma U^*_{ki} \sigma_{ij} \eta_j d\Gamma - \int_\Omega U^*_{ki,j} \sigma_{ij} d\Omega + \int_\Omega U^*_{ki} b_i d\Omega = 0 \tag{2.3}$$

where η_j is the normal vector to Γ. Applying the Cauchy formula (Eq. A.3) and the fundamental problem's displacement-strain relations (Eq. A.25), one writes:

$$\int_\Gamma U^*_{ki} t_i d\Gamma - \int_\Omega E^*_{kij} \sigma_{ij} d\Omega + \int_\Omega U^*_{ki} b_i d\Omega = 0 \tag{2.4}$$

in which E^*_{kij} is the fundamental solution of strains.

Equation 2.4 is the basis to obtain the BEM integral expressions. In order to achieve the elastostatics integral form, the elastic constitutive relation (Eq. A.8) is applied herein, which leads to:

$$\int_{\Gamma} U_{ki}^{*} t_i d\Gamma - \int_{\Gamma} E_{kij}^{*} D_{ijlm} \varepsilon_{lm} d\Omega + \int_{\Omega} U_{ki}^{*} b_i d\Omega = 0 \tag{2.5}$$

where D_{ijlm} is the elastic constitutive tensor.

Then, applying the fundamental problem's constitutive and displacement-strain relations (Eq. A.24 and Eq. A.25), one writes:

$$\int_{\Gamma} U_{ki}^{*} t_i d\Gamma - \int_{\Omega} P_{kij}^{*} u_{i,j} d\Omega + \int_{\Omega} U_{ki}^{*} b_i d\Omega = 0 \tag{2.6}$$

Partial integration can be applied into the second term of Eq. 2.6, which leads to:

$$\int_{\Gamma} U_{ki}^{*} t_i d\Gamma - \int_{\Gamma} P_{kij}^{*} \eta_j u_i d\Gamma + \int_{\Omega} P_{kij,j}^{*} u_i d\Omega + \int_{\Omega} U_{ki}^{*} b_i d\Omega = 0 \tag{2.7}$$

One applies the fundamental problem's equilibrium equation and Cauchy formula (Eq. A.20 and Eq. A.23) into Eq. 2.7, which results in:

$$\int_{\Gamma} U_{ki}^{*} t_i d\Gamma - \int_{\Gamma} T_{ki}^{*} u_i d\Gamma + \int_{\Omega} -\Delta(\mathbf{x}^f - \mathbf{x}^s) \delta_{ki} u_i d\Omega + \int_{\Omega} U_{ki}^{*} b_i d\Omega = 0 \tag{2.8}$$

Therefore, the Dirac function integration property can be considered, which eliminates the domain integration term. Then:

$$u_k(\mathbf{x}^s) = \int_{\Gamma} U_{ki}^{*} t_i d\Gamma - \int_{\Gamma} T_{ki}^{*} u_i d\Gamma + \int_{\Omega} U_{ki}^{*} b_i d\Omega \tag{2.9}$$

in which the free term $u_k(\mathbf{x}^s)$ is the source point displacement along the direction k.

Equation 2.9 is known as Somigliana's identity, which represents a integral formulation in displacements of the BVP. This expression calculates any internal points displacements $\mathbf{x}^s$, being all fields at the boundary and body forces known.

To obtain stress and strain in internal points, Eq. 2.9 is differentiated with respect to the source point coordinates, as follows:

$$\frac{\partial u_k(\mathbf{x}^s)}{\partial x_j^s} + \int_{\Gamma} \frac{\partial T_{ki}^{*}}{\partial x_j^s} u_i d\Gamma = \int_{\Gamma} \frac{\partial U_{ki}^{*}}{\partial x_j^s} t_i d\Gamma + \int_{\Gamma} \frac{\partial U_{ki}^{*}}{\partial x_j^s} b_i d\Gamma \tag{2.10}$$

The fundamental solutions U_{ki}^{*} e T_{ki}^{*} are functions of the vector $\mathbf{r}$, as mentioned in Appendix A. Therefore, the following chain rule must be applied:

$$\frac{\partial U_{ki}^{*}}{\partial x_j^s} = \frac{\partial U_{ki}^{*}}{\partial \mathbf{r}} \frac{\partial \mathbf{r}}{\partial x_j^s} \tag{2.11}$$

what can be similarly written for T_{ki}^{*}.

Considering the orientation definition of $\mathbf{r}$, one writes:

$$\frac{\partial \mathbf{r}}{\partial x_j^s} = -\frac{\partial \mathbf{r}}{\partial x_j^f} \tag{2.12}$$

Applying Eq. 2.12 into Eq. 2.11 for both displacements and tractions, one obtains:

$$\begin{aligned} \frac{\partial U_{ki}}{\partial x_j^s} &= -U_{ki,j} \\ \frac{\partial T_{ki}}{\partial x_j^s} &= -T_{ki,j} \end{aligned} \tag{2.13}$$

The relations from Eq. 2.13 may now be applied into Eq. 2.10, which leads to:

$$u_{k,j}\left(\mathbf{x}^s\right) - \int_\Gamma T^*_{ki,j} u_i d\Gamma = -\int_\Gamma U^*_{ki,j} t_i d\Gamma \tag{2.14}$$

Applying the displacement-strain relation of the fundamental problem (Eq. A.25) and the constitutive law (Eq. A.10) into Eq. 2.14, one writes the following:

$$\sigma_{pq}\left(\mathbf{x}^s\right) = \int_\Gamma D^*_{ipq} t_i d\Gamma - \int_\Gamma S^*_{ipq} u_i d\Gamma + \int_\Omega D^*_{ipq} b_i d\Omega = 0 \tag{2.15}$$

in which D^*_{iqp} e S^*_{iqp} are the hypersingular fundamental kernels. σ_{pq} are the Cauchy stresses.

Equation 2.15 is the integral formulation for stress in internal points, also known as hypersingular equation for internal points. To obtain the hypersingular kernels, one writes from the passage from Eq. 2.14 to Eq. 2.15 the following:

$$D^*_{ipq} = -P^*_{iqp} \tag{2.16}$$

where P^*_{iqp} is the fundamental solution in stress (Eq. A.37).

S^*_{iqp} gathers the tractions terms from Eq. 2.14. Considering isotropic media, one applies the constitutive and displacement-strain relations, which results in:

$$S^*_{ipq} = -2\mu \left[\frac{T^*_{pi,q} + T^*_{qi,p}}{2} + \frac{\nu}{1-2\nu} T^*_{mi,m} \delta_{pq} \right] \tag{2.17}$$

Applying Eq. A.37 and Eq. A.38 into Eq. 2.16 and Eq. 2.17, one writes the hypersingular kernel's expressions as follows:

$$D^*_{ipq} = \frac{1}{8\pi(1-\nu)r^2} \left[(1-2\nu)\left(r_{,i}\delta_{pq} + r_{,p}\delta_{iq} - r_{,q}\delta_{pi}\right) + 3r_{,i}r_{,p}r_{,q} \right] \tag{2.18}$$

$$S^*_{ipq} = \frac{\mu}{4\pi(1-\nu)r^3} \begin{Bmatrix} 3\dfrac{\partial r}{\partial \eta}\left[(1-2\nu)\delta_{pq}r_{,i} + \nu\left(\delta_{pi}r_{,q} + \delta_{qi}r_{,p}\right) - 5r_{,i}r_{,p}r_{,q}\right] + \\ 3\nu\left(\eta_p r_{,q} r_{,i} + \eta_q r_{,p} r_{,i}\right) - (1-4\nu)\eta_i \delta_{pq} + \\ (1-2\nu)\left(3\eta_i r_{,p} r_{,q} + \eta_q \delta_{pi} + \eta_p \delta_{qi}\right) \end{Bmatrix} \tag{2.19}$$

2.3 Boundary integral equations: limiting process

Equations 2.9 and 2.15 are only valid for the evaluation of mechanical fields at internal points. The boundary integral equations can be obtained by placing $\mathbf{x}^s$ at Γ. This process consists of creating a fictitious domain Ω_ε around the point $\mathbf{x}^s$ positioned at Γ. Ω_ε is a semi-sphere with radius equals ε and boundary Γ_{ε^+}. This process can be named as limiting process and is illustrated in Fig. 4.

Figure 4 – Added fictitious boundary Γ_{ε^+} for the limiting process.

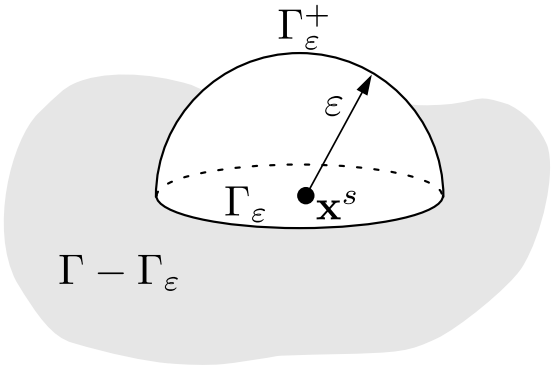

Source: The author.

ε tends to zero in the limiting process, therefore both final domain $(\Omega + \Omega_\varepsilon)$ and boundary $(\Gamma - \Gamma_\varepsilon + \Gamma_\varepsilon^+)$ tend to the initial Ω and Γ, respectively. With that, the integral equations can be evaluated at the boundary.

Applying the limiting process into the Somigliana's identity (Eq. 2.9), one writes:

$$u_i\left(\mathbf{x}^s\right) = \lim_{\varepsilon\to 0} \int\limits_{\Gamma-\Gamma_\varepsilon+\Gamma_\varepsilon^+} U_{ij}^* t_j d\Gamma - \lim_{\varepsilon\to 0} \int\limits_{\Gamma-\Gamma_\varepsilon+\Gamma_\varepsilon^+} T_{ij}^* u_j d\Gamma + \lim_{\varepsilon\to 0} \int\limits_{\Omega+\Omega_\varepsilon} T_{ij}^* b_j d\Omega \tag{2.20}$$

in which Γ_ε is the intersection between Γ and Γ_{ε^+}, as illustrated in Fig. 4.

The singularity orders of the fundamental solutions U_{ij}^* e T_{ij}^* are, respectively, $O(1/r)$ and $O(1/r2)$. $O(1/r)$ is called weak singularity and $O(1/r2)$ is a strong singularity, in the 3D analysis. The weak singularities can be simply solved as improper integrals. The strong singularities are solved by a regularisation process described in (51), which is based on Taylor series expansions of the displacements u_j around $\mathbf{x}^s$. Only the first term of the expansion must be considered, thus:

$$u_j\left(\mathbf{x}^f\right) \cong u_j\left(\mathbf{x}^s\right) \tag{2.21}$$

The second integration in Eq. 2.20 can then be rewritten as follows:

$$\begin{aligned} &\lim_{\varepsilon\to 0} \int\limits_{\Gamma-\Gamma_\varepsilon+\Gamma_\varepsilon^+} T_{ij} u_j d\Gamma = \lim_{\varepsilon\to 0} \int_{\Gamma-\Gamma_\varepsilon} T_{ij} u_j\left(\mathbf{x}^f\right) d\Gamma + \\ &\lim_{\varepsilon\to 0} \int_{\Gamma_\varepsilon^+} T_{ij}\left[u_j\left(\mathbf{x}^f\right) - u_j\left(\mathbf{x}^s\right)\right] d\Gamma + u_j\left(\mathbf{x}^s\right) \int_{\Gamma_\varepsilon^+} T_{ij} d\Gamma \end{aligned} \tag{2.22}$$

The Cauchy Principal Value (CPV) evaluates the first integral term in the right side of Eq. 2.22. The next term results in zero in the limit $\varepsilon \to 0$, because of Hölder continuity condition. The last term leads to the free term $\alpha_{ij}\left(\mathbf{x}^s\right) u_j\left(\mathbf{x}^s\right)$, which can be associated with the original free term from Eq. 2.9 as $c_{ij}(\mathbf{x}^s) = \delta_{ij} + \alpha_{ij}(\mathbf{x}^s)$.

The last integral term from Eq. 2.20 can be splitted into: an integration over Ω and an integration over Ω_ε. The second one tends to zero in the limiting process, because the integration domain $d\Omega$ has a higher order then the singularity of T^*_{ij}. Thus, the boundary integral equation in displacements is as follows:

$$c_{ij}\left(\mathbf{x}^s\right) u_j\left(\mathbf{x}^s\right) + \fint_\Gamma T^*_{ij} u_j\left(\mathbf{x}^f\right) d\Gamma = \int_\Gamma U^*_{ij} t_j\left(\mathbf{x}^f\right) d\Gamma + \int_\Omega U^*_{ki} b_i d\Omega \tag{2.23}$$

in which the symbol $\fint$ denotes the CPV integral.

The free term in Eq. 2.23 results in $c_{ij}(\mathbf{x}^s) = \delta_{ij}/2$ if $\mathbf{x}^s$ is positioned at smooth boundaries. Otherwise, it can be calculated by numerical strategies. More details about this term can be found in (58). This work handles only source points at smooth boundaries, therefore collocation strategies are necessary to deal with corners in the geometry. These strategies are covered ahead in this chapter. Nevertheless, Eq. 2.23 is known as displacement boundary integral equation (DBIE) or singular form of the BEM.

Applying the limiting process into expression for internal stresses (Eq. 2.15), one writes:

$$\sigma_{ij}\left(\mathbf{x}^s\right) = \lim_{\varepsilon\to 0} \int_{\Gamma-\Gamma_\varepsilon+\Gamma^+_\varepsilon} D^*_{kij} t_k d\Gamma - \lim_{\varepsilon\to 0} \int_{\Gamma-\Gamma_\varepsilon+\Gamma^+_\varepsilon} S^*_{kij} u_k d\Gamma + \lim_{\varepsilon\to 0} \int_{\Omega+\Omega_\varepsilon} D^*_{ipq} b_i d\Omega = 0 \tag{2.24}$$

The first integral term in the right side of Eq. 2.24 presents a strong singularity order. Once again, Taylor series are applied to solve this singularity, considering only the first term of the expansion of t_j around $\mathbf{x}^s$:

$$t_j\left(\mathbf{x}^f\right) \cong t_j\left(\mathbf{x}^s\right) \tag{2.25}$$

The first integration in Eq. 2.24 can then be rewritten as follows:

$$\begin{aligned} &\lim_{\varepsilon\to 0} \int_{\Gamma-\Gamma_\varepsilon+\Gamma^+_\varepsilon} D^*_{kij} t_k d\Gamma = \lim_{\varepsilon\to 0} \int_{\Gamma-\Gamma_\varepsilon} D^*_{kij} t_k\left(\mathbf{x}^f\right) d\Gamma + \\ &\lim_{\varepsilon\to 0} \int_{\Gamma^+_\varepsilon} D^*_{kij}\left[t_k\left(\mathbf{x}^f\right) - t_k\left(\mathbf{x}^s\right)\right] d\Gamma + t_k\left(\mathbf{x}^s\right) \int_{\Gamma^+_\varepsilon} D^*_{kij} d\Gamma \end{aligned} \tag{2.26}$$

The CPV evaluates the first integral term in the right side of Eq. 2.26. The next term results in zero in the limit $\varepsilon \to 0$, taking into account the Hölder continuity condition. The last term results in a additional free term $\beta_{ij}(\mathbf{x}^s) u_j(\mathbf{x}^s)$. Thus, Eq. 2.26 can be rewritten as follows:

$$\lim_{\varepsilon\to 0}\int\limits_{\Gamma-\Gamma_\varepsilon+\Gamma_\varepsilon^+} D^*{}_{kij}t_k\left(\mathbf{x}^f\right)d\Gamma = \oint_{\Gamma-\Gamma_\varepsilon} D^*_{kij}t_k\left(\mathbf{x}^f\right)d\Gamma + \beta_{kij}\left(\mathbf{x}^s\right)t_k\left(\mathbf{x}^s\right) \tag{2.27}$$

The second term in the right side of Eq. 2.24 presents a singularity order $O(1/r3)$, which is called hypersingularity. Its regularization can be achieved by expanding u_k around $\mathbf{x}^s$ and considering the first and second terms of the Taylor series, as follows:

$$u_k\left(\mathbf{x}^f\right) \cong u_k\left(\mathbf{x}^s\right) + u_{k,m}\left(\mathbf{x}^s\right) \tag{2.28}$$

Thus:

$$\begin{aligned}
&\lim_{\varepsilon\to 0}\int\limits_{\Gamma-\Gamma_\varepsilon+\Gamma_\varepsilon^+} S^*_{kij}u_k d\Gamma = \lim_{\varepsilon\to 0}\int_{\Gamma-\Gamma_\varepsilon} S^*_{kij}u_k\left(\mathbf{x}^f\right)d\Gamma + \\
&\lim_{\varepsilon\to 0}\int_{\Gamma_\varepsilon^+} S^*_{kij}\left[u_k\left(\mathbf{x}^f\right) - u_k\left(\mathbf{x}^s\right) - u_{k,m}\left(\mathbf{x}^s\right)\left(x^f_m - x^s_m\right)\right]d\Gamma + \\
&u_k\left(\mathbf{x}^s\right)\lim_{\varepsilon\to 0}\int_{\Gamma_\varepsilon^+} S^*_{kij}d\Gamma + u_{k,m}\left(\mathbf{x}^s\right)\int_{\Gamma_\varepsilon^+} S^*_{kij}\left(x^f_m - x^s_m\right)d\Gamma
\end{aligned} \tag{2.29}$$

The second term in the right side of Eq. 2.29 results in zero in the limit $\varepsilon \to 0$, from the Hölder continuity condition. The first and third terms result in equally opposite singularities (59, 60), which allows considering the Hadamard finite-part integral (HFP) as follows:

$$\begin{aligned}
&\lim_{\varepsilon\to 0}\int_{\Gamma-\Gamma_\varepsilon} S_{kij}u_k\left(\mathbf{x}^f\right)d\Gamma + u_k\left(\mathbf{x}^s\right)\lim_{\varepsilon\to 0}\int_{\Gamma_\varepsilon^+} S^*_{kij}d\Gamma = \\
&\lim_{\varepsilon\to 0}\left[\int_{\Gamma-\Gamma_\varepsilon} S^*_{kij}u_k\left(x^s\right)d\Gamma + u_k\left(x^f\right)\frac{b_{kij}\left(x^s\right)}{\varepsilon}\right] = \oint_\Gamma S^*_{kij}u_k\left(\mathbf{x}^f\right)d\Gamma
\end{aligned} \tag{2.30}$$

in which the symbol $\oint$ denotes the HFP integral.

The last integral term in Eq. 2.29 results in a free term $\gamma_{kijm}\left(\mathbf{x}^s\right)u_{k,m}\left(\mathbf{x}^s\right)$, in which γ_{kijm} is constant. This term is proportional to the displacements derivatives. (61) has demonstrated that adding this term to $\beta_{ij}(\mathbf{x}^s)u_j(\mathbf{x}^s)$ from Eq. 2.27 results in the following:

$$\beta_{kij}\left(\mathbf{x}^s\right)t_k\left(\mathbf{x}^s\right) + \gamma_{kijm}\left(\mathbf{x}^s\right)u_{k,m}\left(\mathbf{x}^s\right) = \frac{1}{2}\sigma_{ij}\left(\mathbf{x}^s\right) \tag{2.31}$$

in which $\sigma_{ij}(\mathbf{x}^s)$ is the Cauchy stress tensor. This expression is valid for $\mathbf{x}^s$ positioned at smooth boundaries (61).

The analysis of the domain integration term from Eq. 2.24 is similar to the analysis above-presented for the domain term in Eq. 2.20. Therefore, applying Eqs. 2.27, 2.30, 2.31 into Eq. 2.24, one writes:

$$\frac{1}{2}\sigma_{ij}\left(\mathbf{x}^s\right) + \oint_\Gamma S^*_{kij}u_k\left(\mathbf{x}^f\right)d\Gamma = \oint_\Gamma D^*_{kij}p_k\left(\mathbf{x}^f\right)d\Gamma + \int_\Gamma D^*_{kij}b_k d\Gamma \tag{2.32}$$

The Cauchy formula (Eq. A.3) can be applied into Eq. 2.32, which can then be rewritten as follows:

$$\frac{1}{2}t_j\left(\mathbf{x}^s\right)+\eta_i\left(\mathbf{x}^s\right)\oint\!\!\!\!\!\!-_{\Gamma} S^*_{kij}u_k\left(\mathbf{x}^f\right)d\Gamma = \eta_i\left(\mathbf{x}^s\right)\oint\!\!\!\!\!\!-_{\Gamma} D^*_{kij}t_k\left(\mathbf{x}^f\right)d\Gamma+\eta_i\left(\mathbf{x}^s\right)\int_{\Gamma} D^*_{kij}b_k d\Gamma \tag{2.33}$$

where $\eta_i\left(\mathbf{x}^s\right)$ are the components of the normal vector at $\mathbf{x}^s$. This vector is orthogonal to the boundary and must be pointed to the outside of Ω. This expression is known as tractions boundary integral equation (TBIE) or hypersingular form of the BEM.

It is worth mentioning that this work handles the regular integrals, as well as the CPV and HFP integrals through numerical integration. More details about the numerical schemes can be found in (62).

2.4 Boundary approximations via polynomials

The geometry and the mechanical fields (displacements and tractions) are numerically approximated at the boundary Γ. For that, Γ is subdivided into two-dimensional boundary elements, which may have two distinct approximations: via Lagrange polynomials or NURBS. The first type of approximation handled in this study is through the Lagrange polynomials. In this case, polynomial functions $M_i\left(\xi_1,\xi_2\right)$ are defined over a dimensionless parametric coordinates system $\xi_1\,\mathrm{x}\,\xi_2$, which is also called Gaussian space since $-1\leq\xi_1\leq 1\,,\ -1\leq\xi_2\leq 1$. The polynomial functions describe the geometry of Γ through nodal interpolation of the geometric nodes coordinates. Thus:

$$x_i\left(\xi_1,\xi_2\right)=M_j\left(\xi_1,\xi_2\right)X_i^j \tag{2.34}$$

where ξ_1 and ξ_2 are the dimensionless parametric coordinates of the x_i point, inside its respective element. X_i^j are the nodal coordinates in the global coordinate system of the same element.

Lagrangian isoparametric elements, in general, present the same approximation functions for both geometry and mechanical fields (displacements and tractions). However, defining different approximation functions for each purpose might be necessary due to discontinuities of boundary conditions or geometry. It is worth stressing that the boundary integral equations usually require a C^1 level of continuity at the source points. Therefore, different functions $N_\alpha\left(\xi_1,\xi_2\right)$, which are also Lagrange polynomials, approximate mechanical fields over the boundary elements. These functions interpolate displacements and tractions from their values at the collocation points, which are defined based on the geometric nodes. The approximation of displacements u_i and tractions t_i can be defined in a similar form as Eq. 2.34, as follows:

$$\begin{aligned} u_i\left(\xi_1,\xi_2\right) &= N_\alpha\left(\xi_1,\xi_2\right) u_i^\alpha \\ t_i\left(\xi_1,\xi_2\right) &= N_\alpha\left(\xi_1,\xi_2\right) t_i^\alpha \end{aligned} \tag{2.35}$$

in which u_i^α are the displacements at the collocation points α in the direction i, which is analogous for the tractions t_i^α.

2.4.1 Geometry approximation at the boundary

The interpolation functions $M_i\left(\xi_1,\xi_2\right)$ for the geometry, also called shape functions, are Lagrange polynomials that satisfy portion of unity (PU). This work deals with four different Lagrangian element types: linear quadrilateral (4-node) and triangular (3-node), quadratic quadrilateral (9-node) and triangular (6-node). Figure 5 illustrates the four types of elements in the Gaussian space.

Figure 5 – Lagrangian elements: linear triangular (3-node), quadratic triangular (6-node), linear quadrilateral (4-node) and quadratic quadrilateral (9-node)

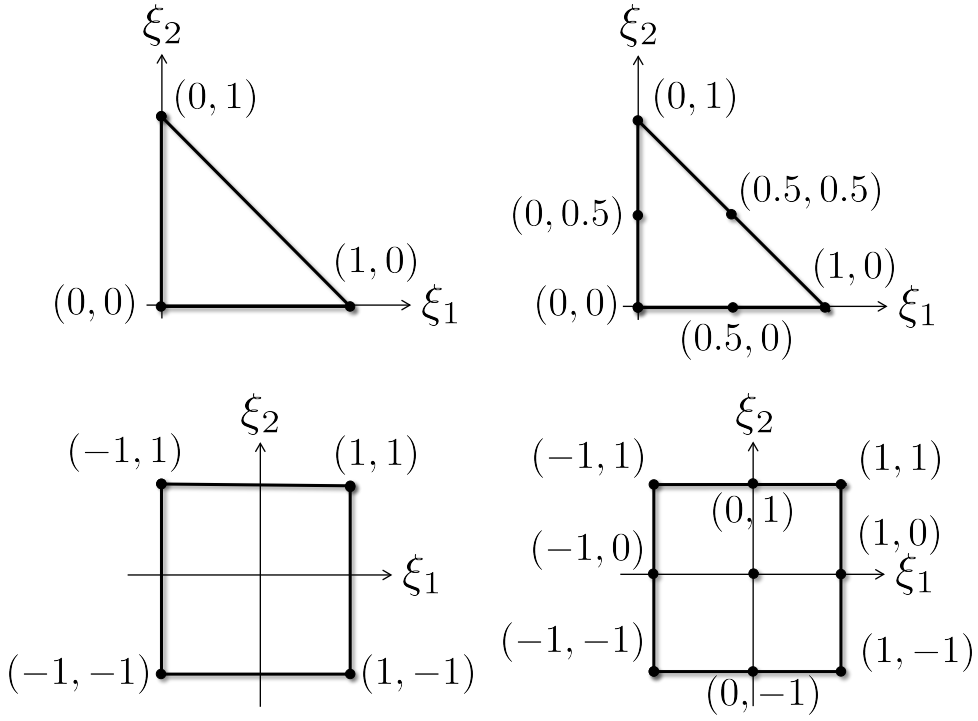

Source: The author.

The Lagrange polynomials are expressed as follows:

$$M_i\left(\xi_1,\xi_2\right) = c_1^i + c_2^i\xi_1 + c_3^i\xi_2 \qquad \text{for the 3-node element} \tag{2.36}$$

$$M_i\left(\xi_1,\xi_2\right) = c_1^i + c_2^i\xi_1 + c_3^i\xi_2 + c_4^i\xi_1\xi_2 + c_5^i\xi_1^2 + c_6^i\xi_2^2 \qquad \text{for the 6-node element} \tag{2.37}$$

$$M_i\left(\xi_1,\xi_2\right) = c_1^i + c_2^i\xi_1 + c_3^i\xi_2 + c_4^i\xi_1\xi_2 \qquad \text{for the 4-node element} \tag{2.38}$$

$$M_i(\xi_1,\xi_2) = c_1^i + c_2^i\xi_1 + c_3^i\xi_2 + c_4^i\xi_1\xi_2 + c_5^i\xi_1^2 + c_6^i\xi_2^2 + c_7^i\xi_1^2\xi_2 + c_8^i\xi_1^2\xi_2 + c_9^i\xi_1^2\xi_2^2 \quad \text{for the 9-node element} \tag{2.39}$$

The parameters c_k^i can be obtained by applying the Kronecker delta property of the shape functions at each node i:

$$M_i\left(\xi_1^j,\xi_2^j\right) = \begin{cases} 1, \text{ if } i = j \\ 0, \text{ if } i \neq j \end{cases} \tag{2.40}$$

in which i and j assume the values from 1 to n, being n the number of nodes in the element. Then, M_i is the shape function related to the node i. $\left(\xi_1^j,\xi_2^j\right)$ are the parametric coordinates of a node j.

The geometry approximation for a given element k, Eq. 2.34, can then be written algebraically as follows:

$$\mathbf{x}(\boldsymbol{\xi}) = \mathbf{M}^k(\boldsymbol{\xi})\,\mathbf{x}^k \tag{2.41}$$

where $\mathbf{x}^k = \left\{X_1^1 \quad X_2^1 \quad X_3^1 \quad \ldots \quad X_1^n \quad X_2^n \quad X_3^n\right\}^\intercal$ are the nodal coordinates (in the global system) of the nodes 1,2,...,n contained in the element k. $\mathbf{x}(\boldsymbol{\xi}) = \left\{x_1 \quad x_2 \quad x_3\right\}^\intercal$ is the vector of global coordinates of a given point inside the element k of parametric coordinates $\boldsymbol{\xi} = \left\{\xi_1 \quad \xi_2\right\}^\intercal$. $\mathbf{M}^k(\boldsymbol{\xi})$ contains the shape functions of each node i of the element k calculated at $\boldsymbol{\xi}$, as follows:

$$\mathbf{M}^k(\boldsymbol{\xi}) = \begin{bmatrix} M_1(\boldsymbol{\xi}) & 0 & 0 & & M_n(\boldsymbol{\xi}) & 0 & 0 \\ 0 & M_1(\boldsymbol{\xi}) & 0 & \cdots & 0 & M_n(\boldsymbol{\xi}) & 0 \\ 0 & 0 & M_1(\boldsymbol{\xi}) & & 0 & 0 & M_n(\boldsymbol{\xi}) \end{bmatrix} \tag{2.42}$$

In order to integrate the BEM kernels over the boundary elements, it is necessary to find the relation between the differential area elements from the global space and the Gaussian space. With that, the integrations may be performed numerically over the Gaussian space, which allows for applying Gaussian integration techniques. Then, for a give point over the surface Γ_e which global coordinates are $\mathbf{x}(\boldsymbol{\xi})$, the differential area element is written as a function of o the parametric coordinates as follows:

$$d\Gamma_e = \left|\frac{\partial \mathbf{x}(\boldsymbol{\xi})}{\partial \xi_1} \times \frac{\partial \mathbf{x}(\boldsymbol{\xi})}{\partial \xi_2}\right| d\xi_1 d\xi_2 = \left|\mathbf{jac}(\boldsymbol{\xi})\right| d\xi_1 d\xi_2 \tag{2.43}$$

where jac($\boldsymbol{\xi}$) is the Jacobian vector defined as the result of the above-presented vector product, which can be written as:

$$\mathbf{jac}(\boldsymbol{\xi}) = \begin{Bmatrix} \frac{\partial x_2(\boldsymbol{\xi})}{\partial \xi_1}\frac{\partial x_3(\boldsymbol{\xi})}{\partial \xi_2} - \frac{\partial x_3(\boldsymbol{\xi})}{\partial \xi_1}\frac{\partial x_2(\boldsymbol{\xi})}{\partial \xi_2} \\ \frac{\partial x_3(\boldsymbol{\xi})}{\partial \xi_1}\frac{\partial x_1(\boldsymbol{\xi})}{\partial \xi_2} - \frac{\partial x_1(\boldsymbol{\xi})}{\partial \xi_1}\frac{\partial x_3(\boldsymbol{\xi})}{\partial \xi_2} \\ \frac{\partial x_1(\boldsymbol{\xi})}{\partial \xi_1}\frac{\partial x_2(\boldsymbol{\xi})}{\partial \xi_2} - \frac{\partial x_1(\boldsymbol{\xi})}{\partial \xi_2}\frac{\partial x_2(\boldsymbol{\xi})}{\partial \xi_1} \end{Bmatrix} \tag{2.44}$$

in which the partial derivatives of x_i with respect to ξ_i are obtained from differentiating Eq. 2.41 with respect to $\boldsymbol{\xi}$. It is possible to notice that the Jacobian expression is in fact a vector product of two tangent vectors. Thus, the Jacobian vector is a normal outward vector of the surface Γ_e at the point $\mathbf{x}(\boldsymbol{\xi})$. Consequently, a unitary normal outward vector $\eta_i(\boldsymbol{\xi})$ can be obtained through:

$$\eta_i(\boldsymbol{\xi}) = \frac{jac_i(\boldsymbol{\xi})}{|\mathbf{jac}(\boldsymbol{\xi})|} \tag{2.45}$$

For the adequate compatibility of the terms from the TBIE (Eq. 2.33), a normal outward matrix $\mathfrak{N}(\boldsymbol{\xi})$ for the point $\boldsymbol{\xi}$ is defined as follows:

$$\mathfrak{N}(\boldsymbol{\xi}) = \begin{bmatrix} \eta_1(\boldsymbol{\xi}) & 0 & 0 & & \eta_3(\boldsymbol{\xi}) & 0 & 0 \\ 0 & \eta_1(\boldsymbol{\xi}) & 0 & \cdots & 0 & \eta_3(\boldsymbol{\xi}) & 0 \\ 0 & 0 & \eta_1(\boldsymbol{\xi}) & & 0 & 0 & \eta_3(\boldsymbol{\xi}) \end{bmatrix} \tag{2.46}$$

2.4.2 Mechanical fields approximation at the boundary

The interpolation functions $N_\alpha(\xi_1,\xi_2)$ adopted to represent the mechanical fields are also Lagrange polynomials. However, their coefficients c_k^i are obtained by applying Eq. 2.40 to the collocation points instead of the geometric nodes. In this case, the collocation points may differ from the geometric nodes by considering the possibility of discontinuous elements, as illustrated in Fig. 6.

In continuous elements, all collocation points coincide with the geometric nodes, thus $N_\alpha(\xi_1,\xi_2) = M_i(\xi_1,\xi_2)$. Nevertheless, discontinuous elements are applied in the case of geometrical or boundary conditions discontinuities between two adjacent elements, which requires moving the collocation points away from the discontinuous edge. Then, those collocation points are positioned inside the element, as illustrated in Fig. 6(b) and 6(c), which guarantees the continuity requirement of the boundary integral equations. Therefore, edge-discontinuous elements are applied when one or more edges of the elements are discontinuous, whereas fully discontinuous elements represent the case in which all edges are discontinuous.

It is worth mentioning the distance that collocation points are moved away from the discontinuous edge, which have been tested in previous studies: (62, 63) for 3D formulations

Figure 6 – Continuous elements (a), edge-discontinuous elements (b) and fully discontinuous elements (c)

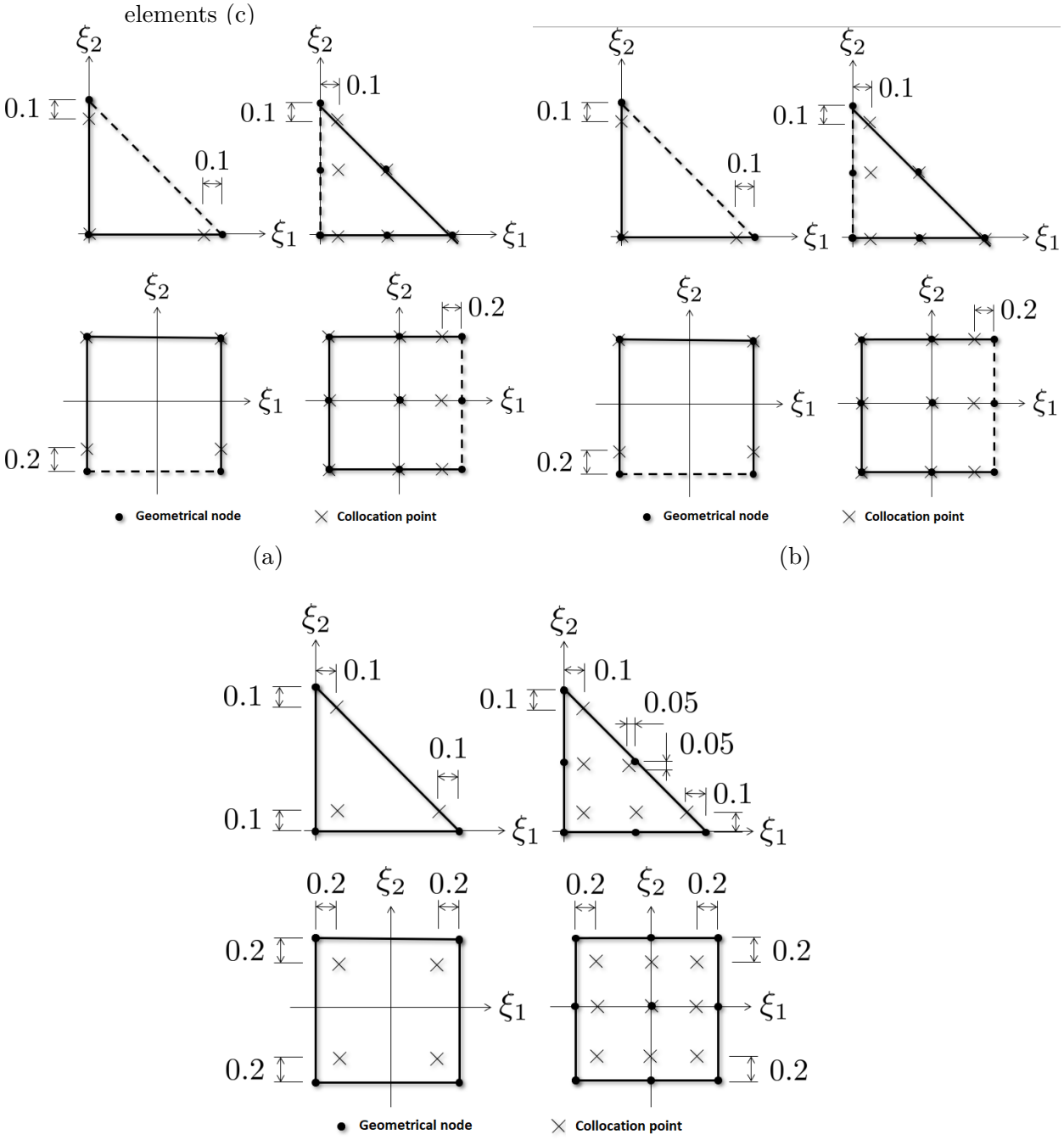

Source: The author.

and (64, 65, 66) for 2D formulations. Besides, the distances illustrated in Fig. 6 follow the ranges for discontinuous elements suggested by Aliabadi (58).

Then, the coefficients of $N_\alpha(\xi_1,\xi_2)$ are defined as follows:

$$N_\alpha\left(\xi_1^j,\xi_2^j\right) = \begin{cases} 1, \text{ se } \alpha = j \\ 0, \text{ se } \alpha \neq j \end{cases} \tag{2.47}$$

in which α and j assume the values of collocation points from 1 to n, being n the total

number of collocation points at the current element.

Having the functions $N_\alpha(\xi_1,\xi_2)$ defined, the mechanical fields approximation (Eq. 2.35) can be algebraically written for a given element α as follows:

$$\begin{aligned}\mathbf{u}(\boldsymbol{\xi}) &= \mathbf{N}^\alpha(\boldsymbol{\xi})\,\mathbf{u}^\alpha \\ \mathbf{t}(\boldsymbol{\xi}) &= \mathbf{N}^\alpha(\boldsymbol{\xi})\,\mathbf{t}^\alpha\end{aligned} \tag{2.48}$$

where $\mathbf{u}^\alpha = \begin{Bmatrix} u_1^1 & u_2^1 & u_3^1 & \dots & u_1^n & u_2^n & u_3^n \end{Bmatrix}^\intercal$ are the displacements at each one of the collocation points 1,2,...,n of the element α. $\mathbf{u}(\boldsymbol{\xi}) = \begin{Bmatrix} u_1 & u_2 & u_3 \end{Bmatrix}^\intercal$ is the vector of displacements at a given point over the surface Γ_α of the element, with parametric coordinates $\boldsymbol{\xi} = \begin{Bmatrix} \xi_1 & \xi_2 \end{Bmatrix}^\intercal$. The same definitions are valid for tractions $\mathbf{t}(\boldsymbol{\xi})$ and $\mathbf{t}^\alpha$. $N_\alpha(\boldsymbol{\xi})$ contains the interpolation functions of the element α calculated at $\boldsymbol{\xi}$ and is organized similarly to Eq. 2.42.

2.5 Boundary approximations via NURBS

The second type of approximation handled in this study is via NURBS, which leads to the IGABEM formulation. This section presents the NURBS formulation and further details about this matter can be found in (16, 62).

NURBS functions can be obtained from the projection of B-splines. The univariate B-splines are piecewise parametric recursive functions defined over a knot vector $\mathbf{U} = \{u_1,u_2,...,u_k\}$ containing k values of the independent parameter u (called knots). It is worth mentioning that, whereas the parametric space is a Gaussian space in the Lagrangian BEM, in the IGABEM the parametric space regards the knot vector space, which is not Gaussian. Then, the knot vector defines the basis functions for the B-spline. The curve may be represented by n geometric parameters called control points and basis functions $N_{i,p}(u)$, as follows:

$$C_j(u) = \sum_{i=1}^{n} N_{i,p}(u) P_j^i \tag{2.49}$$

where C_j represents the position (considering a global coordinate system) of the point with parametric coordinate u. P_j^i is the set that contains the position j of the control point i, where n is the total of control points and p is the degree of the B-spline curve. It is worth mentioning that the size of the knot vector is $t = n + p + 1$ for open knot vectors, which have the first and last knots with a multiplicity $p + 1$ and enforce an interpolatory behavior of the curve at the first and last control points. This study handles only open knot vectors because its use is common in CAD packages (67).

The basis functions $N_{i,p}(u)$ can be defined recursively from the Cox-de-Boor formula (68, 69):

$$N_{i,p}(u) = \frac{u - u_i}{u_{i+p} - u_i} N_{i,p-1}(u) + \frac{u_{i+p+1} - u}{u_{i+p+1} - u_{i+1}} N_{i+1,p-1}(u) \tag{2.50}$$

where the zero order basis functions are:

$$N_{i,0}(u) = \begin{cases} 1 & u_i \leq u < u_{i+1} \\ 0 & \text{otherwise} \end{cases} \tag{2.51}$$

The derivative of the B-spline curve is necessary to calculate tangent and normal outward vectors. Then, the basis function's derivative of order d is also recursive and it is defined as follows:

$$N_{i,p}^{(d)} = p \left(\frac{N_{i,p-1}^{(d-1)}}{u_{i+p} - u_i} - \frac{N_{i+1,p-1}^{(d-1)}}{u_{i+p+1} - u_{i+1}} \right) \tag{2.52}$$

The B-splines basis functions have interesting mathematical properties (70), mainly regarding continuity. $N_{i,p}(u)$ are all C^∞ at points positioned inside knot spans ($u_i < u \leq u_{i+1}$) and are C^{p-k} continuous at the knots ($u = u_i$), in which k is the multiplicity of the knot value u_i. Besides, the B-spline basis functions constitute a partition of unity, i.e., $\sum_{i=1}^{n} N_{i,p}(u) = 1$, $\forall u$ and are all positive, i.e., $N_{i,p} \geq 0$.

It is worth stressing that it is usual to obtain values such as $0/0$ when evaluating the basis functions and their derivatives (Equation 2.50 and 2.52). In these cases, it is adopted $0/0 = 0$ to proceed the analysis (16).

NURBS curves are defined from open B-Spline curves with the addition of an extra parameter for each control point i, called weight w_i. Then, the parametric curve is obtained from a ratio of two basis function, which is weighted by w_i, as follows:

$$C_j(u) = \frac{\sum\limits_{i=1}^{n} N_{i,p}(u) w_i P_j^i}{\sum\limits_{k=1}^{n} N_{k,p}(u) w_k} = \sum_{i=1}^{n} R_{i,p}(u) P_j^i \tag{2.53}$$

in which $R_{i,p}$ are the rational basis functions defined as:

$$R_{i,p}(u) = \frac{N_{i,p}(u) w_i}{\sum\limits_{k=1}^{n} N_{k,p}(u) w_k} \tag{2.54}$$

The rational basis function's derivatives of order d are recursively calculated as:

$$R_{i,p}^{(d)}(u) = \frac{w_i N_{i,p}^{(d)} - \sum\limits_{l=1}^{d} \left[\binom{d}{l} \sum\limits_{j=1}^{n} N_{j,p}^{(l)} w_j R_{i,p}^{(d-l)}(u) \right]}{\sum\limits_{j=1}^{n} N_{j,p}(u) w_j} \tag{2.55}$$

For the 3D IGABEM, two-dimensional surfaces must be represented through NURBS. Then, regular bi-variate NURBS surfaces $\mathbf{S}(\xi,\eta)$ can be obtained by the tensor product of two uni-variate NURBS curves of knot vectors $\Xi = \{\xi_1,...,\xi_{n+p+1}\}$ and $\mathfrak{N} = \{\eta_1,...,\eta_{m+q+1}\}$, where p and q are the respective polynomial orders. In this case, it is defined a net of control points $\mathbf{B}^{ij}$, $i = 1,...,n$ and $j = 1,...,m$, which results in $n * m$ control points with respective weights w_ij. Therefore, one writes the representation of a regular NURBS surface as follows:

$$\mathbf{S}_k(\xi,\eta) = \frac{\sum_{\alpha=1}^{n}\sum_{\beta=1}^{m} N_{\alpha,p}(\xi)M_{\beta,q}(\eta)w_{\alpha\beta}\mathbf{B}_k^{\alpha\beta}}{\sum_{\alpha=1}^{n}\sum_{\beta=1}^{m} N_{\alpha,p}(\xi)M_{\beta,q}(\eta)w_{\alpha\beta}} = \sum_{i=1}^{n}\sum_{j=1}^{m} R_{ij,pq}(\xi,\eta)\mathbf{B}_k^{ij} \tag{2.56}$$

in which $\mathbf{S}_k(\xi,\eta)$ is the position of the point with parametric coordinates ξ and η. $N_{\alpha,p}$ and $M_{\beta,q}$ are the uni-variate basis functions of the directions ξ and η, respectively, and are given by Eq. 2.50. The bi-variate rational basis functions is expressed as follows:

$$R_{ij,pq}(\xi,\eta) = \frac{N_{i,p}(\xi)M_{j,q}(\eta)w_{ij}}{\sum_{i=1}^{n}\sum_{j=1}^{m} N_{i,p}(\xi)M_{j,q}(\eta)w_{ij}} \tag{2.57}$$

The rational basis functions also approximate displacements $\mathbf{u}^e(\xi,\eta)$ and tractions $\mathbf{t}^e(\xi,\eta)$ in a NURBS surface e as follows:

$$\begin{aligned}\mathbf{u}^e(\xi,\eta) &= \sum_{i=1}^{n}\sum_{j=1}^{m} R^e_{ij,pq}(\xi,\eta)\hat{\mathbf{u}}^e_{\mathrm{inc}(i,j,e)} \\ \mathbf{t}^e(\xi,\eta) &= \sum_{i=1}^{n}\sum_{j=1}^{m} R^e_{ij,pq}(\xi,\eta)\hat{\mathbf{t}}^e_{\mathrm{inc}(i,j,e)}\end{aligned} \tag{2.58}$$

where $\hat{\mathbf{u}}_{\mathrm{inc}(i,j,e)}$ and $\hat{\mathbf{t}}_{\mathrm{inc}(i,j,e)}$ are the variables for the displacements and tractions approximations, respectively, at each one of the control points denoted by $\mathrm{inc}(i,j,e)$. Unlike Lagrangian approximations, these variables do not have physical meaning because the rational basis functions do not satisfy the Kronecker delta property at the control points. The function inc() refers to the connectivity of the NURBS regarding the global and local numbering of the control points mesh. This expression can be written in the algebraic form as follows:

$$\begin{aligned}\mathbf{u}(\mathbf{x}) &= \mathbf{N}^\alpha\hat{\mathbf{u}}^\alpha \\ \mathbf{t}(\mathbf{x}) &= \mathbf{N}^\alpha\hat{\mathbf{t}}^\alpha\end{aligned} \tag{2.59}$$

in which $\mathbf{u}(\mathbf{x})$ and $\mathbf{t}(\mathbf{x})$ are, respectively, the displacements and tractions of a given point $\mathbf{x} = \mathbf{x}(\xi) = \mathbf{x}(\xi,\eta)$ with parametric coordinates ξ and η inside the NURBS α. $\mathbf{N}^\alpha$ represents the bi-variate rational basis functions $R^\alpha_{ij,pq}$, defined by Eq. 2.57. $\hat{\mathbf{u}}^\alpha$ and $\hat{\mathbf{t}}^\alpha$ are vectors

that contain $\hat{\mathbf{u}}_{\text{inc}(i,j,e)}$ and $\hat{\mathbf{t}}_{\text{inc}(i,j,e)}$, respectively, of all of the control points present in α. It is worth mentioning that this expression replaces Eq. 2.48 from the Lagrangian approach.

The piecewise parametric behaviour of the B-Splines is also observed in the NURBS curves and surfaces. In fact, NURBS surfaces present two-dimensional piecewise divisions $[\xi_i,\ldots,\xi_{i+p+1}] \times [\eta_j,\ldots,\eta_{j+q+1}]$, which are called knot spans. Figure 7 illustrates the piecewise characteristic of a NURBS surface, highlighting the region correspondent to a knot span. The knot spans represent the domain for integration in the IGABEM formulation, which can be understood as similar to the elements in the Lagrangian BEM. The continuity properties of the B-Splines are still valid for NURBS surfaces, therefore C^∞ is guaranteed inside the knot span.

Figure 7 – Illustration of a NURBS surface in space, highlighting the region correspondent to a knot span.

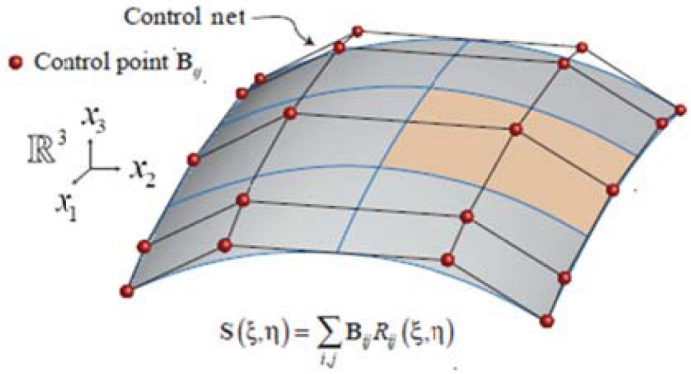

Source: (8), adapted.

Thus, the parametric local space inside a knot span can be converted into a Gaussian space $[-1,1] \times [-1,1]$ for the integration, also called parent space, as follows:

$$\begin{aligned} \xi &= \frac{(\xi_{i+p+1} - \xi_i)\hat{\xi} + (\xi_{i+p+1} + \xi_i)}{2} \\ \eta &= \frac{(\eta_{i+q+1} - \eta_i)\hat{\eta} + (\eta_{i+q+1} + \eta_i)}{2} \end{aligned} \tag{2.60}$$

in which $(\hat{\xi},\hat{\eta}) \in [-1,1] \times [-1,1]$ are the parent space coordinates and $(\xi,\eta) \in [\xi_i,\xi_{i+p+1}] \times [\eta_i,\eta_{i+q+1}]$ are the parametric coordinates. Figure 8 illustrates the transformation between the parametric space (of the knot vectors) and the parent space (Gaussian) for a given NURBS surface. It is worth stressing that this transformation occurs locally inside a knot span.

This transformation allows for using the same standard Gauss-Legendre quadrature from the Lagrangian BEM for the numerical integrations herein. The additional coordinate transformation introduces a new Jacobian $\hat{J}$, in addition to the traditional Jacobian presented in Eq. 2.44. $\hat{J}$ can be written as:

Figure 8 – Example of transformation between parametric space and parent space.

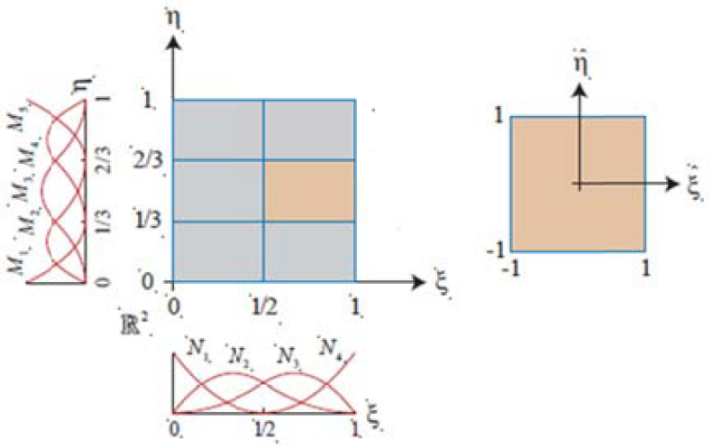

Source: (8).

$$\hat{J} = \frac{\partial \mathbf{S}}{\partial \xi}\frac{(\xi_{i+p+1} - \xi_i)}{2} + \frac{\partial \mathbf{S}}{\partial \eta}\frac{(\eta_{i+q+1} - \eta_i)}{2} \tag{2.61}$$

It is worth mentioning that the multiplicity of knots inside the knot vectors may lead to some knot spans with initial and final knots with the same value. In this case, the knot span is called trivial and does not need to be part of the integration. For instance, Fig. 9 illustrates how a NURBS surface with $\Xi = [0,0,0,1/2,1,1,1]$ and $\mathfrak{N} = [0,0,0,1/3,2/3,1,1,1]$ presents 36 trivial knot spans and only 6 nontrivial ones due to the multiplicity of the first and last knots in the knot vectors.

Figure 9 – Illustration of trivial and non-trivial knot spans in a given NURBS surface. Parametric space.

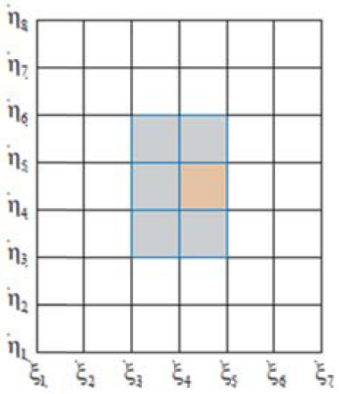

Source: (8).

During the integration process, the equations presented for the Lagrangian BEM (Eq. 2.42 to Eq. 2.46) are still valid herein, considering the adequate approximation functions. Since the integrations are carried out through the same Gaussian scheme for numerical integration, the techniques presented in Sec. 2.3 are properly applied for both

the Lagrangian BEM and the IGABEM. More details about the integration process in the 3D IGABEM are available in the literature (71, 67).

2.5.1 Collocation Strategy

With the discretization of Γ into NURBS surfaces, the collocation points (which are applied in Eq. 2.23 and Eq. 2.33 as source points) must be defined. Unlike Lagrangian formulations, the collocation points differ from the control points that represent the NURBS in the IGA formulation. This happens because the control points are not necessarily positioned at the boundary, thus the integral equations and elasticity relations may not apply to them. Because of that, a collocation strategy based on the Greville abscissae (72) is adopted herein. In this technique, the collocation points parametric coordinates (ξ_i^0,η_i^0) are defined from the original knot vectors $\boldsymbol{\Xi} = \{\xi_1,...,\xi_{n+p+1}\}$ and $\boldsymbol{\mathfrak{N}} = \{\eta_1,...,\eta_{m+q+1}\}$, as follows:

$$\begin{aligned} \xi_i^0 &= \frac{\xi_{i+1} + \xi_{i+1} + \cdots + \xi_{i+p}}{p} \quad , \quad i = 1,2,\ldots,n \\ \eta_j^0 &= \frac{\eta_{j+1} + \eta_{j+1} + \cdots + \eta_{j+q}}{q} \quad , \quad j = 1,2,\ldots,m \end{aligned} \tag{2.62}$$

This technique requires a slight adaptation to guarantee that all collocation points are positioned at smooth boundaries, which means they cannot be at the extremities of the NURBS surfaces. This adaptation is based on the concept of discontinuous NURBS surfaces (67) and it produces updated knot vectors $\boldsymbol{\Xi}^*$ and $\boldsymbol{\mathfrak{N}}^*$ that replace the original ones $\boldsymbol{\Xi}$ and $\boldsymbol{\mathfrak{N}}$. Figure 10 illustrates this technique applied for a NURBS surface with original knot vectors $\boldsymbol{\Xi} = [0,0,0,1,2,3,4,5,5,5]$ and $\boldsymbol{\mathfrak{N}} = [0,0,0,1,2,3,4,5,5,5]$.

Figure 10 – Example of discontinuous NURBS surfaces: (a) original knot vectors and (b) updated knot vectors.

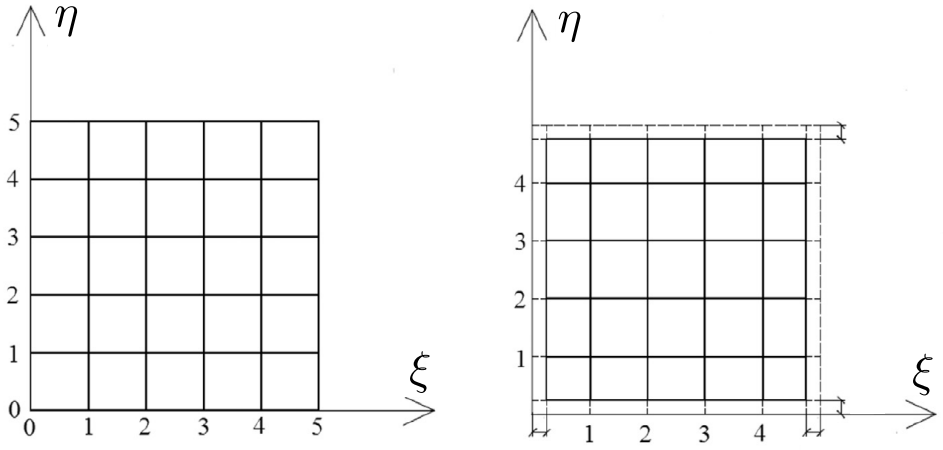

Source: (67), adapted.

For a given knot span $[\xi_a,\xi_b] \times [\eta_a,\eta_b]$, the updated knots are obtained as follows:

$$\xi_a^* = \begin{cases} \xi_a + 0.1(\xi_b - \xi_a) & \text{if multiplicity of } \xi_a \text{ is } p \\ \xi_a & \text{otherwise} \end{cases}$$
$$\xi_b^* = \begin{cases} \xi_b - 0.1(\xi_b - \xi_a) & \text{if multiplicity of } \xi_b \text{ is } p \\ \xi_b & \text{otherwise} \end{cases} \tag{2.63}$$

$$\eta_a^* = \begin{cases} \eta_a + 0.1(\eta_b - \eta_a) & \text{if multiplicity of } \eta_a \text{ is } q \\ \eta_a & \text{otherwise} \end{cases}$$
$$\eta_b^* = \begin{cases} \eta_b - 0.1(\eta_b - \eta_a) & \text{if multiplicity of } \eta_b \text{ is } q \\ \eta_b & \text{otherwise} \end{cases} \tag{2.64}$$

Therefore, the collocation strategy guarantees the continuity C^1 at all collocation points, in addition to produce a number of collocation points always equal to the number of control points.

2.6 The BEM algebraic equations

After applying the numerical technique and discretising Γ into Ne NURBS surfaces (or Lagrangian elements), the continuous boundary integral equations can be written in an algebraic numerical form. The DBIE (Eq. 2.23) and the TBIE (Eq. 2.33), respectively, are evaluated considering each collocation point as the source point $\mathbf{x}^s$ as follows:

$$\begin{aligned} &\mathbf{C}\left(\mathbf{x}^s\right)\mathbf{N}^{\bar{\alpha}}(\mathbf{x}^s)\hat{\mathbf{u}}^{\bar{\alpha}}_{\mathrm{inc}(\mathbf{x}^s)} + \sum_{\alpha=1}^{Ne}\int_{\Gamma_\alpha}\mathbf{T}\left(\mathbf{x}\left(\boldsymbol{\xi}\right),\mathbf{x}^s\right)\mathbf{N}^\alpha\left(\boldsymbol{\xi}\right)\left|\mathbf{jac}^\alpha\left(\boldsymbol{\xi}\right)\right|\hat{J}d\hat{\xi}d\hat{\eta}\;\hat{\mathbf{u}}^\alpha \\ &\qquad = \sum_{\alpha=1}^{Ne}\int_{\Gamma_\alpha}\mathbf{U}\left(\mathbf{x}\left(\boldsymbol{\xi}\right),\mathbf{x}^s\right)\mathbf{N}^\alpha\left(\boldsymbol{\xi}\right)\left|\mathbf{jac}^\alpha\left(\boldsymbol{\xi}\right)\right|\hat{J}d\hat{\xi}d\hat{\eta}\;\hat{\mathbf{t}}^\alpha + \int_\Omega U^*_{ki}b_i d\Omega \end{aligned} \tag{2.65}$$

$$\begin{aligned} &\frac{1}{2}\mathbf{N}^{\bar{\alpha}}(\mathbf{x}^s)\hat{\mathbf{t}}^{\bar{\alpha}}_{\mathrm{inc}(\mathbf{x}^s)} + \mathfrak{N}\left(\mathbf{x}^s\right)\sum_{\alpha=1}^{Ne}\int_{\Gamma_\alpha}\mathbf{S}\left(\mathbf{x}\left(\boldsymbol{\xi}\right),\mathbf{x}^s\right)\mathbf{N}^\alpha\left(\boldsymbol{\xi}\right)\left|\mathbf{jac}^\alpha\left(\boldsymbol{\xi}\right)\right|\hat{J}d\hat{\xi}d\hat{\eta}\;\hat{\mathbf{u}}^\alpha \\ &\qquad = \mathfrak{N}\left(\mathbf{x}^s\right)\sum_{\alpha=1}^{Ne}\int_{\Gamma_\alpha}\mathbf{D}\left(\mathbf{x}\left(\boldsymbol{\xi}\right),\mathbf{x}^s\right)\mathbf{N}^\alpha\left(\boldsymbol{\xi}\right)\left|\mathbf{jac}^\alpha\left(\boldsymbol{\xi}\right)\right|\hat{J}d\hat{\xi}d\hat{\eta}\;\hat{\mathbf{t}}^\alpha + \eta_i\left(\mathbf{x}^s\right)\int_\Omega D^*_{kij}b_k d\Omega \end{aligned} \tag{2.66}$$

in which $\mathbf{U}(\mathbf{x}(\boldsymbol{\xi}),\mathbf{x}^s)$ and $\mathbf{T}(\mathbf{x}(\boldsymbol{\xi}),\mathbf{x}^s)$ contain the fundamental solutions U_{ij} and T_{ij}, respectively, evaluated at the field point $\mathbf{x}(\boldsymbol{\xi})$ considering the source point $\mathbf{x}^s$. $\bar{\alpha}$ is the NURBS surface (or Lagrangian element) that contains $\mathbf{x}^s$. The index $\mathrm{inc}(\mathbf{x}^s)$ represents the variables related to the nodes of $\bar{\alpha}$. The field point $\mathbf{x}(\boldsymbol{\xi})$ is defined by the parametric coordinates, being $\boldsymbol{\xi} = (\xi,\eta)$ for NURBS or $\boldsymbol{\xi} = (\xi_1,\xi_2)$ for Lagrangian elements. $\mathbf{C}\left(\mathbf{x}^s\right)$ represents the free term, which is equal $\delta_{ij}/2$ for source points positioned at smooth boundaries. Γ_α denotes the surface of α, which is defined over the parametric space. $\mathfrak{N}\left(\mathbf{x}^s\right)$

contains the components of the normal outward vector at the source point. $\mathbf{S}(\mathbf{x}(\boldsymbol{\xi}),\mathbf{x}^s)$ and $\mathbf{D}(\mathbf{x}(\boldsymbol{\xi}),\mathbf{x}^s)$ contains the fundamental solutions S_{kij} and D_{kij}, which are arranged as follows:

$$\begin{aligned}\mathbf{S}\left(\mathbf{x}\left(\boldsymbol{\xi}\right),\mathbf{x}^s\right) &= S_{(j+3i-3)k}\left(\mathbf{x}\left(\boldsymbol{\xi}\right),\mathbf{x}^s\right)\\ \mathbf{D}\left(\mathbf{x}\left(\boldsymbol{\xi}\right),\mathbf{x}^s\right) &= D_{(j+3i-3)k}\left(\mathbf{x}\left(\boldsymbol{\xi}\right),\mathbf{x}^s\right)\end{aligned} \tag{2.67}$$

It is worth stressing that the domain terms in both Eq. 2.65 and Eq. 2.66 cannot be algebraically written yet, because they have not been numerically treated so far. This term will be used in the next chapter to write the compatibility with the reinforcements.

The BEM algebraic equations must be evaluated for all collocation points, considering each one as the source point in Eq. 2.65 and Eq. 2.66. Each collocation point produces a DBIE and a TBIE algebraic equation. Thus, when one considers all collocation points in the mesh, systems of algebraic equations can be written as follows:

$$\begin{aligned}&\mathbf{C}_i\mathbf{N}^\alpha\hat{\mathbf{u}}_i + \sum_{\alpha=1}^{Ne}\int_{\Gamma_\alpha}\mathbf{T}\left(\mathbf{x}\left(\boldsymbol{\xi}\right),\mathbf{x}^i\right)\mathbf{N}^\alpha\left(\boldsymbol{\xi}\right)\left|\mathbf{jac}^\alpha\left(\boldsymbol{\xi}\right)\right|\hat{J}d\hat{\xi}d\hat{\eta}\;\hat{\mathbf{u}}_j\\ &\qquad= \sum_{\alpha=1}^{Ne}\int_{\Gamma_\alpha}\mathbf{U}\left(\mathbf{x}\left(\boldsymbol{\xi}\right),\mathbf{x}^i\right)\mathbf{N}^\alpha\left(\boldsymbol{\xi}\right)\left|\mathbf{jac}^\alpha\left(\boldsymbol{\xi}\right)\right|\hat{J}d\hat{\xi}d\hat{\eta}\;\hat{\mathbf{t}}_j + \int_\Omega U^*_{ki}b_i d\Omega\end{aligned} \tag{2.68}$$

$$\begin{aligned}&\frac{1}{2}\mathbf{N}^\alpha\hat{\mathbf{t}}_i + \mathfrak{N}_i\sum_{\alpha=1}^{Ne}\int_{\Gamma_\alpha}\mathbf{S}\left(\mathbf{x}\left(\boldsymbol{\xi}\right),\mathbf{x}^i\right)\mathbf{N}^\alpha\left(\boldsymbol{\xi}\right)\left|\mathbf{jac}^\alpha\left(\boldsymbol{\xi}\right)\right|\hat{J}d\hat{\xi}d\hat{\eta}\;\hat{\mathbf{u}}_j\\ &\qquad= \mathfrak{N}_i\sum_{\alpha=1}^{Ne}\int_{\Gamma_\alpha}\mathbf{D}\left(\mathbf{x}\left(\boldsymbol{\xi}\right),\mathbf{x}^i\right)\mathbf{N}^\alpha\left(\boldsymbol{\xi}\right)\left|\mathbf{jac}^\alpha\left(\boldsymbol{\xi}\right)\right|\hat{J}d\hat{\xi}d\hat{\eta}\;\hat{\mathbf{t}}_j + \eta_i\left(\mathbf{x}^s\right)\int_\Omega D^*_{kij}b_k d\Omega\end{aligned} \tag{2.69}$$

in which $\hat{\mathbf{u}}_j$ and $\hat{\mathbf{t}}_j$ contain the control point's parameters for displacements and tractions as $\mathbf{u}_j = \left\{\mathbf{u}^1 \quad ... \quad \mathbf{u}^\alpha \quad ... \quad \mathbf{u}^{Ne}\right\}^\intercal$ and $\mathbf{t}_j = \left\{\mathbf{t}^1 \quad ... \quad \mathbf{t}^\alpha \quad ... \quad \mathbf{t}^{Ne}\right\}$. It is worth stressing that in the Lagrangian BEM, the control points coincide with the collocation points and the above-mentioned parameters are nodal displacements and tractions.

The terms related to $\mathbf{U}(\mathbf{x}(\boldsymbol{\xi}),\mathbf{x}^s)$ and $\mathbf{T}(\mathbf{x}(\boldsymbol{\xi}),\mathbf{x}^s)$ in Eq. 2.68 can be denoted by $\bar{\mathbf{H}}$ and $\mathbf{G}$, respectively. As well as $\mathbf{H}'$ and $\bar{\mathbf{G}}'$, which denote the terms related to $\mathbf{S}(\mathbf{x}(\boldsymbol{\xi}),\mathbf{x}^s)$ and $\mathbf{D}(\mathbf{x}(\boldsymbol{\xi}),\mathbf{x}^s)$ in Eq. 2.69. Besides, $\mathbf{N}^\alpha$ can be incorporated to the free term matrix $\mathbf{C}_i$. Therefore, those expressions can be rewritten as follows:

$$\mathbf{C}_i\hat{\mathbf{u}}_i + \bar{\mathbf{H}}_{ij}\hat{\mathbf{u}}_j = \mathbf{G}_{ij}\hat{\mathbf{t}}_j + \int_\Omega U^*_{ki}b_i d\Omega \tag{2.70}$$

$$\bar{\mathbf{C}}_i\hat{\mathbf{t}}_i + \mathbf{H'}_{ij}\hat{\mathbf{u}}_j = \bar{\mathbf{G}'}_{ij}\hat{\mathbf{t}}_j + \eta_i\left(\mathbf{x}^s\right)\int_\Gamma D^*_{kij}b_k d\Gamma \tag{2.71}$$

where $\bar{\mathbf{C}}_\mathbf{i}$ contains the TBIE free term for each source point i.

The free term from Eq. 2.70 can be added to $\bar{\mathbf{H}}$ as follows:

$$\mathbf{H}_{ij} = \begin{cases} \bar{\mathbf{H}}_{ij} & if \quad i \neq j \\ \bar{\mathbf{H}}_{ij} + \mathbf{C}_i & if \quad i = j \end{cases} \tag{2.72}$$

The free term from Eq. 2.71 can be added to $\bar{\mathbf{G}}'$ as follows:

$$\mathbf{G'}_{ij} = \begin{cases} \bar{\mathbf{G}}'_{ij} & if \quad i \neq j \\ \bar{\mathbf{G}}'_{ij} - \bar{\mathbf{C}}_i & if \quad i = j \end{cases} \tag{2.73}$$

Equations 2.72 and 2.70 can now be applied into Eq. 2.73 and Eq. 2.71. Therefore, both DBIE and TBIE result in algebraic systems of equations, which can be written as follows:

$$\mathbf{H}\hat{\mathbf{u}} = \mathbf{G}\hat{\mathbf{t}} + \mathfrak{b} \tag{2.74}$$

in which $\hat{\mathbf{u}}$ and $\hat{\mathbf{t}}$ contain all variables for displacements and tractions at the control points, respectively. $\mathbf{H}$ and $\mathbf{G}$ represent the global matrices resulting from $\mathbf{H}_{ij}$ and $\mathbf{G}_{ij}$ for the DBIE, or $\mathbf{H'}_{ij}$ and $\mathbf{G'}_{ij}$ for the TBIE. $\mathfrak{b}$ represent the vector resulting from the domain term, which depends on the chosen equation as follows:

$$\mathfrak{b} = \begin{cases} \int_\Omega U^*_{ki} b_i d\Omega & \text{for DBIE} \\ \eta_i\left(\mathbf{x}^s\right) \int_\Omega D^*_{kij} b_k d\Omega & \text{for TBIE} \end{cases} \tag{2.75}$$

It is worth mentioning that Eq. 2.74 results in a square system (equal number of lines and columns) only if the number of collocation points and control points are the same. In the IGABEM, this feature is guaranteed by the collocation strategy adopted herein and previously presented in Sec. 2.5.1. Whereas in the Lagrangian BEM, such feature is naturally respected.

The algebraic system from Eq. 2.74 does not consider the boundary conditions so far. Applying the boundary conditions in the IGABEM is not as straightforward as in the Lagrangian BEM, since the variables in the system of Eq. 2.74 does not have physical meaning. Thus, the inverse of Eq. 2.58 must be computed to the NURBS $\bar{e}$ in which displacements or tractions are imposed, which makes possible to identify the known values $\hat{\mathbf{u}}^{\bar{e}}$ and $\hat{\mathbf{t}}^{\bar{e}}$. It is worth mentioning that this process is trivial when one applies constant and uniform boundary conditions, since all of the $\hat{\mathbf{u}}^{\bar{e}}$ or $\hat{\mathbf{u}}^{\bar{e}}$ receive the same value corresponding to the applied displacement or traction.

With that, the vectors $\hat{\mathbf{u}}$ and $\hat{\mathbf{t}}$ are divided into their unknown and known portions $\hat{\mathbf{u}} = \left\{\hat{\mathbf{u}} \quad \hat{\mathbf{u}}^{\bar{e}}\right\}^\intercal$ and $\hat{\mathbf{t}} = \left\{\hat{\mathbf{t}} \quad \hat{\mathbf{t}}^{\bar{e}}\right\}^\intercal$, in which $\hat{\mathbf{u}}$ and $\hat{\mathbf{t}}$ are now the unknown values. Hence, Eq. 2.74 can be rewritten as follows:

$$\begin{bmatrix}\mathbf{H} & \bar{\mathbf{H}}\end{bmatrix} \begin{Bmatrix}\hat{\mathbf{u}} \\ \hat{\mathbf{u}}^{\bar{e}}\end{Bmatrix} = \begin{bmatrix}\mathbf{G} & \bar{\mathbf{G}}\end{bmatrix} \begin{Bmatrix}\hat{\mathbf{t}} \\ \hat{\mathbf{t}}^{\bar{e}}\end{Bmatrix} + \{\mathfrak{b}\} \tag{2.76}$$

Then, the known values are moved to the right-hand side of the equation and the unknown ones go to the left-hand side, which leads to:

$$\begin{bmatrix}\mathbf{H} & -\mathbf{G}\end{bmatrix}\begin{Bmatrix}\hat{\mathbf{u}}\\ \hat{\mathbf{t}}\end{Bmatrix} = \begin{bmatrix}-\bar{\mathbf{H}} & \bar{\mathbf{G}}\end{bmatrix}\begin{Bmatrix}\hat{\mathbf{u}}^{\bar{e}}\\ \hat{\mathbf{t}}^{\bar{e}}\end{Bmatrix} + \{\mathbf{b}\} \tag{2.77}$$

in which all values in the right-hand can be written in a single free term $\mathbf{f}$. The matrix resulting from the left-hand side of this expression is invertible, thus the final algebraic system can be summarised as:

$$\mathbf{A}\hat{\mathbf{x}} = \mathbf{f} \tag{2.78}$$

where $\hat{\mathbf{x}}$ contains all unknown boundary values, as $\hat{\mathbf{x}} = \begin{Bmatrix}\hat{\mathbf{u}} & \hat{\mathbf{t}}\end{Bmatrix}^{\mathsf{T}}$. Therefore, the solution of Eq. 2.78 provides all the boundary variables for displacements and tractions. It is worth stressing that such variables does not have physical meaning in the IGABEM, whereas the values of displacements and tractions at the boundary can be obtained by Eq. 2.58.

2.7 Sub-region technique

The BEM sub-region technique (31) is applied herein for the solution of nonhomogeneous structural systems. In this technique, different homogeneous sub-domains are interconnected by interfaces, which results in the mechanical representation of a nonhomogeneous structure. The key-point is dealing with the interfaces, because each BEM integral equation must be applied for the boundary elements of a homogeneous domain. Therefore, pairs or elements with coincident positions are defined over the interfaces. So, each element of the pair describes the boundary of a different homogeneous domain, as illustrated in Fig. 11.

Figure 11 – 2D illustration of the sub-region technique: discretising a nonhomogeneous domain (a) into homogeneous sub-domains (b).

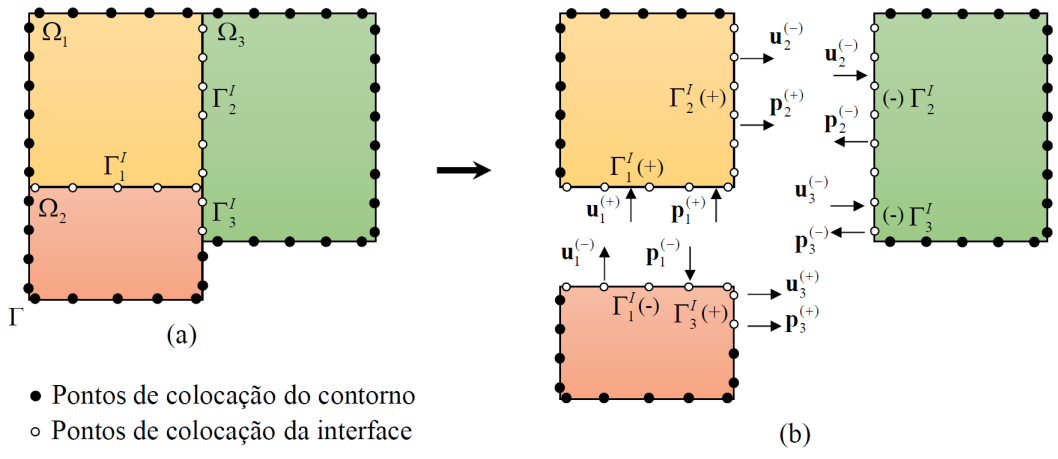

Source: (65), adapted.

The BEM formulation (Eq. 2.74) is applied for each homogeneous sub-domain (k) separately, as follows:

$$\mathbf{H}_k\hat{\mathbf{u}}_k = \mathbf{G}_k\hat{\mathbf{t}}_k + \mathfrak{b}_k \tag{2.79}$$

Displacements and tractions over the interfaces must be coupled. For that, Eq. 2.58 is considered to describe displacements and tractions. However, as long as the discretization (NURBS surfaces or Lagrangian elements) of each interface are identical, i.e., have the same rational basis functions $R_{ij,pq}$ and control points $\mathbf{B}_{ij}$ or the same approximation polynomial functions $M_i(\xi_1,\xi_2)$ and collocation points, the coupling relations may consider directly the variables $\hat{\mathbf{u}}$ and $\hat{\mathbf{t}}$. Such variables are truly displacements and tractions in the Lagrangian BEM and are NURBS parameters in the IGABEM. Thus, for a interface between sub-domains k_1 and k_2, one writes the displacements compatibility and equilibrium of tractions as follows:

$$\begin{aligned} \hat{\mathbf{u}}^I_{k_1} &= \hat{\mathbf{u}}^I_{k_2} \\ \hat{\mathbf{t}}^I_{k_1} + \hat{\mathbf{t}}^I_{k_2} &= 0 \end{aligned} \tag{2.80}$$

in which the index I represents the boundary portion at the interface.

A global system of equations can be written by coupling the expressions from Eq. 2.79 of each sub-domain k. After applying the relations from Eq. 2.80, one writes the following system:

$$\begin{bmatrix} \mathbf{H}^B_{k_1} & \mathbf{H}^I_{k_1} & \mathbf{0} \\ \mathbf{0} & \mathbf{H}^I_{k_2} & \mathbf{H}^B_{k_2} \end{bmatrix} \begin{Bmatrix} \hat{\mathbf{u}}^B_{k_1} \\ \hat{\mathbf{u}}^I_{k_1} \\ \hat{\mathbf{u}}^B_{k_2} \end{Bmatrix} = \begin{bmatrix} \mathbf{G}^B_{k_1} & \mathbf{G}^I_{k_1} & \mathbf{0} \\ \mathbf{0} & \mathbf{G}^I_{k_2} & \mathbf{G}^B_{k_2} \end{bmatrix} \begin{Bmatrix} \hat{\hat{\mathbf{t}}}^B_{k_1} \\ \hat{\hat{\mathbf{t}}}^I_{k_1} \\ \hat{\hat{\mathbf{t}}}^B_{k_2} \end{Bmatrix} + \mathfrak{b}_{k_1} + \mathfrak{b}_{k_2} \tag{2.81}$$

in which the index B represents the external boundary portions (excluding the interfaces). Despite this expression being written for two sub-domains k_1 and k_2, one can consider any number of sub-domains in a similar form.

It is worth stressing that the final expression of the sub-region technique (Eq. 2.81) can be algebraically written in the same form of Eq. 2.74.

2.8 Dual Boundary Element Method

The Dual BEM (DBEM) is a strategy to represent physical discontinuities (cracks) in solids via the BEM. The crack is always composed by two faces that are at the same position when the crack is closed (in the beginning of the analysis). Consequently, the discretization of both faces via the traditional BEM represents the crack collocation points

as internal points, since each face would be represented by the same equation. An elegant approach to overcome this issue is using different integral equations for each crack face: the DBIE and the TBIE. Such strategy was firstly proposed by Hong and Chen (14) and it is known as Dual BEM.

Let Γ_f^+ and Γ_f^- denote each one of the crack faces, as illustrated in Fig. 12. The DBIE (Eq. 2.23) is applied to the collocation points $\mathbf{x}^+$, that are at Γ_f^+, as follows:

$$c_{ij}(\mathbf{x}^+)u_j(\mathbf{x}^+) + c_{ij}(\mathbf{x}^-)u_j(\mathbf{x}^-) + \cancel{\int_\Gamma} T_{ij}^* u_j(\mathbf{x}^f)d\Gamma = \int_\Gamma U_{ij}^* t_j(\mathbf{x}^f)d\Gamma + \int_\Omega U_{ki}^* b_i d\Omega \quad (2.82)$$

in which $\mathbf{x}^-$ are the collocation points at Γ_f^-. It is worth mentioning that the free terms related to these points must also be included in this expression due to the limiting process applied to the crack contour. In this case, both $\mathbf{x}^-$ and Γ_f^- would be encompassed by the fictitious domain illustrated in Fig. 4, which would lead to two free terms.

Figure 12 – Crack faces discretized for the DBEM.

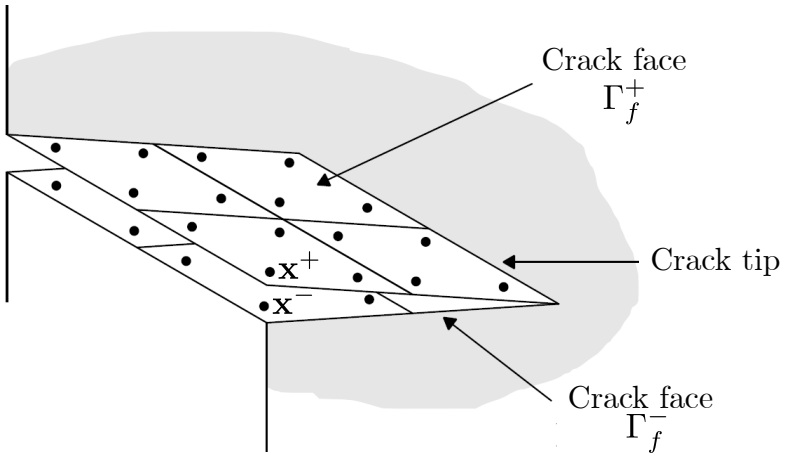

Source: (63), adapted.

The TBIE (Eq. 2.33) is applied to the points $\mathbf{x}^-$ at Γ_f^-, which will present both free terms for similar reasons, as follows:

$$\begin{aligned}\frac{1}{2}t_j(\mathbf{x}^-) + \frac{1}{2}t_j(\mathbf{x}^+) + \eta_i(\mathbf{x}^-)\cancel{\int_\Gamma} S_{kij}^* u_k(\mathbf{x}^f)d\Gamma = \\ \eta_i(\mathbf{x}^-)\cancel{\int_\Gamma} D_{kij}^* t_k(\mathbf{x}^f)d\Gamma + \eta_i(\mathbf{x}^-)\int_\Gamma D_{kij}^* b_k d\Gamma\end{aligned} \quad (2.83)$$

Therefore, the solid's representation in the DBEM is achieved by combining Eq. 2.23 for the source points at the boundaries and Eqs. 2.83 and 2.82 for the cracks faces. After applying the boundary discretization, the process described in Sec. 2.6 can be applied similarly to the DBEM. The resulting system of algebraic equations is as follows:

$$\begin{bmatrix}\mathbf{H} \\ \mathbf{H}^+ \\ \mathbf{H}^-\end{bmatrix}\begin{Bmatrix}\hat{\mathbf{u}} \\ \hat{\mathbf{u}}^+ \\ \hat{\mathbf{u}}^-\end{Bmatrix} = \begin{bmatrix}\mathbf{G} \\ \mathbf{G}^+ \\ \mathbf{G}^-\end{bmatrix}\begin{Bmatrix}\hat{\mathbf{t}} \\ \hat{\mathbf{t}}^+ \\ \hat{\mathbf{t}}^-\end{Bmatrix} + \mathfrak{b} \quad (2.84)$$

in which the indexes + and − represent the variables referent to the collocation points $\mathbf{x}^+$ and $\mathbf{x}^-$, respectively. It is worth stressing that this expression can be written in the same algebraic form as Eq. 2.74 by grouping the variables and matrices into global ones. Hence, the further developments can be coupled to the DBEM, although the formulations consider the BEM algebraic form presented in Eq. 2.74.

2.9 Computational details: The Isogeometric preprocessing

The advantages of IGA formulations over traditional Lagrangian formulations comprehend the effective representations of complex geometries in addition to the straightforward connection between preprocessors and CAD models and accuracy. The process of creating a Lagrangian mesh based on engineering designs is significantly time-consuming (8). In addition to the inherent complexities associated with the mesh construction such as conformity and geometry discontinuities issues, the mesh refinements are complex and require large computational efforts. Therefore, the use of the IGA model itself in the mechanical modelling is computationally efficient. This strategy enables easy and short path connection between geometry design and analysis technique, since the functions describing the geometry can be utilised as the mesh itself.

The preprocessor developed for this study utilises the CAD model information directly by reading IGES files, which contain information of the 3D solid's models. This file format is very common in commercial CAD software. Therefore, the geometric design can be provided by any CAD package. The preprocessor utilised herein requires only the output describing the geometric entities. Besides, the IGES files from CAD represent 3D solids through NURBS surfaces at the boundaries, which is exactly the same representation as the IGABEM. The pyiges library (15) from Python enables reading the IGES files and extracting all information, such as knot vectors, control points and connectivity. This information inputs the IGABEM program, which can calculate the NURBS surfaces as presented in Sec. 2.5. It is worth mentioning that the IGABEM processing kernels are implemented in FORTRAN programming language. Additionally, nonhomogeneous 3D structures can be modelled by coupling two or more IGES files, being each one for a sub-domain.

The knot insertion process (16) has been applied herein when mesh refinement is necessary. This process adds knots and control points, which consequently creates more knot spans and improves the mechanical fields' representation without changing the NURBS surfaces' geometry. Therefore, the implemented IGABEM program is robust and efficient regarding the representation of complex 3D models.

The developed preprocessor also inputs the Lagrangian BEM program. For that, the IGA model provided by the IGES files is used as a basis to construct a polynomial mesh

of linear Lagrangian elements (4-node). The polynomial mesh creator from IGA models was developed by Cordeiro (62) and uses the software Ansys to obtain the Lagrangian elements information (nodes coordinates and elements connectivity). In that case, the knot insertion is not necessary, since the mesh refinement is provided by Ansys itself.

2.10 Numerical application of the 3D IGABEM formulation

This section presents a numerical example that applies the 3D IGABEM formulation implemented in this study for a crack problem. Thus, the DBEM presented in Sec. 2.8 is used to represent the crack in the isogeometric approach. This numerical example is composed by a circular crack in an infinite homogeneous medium, as illustrated in Fig. 13.

Figure 13 – Representation of the infinite crack analysed in the numerical example.

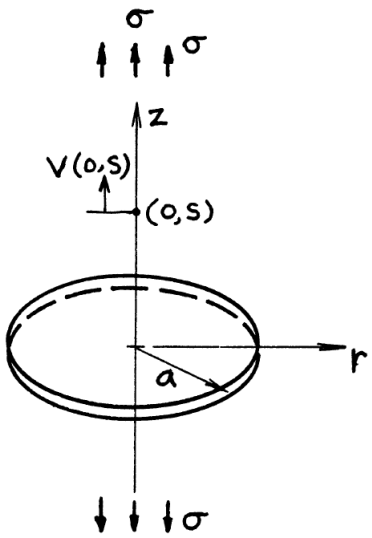

Source: (73).

This problem presents a analytical solution for the opening at the centre of the crack δ (73), which is as follows:

$$\delta = \frac{8(1-\nu^2)}{\pi E}\sigma\, a \tag{2.85}$$

in which σ is the traction applied and a is the radius of the crack.

The physical properties considered in the numerical model are: Young's modulus $E = 3000$ kN/cm^2, Poisson's ratio $\nu = 0.2$, crack dimension $a = 0.5$ cm and the applied traction $\sigma = 50$ kN/cm^2. To represent the infinite medium with Kelvin's fundamental solution, the crack is centred in a prism with dimensions $50 \times 50 \times 100$ (in cm), in which the third one is the direction of σ. The numeric model is based on a isogeometric model that has 6 regular NURBS surfaces to represent the prism and 5 regular NURBS surfaces to represent the circular crack, all bi-quadratic ($p = q = 2$). Four IGABEM meshes are constructed from this model by a knot insertion process (16), in order to verify the mesh convergence of the IGABEM solutions:

- Mesh A: Based on the original isogeometric model. Total of 304 collocation points.

- Mesh B: 1 knot inserted into each NURBS surface of the original model. Total of 510 collocation points.
- Mesh C: 2 knots inserted into each NURBS surface of the original model. Total of 976 collocation points.
- Mesh D: 3 knots inserted into each NURBS surface of the original model. Total of 2200 collocation points.

The meshes A, B, C and D are illustrated in Fig 14, which presents the crack and the prism meshes side by side.

Figure 14 – Prism and crack discretisations considered in the numerical example.

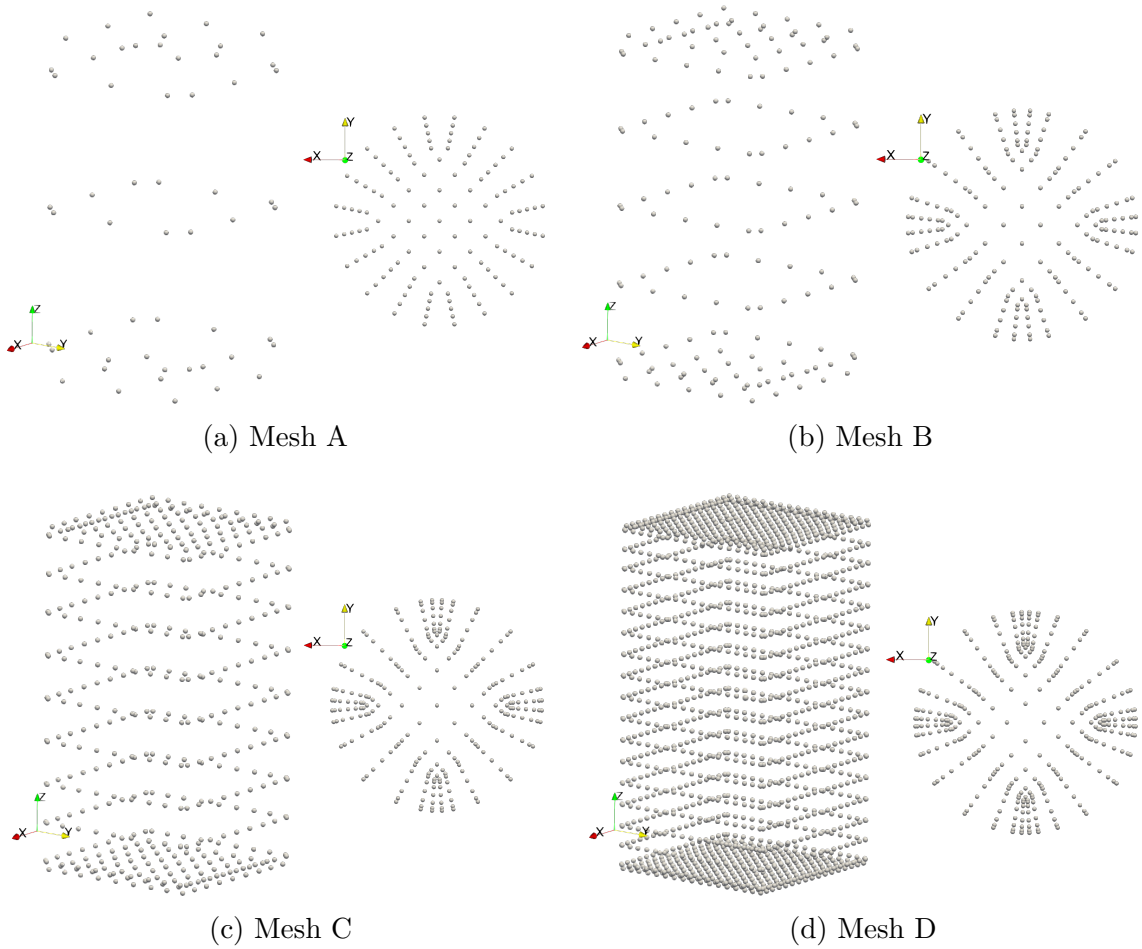

(a) Mesh A (b) Mesh B

(c) Mesh C (d) Mesh D

Source: The author.

Figure 15 illustrates the z displacements fields obtained through the 4 proposed meshes over the crack. The NURBS surfaces are subdivided into 20 auxiliary Lagrangian elements (4 nodes) to generate the visualisation with the software *Paraview*. The deformed shape is constructed considering a scale factor of 25 for all meshes. In this figure, one observes the coherence of the displacements obtained by the numerical analyses. All of the results are in agreement with the expected behaviour. Besides, it is worth mentioning that

the continuity of the crack's deformed shape is improved with the more refined meshes, specially at the NURBS surfaces' intersections.

Figure 15 – Displacements field over the crack in z direction obtained via the IGABEM. Scale factor equals 25.

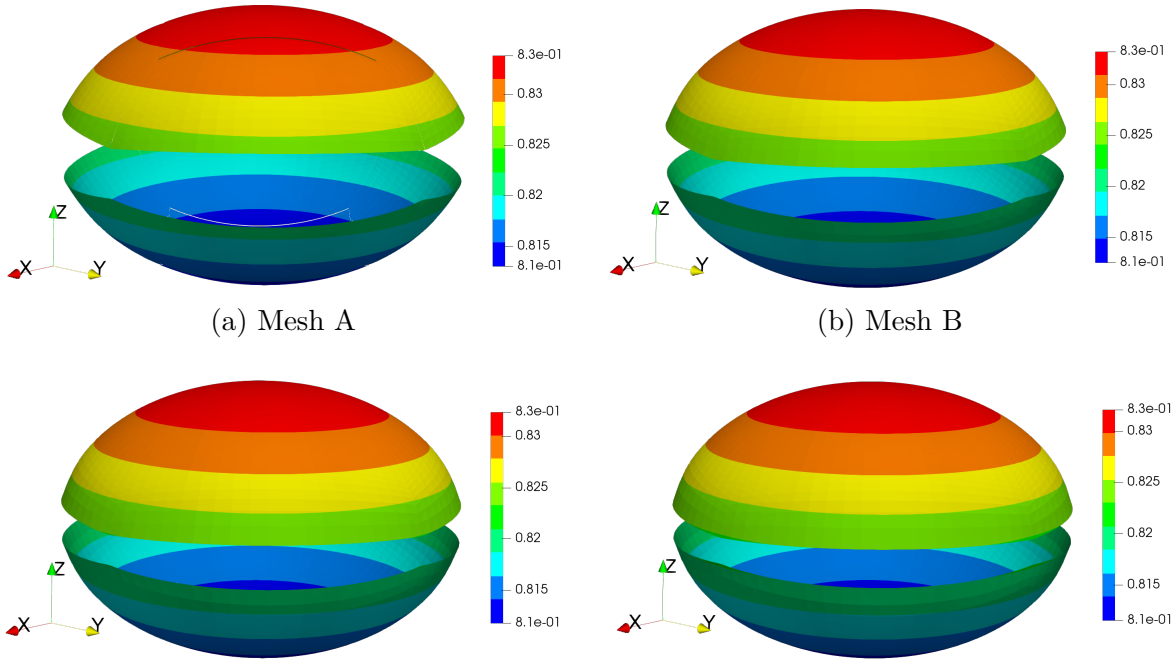

(a) Mesh A (b) Mesh B

(c) Mesh C (d) Mesh D

Source: The author.

Figure 16 illustrates the convergence of the error in percentage, considering the crack opening at centre given by Eq. 2.85. The error is presented as a function of the number of collocation points N_c. These results are obtained from the numerical models by computing the difference between the z displacements of each side of the crack, at its centre. One observes good convergence of the results throughout the 4 proposed meshes. Besides, the error values are around 1% for both meshes C and D. Therefore, the 3D IGABEM formulations for cracked bodies via the Dual BEM can be considered precise and adequate to represent such problem.

Figure 16 – Convergence of the IGABEM error considering the analytical result for the crack opening.

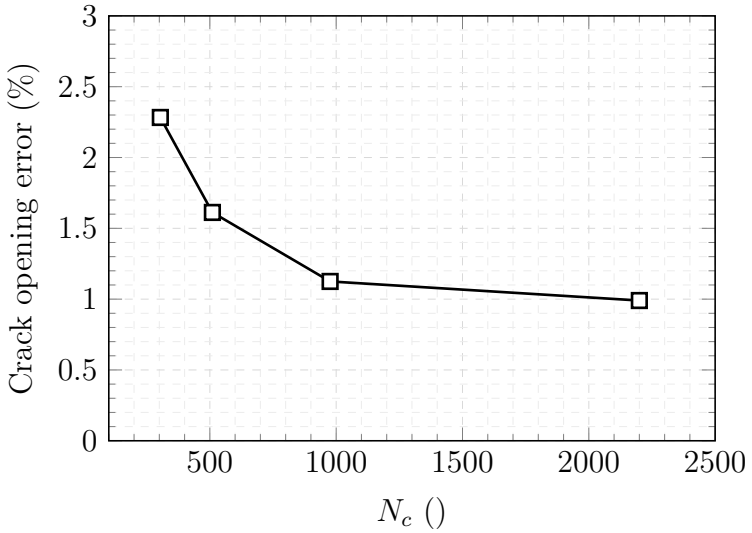

Source: The author.

3

Domain/Reinforcement Coupling

In this study, reinforced domains are modelled through a numerical coupling technique based on the BEM. The solid is represented by either the 3D IGABEM or 3D BEM, whereas the 1DBEM represent embedded fibres. This chapter presents the coupling formulation in its elastic approach, as well as numerical examples that demonstrate the robustness and accuracy of the proposed coupling scheme.

3.1 Coupled formulations: Literature Review

The coupling between the numerical methods FEM and BEM (FEM/BEM coupling) for the modelling of reinforced structures was previously presented in (9) and (74). Since then, several studies have been published regarding this theme, which made the coupling technique well-recognised and established. A comprehensive literature review on this matter can be found in (75) and (76). Besides, (77) and (78) present further details about the state of the art, whereas (79) discusses limitations and advantages of this type of coupling.

Among the several citations of the coupling technique in the literature for numerous applications, one may highlight: (39) presented a formulation that treats BEM sub-regions as equivalent FEM domains; (80) applied the coupling technique to handle fracture mechanics problems, with the use of boundary elements at crack faces whereas the remaining domain was represented via FEM; (81) demonstrated accurate results by the FEM/BEM coupling regarding the modelling of composite materials with elastic and viscoelastic behaviour from experimental tests and pure-FEM approaches; (82) presented a multi-scale analysis for nonhomogeneous materials based on the coupling technique; soil-structure interaction problems have also been treated by this scheme (83, 84).

The FEM/BEM coupling is particularly applied for fracture mechanics problems

in reinforced media. This approach becomes effective in such problems since one may take advantage from the strong points of each numerical method. Most applications have been found in aeronautic engineering, but the literature also presents applications in different fields (85, 86, 87). Studies carried out in the Department of Structural Engineering SET/EESC-USP deserved to be mentioned as well: (41) applied the coupling technique for elasto-dynamic analyses of 2D problems and posteriorly 3D (88); (89) modelled the reinforcements via the sub-region BEM technique and compared it against the coupled formulation, which demonstrated the efficiency of the coupled strategy; (90, 91) presented reinforced viscoelastic formulations based on Lagrangian FEM/BEM approaches; (92) studied contact problems in the interface matrix/reinforcement by considering a nonlinear bond-slip modelling.

More recently, the research group under Prof. Edson Leonel supervision studied the alternative technique based on the FEM/BEM coupling for 2D linear-elastic homogeneous domains. In that case, 1D BEM elements represent the fibre-reinforcements instead of the FEM. The 1DBEM is based on a axial fundamental solution for 1D domains available in the literature (93, 94, 95). This alternative is called 1DBEM/BEM coupling and it demonstrated superior results when compared against the traditional FEM/BEM (13), especially in some aspects that the FEM/BEM shows some instabilities. Moreover, this author proposed a strategy called connection element to represent nonhomogeneous reinforced domains through the 1DBEM/BEM in 2D analyses, in addition to present a detailed analysis of the comparison between the 1DBEM/BEM and the FEM/BEM results (13). Therefore, the extension of the 1DBEM/BEM coupling for 3D problems using the IGABEM is a subject of this work.

3.2 Algebraic representation of the elastic coupling

Let Ω be the three-dimensional solid and the reinforcing fibres be positioned along the line $\bar{\Gamma}$, which is totally immersed into Ω. Figure 17(a) illustrates this scheme. The interaction between the substructures (solid and reinforcement) is represented by an adherence force, which arises when the substructures are detached. In that situation, one split $\bar{\Gamma}$ into two different lines: $\bar{\Gamma}_E$ along the reinforcements and $\bar{\Gamma}_D$ within the domain, as illustrated by Fig. 17(b). $\bar{\Gamma}_D$ determines the direction of the adherence force applied into Ω, therefore it is also called “load line”. In addition, the reinforcements node’s positions can be understood as internal points in Ω, which defines the line $\bar{\Gamma}_D$.

By the action-reaction principle, one can establish that the adherence force in the reinforcements ($f_E(\Gamma)$) are equal and opposite to the adherence force applied into Ω ($f_D(\Gamma)$). Besides, one considers initially perfect bond conditions between reinforcements and domain. Hence, the displacements’ compatibility and the adherence force’s equilibrium

Figure 17 – Scheme of the matrix/reinforcement coupling technique.

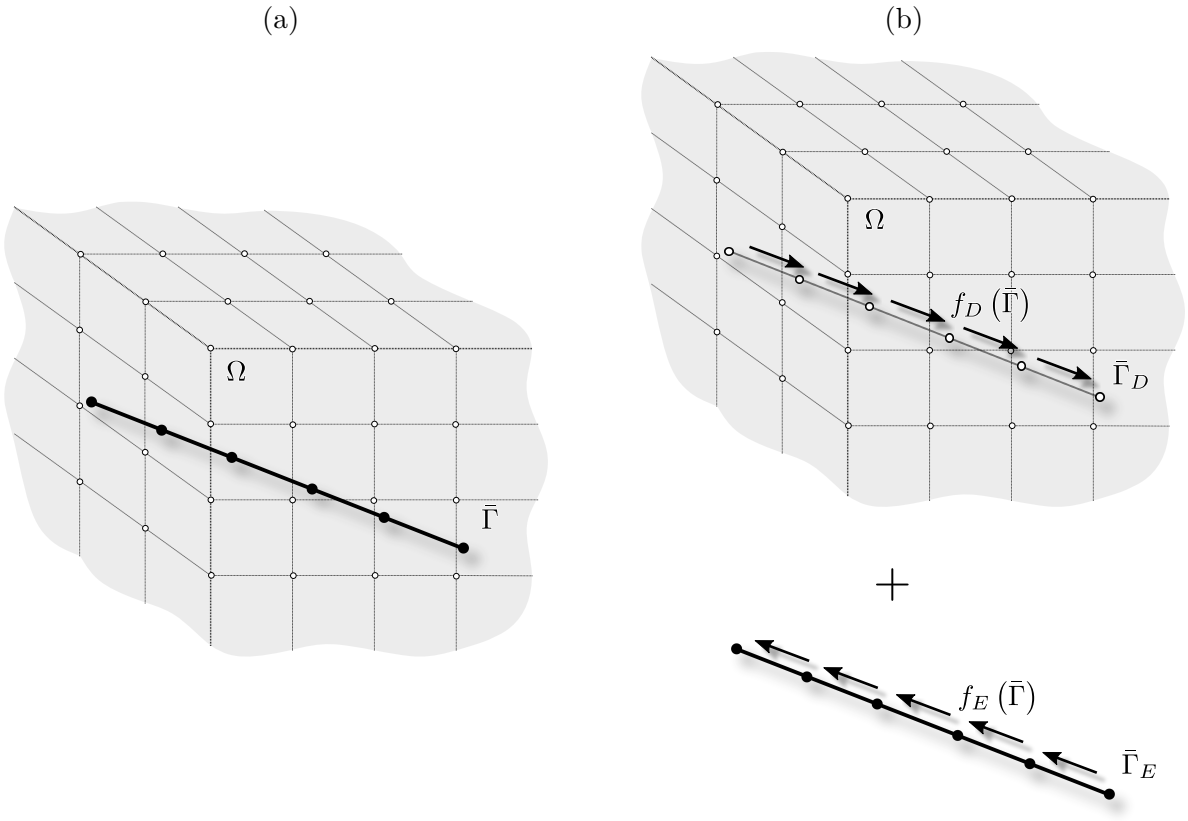

Source: The author.

can be written as follows:

$$\begin{aligned} f_E\left(\bar{\Gamma}\right) &= -f_D\left(\bar{\Gamma}\right) \\ u_E\left(\bar{\Gamma}\right) &= u_D\left(\bar{\Gamma}\right) \end{aligned} \tag{3.1}$$

in which the indexes D and E represent domain and reinforcement, respectively.

Both displacements and adherence force are numerically approximated by linear combinations of similar functions in the domain and in the reinforcements. Therefore, the continuous relation from Eq. 3.1 can be represented by a discretized relation between the nodal parameters, as follows:

$$\mathbf{f_E} = -\mathbf{f_D} \tag{3.2a}$$

$$\mathbf{u_E} = \mathbf{u_D} \tag{3.2b}$$

in which $\mathbf{u}$ and $\mathbf{f}$ contain nodal values of displacements and adherence forces, respectively.

The adherence force is accounted as a body force (b_i) into the BEM formulation of the 3D solid. Thus, the domain integral term in Eq. 2.9 becomes a line integral term and is evaluated solely over $\bar{\Gamma}$. It is worth mentioning that this assumption requires a particular

integration scheme, which is properly described in the next section of this chapter. Hence, the IGABEM integral equation for boundary points can be written as follows:

$$c_{ij}^{s}u_{j}^{s}+\int_{\Gamma}T_{ij}^{*}u_{j}d\Gamma=\int_{\Gamma}U_{ij}^{*}t_{j}d\Gamma+\int_{\bar{\Gamma}}U_{ij}^{*}(\mathbf{f_D})_{j}d\bar{\Gamma} \tag{3.3}$$

where the index s indicates the mechanical fields evaluated at the source point $\mathbf{x}^s$.

The BEM integral equation for internal points displacements must be written for the $\bar{\Gamma}_D$ points. Considering the adherence force contribution in the domain term, this integral equation can be written as follows:

$$(u_D)_i=\int_{\Gamma}U_{ij}^{*}t_{j}d\Gamma-\int_{\Gamma}T_{ij}^{*}u_{j}d\Gamma+\int_{\bar{\Gamma}}U_{ij}^{*}(\mathbf{f_D})_{i}d\bar{\Gamma} \tag{3.4}$$

Equations 3.3 and 3.4 can be algebraically written considering the numerical discretization of the reinforcements and the solid's contour, which results in:

$$\mathbf{H_{CC}\hat{u}_C}=\mathbf{G_{CC}\hat{t}_C}+\mathbf{G_{CF}f_D} \tag{3.5}$$

$$\mathbf{u_D}=\mathbf{G_{FC}\hat{t}_C}-\mathbf{H_{FC}\hat{u}_C}+\mathbf{G_{FF}f_D} \tag{3.6}$$

in which the index $\mathbf{C}$ in the vectors $\hat{\mathbf{u}}$ and $\hat{\mathbf{t}}$ indicates that these fields are evaluated at the boundary. The index $\mathbf{D}$ indicates the fields evaluated over the reinforcements line $\bar{\Gamma}$. Note that the above-presented expressions can represent both the IGABEM and the Lagrangian BEM, in which the vectors $\hat{\mathbf{u}}$ and $\hat{\mathbf{t}}$ are control points parameters for the IGABEM or nodal displacements and tractions for the Lagrangian BEM. Besides, the matrices names consider the following system:

- $\mathbf{H_{CC}}$ is the $\mathbf{H}$ matrix of the BEM considering source points at the boundary and integrating over the boundary;
- $\mathbf{G_{CC}}$ is the $\mathbf{G}$ matrix of the BEM considering source points at the boundary and integrating over the boundary;
- $\mathbf{G_{CF}}$ is the $\mathbf{G}$ matrix of the BEM considering source points at the boundary and integrating over the reinforcements;
- $\mathbf{G_{FC}}$ is the $\mathbf{G}$ matrix of the BEM considering source points at the reinforcements and integrating over the boundary;
- $\mathbf{H_{FC}}$ is the $\mathbf{H}$ matrix of the BEM considering source points at the reinforcements and integrating over the boundary;
- $\mathbf{G_{FF}}$ is the $\mathbf{G}$ matrix of the BEM considering source points at the reinforcements and integrating over the reinforcements;

The last required expression is the reinforcements mechanical representation, which can be described by any numerical method for 1D domains under axial loads. In this

study, either the FEM or the 1DBEM can be considered. For both numerical methods, this expression can be algebraically written as follows:

$$\mathbf{K_E u_E} = \mathbf{G_E f_E} \tag{3.7}$$

in which $\mathbf{u_E}$ and $\mathbf{f_E}$ are the nodal values of displacements and adherence force evaluated over the reinforcements, respectively. The matrices $\mathbf{K_E}$ are $\mathbf{G_E}$ are properly defined for each numerical method afterwards.

Thus, the resulting linear system of equations is defined by coupling the Eq. 3.5, 3.6 and 3.7. The compatibility and equilibrium relations from Eq. 3.2 are also applied in the coupling system, which leads to:

$$\begin{bmatrix} \mathbf{H_{CC}} & \mathbf{0} & -\mathbf{G_{CF}} \\ \mathbf{H_{FC}} & \mathbf{I} & -\mathbf{G_{FF}} \\ \mathbf{0} & \mathbf{K_E} & \mathbf{G_E} \end{bmatrix} \begin{Bmatrix} \hat{\mathbf{u}}_\mathbf{C} \\ \mathbf{u_D} \\ \mathbf{f_D} \end{Bmatrix} = \begin{bmatrix} \mathbf{G_{CC}} \\ \mathbf{G_{FC}} \\ \mathbf{0} \end{bmatrix} \left\{ \hat{\mathbf{t}}_\mathbf{C} \right\} \tag{3.8}$$

where $\mathbf{I}$ is the identity matrix.

Equation 3.8 can be solved by enforcing the boundary conditions applied over Γ, as usual in BEM formulations. The final system of equations is as follows:

$$\begin{bmatrix} \mathbf{A_{CC}} & \mathbf{0} & -\mathbf{G_{CF}} \\ \mathbf{B_{FC}} & \mathbf{I} & -\mathbf{G_{FF}} \\ \mathbf{0} & \mathbf{K_E} & \mathbf{G_E} \end{bmatrix} \begin{Bmatrix} \hat{\mathbf{x}}_\mathbf{C} \\ \mathbf{u_D} \\ \mathbf{f_D} \end{Bmatrix} = \begin{bmatrix} \bar{\mathbf{A}}_\mathbf{CC} \\ \bar{\mathbf{B}}_\mathbf{FC} \\ \mathbf{0} \end{bmatrix} \{ \hat{\mathbf{p}}_\mathbf{C} \} \tag{3.9}$$

in which $\hat{\mathbf{x}}_\mathbf{C}$ and $\hat{\mathbf{p}}_\mathbf{C}$ are, respectively, the unknown and the known boundary values.

Equation 3.9 results in a linear system of equations likewise $\mathbf{Ax} = \mathbf{f}$. This system presents a straightforward solution, which leads to the displacements and traction values at the boundary, in addition to the displacements and adherence force values at the reinforcements.

Te mechanical fields can be evaluated at other internal points rather than the $\bar{\Gamma}$ points. The internal displacements u_i can be determined through Eq. 3.4, considering $(u_D)_i$ as u_i. The hypersingular integral equation (Eq. 2.15) must be rewritten in order to evaluate stresses and strains. Considering the adherence force into the b_i in Eq. 2.15, one writes:

$$\sigma^s_{jk} = \int_\Gamma D^*_{ijk} t_i d\Gamma + \int_{\bar{\Gamma}} D^*_{ijk} (\mathbf{f_D})_i d\bar{\Gamma} - \int_\Gamma S^*_{ijk} u_i d\Gamma \tag{3.10}$$

in which the integral kernels D^*_{ijk} e S^*_{ijk} can be found in Eq. 2.18 and 2.19, respectively.

3.3 Load line integration scheme

The load line integration scheme regards the last integral terms of Eq. 3.3 and Eq. 3.4. The reinforcements are assumed as one-dimensional, then these integrations should hypothetically be performed along the line $\bar{\Gamma}_D$. This approach is adequate when dealing with 2D BEM formulations, because the kernels integration scheme is already formulated along the one-dimensional elements that represents the boundary. In 3D BEM formulations, the fundamental solutions are integrated over areas at the boundary. Thus, integrating U^*_{ij} (Eq. A.32) along the line $\bar{\Gamma}_D$ leads to significant errors, which are directly proportional to the reinforcement element area and inversely proportional to the distance between source and field points. Besides, the integration of reinforcement elements that contain the source point results in divergent singular values, i.e., which cannot be regularised.

This study adopts a particular integration scheme, based on the strategy proposed in (41, 96) for 3D FEM/BEM coupling techniques. The integration is performed over a 2D domain, which is considered to be the surface area of the reinforcements. One considers a cylindrical shell, as a result of hypothetical cylindrical fibre-reinforcements. Then, the filed points remain positioned along the reinforcements central axis ($\bar{\Gamma}$) in Eq. 3.4, which allow for the proper displacements compatibility (Eq. 3.2). However, the fields points are now positioned over the cylindrical shell of radius R_F that covers $\bar{\Gamma}$, as illustrated in Fig. 18.

Figure 18 – Integration scheme over a reinforcement element, considering 4 integration points over the angular coordinate and a fixed axial coordinate.

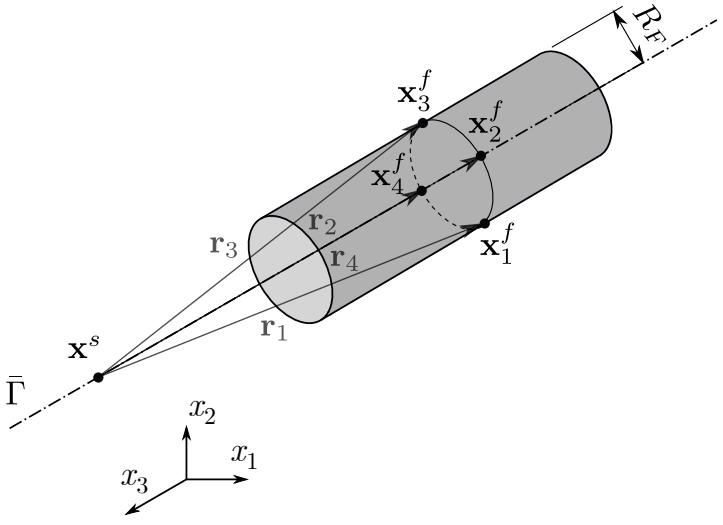

Source: The author.

At first sight, the adopted integration scheme might seem equivalent to applying the BEM sub-region technique (97) to represent the fibre-reinforcements. However, the sub-region technique would require a much higher number of source points, which would be positioned over the cylindrical shell. The adopted scheme is more efficient because all source points are along the fibre central axis. In addition, this aspect results in no singular

integrations, because the distance between source and field points is always higher or equal R_F.

The tractions distribuited over the cylindrical Shell are named $\mathbf{Q_i}$ and are illustrated in Fig. 19(a). For thin fibres (much higher length than radius), one can simplify $\mathbf{Q_i}$ as constant along θ for a given $d\bar{\Gamma}$. Then, this value can be represented by a resulting concentrated force $\mathbf{f_D}$, which is positioned at the fibre centre axis as illustrated by Fig 19(b). This resulting force is given by:

$$\mathbf{f_D} = 2\pi R_F \mathbf{Q_i} \tag{3.11}$$

Figure 19 – Adherence force over reinforcements elements: three-dimensional representation (a) and one-dimensional approximation (b).

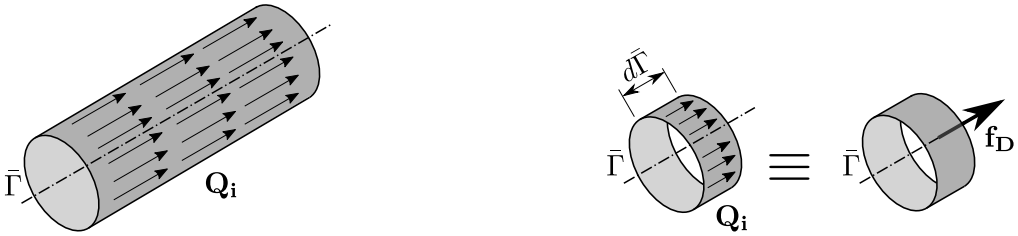

Source: The author.

Then, the integration can be numerically evaluated by applying twice the Gauss-Legendre quadrature: g_1 to map the centre axis direction ($\bar{x}$) and g_2 to map the cylindrical coordinate θ. The radius in θ is always constant and equals R_F. Thus, the numerical integration results in the following:

$$\int_{\bar{\Gamma}} U^*_{ij}(\mathbf{Q_i})_j d\Gamma = \sum_{g_1=1}^{np_1} \left[\sum_{g_2=1}^{np_2} \left[U_{ij}\left(\mathbf{x}^f(\xi_{g_1},\xi_{g_2}),\mathbf{x}^s\right) |\mathbf{jac_2}(\xi_{g_2})|\, \omega_{g_2} \right] |\mathbf{jac_1}(\xi_{g_1})|\, \omega_{g_1} \phi_m(\xi_{g_1}) \right] \frac{(\mathbf{f_D})_j}{2\pi R_F} \tag{3.12}$$

where np_1 and np_2 are the total amount of integration points along $\bar{x}$ and θ directions, respectively. ω are the quadrature weights. The integrations Jacobians are as follows:

$$|\mathbf{jac_1}(\xi_{g_1})| = \sqrt{\left(x^b_{1,\xi}(\xi_{g_1})\right)^2 + \left(x^b_{2,\xi}(\xi_{g_1})\right)^2} \tag{3.13}$$

$$|\mathbf{jac_2}(\xi_{g_2})| = \pi R_F \tag{3.14}$$

in which $\mathbf{x}^b$ is the field point's projection over $\bar{x}$. Its global coordinates (x^b_i) can be found from the g_1 mapping through the nodal values interpolation, which considers the Lagrangian polynomial functions. θ is mapped by the following:

$$\theta(\xi_{g_2}) = \pi\left(\xi_{g_2} + 1\right) \tag{3.15}$$

Based on $\mathbf{x}^b$ and θ, one can find the field point ($\mathbf{x}^f$) coordinates, which is applied in Eq. 3.12, as follows:

$$\mathbf{x}^f = \mathbf{x}^b + \mathbf{f}\left(\theta\right) R_F \tag{3.16}$$

where $\mathbf{f}\left(\theta\right)$ is a vector-valued function as follows:

$$\mathbf{f}(\theta) = \frac{1}{\sqrt{\cos^2(\alpha_1) + \cos^2(\alpha_2)}} \begin{Bmatrix} -\cos(\alpha_2)\cos(\theta) - \cos(\alpha_1)\cos(\alpha_3)\text{sen}(\theta) \\ \cos(\alpha_1)\cos(\theta) - \cos(\alpha_2)\cos(\alpha_3)\text{sen}(\theta) \\ \left[\cos^2(\alpha_1) + \cos^2(\alpha_2)\right]\text{sen}(\theta) \end{Bmatrix} \tag{3.17}$$

in which α_i are angles the between the local axis $\bar{x}$ and the global axis x_i at $\mathbf{x}^b$. In the particular scenario that the reinforcement is aligned with the global x_3, i.e., $\cos(\alpha_1) = cos(\alpha_2) = 0$, Eq. 3.17 must be replaced by:

$$\mathbf{f}\left(\theta\right) = \begin{Bmatrix} -\text{sen}(\theta) \\ \cos(\theta) \\ 0 \end{Bmatrix} \tag{3.18}$$

It is worth remarking that integrating the load line simply along $\bar{\Gamma}$ is equivalent to neglect the θ dependent portion in Eq. 3.16. In fact, this assumption is reasonable for reinforcement elements that do not contain the source point and with R_F significantly small in relation to $\mathbf{x}^b$. Thus, this simplified integration could be applied for elements considerably far way from the source point, which results in minor integration errors. Nevertheless, the proposed integration scheme over a cylindrical shell must be applied when the integration over $\bar{\Gamma}$ results in singular or quasi-singular values and when R_F is significant.

3.4 Reinforcements modelling via FEM

Let V be a 3D solid with boundary Γ, in which external loads $\mathbf{p}$ are applied over Γ_p and displacement are prescribed over $\Gamma - \Gamma_p$. $\mathbf{b}$ are the body forces applied in V. That is a BVP, which can be described by the Principle of Virtual Works (PVW) as follows:

$$\int_V \delta\varepsilon^\intercal \sigma dV = \int_V \delta\mathbf{u}^\intercal \mathbf{b} dV + \int_{\Gamma_p} \delta\mathbf{u}^\intercal \mathbf{p} d\Gamma \quad , \quad \forall\delta\mathbf{u} \tag{3.19}$$

where δ indicates the virtual fields.

Any given point in V has three components of displacements: (u,v,w). The vector $\mathbf{u}$ contain them. Stress and strain can also be represented in the vectors σ and ε, which consider the Voigt notation. Thus, one can write the compatibility relation (Eq. A.7) in a algebraic form through the matrix of differential operators ($\mathbf{B}$), as follows:

$$\begin{aligned} \varepsilon &= \mathbf{B}\mathbf{u} \\ \delta\varepsilon &= \mathbf{B}\delta\mathbf{u} \end{aligned} \tag{3.20}$$

Besides, the constitutive relation can also be algebraically written through the constitutive matrix $\mathbf{D}$, as follows:

$$\sigma = \mathbf{D}\varepsilon \tag{3.21}$$

Applying Eq. 3.20 and Eq. 3.21 into the PVW expression (Eq. 3.19), one writes:

$$\int_V \delta\mathbf{u}^\intercal\mathbf{B}^\intercal\mathbf{D}\mathbf{B}\mathbf{u}dV = \int_V \delta\mathbf{u}^\intercal\mathbf{b}dV + \int_{\Gamma_p} \delta\mathbf{u}^\intercal\mathbf{p}d\Gamma \quad , \quad \forall\delta\mathbf{u} \tag{3.22}$$

In the FEM, the mechanical fields of displacements and tractions are represented by linear combinations of the Lagrangian functions, as follows:

$$\begin{aligned} u(\mathbf{x}) &= \phi_i(\mathbf{x})u_i \\ v(\mathbf{x}) &= \phi_i(\mathbf{x})v_i \\ p(\mathbf{x}) &= \phi_i(\mathbf{x})p_i \end{aligned} \tag{3.23}$$

where u_i and v_i are the nodal values of horizontal and vertical displacements, respectively. p_i are the nodal values of tractions, which can be considered oriented along the axial direction $\bar{x}$ in 1D domains. $\mathbf{x}$ represents the problem's dimension ($\bar{x}_1$, $\bar{x}_2$ e $\bar{x}_3$).

Equation 3.23 can be algebraically written, considering the matrix $\mathbf{\Phi}$ of the Lagrangian functions, as follows:

$$\begin{aligned} \mathbf{u}(\mathbf{x}) &= \mathbf{\Phi}\mathbf{u_n} \\ \delta\mathbf{u}(\mathbf{x}) &= \mathbf{\Phi}\delta\mathbf{u_n} \end{aligned} \tag{3.24}$$

in which both real and virtual mechanical fields are expressed. $\mathbf{u}(\mathbf{x})$ contains the displacements at a given point and $\mathbf{u_n}$ contains the nodal displacements. Besides, real and virtual fields of strains can also be represented likewise:

$$\begin{aligned} \varepsilon(\mathbf{x}) &= \mathbf{B}\mathbf{\Phi}\mathbf{u_n} \\ \delta\varepsilon(\mathbf{x}) &= \mathbf{B}\mathbf{\Phi}\delta\mathbf{u_n} \end{aligned} \tag{3.25}$$

It is worth remarking that both virtual and real fields are approximated by the same functions $\mathbf{\Phi}$, which characterises this formulation as a Galerkin method.

One applies Eq. 3.24 and Eq. 3.25 into the algebraic form of PVW (Eq. 3.22). The condition to establish the PVW as valid for any $\delta\mathbf{u_n}$ is as follows:

$$\int_v (\mathbf{B\Phi})^\intercal \mathbf{D} (\mathbf{B\Phi}) \mathbf{u_n} dV = \int_V \mathbf{\Phi}^\intercal \mathbf{b} dV + \int_{\Gamma_p} \mathbf{\Phi}^\intercal \mathbf{p} d\Gamma \tag{3.26}$$

Since the nodal values $\mathbf{u_n}$ are constant, the integration of $\mathbf{u_n}$ is not required in Eq. 3.26. Thus, this expression defines a linear system of equations with $\mathbf{u_n}$ as unknown values and a matrix called stiffness ($\mathbf{K_F}$), as follows:

$$\mathbf{K_F} = \int_V (\mathbf{B\Phi})^\intercal \mathbf{D} (\mathbf{B\Phi}) dV \tag{3.27}$$

The right-hand side of Eq. 3.26 is composed by a vector of free terms, which is usually denoted as $\mathbf{f_{eq}}$:

$$\mathbf{f_{eq}} = \int_V \mathbf{\Phi}^\intercal \mathbf{b} dV + \int_{\Gamma_p} \mathbf{\Phi}^\intercal \mathbf{p} d\Gamma \tag{3.28}$$

Therefore, the final linear system of the FEM in the local coordinate system is:

$$\mathbf{K_F u_n} = \mathbf{f_{eq}} \tag{3.29}$$

Equation 3.29 enable determining the nodal displacements through the discretization of the domain into finite elements and the application of boundary conditions. The global fields are then composed by a linear combination of the local solutions in each finite element.

The FEM formulation is then particularised for 1D domains defined by any number of points, as illustrated in Fig. 20.

In this 1D element, only axial fields (displacements, tractions and internal forces) are approximated, which is illustrated as $\bar{x}_1$ in Fig. 20. Orthogonal directions present free displacements and no stiffness. Therefore, the stiffness matrix is as follows:

$$(\mathbf{K_F})_{ij} = EA \int_0^L \phi_{i,x} (\bar{x}_1) \phi_{j,x} (\bar{x}_1) d\bar{x}_1 \tag{3.30}$$

in which E is the Young's modulus and A the cross section area. These values are considered constant and uniform.

The stiffness matrix integration is numerically solved by a Gauss-Legendre quadrature. Its Jacobian is given by:

Figure 20 – 1D fibre-reinforcement element illustration with a $n-1$ degree approximation.

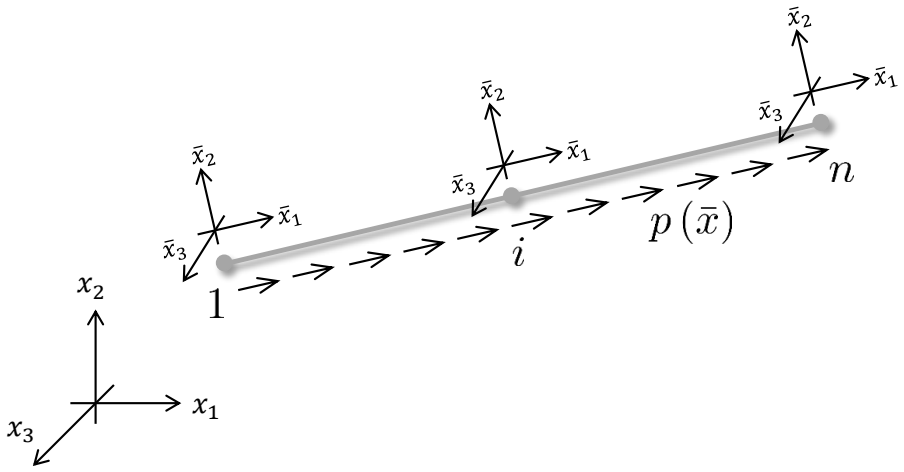

Source: The author.

$$|\mathbf{jac}(\xi)| = \sqrt{\left(\phi_{k,\xi}(\xi)X_k\right)^2 + \left(\phi_{k,\xi}(\xi)Y_k\right)^2} \tag{3.31}$$

where X_k and Y_k are the global coordinates of the finite element nodes.

Thus, Eq. 3.30 is numerically evaluated as follows:

$$\left(\mathbf{K_F}\right)_{ij} = EA\left[\sum_{k=1}^{N_p} \phi_{i,\xi}(\xi_k)\phi_{j,\xi}(\xi_k)\,|\mathbf{jac}(\xi_k)|\,\omega_k\right] \tag{3.32}$$

in which N_p is the number of integration points used in each finite element.

Equation 3.28 leads to the lumping matrix ($\mathbf{G_E}$ in Eq. 3.7) by considering nill concentrated forces at the boundaries $\mathbf{p} = \mathbf{0}$ the following approximation of the body forces $\mathbf{b}$:

$$\mathbf{b} = \mathbf{\Phi}\mathbf{f_E} \tag{3.33}$$

in which $\mathbf{f_E}$ are the nodal values of the distribuited force along the 1D domain.

Applying Eq. 3.33 into Eq. 3.28 and considering $\mathbf{p} = \mathbf{0}$, one can express $\mathbf{f_{eq}}$ as follows:

$$\left(\mathbf{f_{eq}}\right)_{ij} = \left[\int_0^L \phi_i\phi_j dx\right]\left(\mathbf{f_E}\right)_i \tag{3.34}$$

Vector $\mathbf{f_E}$ in constant, therefore its integration is not required in Eq. 3.34. Then, the lumping matrix is defind as follows:

$$\left(\mathbf{G_F}\right)_{ij} = \int_0^L \phi_i\left(\bar{x}_1\right)\phi_j\left(\bar{x}_1\right)d\bar{x}_1 \tag{3.35}$$

Equation 3.35 is also numerically solved by a Gauss-Legendre quadrature.

It is worth mention the functions ϕ_i calculation, which are based on the Lagrangian polynomials and the nodal dimensionless coordinates ξ_j. At a given point of dimensionless coordinate ξ inside a finite element, one writes:

$$\phi_i(\xi) = \prod_{\substack{j=1 \\ j \neq i}}^{n_p} \left(\frac{\xi - \xi_j}{\xi_i - \xi_j} \right) \tag{3.36}$$

in which n_p is the finite element's number of nodes.

The derivatives of ϕ_i are as follows:

$$\phi_{i,\xi}(\xi) = \sum_{\substack{j=1 \\ j \neq i}}^{n_p} \left[\frac{1}{\xi_i - \xi_j} \prod_{\substack{k=i \\ k \neq j}}^{n_p} \left(\frac{\xi - \xi_k}{\xi_i - \xi_k} \right) \right] \tag{3.37}$$

All developments presented so far consider the local coordinate system of the finite element. To assemble the global matrices, one must rotate the local system to the global (x_1, x_2, x_3) through a rotation matrix $\mathbf{R}$ as follows:

$$\begin{aligned} \mathbf{u_n} &= \mathbf{R}\mathbf{u_n^G} \\ \mathbf{f_E} &= \mathbf{R}\mathbf{f_E^G} \end{aligned} \tag{3.38}$$

in which the indexes $\mathbf{G}$ indicate the global system. For 1D elements in spece, $\mathbf{R}$ is as follows (98, 99):

$$\mathbf{R}_i = \begin{bmatrix} c_1^i & c_2^i & c_3^i \\ -\dfrac{c_1^i c_3^i}{\sqrt{(c_1^i)^2 + (c_3^i)^2}} & \sqrt{(c_1^i)^2 + (c_3^i)^2} & -\dfrac{c_2^i c_3^i}{\sqrt{(c_1^i)^2 + (c_3^i)^2}} \\ -\dfrac{-c_3^i}{\sqrt{(c_1^i)^2 + (c_3^i)^2}} & 0 & \dfrac{c_3^i}{\sqrt{(c_1^i)^2 + (c_3^i)^2}} \end{bmatrix} \tag{3.39}$$

where $c_i^j = \cos(\alpha_i^j)$ and α_i^j is the angle between the local axis $(\bar{x}_1)$ and the global axis (x_i) calculated at the j point. $\mathbf{R}_i$ is the component of the rotation matrix associated with a given i node of the finite element. Let n be the total number of nodes of the finite element, then its rotation matrix is composed by:

$$\mathbf{R} = \begin{bmatrix} \mathbf{R}_1 & \cdots & 0 \\ & \ddots & \\ \vdots & \mathbf{R}_i & \vdots \\ & & \ddots \\ 0 & \cdots & \mathbf{R}_n \end{bmatrix} \tag{3.40}$$

It is worth stressing that for elements aligned with the x_2 axis (in which $c_3^i = c_1^i = 0$), Eq. 3.39 must be replaced by the following:

$$\mathbf{R}_i = \begin{bmatrix} 0 & c_2^i & 0 \\ -c_2^i & 0 & 0 \\ 0 & 0 & 1 \end{bmatrix} \tag{3.41}$$

Thus, the global matrices $\mathbf{K_E}$ and $\mathbf{G_E}$ from Eq. 3.7 are as follows:

$$\begin{aligned} \mathbf{K_E} &= (\mathbf{R})^\intercal \, \mathbf{K_F}(\mathbf{R}) \\ \mathbf{G_E} &= (\mathbf{R})^\intercal \, \mathbf{G_F}(\mathbf{R}) \end{aligned} \tag{3.42}$$

The global linear system of equations of the 1D FEM is then given by:

$$\mathbf{K_E u_n} = \mathbf{f} + \mathbf{G_E f_E} \tag{3.43}$$

in which $\mathbf{f}$ are the nodal applied forces and $\mathbf{f_E}$ the nodal values that interpolate the traction distribuited along the element. It is woroth mentioning the equivalence between Eq. 3.43 and Eq. 3.7, when one considers $\mathbf{f} = \mathbf{0}$ and $\mathbf{u_n} = \mathbf{u_E}$.

3.5 Reinforcements modelling via 1DBEM

Consider a 1D element as illustrated in Fig. 20, in which a distribuited traction $p(\bar{x})$ is applied. The BVP is governed by a expression called strong form, as follows:

$$EAu_{,\bar{x}\bar{x}}(\bar{x}) = -p(\bar{x}) \tag{3.44}$$

in which $u(\bar{x})$ is the displacement along the axial direction $\bar{x}$ in the local system. This orientation is equivalent to $\bar{x}_1$ in Fig. 20.

The weighted residual technique is adopted herein, using the fundamental solution of displacements $u^*(\bar{x})$, which leads to:

$$\int_0^L [EAu_{,\bar{x}\bar{x}}(\bar{x}) + p(\bar{x})]u^*(\bar{x})d\bar{x} = 0 \tag{3.45}$$

Partial integration is applied twice over Eq. 3.45, which results in the following:

$$(EAu^*(\bar{x})u_{,\bar{x}}(\bar{x}))\Big|_0^L - \Big(EAu^*_{,\bar{x}}(\bar{x})u(\bar{x})\Big)\Big|_0^L + \int_0^L \Big[u(\bar{x})EAu^*_{,\bar{x}\bar{x}}(\bar{x}) + p(\bar{x})u^*(\bar{x})\Big]d\bar{x} = 0 \tag{3.46}$$

Equation 3.44) can also represent the fundamental problem as follows:

$$EAu^*_{,\bar{x}\bar{x}}(\bar{x}) = -p^*(\bar{x}) \tag{3.47}$$

Applying Eq. 3.47, the constitutive and compatibility relations (Eq. A.8 and Eq. A.7) particularized for 1D domains into Eq. 3.46, one writes:

$$(Nu^*)\Big|_0^L - (uN^*)\Big|_0^L - \int_0^L up^* dx + \int_0^L pu^* dx = 0 \tag{3.48}$$

where N is the axial force. The $(\bar{x})$ terms have been suppressed in this expression, although the mechanical fields dependency on $\bar{x}$ is implicit.

The Dirac delta function (Δ) applied at the source point s represents the body forces in the fundamental problem. For 1D domains, the body force is uni-dimensinal and can be expressed as follows:

$$p^* = \Delta(\mathbf{x}^f - \mathbf{x}^s) \tag{3.49}$$

Applying Eq. 3.49 into Eq. 3.48, one eliminates the domain integration and writes:

$$u^s - (Nu^*)\Big|_0^L + (uN^*)\Big|_0^L - \int_0^L pu^* dx = 0 \tag{3.50}$$

where u^s is the source point displacement. The fundamental solutions for 1D domains can be obtained in the literature (93, 94, 95) and is expressed as follows:

$$u^*_s(\bar{x_f}) = -\frac{|\bar{x}_f - \bar{x}_s|}{2EA} \tag{3.51}$$

$$N^*_s(\bar{x_f}) = \frac{\text{sign}\,(\bar{x}_f - \bar{x}_s)}{2} \tag{3.52}$$

in which sign () is the sign function. $\bar{x}_f$ and $\bar{x}_s$ are the local coordinates of field and source points, respectively. The index s of the fundamental solutions indicates their dependency on the source point position $\bar{x}_s$.

Equation 3.50 must be evaluated for each source point that describes the boundary to obtain the 1DBEM representation. The boundary is composed solely of the endpoints 1 and n, which results in the following 2x2 system:

$$\begin{bmatrix} 1 - N^*_1(\bar{x}_1) & N^*_1(\bar{x}_n) \\ -N^*_n(\bar{x}_1) & 1 + N^*_n(\bar{x}_n) \end{bmatrix} \begin{Bmatrix} u_1 \\ u_n \end{Bmatrix} = \begin{bmatrix} -u^*_1(\bar{x}_1) & u^*_1(\bar{x}_n) \\ -u^*_n(\bar{x}_1) & u^*_n(\bar{x}_n) \end{bmatrix} \begin{Bmatrix} N_1 \\ N_n \end{Bmatrix} + \begin{Bmatrix} q_1 \\ q_n \end{Bmatrix} \tag{3.53}$$

where q_1 are q_n are as follows:

$$q_i = \int_0^L p(\bar{x}) u^*_i(\bar{x}) d\bar{x} \tag{3.54}$$

The integration from Eq. 3.54 can be numerically solved by the Gauss-Legendre quadrature. However, $p(\bar{x})$ must be numerically evaluated by interpolating its nodal values f_j with the Lagrangian polynomials, similar to Eq. 3.23. With that, Eq. 3.54 can be rewritten as follows:

$$q_i = \int_0^L \phi_j(\bar{x}) f_j u_i^*(\bar{x}) d\bar{x} = \left[\int_0^L \phi_j(\bar{x}) u_i^*(\bar{x}) d\bar{x}\right] f_j = \bar{\mathbf{G}}\mathbf{f} \tag{3.55}$$

in which $\mathbf{f}$ contain the nodal values f_j. This integration can be properly solved by the numerical quadrature, which results in the matrix $\bar{\mathbf{G}}$.

Besides, the matrices from Eq. 3.53 that are composed by the fundamental kernels are denoted by $\mathbf{H}$ and $\mathbf{G}$, in an analogy with the 3D BEM formulation. Thus, one writes the following algebraic system from Eq. 3.53:

$$\mathbf{Hu} = \mathbf{Gn} + \bar{\mathbf{G}}\mathbf{f} \tag{3.56}$$

in which $\mathbf{u}$ contains u_1 and u_n. $\mathbf{n}$ contain N_1 and N_n. $\mathbf{q}$ is given by Eq. 3.54. This expression is directly equivalent of Eq. 2.9 from 3D BEM.

However, the reinforcement element representation by Eq. 3.56 produce a poor distribuited traction modeling ($p(\bar{x})$), which is limited by a linear behavior. This aspect is relevant in the coupling technique applied in this study, because $p(\bar{x})$ represents the adherence force. Therefore, internal points can be accounted into the 1DBEM system in order to improve the $p(\bar{x})$ representation. From Eq. 3.50, one can write the following equation for a given internal point j:

$$u_j - N_j^*(\bar{x}_1)u_1 + N_j^*(\bar{x}_n)u_n = -u_j^*(\bar{x}_1)N_1 + u_j^*(\bar{x}_n)N_n + q_j \tag{3.57}$$

Equation 3.57 and Eq. 3.55 are applied into the system from Eq. 3.53, which results in the following:

$$\begin{bmatrix} 1 - N_1^*(\bar{x}_1) & 0 & N_1^*(\bar{x}_n) \\ -N_j^*(\bar{x}_1) & 1 & N_j^*(\bar{x}_n) \\ -N_n^*(\bar{x}_1) & 0 & 1 + N_n^*(\bar{x}_n) \end{bmatrix} \begin{Bmatrix} u_1 \\ u_j \\ u_n \end{Bmatrix} = \begin{bmatrix} -u_1^*(\bar{x}_1) & 0 & u_1^*(\bar{x}_n) \\ -u_j^*(\bar{x}_1) & 0 & u_j^*(\bar{x}_n) \\ -u_n^*(\bar{x}_1) & 0 & u_n^*(\bar{x}_n) \end{bmatrix} \begin{Bmatrix} N_1 \\ N_j \\ N_n \end{Bmatrix} + \int_0^L \begin{bmatrix} \phi_1(\bar{x})u_1^*(\bar{x}) & \phi_j(\bar{x})u_1^*(\bar{x}) & \phi_n(\bar{x})u_1^*(\bar{x}) \\ \phi_1(\bar{x})u_j^*(\bar{x}) & \phi_j(\bar{x})u_j^*(\bar{x}) & \phi_n(\bar{x})u_j^*(\bar{x}) \\ \phi_1(\bar{x})u_n^*(\bar{x}) & \phi_j(\bar{x})u_n^*(\bar{x}) & \phi_n(\bar{x})u_n^*(\bar{x}) \end{bmatrix} d\bar{x} \begin{Bmatrix} f_1 \\ f_j \\ f_n \end{Bmatrix} \tag{3.58}$$

One can represent any number of internal points together with the endpoints through Eq. 3.58. Regardless of its final dimension, this system of equations can still be algebraically written by Eq. 3.56. To obtain the solution of this system, one must multiply its expression by the inverse of $\mathbf{G}$, which leads to:

$$\mathbf{G^{-1}Hu} = \mathbf{n} + \mathbf{G^{-1}\bar{G}f} \tag{3.59}$$

It is worth mentioning that $\mathbf{G}$, as defined in Eq. 3.58, is not invertible. However, the internal points equations that compose the centre lines of the system does not affect the boundary solutions. Their purpose is only to improve the distributed force representation. Hence, one may impose the terms correspondent to internal points equations as $(\mathbf{G})_{jj} = EA/L$ for $jj \neq 1$ and $jj \neq n$ by establishing $N_j = 0$. This procedure does not affect the product $\mathbf{Gn}$ in any way. With that, $\mathbf{G}$ becomes invertible without disturbing the 1DBEM system solution. Besides, N_j values of internal points can be recovered from the equilibrium relation, once the solution of $\mathbf{u}$ and $\mathbf{f}$ is known.

Equation 3.59 format is equivalent to Eq. 3.43. Thus, this expression can be represented by the same algebraic form by stating the matrices $\mathbf{K_E}$ and $\mathbf{G_E}$ as:

$$\begin{aligned} \mathbf{K_E} &= (\mathbf{R})^{\intercal}\,\mathbf{G^{-1}H}(\mathbf{R}) \\ \mathbf{G_E} &= (\mathbf{R})^{\intercal}\,\mathbf{G^{-1}\bar{G}}(\mathbf{R}) \end{aligned} \tag{3.60}$$

Equation 3.59 can now represent the global system as follows:

$$\mathbf{K_E u} = \mathbf{n} + \mathbf{G_E f} \tag{3.61}$$

which allows obtaining the problems solution regarding displacements. This expression is also equivalent to Eq. 3.7 by considering $\mathbf{n} = \mathbf{0}$, similar to the equations obtained via FEM.

The internal axial forces can be found via 1DBEM by rearranging Eq. 3.61, which results in the follow:

$$\mathbf{n} = \mathbf{K_E u} - \mathbf{G_E f} \tag{3.62}$$

which results in the axial force results at the reinforcements interfaces, i.e., the endpoints. All internal points $\mathbf{n}$ result in zero, because of the procedure above-mentioned to make $\mathbf{G}$ invertible. These values can be obtained from the equilibrium relation, as follows:

$$N_{,\bar{x}} = -p(\bar{x}) \tag{3.63}$$

Integrating Eq. 3.63 and applying Eq. 3.33, one writes the following:

$$N_j = N_1 - \int_0^{\bar{X}_j} \phi_i(\bar{x}) d\bar{x} f_i \tag{3.64}$$

which leads to the axial force at a internal point j of local coordinate $\bar{X}_j$.

Equation 3.64 is also numerically solved by the Gauss-Legendre quadrature. However, an additional coordinates transformation is required, regarding the dimensionless system $[-1, 1]$ and the partial interval $[-1, \xi_j]$. ξ_j is the dimensionless coordinate associated with $\bar{X}_j$. Thus, the additional integration's Jacobian is written as follows:

$$J_E = \frac{\xi_j + 1}{2} \tag{3.65}$$

Besides, the dimensionless coordinate resulting from both transfornations is:

$$\xi = (\xi_E + 1)\,\frac{\xi_j + 1}{2} - 1 \tag{3.66}$$

3.6 Crossing between fibres and boundaries: the connection element

The coupling formulation presented so far requires all reinforcements fully embedded into a solely 3D BEM domain. This fact is a well known limitation of the coupling formulations found in the literature (100). Together with the sub-region technique, one must overcome this limitation in order to properly model nonhomogeneous domains. A special element scheme, called connection element, is applied herein for that purpose. It is worth mentioning that the authors initially proposed this approach for 2D reinforced domains (13).

The main challenge to model reinforcements that cross 3D BEM sub-region interfaces is in Eq. 3.5 and Eq. 3.6. These expressions require a defined 3D BEM sub-region for all reinforcement elements. Besides, all reinforcement nodes must be internal nodes of the 3D BEM formulation.

Figure 21 illustrates the possible crossing scenarios: an element J over the interface in (a) or a node i over the interface in (b). Both options fail to follow the requirements mentioned in the previous paragraph.

The connection element stands out as an alternative approach, which follows all requirements. Figure 22 illustrates the connection element between the nodes i and $i+1$. These nodes are moved along its respective elements, which accomplish the requirement of the nodes internal position. The connection element is positioned in the created gap, which provides the reinforcements' material continuity between elements $J-1$ and J. This element contributes only in the reinforcement expression, i.e., matrices $\mathbf{K_E}$ and $\mathbf{G_E}$ from Eq. 3.7.

In this approach, all reinforcement nodes remain as internal nodes of the 3D BEM formulation. Besides, the connection element is neglected in Eq. 3.5 and Eq. 3.6. Thus, both above-mentioned demands are attended. This approach does not affect the 3D boundary

Figure 21 – Possible crossing situations between reinforcement and boundary.

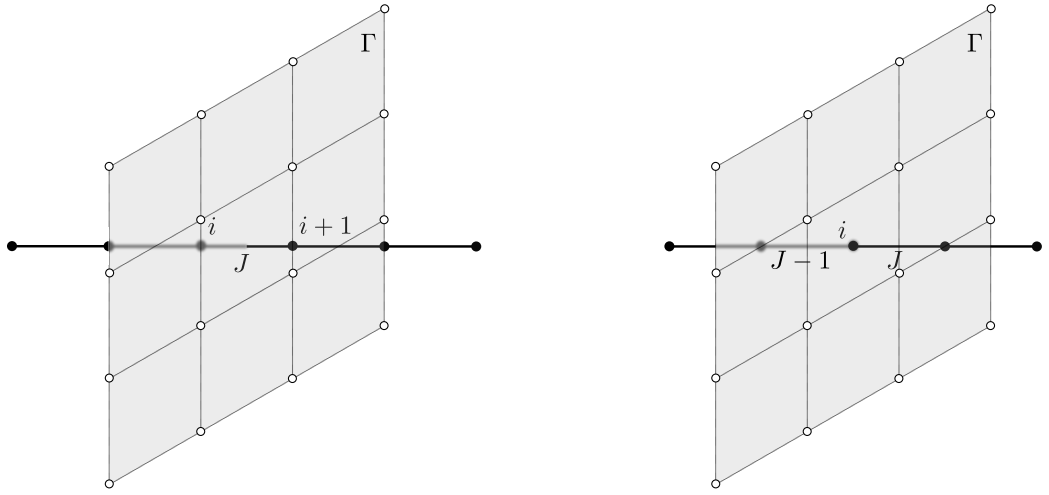

Source: The author.

Figure 22 – Approach adopted for crossings between reinforcements and sub-domains interfaces: Connection element positioned at discontinuous reinforcement mesh.

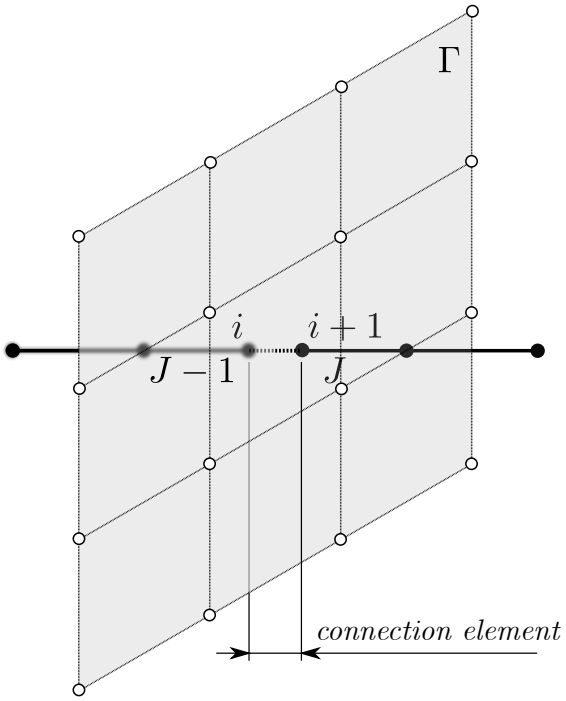

Source: The author.

integral equations or the compatibility relations on the interface from the sub-region technique. Furthermore, there is no need to modify the boundary mesh, which highlights the efficiency and robustness of this approach, especially when dealing with complex geometries.

The connection element formulation is simple. It is always a linear element defined by the nodes i and $i+1$ illustrated in Fig. 22, so numerical integration is not necessary.

Besides, it usually has small dimensions, therefore its poor approximation does not disturb the reinforcement global response. When the FEM represents the reinforcements, the connection element's stiffness and lumping matrix are as follows:

$$\mathbf{K} = \begin{bmatrix} 1 & -1 \\ -1 & 1 \end{bmatrix} \frac{EA}{L} \tag{3.67}$$

$$\mathbf{G_F} = \begin{bmatrix} 1/3 & 1/6 \\ 1/6 & 1/3 \end{bmatrix} L \tag{3.68}$$

When the 1DBEM represents the reinforcements, the connection element matrices from Eq. 3.59 are the following:

$$\mathbf{H} = \begin{bmatrix} 1/2 & -1/2 \\ -1/2 & 1/2 \end{bmatrix} \tag{3.69}$$

$$\mathbf{G} = \begin{bmatrix} 0 & -1 \\ -1 & 0 \end{bmatrix} \frac{L}{2EA} \tag{3.70}$$

$$\bar{\mathbf{G}} = \begin{bmatrix} 1/6 & 1/3 \\ 1/3 & 1/6 \end{bmatrix} \frac{-L^2}{2EA} \tag{3.71}$$

The connection element's mechanical properties (E, A) are the same as the adjacent element's. Furthermore, rotation (Eq. 3.42) must be applied into the above-presented expressions in order to properly consider them into the global matrices $\mathbf{K_E}$ and $\mathbf{G_E}$.

3.7 Numerical applications of the linear coupling formulation

This Section presents the numerical applications executed with the proposed reinforced formulation. The first application validates the numerical results with experimental reference results for a random fibre reinforced structure, whereas the second presents the robustness of the formulation to present a cracked reinforced structure.

3.7.1 Reinforced Lagrangian BEM application: Random fibres modelling

This application handles the mechanical analysis of a concrete matrix reinforced by short fibres distributed randomly/pseudo-randomly inside the domain. The stiffening effect of different fibre volumes can be measured through the equivalent longitudinal elastic modulus (E_{ef}). For this purpose, an uniaxial stress scenario is simulated as illustrated in Fig. 23(a), which involves the compression test. Figure 23(b) illustrates the test scheme, whereas (101) presents the experimental results. The numerical model (Fig. 23(a)) consists

of a cylinder with diameter of 20 mm and length of 20 mm. The material properties for the matrix are: Young's modulus $E_M = 39.6$ GPa and Poisson ratio $\nu = 0.2$. The applied load simulates an uniform uniaxial stress by a unitary applied displacement $\bar{\mathbf{u}}$. The steel fibres have the following mechanical properties: Young's modulus $E_f = 220$ GPa, length $l_F = 13$ mm and cross-section radius $r_F = 0.1$ mm.

Figure 23 – Numerical application of the elastic coupling: numerical model (a) and experimental scheme (b) for an uniaxial compression test (1).

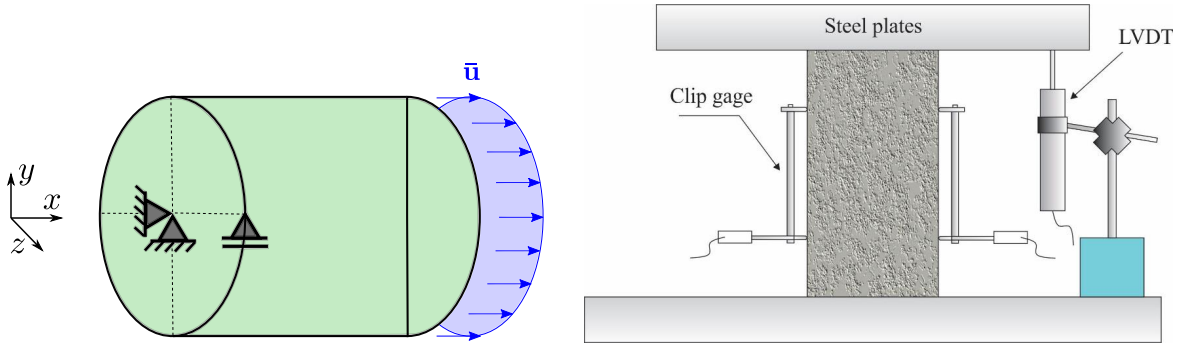

(a) (b)

Source: The author and (102), adapted.

The equivalent longitudinal elastic modulus can be determined as follows:

$$E_{ef} = \frac{L}{\bar{u}_1 \pi r^2} \int_{\Gamma_s} t_1(\Gamma)\, d\Gamma \tag{3.72}$$

where L is the structure's length in the axial direction (x), r is the cylinder radius (in the plane $x_2\, x_3$), Γ_s is the cylinder face where $\bar{\mathbf{u}}$ is applied and $t_1(\Gamma)$ are the traction results at the boundary.

The Lagrangian BEM mesh of the contour is composed by 4250 linear quadrilateral elements and 4442 collocation points. Figure 24 illustrates this mesh. 5 quadratic 1DBEM elements discretise each short fibre. Previous analyses have shown mesh convergence of these meshes regarding displacements.

The numerical results of the Lagrangian 1DBEM/BEM are compared against experimental responses from (101). A steel-fibre reinforced concrete was used in the tests, which match the material properties previously presented for this numerical application. This application accounts for three different fibre's contents V_f: 0%, 1% and 2% in volume. The experimental tests assume linear-elastic material behaviour. Thus, the numerical approach disregards the material nonlinearities. It is worth mentioning that the sense (compression or tension) is indifferent for the numerical analysis, since the constitutive model is symmetric.

Three different fibre's Random/pseudo-random distributions represent the fibres spacial position:

Figure 24 – Boundary mesh utilised for the cylinder representation.

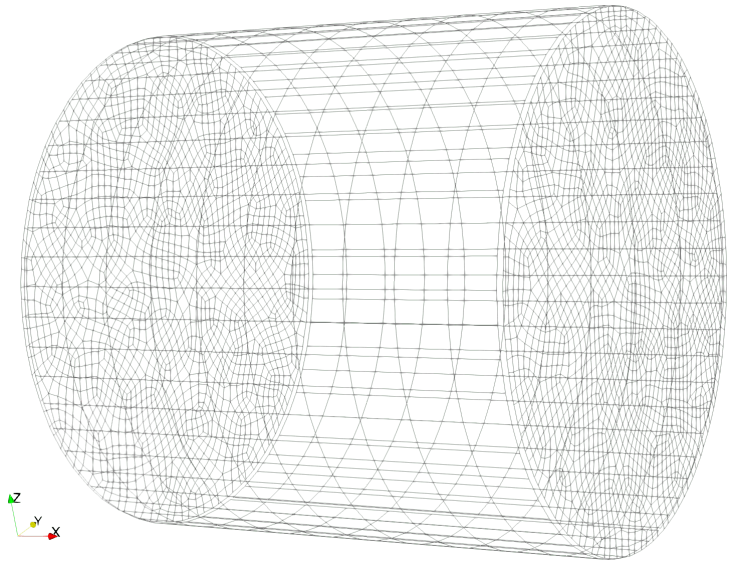

Source: The author.

- "BEM_{rand}" assumes fibre position and fibre inclination governed by uniform statistical distribution. This assumption leads to random distributed fibres;
- "BEM_{alig}" assumes fibre position governed by uniform statistical distribution and inclination aligned with the x axis;
- "$\text{BEM}_{\text{transv}}$" assumes fibre position governed by uniform statistical distribution and inclination aligned with y axis.

The pseudo-random fibres generation starts by determining the first fibre's endpoint, which must be positioned inside the cylinder from Fig. 23(a). Then, the opposite endpoint can be defined through a spherical coordinates system (l_F,θ,φ) originated in the first endpoint. In BEM_{rand}, both θ and φ are uniformly distributed within [0,π] and [0,2π] respectively. In BEM_{alig} and $\text{BEM}_{\text{transv}}$, such angles are both constant and equal to ($\theta = 0$,$\varphi = \pi/2$) and ($\theta = \pi/2$,$\varphi = \pi/2$), respectively. One generates each single fibre consecutively until the specified fibre content in volume is reached.

Figure 25 illustrates the results obtained from the three above-mentioned distributions and its comparison with experimental responses. Such comparison has been performed through the relation between the equivalent elastic modulus (E_{ef}) and the matrix Young's modulus (E_M). In this figure, the results are tendency lines (from linear regression) of the multiple values obtained for each point. The experimental values refer to the mean "Exp. val." and the respective maximum and minimum responses, "Exp_{max}" and "Exp_{min}".

The results on Fig. 25 demonstrate the accuracy of the proposed formulation in modelling the mechanical influence of fibres. It is worth remarking that the experimental mean responses lead to a behaviour between BEM_{rand} and BEM_{alig}. It suggests a possible

Figure 25 – Stiffness variation as a function of the fibre volume.

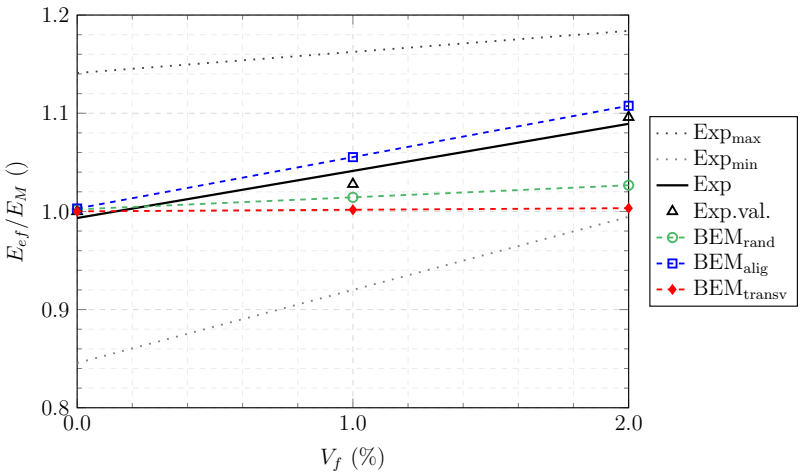

Source: The author.

randomness over the real fibre spacial position. Such randomness influence on the fibre position has been indicated in the literature, as mentioned by (103, 104).

In this regard, a fourth pseudo-random distribution, called $\text{BEM}_{\text{normal}}$, has been accounted for achieving the experimental mean values. In this additional scenario, the fibre spacial position is random and its inclination follows a Gaussian bi-variate statistical distribution. The inclination's mean values are nil in relation to x axis and the standard deviations are calibrated based on the experimental results (101). Previous analyses have indicated that the accurate standard deviation is 0.23 rad. Figure 26 illustrates the results obtained with the calibrated distribution: its values in one simulation ($\text{BEM}_{\text{normal}}$ val.), its the tendency line ($\text{BEM}_{\text{normal}}$), the reference results and the transversely and aligned fibres distributions results.

Figure 26 – Stiffness variation as a function of the fibre volume using different distributions of fibres in the numerical model.

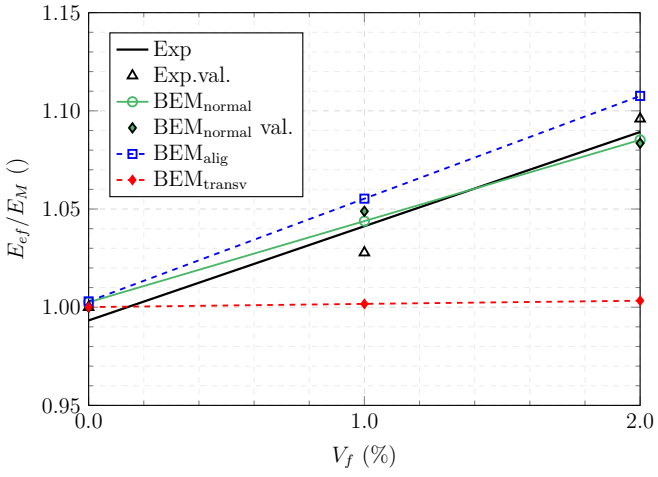

Source: The author.

Figure 26 illustrates the good agreement among the responses of $\text{BEM}_{\text{normal}}$ and the experimental results. Therefore, these results successfully demonstrate the accuracy of the proposed formulation in the mechanical representation of the coupling between matrix and reinforcements in a linear-elastic condition. Besides, these results demonstrate the influence of the spacial fibre position randomness on the mechanical response of fibre reinforced concrete specimens. Further researches could perform a parametric study using the proposed formulation. Then, the statistical characterisation could be properly handled. Nevertheless, this suggestion is beyond the purpose of the present article.

Because all simulations consider pseudo-random fibre distribution, 5 simulations of each scenario were performed for each fibre content. Thus, standard deviation values have been assessed, which can measure the variability of the analysis. The higher variability was observed in the BEM_{rand} model with $V_f = 1\%$, which led to a standard deviation of 0.8%. Nevertheless, the variability of the experimental test is considerably larger, with standard deviations up to 5.8%.

The next Figures 27, 28, 29 and 30 illustrate the fibre displacements along x direction obtained with the different fibres' distributions. Figure 27 refers to the BEM_{alig} case, Fig. 28 refers to $\text{BEM}_{\text{transv}}$, Fig. 29 refers to BEM_{rand} and Fig. 30 to $\text{BEM}_{\text{normal}}$. All of these figures exhibit both the fibres content $V_f = 1\%$ and $V_f = 2\%$. A tension scenario ($\bar{\mathbf{u}}_{\mathbf{D}} = 1$ mm) was considered in these figures.

The analysis of Figures 27, 28, 29 and 30 allows concluding that, in all scenarios, the displacements obtained at the fibres are in agreement with the applied load and within the expected range. Besides, one observes the fibres' position for each case. It is worth stressing that the calibrated pseudo-random distribution proposed exhibits a coherent fibres' positioning, which agrees with the expected behaviour in the experimental tests.

Figure 27 – Displacements in x direction over the reinforcements using: BEM_{alig} with $V_f = 1\%$ (a) $V_f = 2\%$ (b).

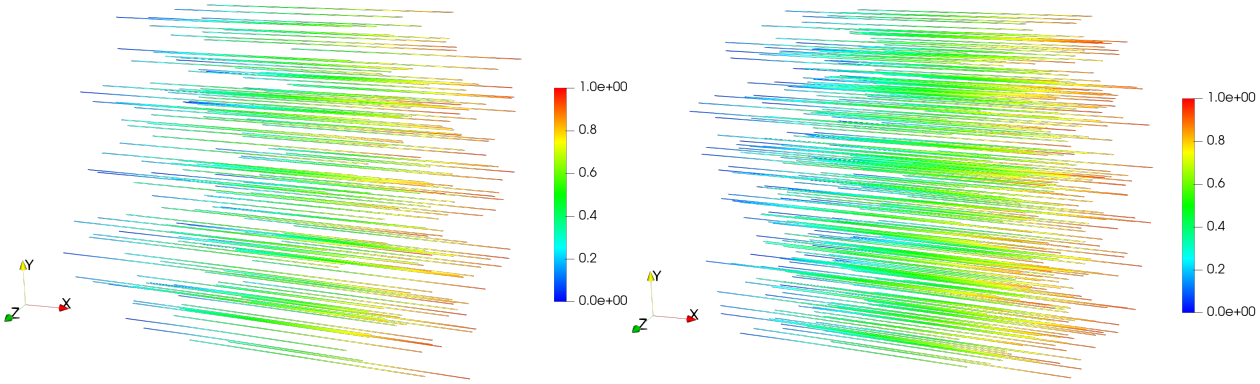

(a) (b)

Source: The author.

Figure 28 – Displacements in x direction over the reinforcements using: $\text{BEM}_{\text{transv}}$ with $V_f = 1\%$ (a) $V_f = 2\%$ (b).

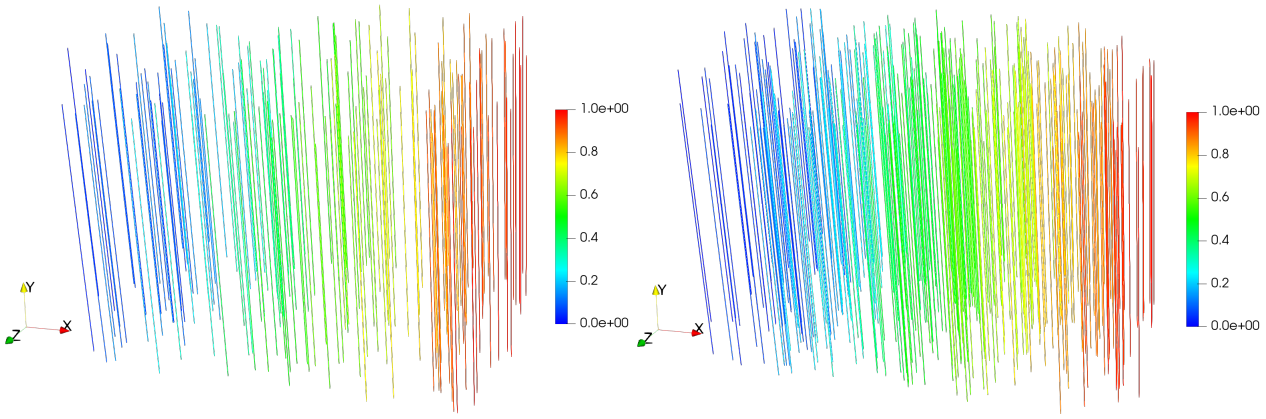

(a) (b)

Source: The author.

Figure 29 – Displacements in x direction over the reinforcements using: BEM_{rand} with $V_f = 1\%$ (a) $V_f = 2\%$ (b).

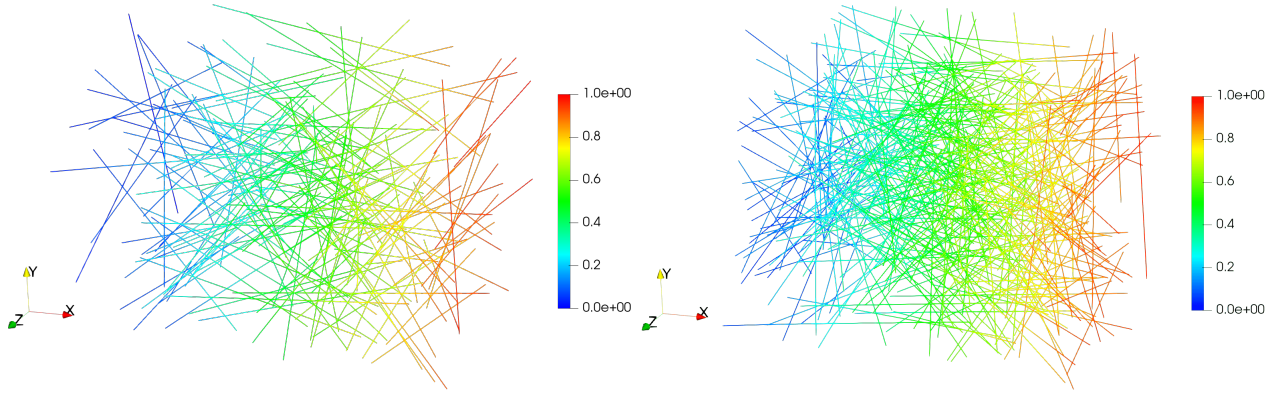

(a) (b)

Source: The author.

Figure 30 – Displacements in x direction over the reinforcements using: $\text{BEM}_{\text{normal}}$ with $V_f = 1\%$ (a) $V_f = 2\%$ (b).

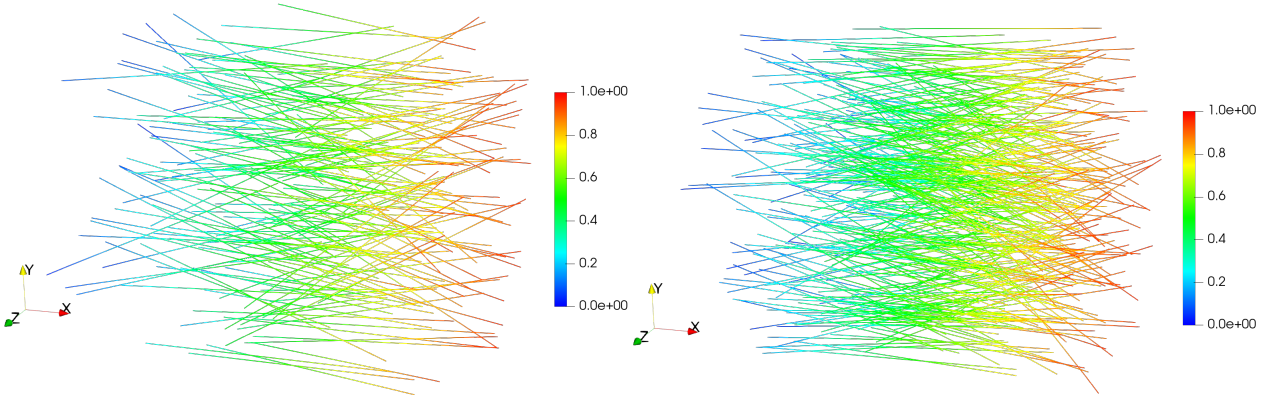

(a) (b)

Source: The author.

3.7.2 Reinforced IGABEM application: Single-edge notched body

This numerical example consists of applying the linear fracture mechanics approach to a solid with a single-edge notch, as illustrated in Fig. 31. Thus, the coupling technique presented herein considers the DBEM formulation (Sec. 2.8) to represent the crack. The physical properties illustrated in Fig. 31 are: $h = 10$ cm, $b = 5$ cm, $a = 2.5$ cm and $\sigma = 1$ kN/cm^2. In addition, the material properties of the solid are: Young's modulus $E = 1000$ kN/cm^2 and Poisson's ratio $\nu = 0.2$. The fibres present circular cross-section with radius $r = 0.2$ cm and three different values of Young's modulus are analysed: $E_0 = 0$, $E_{500} = 500$, $E_{1000} = 1000$ and $E_{1500} = 1500$ kN/cm^2.

Figure 31 – Reinforced cracked solid analysed with linear IGABEM coupling formulation.

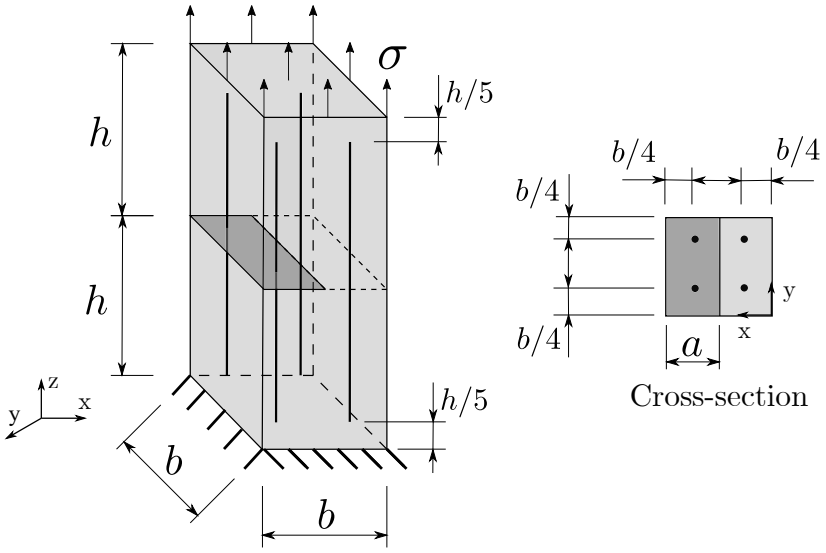

Source: The author.

Reference results are found in the literature (73) for a 2D equivalent problem without the fibres. The results are presented as the crack mouth opening displacement (CMOD) values, which can be used as reference for the scenario with $E_F = 0$. The CMOD (δ) present in (73) is:

$$\delta = \left(\frac{4\sigma a}{E'}\right) \frac{1.46 + 3.42\left(1 - \cos\frac{\pi a}{2b}\right)}{\left(\cos\frac{\pi a}{2b}\right)^2} \tag{3.73}$$

in which $E' = E/(1-\nu^2)$. It is worth mentioning that the reference results are constant along the dimension y of the analysed model, since they come from a 2D equivalent problem.

Two isogeometric meshes are used to represent the solid in this example. Both of them are composed by 14 bi-quadratic ($p = q = 2$) regular NURBS surfaces that represent the external boundaries and 2 regular NURBS surfaces of $p = q = 4$ that represent the

crack faces. Mesh A is used for the mechanical analyses without fibres (scenario $E_F = 0$) and presents all NURBS surfaces with only one knot span, which results in 176 collocation points. Mesh B is derived from Mesh A and it is obtained by refining the crack surfaces with 3 knot insertions (16), which results in 254 collocation points. The second mesh is used in the analyses with the presence of fibres, which require thinner discretization of the crack due to its complex mechanical behaviour when affected by the crossing fibres. Figure 32 illustrates both meshes. Mesh convergence has been previously verified regarding displacements at the crack mouth opening.

Figure 32 – Isogeometric meshes considered in the numerical example's analyses.

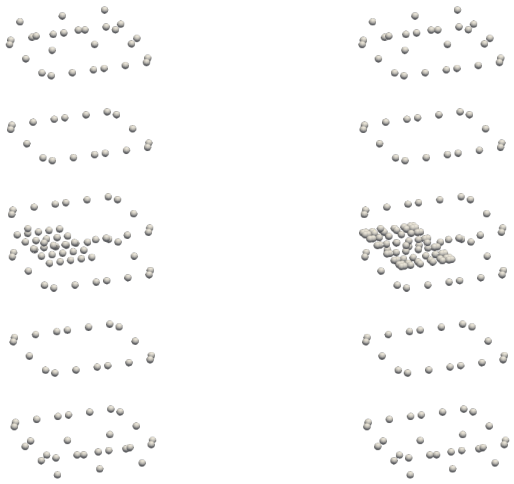

(a) Mesh A (b) Mesh B

Source: The author.

The fibres discretisation is the same in all of the scenarios. Each one of the four long fibres is represented by 16 quadratic elements, which leads to a total of 134 collocation points. The crossing between the fibres and the crack is represented by the connection element strategy, as presented in Sec. 3.6.

Figure 33 illustrates the results of CMOD along the crack mouth (direction y) obtained in all of the three scenarios and the reference results (from Eq. 3.73) labelled as "Analytical". In the numerical models, the CMOD is calculated from the difference between the z displacements of the superior and the inferior crack faces, at the crack mouth. In this figure, one observes that increasing the fibres Young's modulus leads to a decrease in the value of the CMOD, as expected. In fact, all of the scenarios with non-zero fibres Young's modulus are significantly far from the results without fibres, which is expected since the presence of fibres introduces a linear continuity at the crack surface. Provided that this analysis imposes a linear behaviour in the fibres, they surely must drastically affect the crack opening.

It is worth mentioning that the greatest error value between E_0 and the analytical results from Eq. 3.73 was 0.72%. Thus, the results demonstrate accuracy as far as the

Figure 33 – Crack opening displacements along the crack mouth (direction x).

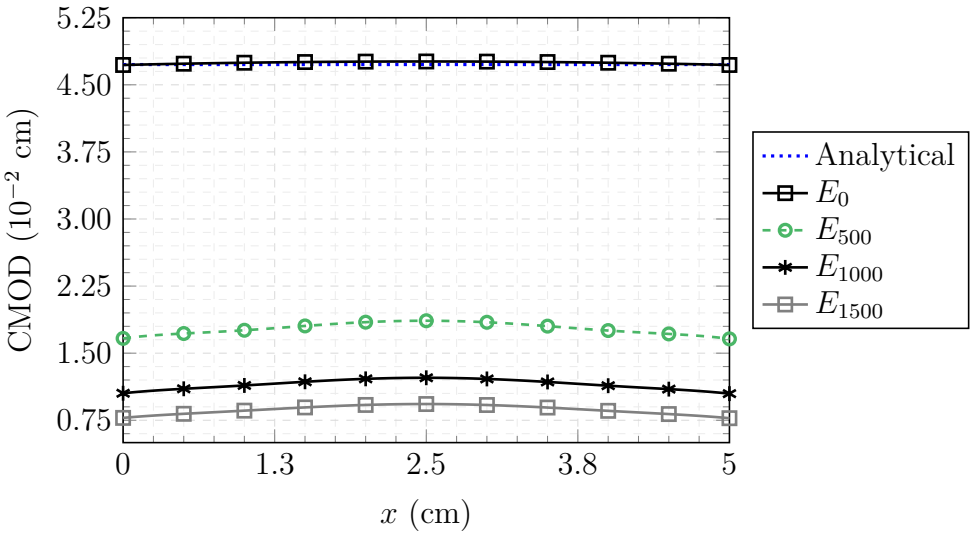

Source: The author.

reference comparison is valid. Although there is no reference results for the reinforced analyses, the obtained CMOD's are in agreement with the expected behaviour.

Figure 34 illustrates the z displacements fields over the solid's deformed shape obtained in all of the four scenarios. A scale factor of 50 is considered. The NURBS surfaces are subdivided into 100 auxiliary Lagrangian elements (4 nodes) to generate the visualisation with the software *Paraview*. This figure demonstrates that the solid's deformed shape is coherent in all of the analyses. Besides, it is interesting to observe the effect of the fibres in the resulting displacement fields. It is clear how the linear and continuous fibres prevented the crack opening, as expected. Furthermore, one observes the fibre's effect on the crack surface, which presents a slight deformation that reminds a fibre pullout. All of the mentioned observations are in agreement with the expected behaviour.

Figure 35 presents the axial stresses obtained in each scenario along the fibre's length (S_f), considering the fibre that crosses the crack. It is worth mentioning that the results at both fibres that cross the crack are identical due to symmetry. In this figure, one observes a massive stress concentration in the fibre's region near the crack (around $S = 8$ cm, which is the crossing). This extreme behaviour is explained by the fact that the fibres remain linear-elastic in these analyses. In a real scenario, that region would present both yielding and slipping, which would cause energy dissipation and decrease the stress concentration. Since the formulation applied herein does not allow for these nonlinearities so far, this behaviour is expected. Besides, it is worth highlighting that the scenarios with higher fibres Young's modulus show higher values of axial stress along the fibre, which is also in agreement to what is expected.

Therefore, this numerical example demonstrates that the proposed elastic reinforced

Figure 34 – Deformed shape and z displacements field obtained via the IGABEM for each scenario. Scale factor equals 50.

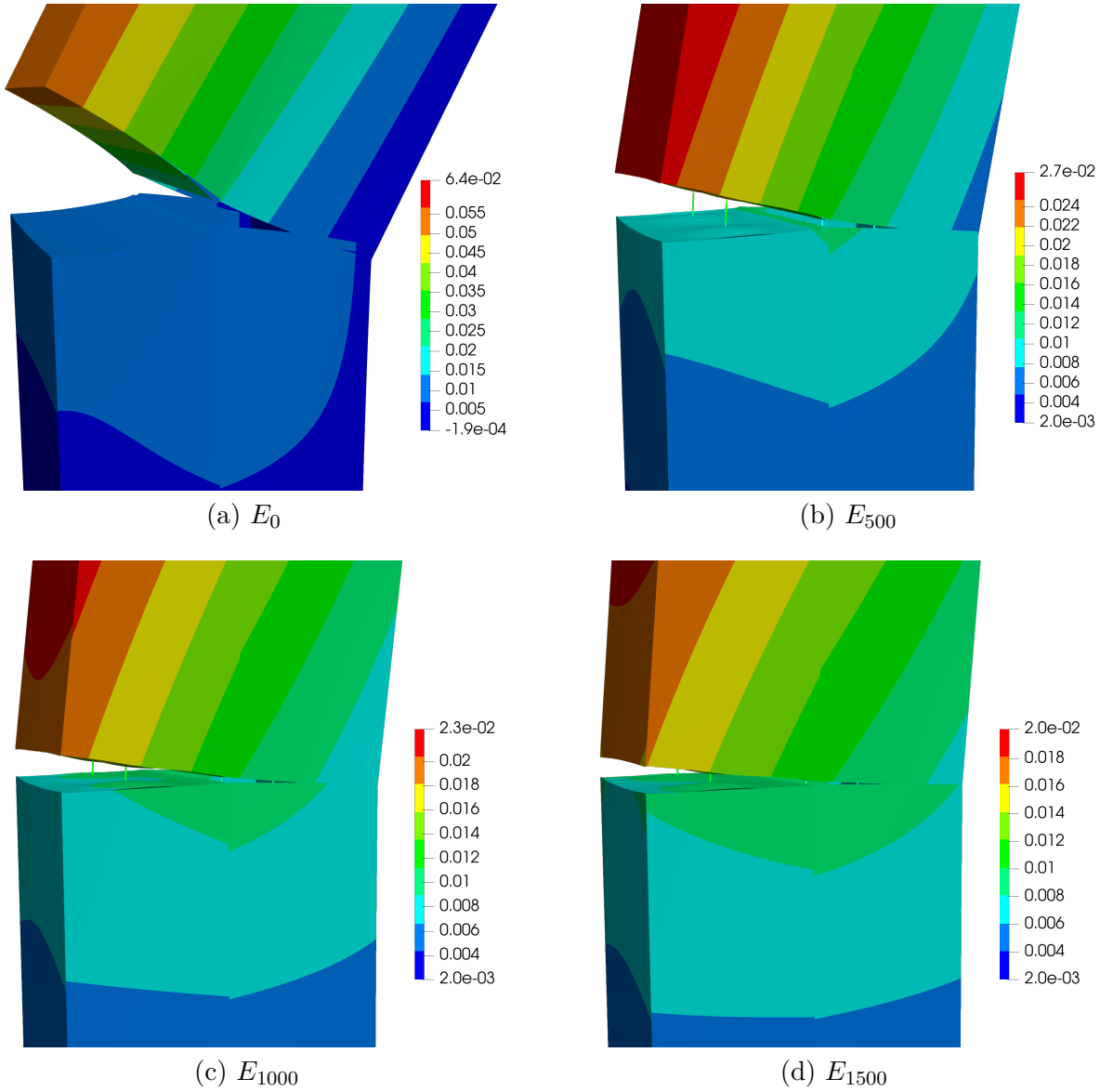

(a) E_0 (b) E_{500}

(c) E_{1000} (d) E_{1500}

Source: The author.

formulation is adequate to simulate reinforced cracked problems. Later in this study, the addition of the yield and the bond-slip behaviours to this formulation is expected to lead to more accurate and representative models, which would be able to model real-life engineering problems regarding cracked reinforced solids.

Figure 35 – Axial stresses along the fiber that crosses the crack obtained in each reinforced scenario.

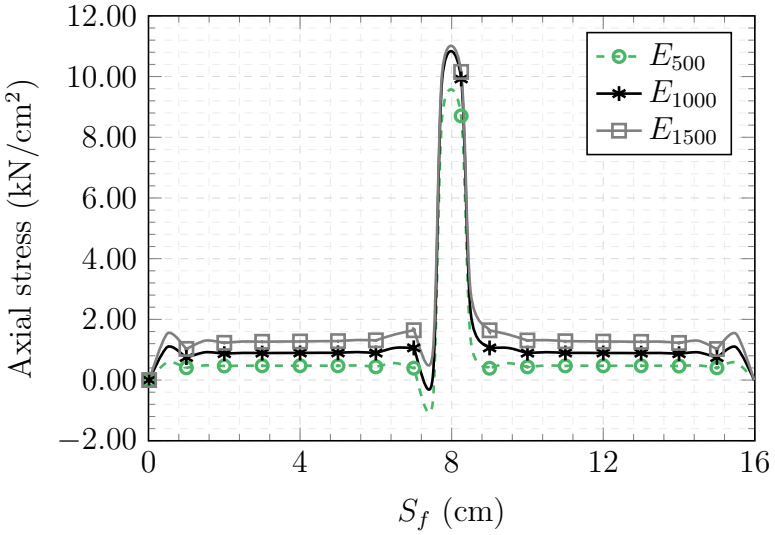

Source: The author.

4

Nonlinear Reinforced Formulations

This study consider two nonlinear behaviours at the reinforcements: the bond-slip and the elastoplasticity. The first one allows for representing the adherence loss phenomenon, i.e., the mechanical degradation of the interface matrix/reinforcement. The second one properly represents the degradation of the reinforcement's material, specially when dealing with steel. This chapter presents each formulation in details separately. Then, it presents the proper approach to combine the two nonlinearities into one solely nonlinear formulation, which is able to represent the mechanical degradation of both the reinforcement's material and the interface.

4.1 Bond-slip modelling: Literature Review

The adherence stress analysis in the classic pullout tests (105) can be considered the starting point of the study of adherence mechanisms between matrix and reinforcing elements. In the pullout test, a concrete specimen is reinforced by a steel rebar at its centre, which presents an outward extremity. A machine claw pulls this extremity under tension. Several studies were able to investigate the adherence mechanism in a deeper level using this experimental scheme: (106) experimented with loading cycles, being able to analyse the load history's contribution and cumulative effects; (107) analysed high-performance concrete reinforced by steel bars. More recently, several studies have worked on experimental analyses focused on ultra high-performance concrete reinforced by steel bars, as mentioned in (108). (109) presents a modified pullout test, in which only half of the steel bar's length is adhered to the concrete. Comparing against the classical methodology, this strategy would take to smaller perturbations in the adherence region, which are caused by its proximity to the support plate. In addition, the traditional experimental

scheme usually consists of a squared-base concrete prism. However, several authors adopt cylindrical concrete specimens (110, 108), which provides a constant concrete cover to protect the reinforcing bar.

It is clear that the adherence mechanism in reinforced concrete is significantly complex. Although one can easily measure the consequences of the adherence loss (called slip), its causes consist of the combination of several physical phenomena. According to (111) and (112), the adherence is virtually composed by three distinct portions, however it is impossible to measure each one of them separately. The first portion is the adhesion related to the physicochemical bonds between the materials from matrix and reinforcement. The second portion is the friction, which emerges from the energy transmission between matrix and reinforcement as a result of the contact. The third is the mechanical adherence due to overhangs usually present on reinforcing bars. Considering all of the variables and phenomena related to the adherence, the use of various different models to describe the adherence loss mechanism is understandable. Besides, these models are usually applicable to specific pairs of materials and might present a few discontinuous regions, in which each region is meant to represent a different adherence phenomena. The models proposed by (113, 114) and (115) are examples of reinforced concrete adherence models.

The numerical simulation of adherence models for structures has always been a relevant topic in this field. The FEM was initially applied by (116), which used bond link elements to represent the adherence. This element's parameter are given by a constitutive adherence law (adherence stress *vs* slip). (117) applied the same approach to develop analytical models that represent eccentric pullout tests. (118) expanded the formulation with two-dimensional bond link elements, which incorporate parameter from the steel, the concrete and the adherence law. (119) presented static and dynamic FEM formulations, which consider the adherence loss effects.

Therefore, this context demonstrates the importance of studying the adherence effects on concrete structures, as well as incorporating them to the structural designs and analyses. In this regard, BEM formulations have been marginally treated in the literature. (64) and (120) dealt with BEM approaches for adherence loss only in 2D formulations using the FEM/BEM coupling. Hence, it is a contribution of this study the proposition of 3D BEM formulations considering the adherence loss using the 1DBEM/BEM coupling technique. It is worth mentioning that the 1DBEM/BEM stands out as more suitable for this problem than the classic FEM/BEM, since it shows smaller oscillations in force results (13). Besides, the 3D approach is more adequate to represent real-world structures through effective numerical models.

4.2 Bond-slip modelling

The bond-slip modelling is based on the existence of a relative displacement between the reinforcement and the domain. Hence, the displacements compatibility presented in Eq. 3.2b is no loger valid. This relation can be rewritten as follows:

$$\mathbf{s} = \mathbf{u_D} - \mathbf{u_E} \tag{4.1}$$

in which $\mathbf{s}$ is the relative displacements vector. This expression is applied into Eq. 3.7 as follows:

$$\mathbf{K_E u_D} + \mathbf{G_E f_D} = \mathbf{K_E s} \tag{4.2}$$

Thus, one updates the coupling algebraic system as:

$$\begin{bmatrix} \mathbf{H_{CC}} & \mathbf{0} & -\mathbf{G_{CF}} \\ \mathbf{H_{FC}} & \mathbf{I} & -\mathbf{G_{FF}} \\ \mathbf{0} & \mathbf{K_E} & \mathbf{G_E} \end{bmatrix} \begin{Bmatrix} \hat{\mathbf{u}}_\mathbf{C} \\ \mathbf{u_D} \\ \mathbf{f_D} \end{Bmatrix} = \begin{bmatrix} \mathbf{G_{CC}} \\ \mathbf{G_{FC}} \\ \mathbf{0} \end{bmatrix} \left\{ \hat{\mathbf{t}}_\mathbf{C} \right\} + \begin{bmatrix} \mathbf{0} \\ \mathbf{0} \\ \mathbf{K_E} \end{bmatrix} \{\mathbf{s}\} \tag{4.3}$$

Equation 4.3 is the starting point of the nonlinear modelling of the bond-slip. The adherence law express the relation between the slip values and the adherence force values. Then, this process become similar to the cohesive procedures. This study deals with three different adherence laws: (a) constant law, (b) linear law and (c) multi-linear law, as illustrated in Fig. 36. The laws (a) and (b) are generally used in purely theoretical applications. Whereas (c) is based on a linearisation of the most suggested empirical laws used to model reinforced concrete structures (113, 114).

The constant law (Fig. 36(a)) is composed only by a maximum constant value for the adherence force (f_{max}). When one reaches this value, the slip can grow indefinitely. Thus, this law can be mathematically represented as follows:

$$\begin{aligned} f(s) &\leq f_{MAX} \quad , \quad s = 0 \\ f(s) &= f_{MAX} \quad , \quad s > 0 \end{aligned} \tag{4.4}$$

The linear law (Fig. 36(b)) allows for the adherence force relaxation after a peak plateau of f_{MAX}. The relaxation phase ends in a constant residual value f_{RES}. This law can be mathematically represented as follows:

$$\begin{aligned} f(s) &\leq f_{MAX} && , \quad s = 0 \\ f(s) &= f_{MAX} && , \quad 0 < s \leq s_1 \\ f(s) &= f_{MAX} - \left(\frac{f_{MAX} - f_{RES}}{s_2 - s_1} \right) (s - s_1) && , \quad s_1 < s \leq s_2 \\ f(s) &= f_{RES} && , \quad s > s_2 \end{aligned} \tag{4.5}$$

Figure 36 – Different laws considered for the bond-slip behaviour modelling.

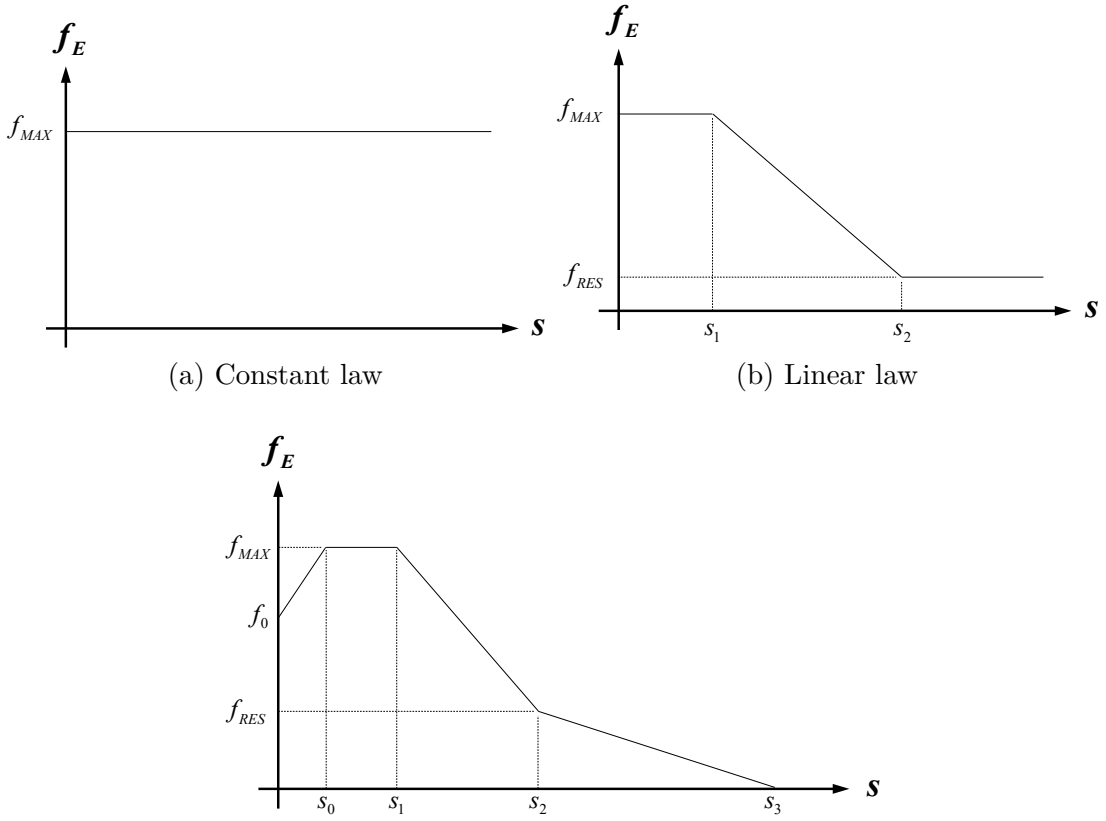

(a) Constant law

(b) Linear law

(c) Multi-linear law

Source: The author.

The multi-linear law (Fig. 36(c)) presents a upward phase, which is limited by the slip value s_0. When this point is passed, the law still has a peak plateau and two relaxation phases until the slip values goes to zero. One expect to obtain results more close to experimental data with this adherence law, due to its inspiration in empirical laws, as above-mentioned. Besides, its piecewise linear behavior should guarantee a good convergence rate in the iterative process. This law can be mathematically expressed as follows:

$$\begin{aligned}
f(s) &\leq f_0 && , \quad s = 0 \\
f(s) &= f_0 + \left(\frac{f_{MAX} - f_0}{s_0}\right) s && , \quad 0 < s \leq s_0 \\
f(s) &= f_{MAX} && , \quad s_0 < s \leq s_1 \\
f(s) &= f_{MAX} - \left(\frac{f_{MAX} - f_{RES}}{s_2 - s_1}\right)(s - s_1) && , \quad s_1 < s \leq s_2 \\
f(s) &= f_{RES} - f_{RES}\left(\frac{s - s_2}{s_3 - s_2}\right) && , \quad s_2 < s \leq s_3
\end{aligned} \tag{4.6}$$

The laws' parameters (f_{MAX}, f_{RES}, f_0, s_0, s_1, s_2 e s_3) must be adequately informed in each application.

4.2.1 Prescribed displacements applied at reinforcement nodes

The formulations developed so far consider only prescribed boundary conditions at the external boundaries, through $\hat{\mathbf{p}}_\mathbf{C}$ in Eq. 3.9. However, it is worth considering to apply prescribed displacements directly at reinforcement nodes, which allows the modelling of pullout tests. In this experimental test, displacement controlling is applied into a external point of the reinforcing steel bar.

The solution scheme requires the connection element (Sec. 3.6), positioned over the external boundary as illustrated in Fig. 37. This element shall transfer the applied load/displacement to the nearest reinforcement node.

Figure 37 – Connection element applied for the prescribed displacement directly at the fires.

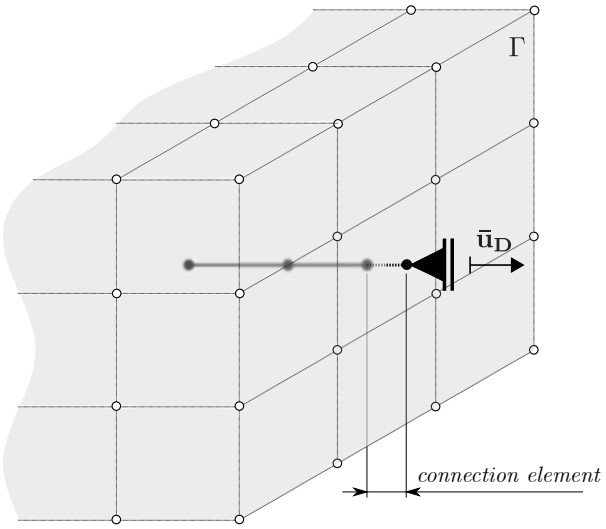

Source: The author.

Unlike the formulation presented in Sec. 3.6, the connection element herein has only one adjacent reinforcement element. Therefore, its other end consists of a new node that must be added to the global matrices $\bar{\mathbf{K}}_E$ and $\bar{\mathbf{G}}_E$. The degrees of freedom related to these additional nodes are positioned at the end of the reinforcement mesh, thus the global matrices can be rewritten as follows:

$$\bar{\mathbf{K}}_\mathbf{E} = \begin{bmatrix} \mathbf{K}_\mathbf{E} & \bar{\bar{\mathbf{K}}}_{\text{sup}} \\ \bar{\bar{\mathbf{K}}}_{\text{inf}} & \bar{\bar{\mathbf{K}}}_{\text{diag}} \end{bmatrix} \tag{4.7a}$$

$$\bar{\mathbf{G}}_\mathbf{E} = \begin{bmatrix} \mathbf{G}_\mathbf{E} & \bar{\bar{\mathbf{G}}}_{\text{sup}} \\ \bar{\bar{\mathbf{G}}}_{\text{inf}} & \bar{\bar{\mathbf{G}}}_{\text{diag}} \end{bmatrix} \tag{4.7b}$$

where $\mathbf{K}_\mathbf{E}$ and $\mathbf{G}_\mathbf{E}$ are the original global matrices, which does not consider the additional nodes contribution. $\bar{\mathbf{K}}_\mathbf{E}$ and $\bar{\mathbf{G}}_\mathbf{E}$ are the updated global matrices that must be considered into the algebraic system.

Equation 4.7 allows splitting the degrees of freedom into the original ones and the additional ones, which have been created by the connection elements. Then, the prescribed

displacements are applied into the additional ones. Equation 4.2 can now be rewritten, by setting the reinforcements prescribed displacements ($\bar{\mathbf{u}}_\mathbf{D}$) apart from the unknown displacements ($\mathbf{u_D}$), which results in the following:

$$\mathbf{K_E u_D} + \bar{\bar{\mathbf{K}}}_{\text{sup}}\bar{\mathbf{u}}_\mathbf{D} + \mathbf{G_E f_D} = \mathbf{K_E s} \tag{4.8}$$

Equation 4.8 represents the original reinforcement nodes equilibrium. In addition to this expression, one also writes the reinforcement's formulation for the additional nodes, as follows:

$$\bar{\bar{\mathbf{K}}}_{\text{inf}}\mathbf{u_D} + \bar{\bar{\mathbf{K}}}_{\text{diag}}\bar{\mathbf{u}}_\mathbf{D} + \bar{\bar{\mathbf{G}}}_{\text{inf}}\mathbf{f_D} = \mathbf{f}_{\text{reac}} + \bar{\bar{\mathbf{K}}}_{\text{inf}}\mathbf{s} \tag{4.9}$$

where $\mathbf{f}_{\text{reac}}$ is the reaction force related to the prescribed $\bar{\mathbf{u}}_\mathbf{D}$. It is worth stressing that Eq. 4.9 and Eq. 4.8 consider null adherence force at those nodes.

Then, one rewrites the algebraic system from Eq. 4.3 as follows:

$$\begin{bmatrix} \mathbf{H_{CC}} & \mathbf{0} & -\mathbf{G_{CF}} & \mathbf{0} \\ \mathbf{H_{FC}} & \mathbf{I} & -\mathbf{G_{FF}} & \mathbf{0} \\ \mathbf{0} & \mathbf{K_E} & \mathbf{G_E} & \bar{\bar{\mathbf{K}}}_{\text{sup}} \\ \mathbf{0} & \bar{\bar{\mathbf{K}}}_{\text{inf}} & \bar{\bar{\mathbf{G}}}_{\text{inf}} & \bar{\bar{\mathbf{K}}}_{\text{diag}} \end{bmatrix} \begin{Bmatrix} \hat{\mathbf{u}}_\mathbf{C} \\ \mathbf{u_D} \\ \mathbf{f_D} \\ \bar{\mathbf{u}}_\mathbf{D} \end{Bmatrix} = \begin{bmatrix} \mathbf{G_{CC}} \\ \mathbf{G_{FC}} \\ \mathbf{0} \\ \mathbf{0} \end{bmatrix} \left\{\hat{\mathbf{t}}_\mathbf{C}\right\} + \begin{bmatrix} \mathbf{0} \\ \mathbf{0} \\ \mathbf{0} \\ \mathbf{I} \end{bmatrix} \{\mathbf{f}_{\text{reac}}\} + \begin{bmatrix} \mathbf{0} \\ \mathbf{0} \\ \mathbf{K_E} \\ \bar{\bar{\mathbf{K}}}_{\text{inf}} \end{bmatrix} \{\mathbf{s}\} \tag{4.10}$$

One must considered the prescribed $\bar{\mathbf{u}}_\mathbf{D}$ when applying the boundary conditions, which results in the following:

$$\begin{bmatrix} \mathbf{A_{CC}} & \mathbf{0} & -\mathbf{G_{CF}} & \mathbf{0} \\ \mathbf{B_{FC}} & \mathbf{I} & -\mathbf{G_{FF}} & \mathbf{0} \\ \mathbf{0} & \mathbf{K_E} & \mathbf{G_E} & \mathbf{0} \\ \mathbf{0} & \bar{\bar{\mathbf{K}}}_{\text{inf}} & \bar{\bar{\mathbf{G}}}_{\text{inf}} & -\mathbf{I} \end{bmatrix} \begin{Bmatrix} \hat{\mathbf{x}}_\mathbf{C} \\ \mathbf{u_D} \\ \mathbf{f_D} \\ \mathbf{f}_{\text{reac}} \end{Bmatrix} = \begin{bmatrix} \bar{\mathbf{A}}_{\mathbf{CC}} \\ \bar{\mathbf{B}}_{\mathbf{FC}} \\ \mathbf{0} \\ \mathbf{0} \end{bmatrix} \{\hat{\mathbf{p}}_\mathbf{C}\} + \begin{bmatrix} \mathbf{0} \\ \mathbf{0} \\ -\bar{\bar{\mathbf{K}}}_{\text{sup}} \\ -\bar{\bar{\mathbf{K}}}_{\text{diag}} \end{bmatrix} \{\bar{\mathbf{u}}_\mathbf{D}\} + \begin{bmatrix} \mathbf{0} \\ \mathbf{0} \\ \mathbf{K_E} \\ \bar{\bar{\mathbf{K}}}_{\text{inf}} \end{bmatrix} \{\mathbf{s}\} \tag{4.11}$$

4.2.2 The nonlinear coupling formulation considering bond-slip effects

The numerical solution of the bond-slip nonlinear problem is also performed by a Newton-Raphson solution technique, which enforces trial and correction phases. The prescribed boundary conditions are sub-divided into load steps: $\mathbf{\Delta\tilde{p}_C}$ and $\mathbf{\Delta\tilde{u}_D}$. In the trial phase, the slip variation $\mathbf{\Delta s}$ is assumed as nill and the loads are applied into Eq. 4.10 as follows:

$$\begin{bmatrix} \mathbf{A_{CC}} & \mathbf{0} & -\mathbf{G_{CF}} & \mathbf{0} \\ \mathbf{B_{FC}} & \mathbf{I} & -\mathbf{G_{FF}} & \mathbf{0} \\ \mathbf{0} & \mathbf{K_E} & \mathbf{G_E} & \mathbf{0} \\ \mathbf{0} & \bar{\bar{\mathbf{K}}}_{\text{inf}} & \bar{\bar{\mathbf{G}}}_{\text{inf}} & -\mathbf{I} \end{bmatrix} \begin{Bmatrix} \mathbf{\Delta}\hat{\mathbf{x}}_\mathbf{C} \\ \mathbf{\Delta u_D} \\ \mathbf{\Delta f_D} \\ \mathbf{\Delta f}_{\text{reac}} \end{Bmatrix} = \begin{bmatrix} \bar{\mathbf{A}}_{\mathbf{CC}} \\ \bar{\mathbf{B}}_{\mathbf{FC}} \\ \mathbf{0} \\ \mathbf{0} \end{bmatrix} \{\mathbf{\Delta}\hat{\mathbf{p}}_\mathbf{C}\} + \begin{bmatrix} \mathbf{0} \\ \mathbf{0} \\ -\bar{\bar{\mathbf{K}}}_{\text{sup}} \\ -\bar{\bar{\mathbf{K}}}_{\text{diag}} \end{bmatrix} \{\mathbf{\Delta}\bar{\mathbf{u}}_\mathbf{D}\} \tag{4.12}$$

The adherence force variations at the reinforcement nodes are given by:

$$\mathbf{\Delta f_E} = -\mathbf{\Delta f_D} \tag{4.13}$$

Then, the unbalanced adherence force $\mathbf{\Delta f_{des}}$ appears from the adherence law threshold values $\mathbf{f_{adm}}$, which are given by Eq. 4.4, 4.5 or 4.6 and the accumulated slip responses $\mathbf{s}$. Thus:

$$\mathbf{\Delta f_{des}} = -\mathbf{f_D} + \mathbf{\Delta f_E} - \mathbf{f_{ADM}} \tag{4.14}$$

The k nodes in which $||\mathbf{\Delta f_{des}}^k|| \neq 0$ are identified for running the correction phase. The current iteration reapplies these unbalanced values into the structure, by considering these nodes unbound from the domain. Then, the increment on the slip values $\delta\mathbf{s}^k$ is determined at the k nodes. On the other hand, the j nodes in which $\mathbf{\Delta f_{des}}^j = 0$ are assumed as perfectly bonded and the increment on the adherence force $\delta\mathbf{f_{des}}^j$ is determined during the iterations. This process results in an algebraic system of equations as follows:

$$\begin{bmatrix} \mathbf{A_{CC}} & \mathbf{0} & \mathbf{0}^k & -\mathbf{G}^j_{\mathbf{CF}} & \mathbf{0} \\ \mathbf{B_{FC}} & \mathbf{I} & \mathbf{0}^k & -\mathbf{G}^j_{\mathbf{FF}} & \mathbf{0} \\ \mathbf{0} & \mathbf{K_E} & -\mathbf{K}^k_{\mathbf{E}} & \mathbf{G}^j_{\mathbf{E}} & \mathbf{0} \\ \mathbf{0} & \bar{\bar{\mathbf{K}}}_{\text{inf}} & -\bar{\bar{\mathbf{K}}}^k_{\text{inf}} & \bar{\bar{\mathbf{G}}}^j_{\text{inf}} & -\mathbf{I} \end{bmatrix} \begin{Bmatrix} \delta\hat{\mathbf{x}}_{\mathbf{C}} \\ \delta\mathbf{u_D} \\ \delta\mathbf{s}^k \\ \delta\mathbf{f}^j_{\mathbf{D}} \\ \delta\mathbf{f}_{\text{reac}} \end{Bmatrix} = \begin{bmatrix} \mathbf{G}^k_{\mathbf{CF}} \\ \mathbf{G}^k_{\mathbf{FF}} \\ -\mathbf{G}^k_{\mathbf{E}} \\ -\bar{\bar{\mathbf{G}}}^k_{\text{inf}} \end{bmatrix} \left\{\mathbf{\Delta f}^k_{\mathbf{des}}\right\} \tag{4.15}$$

As a consequence of the analysis evolution, particularly near the collapse, all reinforcements nodes become k nodes in Eq. 4.15. Then, the algebraic system is written as Eq. 4.16. At this point, rigid body movement may occurs, which may lead to the instabilities during the numerical procedure. The prescribed displacement applied directly at the reinforcements allows the solution of the algebraic system in all situations. Otherwise, the responses could be undetermined due to the possible rigid body movement.

$$\begin{bmatrix} \mathbf{A_{CC}} & \mathbf{0} & \mathbf{0} & \mathbf{0} \\ \mathbf{B_{FC}} & \mathbf{I} & \mathbf{0} & \mathbf{0} \\ \mathbf{0} & \mathbf{K_E} & -\mathbf{K_E} & \mathbf{0} \\ \mathbf{0} & \bar{\bar{\mathbf{K}}}_{\text{inf}} & -\bar{\bar{\mathbf{K}}}_{\text{inf}} & -\mathbf{I} \end{bmatrix} \begin{Bmatrix} \delta\hat{\mathbf{x}}_{\mathbf{C}} \\ \delta\mathbf{u_D} \\ \delta\mathbf{s} \\ \delta\mathbf{f}_{\text{reac}} \end{Bmatrix} = \begin{bmatrix} \mathbf{G_{CF}} \\ \mathbf{G_{FF}} \\ -\mathbf{G_E} \\ -\bar{\bar{\mathbf{G}}}_{\text{inf}} \end{bmatrix} \{\mathbf{\Delta f_{des}}\} \tag{4.16}$$

After solving the algebraic system, all variables are accumulated as follows:

$$\begin{aligned} \mathbf{\Delta}\hat{\mathbf{x}}_{\mathbf{C}} &= \mathbf{\Delta}\hat{\mathbf{x}}_{\mathbf{C}} + \delta\hat{\mathbf{x}}_{\mathbf{C}} \\ \mathbf{\Delta u_D} &= \mathbf{\Delta u_D} + \delta\mathbf{u_D} \\ \mathbf{\Delta s}^k &= \mathbf{\Delta s}^k + \delta\mathbf{s}^k \\ \mathbf{\Delta f}^k_{\mathbf{D}} &= \mathbf{\Delta f}^k_{\mathbf{D}} + \mathbf{\Delta f}^k_{\mathbf{des}} \\ \mathbf{\Delta f}^j_{\mathbf{D}} &= \mathbf{\Delta f}^j_{\mathbf{D}} + \delta\mathbf{f}^j_{\mathbf{D}} \end{aligned} \tag{4.17}$$

The adherence law is once again verified considering the accumulated values. If any unbalanced adherence forces $\mathbf{\Delta f_{des}}^{k} \neq 0$ are found, the process advances to the next iteration. The convergence is verified accounting for the modulus of $\mathbf{\Delta f_{des}}$ normalised by the accumulated values $\mathbf{f_D}$, as follows:

$$\varepsilon_s = \frac{||\mathbf{\Delta f_{des}}||}{||\mathbf{f_D}||} \tag{4.18}$$

which defined the convergence of a given load step by the point in which ε_s becomes smaller than the prescribed tolerance. It is worth mentioning that the vector $\mathbf{f_D}$ may achieve a nill value, when the multi-linear law is considered. At this point, ε_s is simply given by the norm of $\mathbf{\Delta f}_{\text{des}}$.

At the end of the load step, all variables obtained by Eq. 4.17 can be accumulated into their total values.

4.3 Elastoplasticity: Literature Review

The plasticity theory is applied in this work to the fibre elements and it is based on a well-consolidated classical approach. The beginnings of this theory date back to the XIX$^{\text{th}}$ and XX$^{\text{th}}$ centuries (121, 122). Initially, the theories were based on the perfect plastic behaviour, in which the stress is limited by a horizontal plateau at the yielding stress. Then, the elastoplasticity with positive hardening behaviour was presented (123, 124), which allows for increments of stress above the yielding point. From these works, the following could be defined: the concept of constitutive relations of elastoplasticity, load and unload conditions, consistency relation of elastoplasticity and permanent (Plastic) strains. These concepts establish the elastoplasticity theory as known nowadays. Further details about it can be found in the literature (125) and in disciplines material (126).

The treatment of elastoplastic problems via the BEM initiated in the 70's (127, 128). Domain discretization is necessary to represent it at least in the regions in which plastic strains occur, which is usually called internal cells in the context of the BEM. However, as pointed by Telles and Brebbia (129), there is still advantage of using the BEM for these problems, such as a reduced amount of information and degrees of freedom to obtain the solution. Researches of the Department of Structural Engineering (SET-EESC-USP) have worked with elastoplastic BEM formulations (130), in which the visco-elastic-plastic behaviour for anisotropic media was properly represented with the use of internal cells. Besides, Leonel (64) worked with reinforced 2D domains by the FEM/BEM, in which plastification could occur at the fibres represented by FEM trusses. In this last work, the elastoplastic behaviour was able to represent positive hardening only by the FEM and such formulation was also applied to fracture analyses of reinforced domains.

Using the FEM/BEM coupling to represent the plastic region by the FEM is a well-known and successful approach available in the literature (78, 40). Whereas the representation of plasticity by the BEM itself is yet not further developed, as well as the application of the 1DBEM/BEM coupling. A elastoplastic 1DBEM/BEM formulation to represent the fibre's plastification was already presented by these authors for 2D analyses (13). Thus, this work presents the extension of that formulation for 3D problems and for Isogeometric formulations. With that, the final formulation will be much more representative and effective.

4.4 Elastoplasticity modelling at the reinforcements

The classical elastoplasticity theory is applied herein. It is based on the principle of additive decomposition of strains, in which a permanent deformation portion exists and is called plastic strain. This strain occur when the applied loads exceed the elastic limit, also called yielding point. There is a change in the material's stiffness when the plastic region is achieved, as illustrated in Figs. 38(a) and 38(b). The solution of the mechanical response of a elastoplastic material then becomes nonlinear, since the stiffness depend on the stress current level and its evolution. Deeper details about the elastoplasticity theory applied herein are found in (131) and (126).

The strains additive decomposition into the elastic and (ε_e) and plastic (ε_{pl}) portions can be stated as:

$$\varepsilon = \varepsilon_e + \varepsilon_{pl} \tag{4.19}$$

Thus, the Hooke's law application leads to:

$$\sigma = E\varepsilon_e = E\left(\varepsilon - \varepsilon_{pl}\right) \tag{4.20}$$

It is worth stressing that the elastoplasticity formulated herein is a one-dimensional approach, since it is applied to the reinforcement elements.

The definition of the elastoplastic model is the next step. The simplest option would be the perfect plasticity, illustrated in Fig. 38(a). In this model, the yield stress is the maximum value of stress and the plastic strains can grow indefinitely after the yielding point. Hence, a nill stiffness is observed in the plastic region of the constitutive law. More representative models consider the hardening behaviour in the plastic region. In that case, there may be stress increasing above the yield stress, as illustrated in Fig. 38(b). Thus, there is a non-null stiffness in the plastic region, called tangent stiffness, which is usually smaller than the initial elastic stiffness. Besides, the evolution of plastic strains causes an increase of the elastic limit in the case of an unload and reload situation. This specific

Figure 38 – Constitutive elastoplastic: perfect yielding (a) and hardening (b).

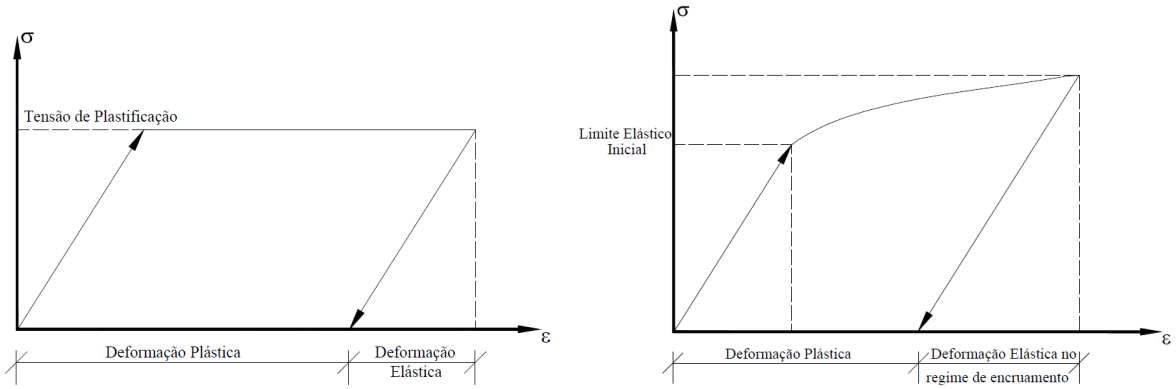

(a) (b)

Source: The author.

behaviour can follow two different models: isotropic or kinematic hardening. Figure 39 illustrates both this models.

Figure 39 – Bi-linear hardening models: isotropic (a) and kinematic (b).

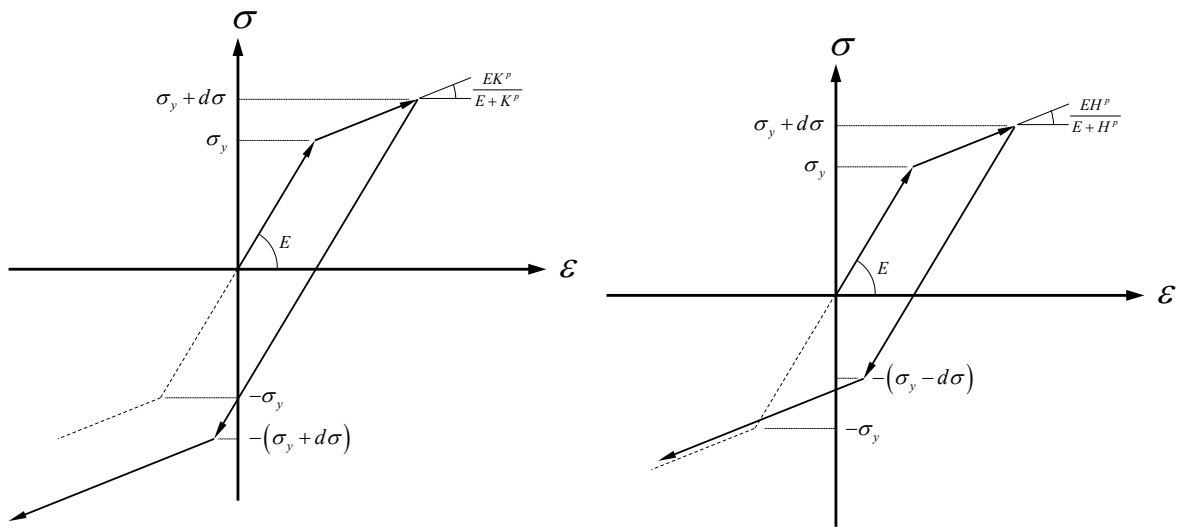

(a) (b)

Source: The author.

This study adopts a bi-linear isotropic hardening model, illustrated by Fig. 39(a). The bi-linear term refers to the piecewise linear behaviour of the model. The isotropic hardening considers a symmetric expansion of the elastic limit in relation to the reload interval centre. In bi-linear models, the hardening is directly proportional to the accumulated plastic strain in modulus, which is defined as the parameter α. Thus:

$$\alpha = \int_t |d\varepsilon^p| dt \tag{4.21}$$

The constant of proportionality between α and the hardening is the plastic modulus K^p. Therefore, one writes the yield function $f(\sigma,\alpha)$ as follows:

$$f\left(\sigma,\alpha\right) = |\sigma| - \left(\sigma_y + K^p\alpha\right) \quad \leq \quad 0 \tag{4.22}$$

in which σ_y is the yield stress. This function defines the threshold stress values by $f\left(\sigma,\alpha\right) < 0$. In the case of $f\left(\sigma,\alpha\right) > 0$, the stress state is not valid and there must be plastic strains evolution in order to find a valid point.

The nonlinear elastoplastic problem is solved by a Newton-Raphson scheme. Thus, The prescribed boundary conditions are sub-divided into load steps $\mathbf{\Delta\tilde{p}_C}$. The incremental unknown variables are found by applying $\mathbf{\Delta\tilde{p}_C}$ into Eq. 3.9. Then, one calculates the incremental predicted elastic strains $d\varepsilon$ by applying Eq. 3.62, Eq. 3.64 and the 1D Hooke's law. The yield function (Eq. 4.22) is verified considering the obtained responses and predicted strains. Then, the plastic strains evolution is governed by the consistency and complementary conditions, which are as follows:

$$\begin{aligned} d\lambda f\left(\sigma,\alpha\right) &= 0 \\ d\lambda df\left(\sigma,\alpha\right) &= 0 \end{aligned} \tag{4.23}$$

in which $df\left(\sigma,\alpha\right)$ is the yield function increment and $d\lambda$ is equal the increment of α, i.e., $d\lambda = d\alpha$.

From Eq. 4.23 and Eq. 4.22, one writes the following expression for $d\lambda$:

$$d\lambda = \frac{\text{sign}\left(\sigma\right)}{E + K^p} d\varepsilon \tag{4.24}$$

which relates to the plastic strain increment as follows:

$$d\varepsilon_{pl} = d\lambda\,\text{sign}\left(\sigma\right) \tag{4.25}$$

The real stress increment $d\sigma$ can then be calculated through Eq. 4.20 in its incremental form and Eq. 4.25, which results in:

$$d\sigma = E\left(d\varepsilon - d\varepsilon^p\right) \tag{4.26}$$

The stress and plastic strain increments calculated in Eq. 4.25 and Eq. 4.26 represent the correction phase of the Newton-Raphson scheme.

Besides, Eq. 4.26, 4.24 and 4.25 allow finding the material's stiffness at the plastic region of the constitutive law, which is called elastoplastic modulus (E^{EP}). This stiffness is constant in the plastic region due to the bi-linear characteristic of the model (Fig. 39(a)). Thus, the constitutive law's inclinations can be stated as:

$$E^{EP} = \begin{array}{lll} E & , & \text{se} \quad |\sigma| \leq \sigma_y \\ \dfrac{EK^p}{E + K^p} & , & \text{se} \quad |\sigma| > \sigma_y \end{array} \tag{4.27}$$

In order to numerically apply the Newton-Raphson scheme, the incremental variables are treated as finite increments. Therefore, the above-presented expressions are evaluated for all integration points of the reinforcement elements mesh, considering the finite increments $\Delta\varepsilon$, $\Delta\varepsilon_{pl}$ and $\Delta\sigma$. The mechanical fields at the integration points can be determined through the Lagrangian polynomials interpolation, as follows:

$$\Delta\varepsilon = \phi_j\left(\xi_i\right)\Delta\varepsilon_j \tag{4.28}$$

where ξ_i is the dimensionless coordinate of the integration point. $\Delta\varepsilon_j$ and $\Delta\varepsilon$ are the nodal strain values and the strain at the integration point, respectively. This expression is valid for each one of the reinforcement elements and can be similarly applied for stresses and plastic strains.

From the predicted elastic strain $\Delta\varepsilon$, the objective of a given iteration is to determine the final finite increments of plastic strains, hardening parameter, plastic and elastic stresses. The obtained values must satisfy the elastoplastic model relations, which allows accumulating them as follows:

$$\begin{aligned}\varepsilon^{n+1} &= \varepsilon^n + \Delta\varepsilon^n \\ \varepsilon_{pl}^{n+1} &= \varepsilon_{pl}^n + \Delta\varepsilon_{pl}^n \\ \alpha^{n+1} &= \alpha^n + \Delta\alpha^n\end{aligned} \tag{4.29}$$

The finite increment of the elastically predicted stress σ_t^{n+1} is calculated from Eq. 4.28 as follows:

$$\sigma_t^{n+1} = E\left(\varepsilon^n + \Delta\varepsilon^n - \varepsilon_{pl}^n\right) \tag{4.30}$$

which represents the trial phase. Then, the finite yield function is as follows:

$$f_t^{n+1} = \left|\sigma_t^{n+1}\right| - \left(\sigma_y + K^p\alpha^n\right) \tag{4.31}$$

Equation 4.31 verifies if the trial phase is valid, as above-described for Eq. 4.22. If the trial is confirmed, there is no correction phase and Eq. 4.29 is applied to accumulate all mechanical fields, considering $\Delta\varepsilon_{pl}^n = \Delta\alpha^n = 0$.

Otherwise, the plastic strain finite increment is determined by imposing $f_{n+1} = 0$, which results in:

$$\begin{aligned}\Delta\varepsilon_{pl}^n &= \Delta\lambda^n \text{sign}\left(\sigma_t^{n+1}\right) \\ \Delta\alpha^n &= \Delta\lambda^n\end{aligned} \tag{4.32}$$

in which the parameter $\Delta\lambda^n$ is as follows:

$$\Delta\lambda_n = \frac{f_t^{n+1}}{E + K^P} \tag{4.33}$$

Thus, Eq. 4.29 accumulates all mechanical fields. Nevertheless, the stress value is corrected and accumulated as follows:

$$\begin{aligned} \Delta\sigma^n &= E\Delta\varepsilon^n - E\Delta\varepsilon_{pl}^n \\ \sigma^{n+1} &= \sigma^n + \Delta\sigma^n \end{aligned} \tag{4.34}$$

which represents the correction phase.

The trial and correction phases above-presented must be applied for all integration points of the reinforcements elements mesh. Thus, one determines all the mechanical fields values at the step $n+1$. These values must be interpolated back to the reinforcements nodes. For this, new Lagrangian functions ϕ_j are defined based on the integration points and then evaluated at the nodal dimensionless coordinates ξ_i. With that, Eq. 4.28 provides the inverse interpolation, which allows determining the nodal mechanical fields values from the known integration points values.

The corrected adherence forces $\mathbf{\Delta f_E}$ can be obtained considering the nodal updated mechanical fields. Equation 3.64 provides this result, by considering f_i as unknown values and all of the N_j as known ones. Equation 3.2 transforms the obtained results into the updated adherence forces, which are given by $\mathbf{\Delta f_D} + \mathbf{\Delta f_D}^{corr}$. The final expression for the correction portion $\mathbf{\Delta f_D}^{corr}$ is as follows:

$$\{\mathbf{\Delta f_D}^{corr}\} = \left[\int_0^{\bar{X}_j} \phi_i(\xi(\bar{x}))d\bar{x}\right]^{-1} \left\{E\Delta\varepsilon_{pl}^j - E\Delta\varepsilon_{pl}^1\right\} \tag{4.35}$$

in which i is in the range of nodes and j is in the range of integration points, both within a given reinforcement element. This expression results in a linear system of equations, which can be determined if the number of nodes and integration points are equal. Otherwise, the least squares method is applied herein to obtain an approximate solution.

The updated and the initially predicted adherence force vectors might differ from each other. This indicates the existence of unbalanced forces, which is also known as residual. The nonlinear iterative process consist of reapplying the residuals into the structure in the next iteration step. In theory, the actual level of external loads in the current load step is only achieved when the residuals become nill.

The residual consists of a balance between the structure's internal response and the external loads. In the reinforced BEM formulations, this balance considers the whole reinforced system (Eq. 3.9), as follows:

$$\mathbf{f_{des}} = \begin{bmatrix} \bar{\mathbf{A}}_{\mathbf{CC}} \\ \bar{\mathbf{B}}_{\mathbf{FC}} \\ \mathbf{0} \end{bmatrix} \{\mathbf{\Delta\hat{p}_C}\} - \begin{bmatrix} \mathbf{A_{CC}} & \mathbf{0} & -\mathbf{G_{CF}} \\ \mathbf{B_{FC}} & \mathbf{I} & -\mathbf{G_{FF}} \\ \mathbf{0} & \mathbf{K_E} & \mathbf{G_E} \end{bmatrix} \begin{Bmatrix} \mathbf{\Delta\hat{x}_C} \\ \mathbf{\Delta u_D} \\ \mathbf{\Delta f_D} + \mathbf{\Delta f_D}^{corr} \end{Bmatrix} \tag{4.36}$$

in which $\mathbf{f_{des}}$ is the unbalanced force vector that represents the residual. The matrices $\bar{\mathbf{A}}_{\mathbf{CC}}$, $\bar{\mathbf{B}}_{\mathbf{FC}}$, $\mathbf{A_{CC}}$ and $\mathbf{B_{FC}}$ have been previously presented for Eq. 3.9. $\mathbf{\Delta x_C}$, $\mathbf{\Delta u_D}$ and $\mathbf{\Delta f_D}$ are the elastically predicted values in the trial phase. $\mathbf{\Delta f_D}^{corr}$ are the correction values of adherence force from Eq. 4.35.

Thus, the reapplication of $\mathbf{f_{des}}$ in the next iteration proceeds as follows:

$$\begin{bmatrix} \mathbf{A_{CC}} & \mathbf{0} & -\mathbf{G_{CF}} \\ \mathbf{B_{FC}} & \mathbf{I} & -\mathbf{G_{FF}} \\ \mathbf{0} & \mathbf{K_E} & \mathbf{G_E} \end{bmatrix} \begin{Bmatrix} \delta\mathbf{\Delta \hat{x}_c} \\ \delta\mathbf{\Delta u_D} \\ \delta\mathbf{\Delta f_D} \end{Bmatrix} = \{\mathbf{f_{des}}\} \tag{4.37}$$

where the values $\delta\mathbf{\Delta x_C}$, $\delta\mathbf{\Delta u_D}$ and $\delta\mathbf{\Delta f_D}$ are unknown variables of the next iteration. Hence, the elastoplastic equations above-presented are once again verified. One repeats this process until the stipulated convergence is achieved. The convergence criteria is based on the normalised norm of $\mathbf{f_{des}}$, as follows:

$$\|\mathbf{f_{des}}\| = \frac{\sqrt{\left(\sum_i^n \{\mathbf{f_{des}}\}_i\right)^2}}{\sqrt{\left(\sum_i^n \{\mathbf{f_D}\}_i\right)^2}} \tag{4.38}$$

in which n is the total number of nodes of the reinforcements mesh.

It is worth mentioning that there are at least two different approaches for the unbalanced forces reapplication in the Newton-Raphson technique. The stiffness of the reinforcement elements can be updated in $\mathbf{K_E}$ considering the current constitutive region (plastic or elastic) of each element. For this, the elastoplastic modulus E^{EP} from Eq. 4.27 is applied at the elements in the plastic regions. This procedure is usually known as Tangent Operator of Tangent Stiffness method and it is applied in classical approaches of the Newton-Raphson method.

Alternatively, the initial elastic stiffness can be considered in all reinforcement elements, regardless of their current constitutive region. In this case, all matrices of the algebraic system from Eq. 3.9 and 4.37 remain unmodified throughout the iterative process. This approach is known as Constant Operator or Modified Newton-Raphson method. Despite it takes a larger number of iterations to achieve convergence, every iteration herein is faster than in the Tangent Operator.

This study applies the Constant Operator. In the context of BEM formulations, re-evaluating the matrices and changing the system of equations at all iterations has significantly bigger computational costs. This is mainly due to the fully-populated and non-symmetric matrices found in BEM formulations. Therefore, it is highly efficient to reduce the number of different algebraic systems to be solved throughout the iterative procedure, which is elegantly accomplished in the adopted Constant Operator.

4.5 Bond-slip modelling and elastoplasticity reinforcements formulation

The previously presented nonlinear formulations can be coupled into an unified nonlinear process. With that, the proposed formulation is able represent the mechanical degradation of both the reinforcements material and the interface reinforcement/domain, which is The superposition principle can be considered in each of trial and correction phases because the Newton-Raphson technique handles the nonlinear solution problem.

Equation 4.3 represents the trail phase considering $\mathbf{\Delta \hat{p}_C}$ and $\mathbf{s} = \mathbf{0}$ in the right hand-side of the expression. Then, the unbalanced forces of bond-slip $\mathbf{\Delta p^{bs}_{des}}$ can be obtained by Eq. 4.14. The unbalanced force of elastoplasticity $\mathbf{f^{pl}_{des}}$ is defined by Eq. 4.36, which can be rearranged as follows:

$$\mathbf{f^{pl}_{des}} = - \begin{bmatrix} -\mathbf{G_{CF}} \\ -\mathbf{G_{FF}} \\ \mathbf{G_F} \end{bmatrix} \{ \mathbf{\Delta f_D}^{corr} \} \tag{4.39}$$

which defines the unbalanced force of elastoplasticity modelling.

Therefore, $\mathbf{\Delta p^{bs}_{des}}$ is reapplied by Eq. 4.15 and $\mathbf{f^{pl}_{des}}$, by Eq. 4.37. The obtained correction values of all variables can be accumulated together. The total error norm $||\mathfrak{e}||$ is defined by:

$$||\mathfrak{e}|| = \frac{\mathbf{\Delta p^{bs}_{des}}}{\mathbf{p_D}} + \frac{\mathbf{f^{pl}_{des}}}{\mathbf{f_{ext}}} \tag{4.40}$$

The unified nonlinear process follows the Newton-Raphson technique, dividing the problem into n load steps and applying trail and correction phases, as above presented, until convergence is achieved in Eq. 4.40.

4.6 Numerical applications of the nonlinear coupled formulations

This Section presents the numerical applications executed with the proposed nonlinear reinforced formulations. The first application compares the accuracy and efficiency of the Lagrangian and the IGABEM reinforced formulations. The second application models the pull-out text with a 3D reinforced IGABEM model. The third application presents and example of the complete nonlinear formulation, in which both bond-slip and yielding are modelled.

4.6.1 Elastoplasticity modelling: Nonhomogeneous reinforced cylinder

This application handles the mechanical analysis of a nonhomogeneous structure reinforced by fibres, which follow elastoplastic behaviour as illustrated in Fig. 40. Thus, the formulation presented in Sec. 4.4 is applied herein. Figure 40(a) exhibits geometry, boundary conditions and the positioning of the 17 long fibres, which cross the sub-region interface between materials I and II. Figure 40(b) presents the fibres positioning along the cylinder cross-section. The following geometry and load parameters are considered: $D = 2$ cm, $L = 10$ cm $\phi d_1 = 0.6$ cm, $\phi d_2 = 1.4$ cm, $\mathbf{p} = 5$ kN/cm^2 and $\mathbf{q} = 0{,}5$ kN/cm^2. The material properties of the 3D domains are: Young's modulus $E_I = 1000$ kN/cm^2, $E_{II} = 500$ kN/cm^2 and Poisson ratio $\nu_I = \nu_{II} = 0.2$. The long fibres are composed by two materials, with $E_{f1} = 2500$ kN/cm^2, $E_{f2} = 1500$ kN/cm^2, Yield stresses $\sigma_Y^{f1} = 20$ kN/cm^2, $\sigma_Y^{f2} = 7.5$ kN/cm^2 and plastic modulus $K_{f1}^p = 250$ kN/cm^2 and $K_{f2}^p = 150$ kN/cm^2. Fibres positioned at $y > 0$ (illustrated in green colour in Fig. 40(b)) consider material $f2$ and the other fibres (illustrated in blue colour) consider $f1$. All fibres have circular cross-section with radius equals to 0.1 cm.

Figure 40 – Structure for the elastoplastic modelling: external dimensions (a) and fibres positioning (b).

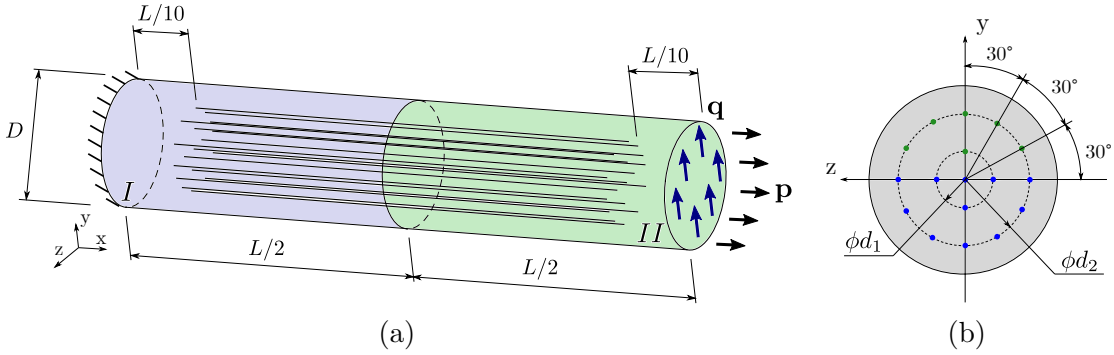

Source: The author.

The Lagrangian and the isogeometric models handle the problem modelling herein. The Lagrangian mesh is composed by 2064 quadrilateral linear elements and 2604 collocation points. The IGABEM mesh is based on an isogeometric model of 28 regular NURBS surfaces with bi-quadratic basis functions, i.e. $p = q = 2$. The IGABEM mechanical model results in 356 collocation points. Figure 41(a) and 41(b) exhibit both numerical models. Figure 41(b) illustrates only the collocation points of the isogeometric model. 28 quadratic reinforcement elements represent each long fibre in the mechanical modelling, which result in 986 nodes. These models have demonstrated mesh convergence in previous analysis, regarding displacements at the boundary and both displacements and stresses results at the fibres.

The nonlinear analysis is performed within 10 load steps and a tolerance for convergence of 10^{-6} is prescribed because fibres allow for elastoplastic behaviour. The

Figure 41 – Lagrangian model with linear quadrilateral elements (a) and collocation points of the IGABEM model (b).

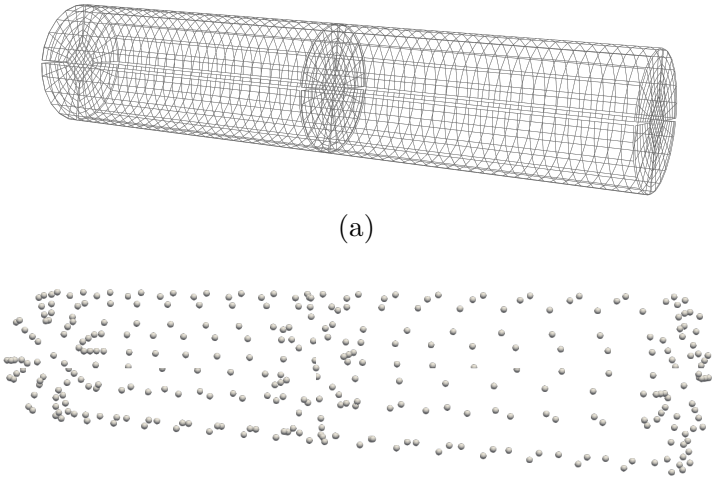

(a) (b)

Source: The author.

average number of iterations to achieve convergence at each load step is 25. The isogeometric and Lagrangian formulations do not differ considerably in this aspect.

The upper fibre (positioned at $y = 0.7$, $z = 0$ cm) and the lower fibre (positioned at $y = -0.7$, $z = 0$ cm) illustrate the mechanical results at the reinforcements. Figures 42 and 43 illustrate the normal stress and the plastic strain results as a function of each one of the above-mentioned fibres length (S_f), respectively.

Figure 42 – Normal stress (a) and plastic strain (b) along the upper fibre.

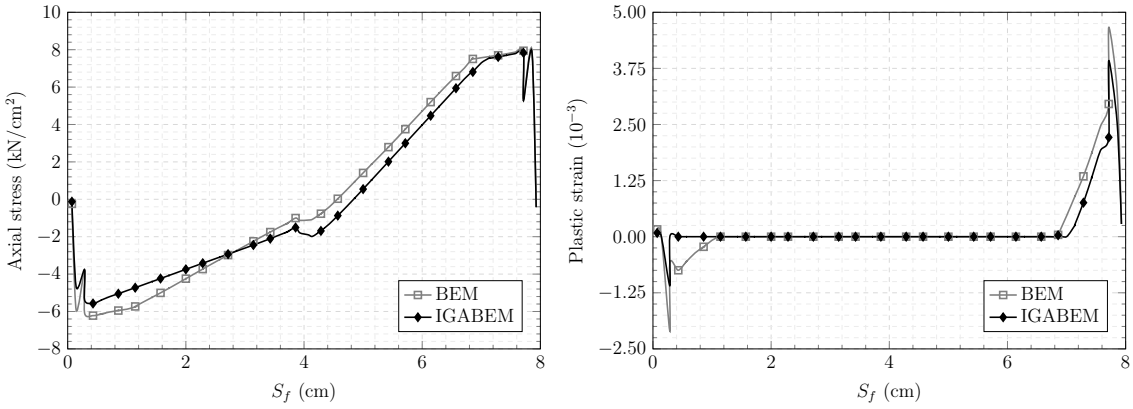

(a) (b)

Source: The author.

Figure 44(a) illustrates displacements obtained along the centre fibre (positioned at $y = 0$, $z = 0$ cm), in which x displacements are nil due to the symmetry of the problem. The right fibre (positioned at $y = 0$, $z = -0.7$ cm) illustrates the x displacements, which can be observed in Fig. 44(b).

Figure 43 – Normal stress (a) and plastic strain (b) along the lower fibre.

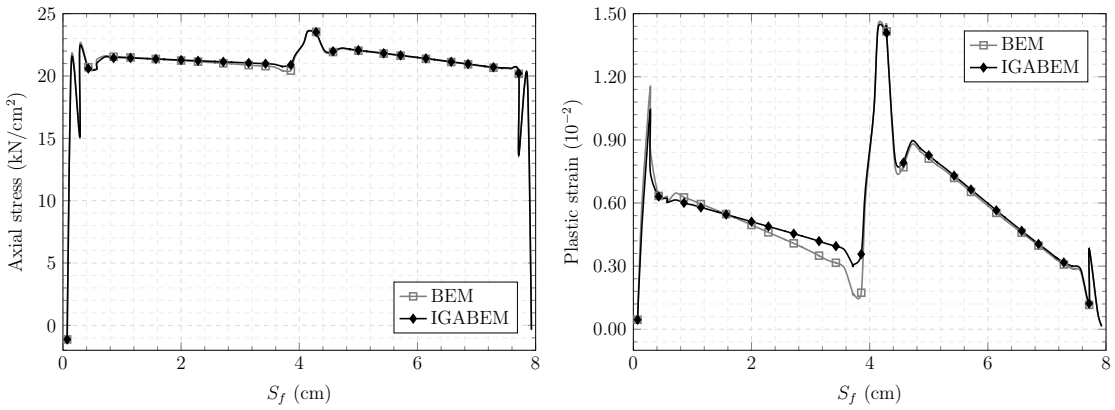

(a) (b)

Source: The author.

Figure 44 – u_y and u_z displacements along the centre-fibre (a) and u_x displacements along the right fibre (b).

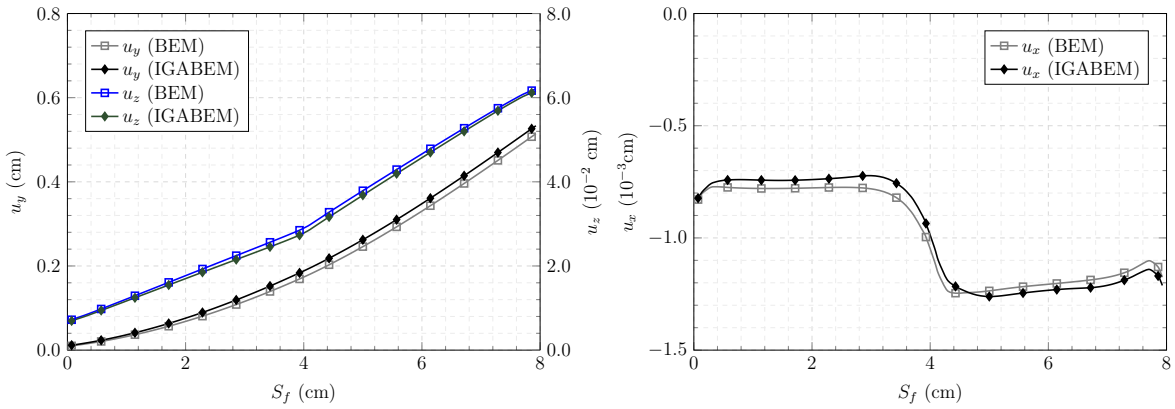

(a) (b)

Source: The author.

All results presented along fibres compare the Reinforced IGABEM formulation with the Lagrangian reference formulation (BEM) (132). One observes good agreement in all figures, regarding stresses, plastic strains and displacements. Some results exhibit a slight difference between the two models (as observed in Figura 42) because of the usual perturbations observed near fibres ends and discontinuity points. However, these perturbations have already been reported in the literature (133, 13) because of the stress/force fields discontinuity at the interface.

Figura 45 illustrates the displacements along the boundary in the form of colour maps. This figure presents the displacements magnitude ($\sqrt{u_x^2 + u_y^2 + u_z^2}$) and the deformed shape considers real scale. Besides, it compares the Lagrangian formulation (a) with the IGABEM formulation (b) results. Each direction of the NURBS surfaces was subdivided into 30 linear auxiliary cells to visualise the mechanical fields. The *Paraview*® software uses the auxiliary cells for generation the images without the support for NURBS basis

functions. One observes good agreement between the results from both Lagrangian and isogeometric formulations in Figura 45. It is worth mentioning that the u_y displacements exhibit the highest differences, which do not exceed a limit of 3%.

Figure 45 – Colour map of displacements magnitude (in cm) along the boundary obtained by the Lagrangian formulation (a) and the isogeometric formulation (b).

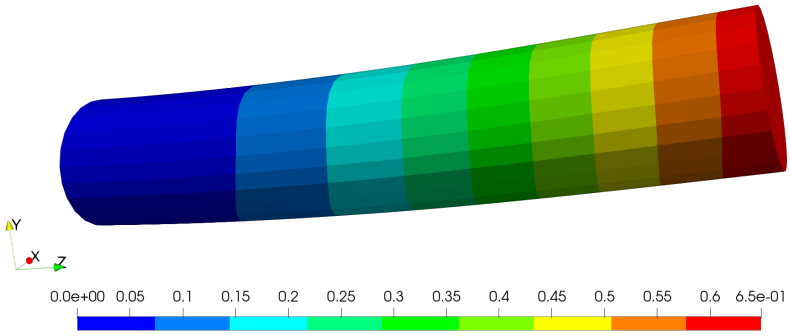

(a) Lagrangian results

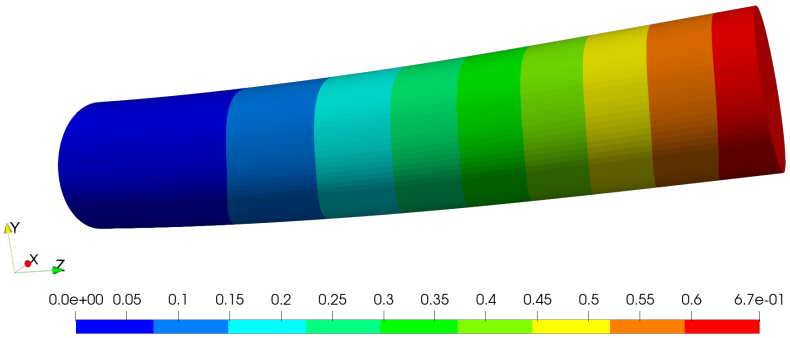

(b) IGABEM results

Source: The author.

Figure 46 illustrates the colour map of plastic strains distribution along the fibres. The results obtained by the Lagrangian formulation (a) and isogeometric formulation (b) are compared in this figure. One observes excellent agreement between them, with maximum difference below than 1%. Besides, one notices that a considerable part of the reinforcements exhibit yielding behaviour, which has been obtained due to the use of $f1$ and $f2$ materials, with different Yield stresses.

Figure 46 – Colour map of plastic strains along all fibres, obtained by the Lagrangian formulation (a) and the isogeometric formulation (b).

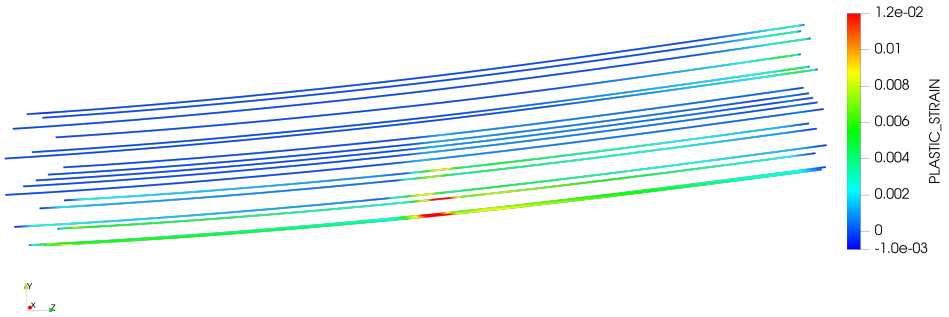

(a) Lagrangian results

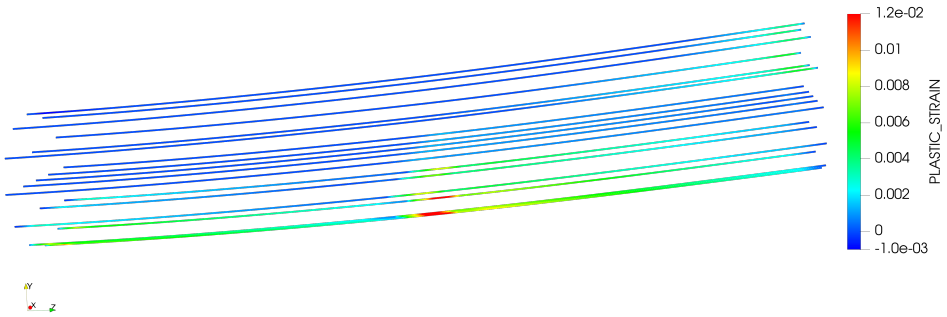

(b) IGABEM results
Source: The author.

It is worth mentioning that the Isogeometric mesh required a significant lower number of degrees of freedom to achieve the same level of accuracy of the Lagrangian mesh. Although, the computational time of both models doesn't differ by a significant amount, because the integrations on the Isogeometric model are far more computationally demanding. Yet, the fewer number of degrees of freedom is a big advantage in terms of memory consumption, since BEM formulations have non-sparse matrices.

4.6.2 Bond-slip modelling: Pull-out test

This application handles the numerical modelling of the pull-out test. Thus, this application illustrates the performance of the formulation described in Sec. 4.2. The specimen for this classical test is composed by a steel bar immersed into a concrete cylinder, as illustrated in Figura 47(a). The steel bar is pulled-out by the machine claw, which enables the adherence behaviour analysis by force versus displacement curves. Experimental results of this test have been presented by (108), which used the experimental scheme illustrated in Figura 47(b).

Figura 47(a) illustrates the specimen dimensions. Only a central zone of 48 mm length in the steel bar has contact with the concrete. The specimen's extremities regions of

80 mm length each (called upper and bottom regions) are contactless zones. The bottom concrete region performs the mechanical stresses transmission between the steel bar and the support plate. The upper concrete region is free of mechanical loading. Therefore, the displacements assessed by the transducer can be numerically represented by the displacements at the last contact point of steel bar and concrete (p_1 in Figura 48). Hence, the numerical model does not require the representation of the 80-mm concrete upper region.

Figure 47 – Pull-out test in reinforced concrete: specimen's dimensions, in mm, (a) and experimental scheme (b).

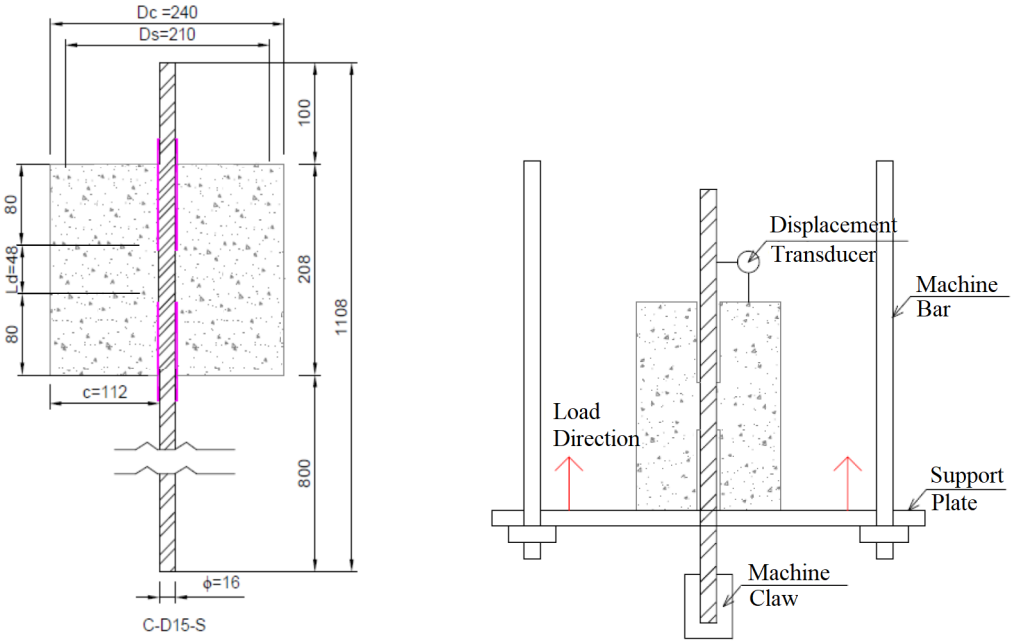

(a) (b)

Source: (108),adapted.

Figure 48(a) illustrates the collocation points for the IGABEM model. The isogeometric model is composed by 26 regular NURBS surfaces with $p = q = 2$ and a total of 762 collocation points. A Lagrangian mesh is also constructed for the mechanical analysis of this application, which is illustrated in Fig. 48(b). This mesh is composed by 3861 linear quadrilateral Lagrangian elements and 4271 collocation points. For both models, 100 quadratic Lagrangian reinforcement elements (202 nodes) discretise the steel bar. Previous analyses have shown mesh convergence for these models, regarding displacements at the boundary and all mechanical fields along the reinforcements.

The experimental results provide the relative displacement between the upper concrete end and the steel bar as normalised adherence stress (τ_{ad}). This relative displacement is numerically represented by the slip value at p_1 (Figura 48). τ_{ad} is evaluated from the reaction force $\mathbf{f}_{\text{reac}}$ at the opposite fibre extremity as follows:

$$\tau_{\text{ad}} = \frac{\mathbf{f}_{\text{reac}}/\pi\phi l_b}{(70/f_{cm})^{1/4}} \tag{4.41}$$

Figure 48 – BEM model collocation points meshes.

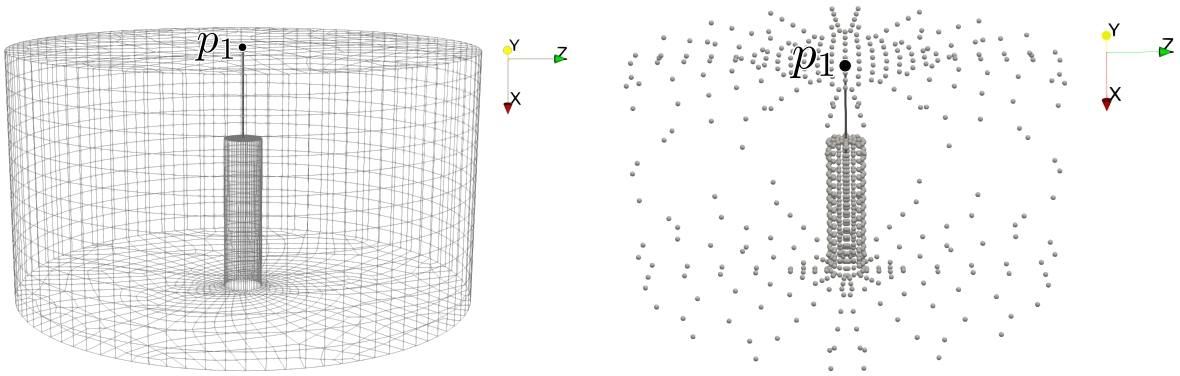

(a) IGABEM (b) Lagrangian BEM

Source: The author.

where ϕ is the steel bar diameter, l_b is the length of the adherence region and f_{cm} is the concrete compression strength.

The mechanical properties considered in this application are (108): Young modulus and Poisson ratio of concrete equal to 41.16 GPa and 0.2, respectively; $f_{cm} = 67.44$ MPa; Young modulus of the steel bar equals to 201.8 GPa and $\phi = 16$ mm. The prescribed displacement at the steel bar end ($\bar{\mathbf{u}}_\mathbf{D} = 10$ mm) represents the action of the claw machine illustrated in Fig. 47(b). The following parameters govern the adherence law, which are based on suggested values (114):

- $s_0 = 0.8$ mm;
- $s_1 = 2.0$ mm;
- $s_2 = 10.0$ mm;
- $s_3 = 3\, s_2$;
- $f_{MAX} = 0.55\,(f_{cm}\pi\phi)$;
- $f_{RES} = 0.4 f_{MAX}$.

The nonlinear process for the bond-slip analysis has been solved within 150 load steps. Besides, the tolerance for convergence is 10^{-6} in terms of the norm of unbalanced forces. The iterative process required a number of iterations in the range of 3 to 20 for convergence within each load step.

Figura 49 illustrates the results achieved by the proposed model (IGABEM), the Experimental analysis (Experimental) and the equivalent Lagrangian BEM model (BEM). This figure demonstrates excellent agreement among numerical and experimental responses for all slip values. The proposed numerical approach predicted accurately the experimental behaviour. Particularly, both the accuracy on the maximum adherence stress value and on the post-peak behaviour are excellent. Besides, the obtained IGABEM and BEM results are almost indistinguishable.

Figure 49 – Adherence stress (τ_{ad}) as function of the slip at point p_1.

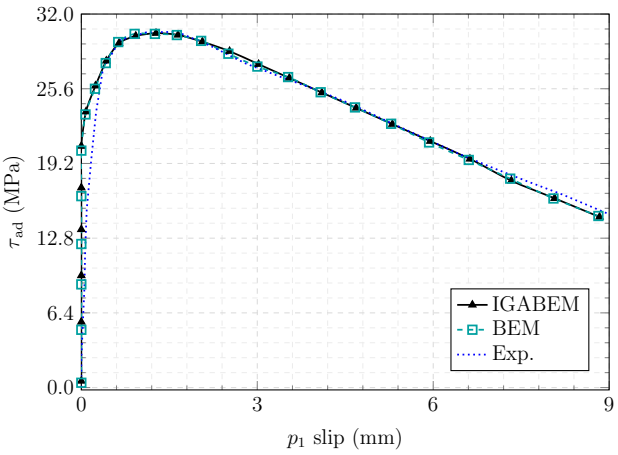

Source: The author.

Figura 50 exhibits fibre displacements (u_E) and the load line displacements (u_D), which is the group of domain internal points of coincident position with the reinforcements nodes. These results account for the bar length S_f and were obtained via the IGABEM. Four distinct steps along the analysis were assessed: at 2.5% of $\bar{u}$ applied (a), 10% (b), 40% (c) and 100% (c). These load levels have been chosen for better illustrating the slip behaviour evolution throughout the analysis.

Figure 50 – Reinforcements and domain displacements (u_E and u_D respectively) in x direction, as a function of the bar length S_f, at different load levels.

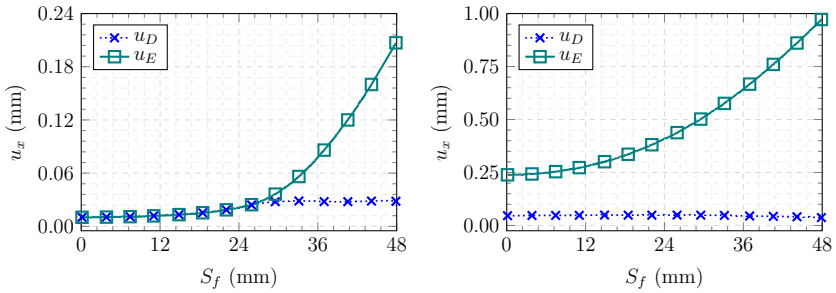

(a) 2.5%

(b) 10%

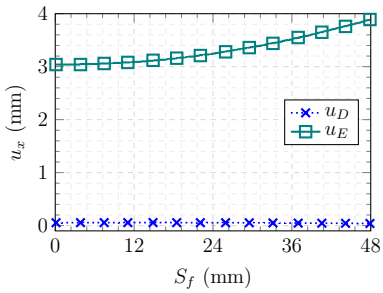

(c) 40%

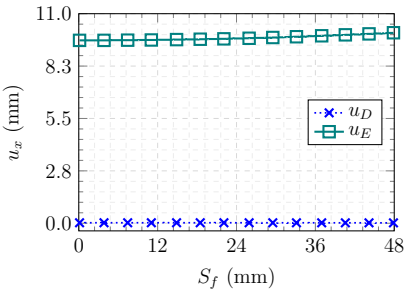

(d) 100%

Source: The author.

One clearly observes the slip evolution process along the bar length in Figura 50. As expected, the slip evolution begins at the bar right-end, which is $\bar{u}$ application point. As the analysis evolves, the slipping intensity is transferred to the other bar end, leading to an uniform slip along S_f at the analysis end. This behaviour can be explained by the slipping contribution modelling in the reinforcements equation as proportional to the stiffness (Eq. 4.2) and the adherence law, which limits the intensity of energy transmitted between domain and fibre.

Figures 51(a) and 51(b) illustrate, respectively, the displacements over the boundary in x and z directions obtained via the IGABEM. u_y are not illustrated herein because it is identical to Figura 51(b), rotated 90°. For the visualisation, each NURBS surfaces direction was subdivided into 45 auxiliary 4-node cells. Figures 52(a) and 52(b) illustrate the same results obtained via the Lagrangian BEM. Both figures illustrate reinforcements and boundary results.

Figures 51 and 52 present consistent behaviour for displacements over the concrete specimen. Besides, the proposed coupling procedure leads to the accurate stress transfer among the structural elements involved in system. Such behaviour has major importance during the nonlinear process. Moreover, Figs. 51(b) and 52(b) show clearly the symmetrical response obtained around the cylinder's central axis, which is within the expected behaviour. The results obtained via the IGABEM and the Lagrangian BEM are in excellent agreement between each-other, which is expected in this application since the fibre's behaviour is predominant for the overall results.

It is worth stressing that the Lagrangian BEM requires 4271 collocation points at the boundary, whereas the IGABEM requires only 762. Therefore, the IGABEM model proposed herein requires less collocation points than the Lagrangian model to represent the same mechanical behaviour with an equivalent accuracy. Thus, the IGABEM formulation demonstrates an excellent numerical and computational efficiency in addition to the observed precision.

Figure 51 – Colour map of displacements (in mm) over the boundary obtained via the IGABEM.

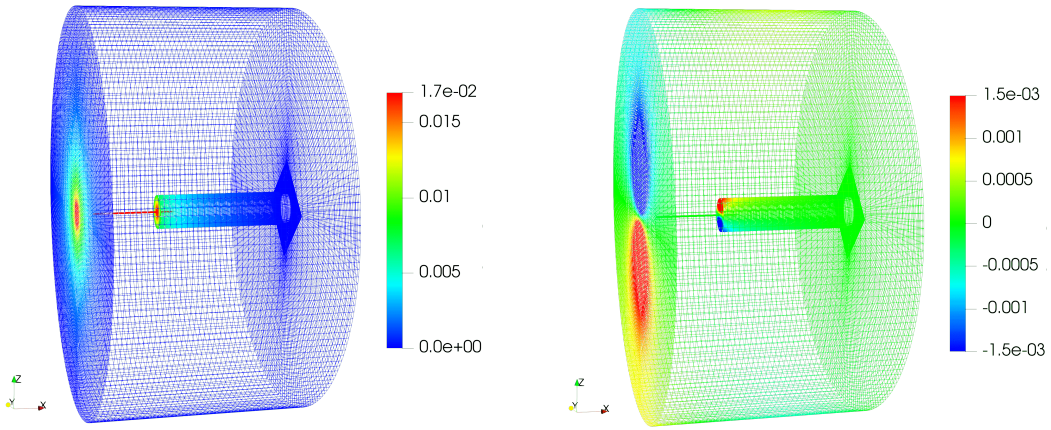

(a) Displacements x (b) Displacements z

Source: The author.

Figure 52 – Colour map of displacements (in mm) over the boundary obtained via the Lagrangian BEM.

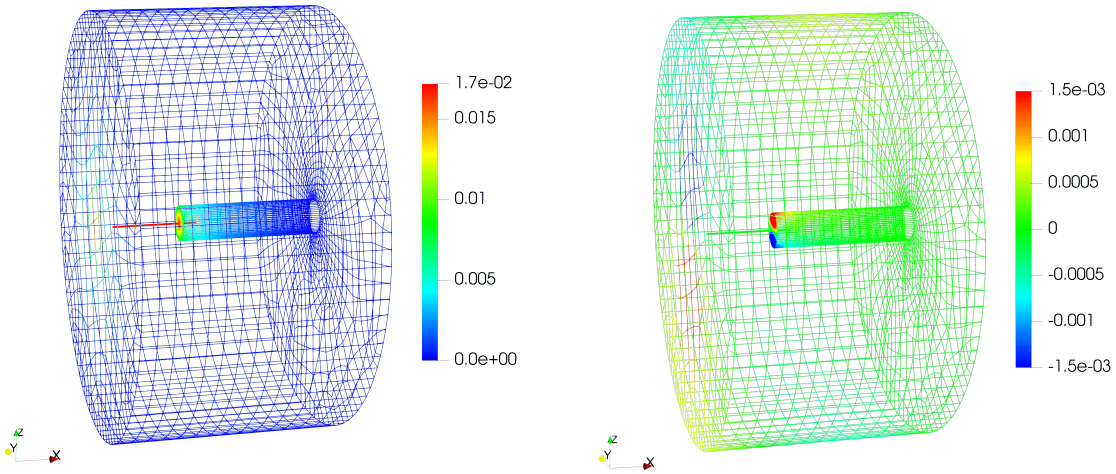

(a) Displacements x (b) Displacements z

Source: The author.

4.6.3 Bond-slip modelling in elastoplastic fibre

This application handles the bond-slip modelling of a long fibre with elastoplastic behaviour, which reinforces a prismatic solid as illustrated in Fig. 53. Thus, this application demonstrates the performance of the formulation described in Sec. 4.5. The following material properties are considered: domain Young's modulus $E = 3$ kN/cm^2, Poisson ratio $\nu = 0$, fibre Young's modulus $E_f = 10$ kN/cm^2 and fibre cross-section area $A_f = 0.1$ cm^2. The applied load is $\mathbf{p} = 0.01$ kN/cm^2. The long fibre has yield stress and plastic modulus, respectively, equal to $\sigma_y = 0.05$ and $K^p = 1$ kN/cm^2. A linear adherence law is considered herein, with the following parameters:

- $s_1 = 0.5$ cm;
- $s_2 = 2.5$ cm;
- $f_{MAX} = 0.08$ kN/cm;
- $f_{RES} = 0.4 f_{MAX}$.

The isogeometric model is composed by 6 regular NURBS surfaces with $p = q = 2$. The number of control points is equal to 17 in the solid axial direction (global x) and 6 in the transverse directions (global y and z). The mechanical model totalises 464 collocation points. 25 quadratic Lagrangian reinforcement elements discretise the long fibre, which lead to 51 nodes. This model demonstrated mesh convergence in previous analyses, regarding displacements at the boundary and both displacements and all mechanical fields over the fibre. Only the IGABEM model is considered for this application.

Figure 53 – Structure analysed in Application 3: geometry (dimensions in cm) and loads.

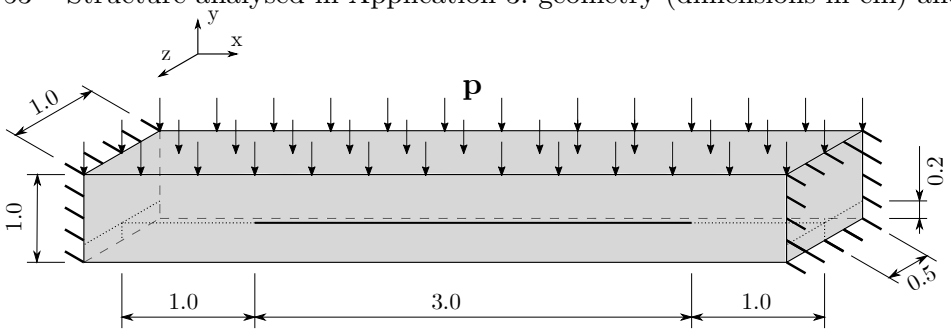

Source: The author.

The nonlinear process has been solved into 50 load steps whereas the tolerance for convergence was 10^{-6}. This application considers four distinct scenarios:

- "e": elastic reinforcements;
- "ep": elastoplastic reinforcements;
- "bs": bond-slip behaviour in elastic reinforcements;
- "bsp": bond-slip behaviour in elastoplastic reinforcements;

where the scenarios consider different available nonlinear behaviours of the reinforcements. The four scenarios responses can be compared against each other to demonstrate consistency of the obtained results.

Figure 54 exhibits the normal force results N along the long fibre length S obtained in all scenarios. The elastic result N_e corresponds to the expected mechanical behaviour considering the applied external load, i.e., maximum tensile value at the fibre centre point and nil value at the end-points. One observes a considerable decrease of the normal force values (comparing against N_e) in the scenarios with elastoplasticity (N_{ep} and N_{bsp}). These scenarios achieved the fibre elastic limit and presented the hardening behaviour.

Furthermore, *bs* scenario also shows an attenuation of normal forces due to the slipping behaviour, which is more pronounced near the fibre ends. The yielding clearly influences the central region of the fibre because of the higher stress values.

Figure 54 – Normal force N along the fibre length S, considering all four scenarios.

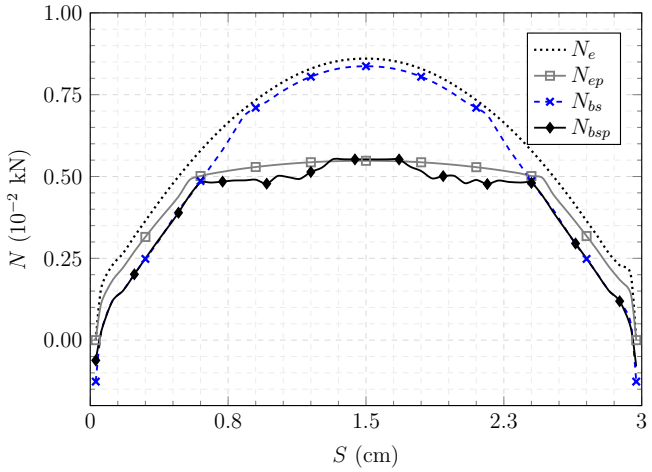

Source: The author.

Figure 55 illustrates the adherence force values f_D along the fibre length S, considering the four scenarios. One observes a symmetric behaviour in the elastic results $(f_D)_e$ (in relation to the fibre centre point) with the maximum values at the end points, which agrees with the adherence forces results available in the literature (89) for similar structures. The bond-slip effects can be observed in $(f_D)_{bs}$ and $(f_D)_{bsp}$, in which f_{MAX} limited the adherence force values. Besides, the presence of the elastoplasticity in *bsp* leads to an extension of the f_D limited region, which indicates that the yielding causes an increase in the slipping behaviour.

Figure 55 – Adherence force values f_D along the fibre length S, considering all four scenarios.

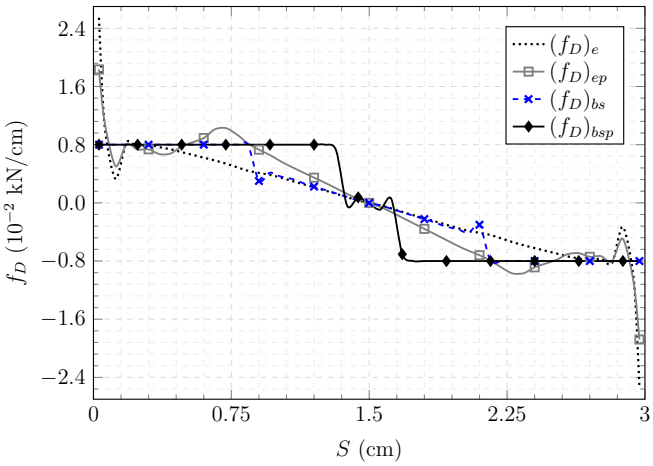

Source: The author.

Figure 56 exhibits the plastic strain results ε_{pl} along the long fibre length S obtained in *ep* and *bsp* scenarios. The obtained results match the expected behaviour. Then, the

fibres central region exhibits the yielding, which is the region with higher stress levels (Fig. 54). Besides, one notices the effect of the bond-slip in these results: intensifying the plastic strains in the central region and reducing the intensity of yielding as approaching the fibre ends. This behaviour is related to the slipping near the extremities.

Figure 57 shows the slip values s along the long fibre length S obtained in *bs* and *bsp* scenarios. Both scenarios demonstrate pronounced slipping behaviour near the extremities, with opposite sign in each side. This behaviour is a result of the observed adherence force (Fig. 55). When elastoplasticity is accounted, which occurs in the central region, one observes an increase in the slip values (s_{bsp}) on that region. Besides, the slip s_{bsp} is attenuated near the fibre ends because it is non-nil in a large S range when compared against s_{bs}.

Figure 56 – Plastic strains ε_{pl} along the fibre length S, considering *ep* and *bsp* scenarios.

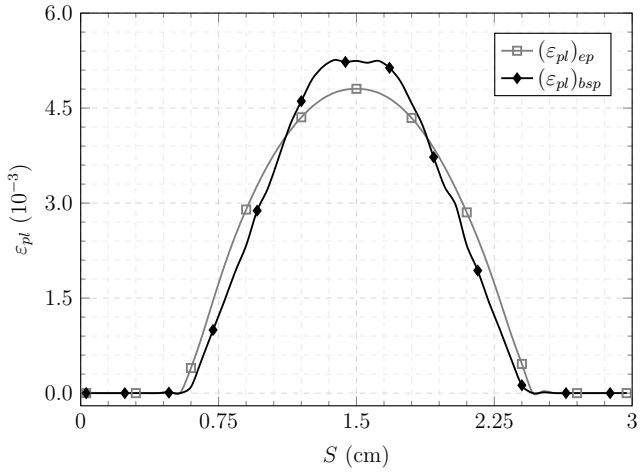

Source: The author.

Figure 57 – Slip results s along the fibre length S, considering *bs* and *bsp* scenarios.

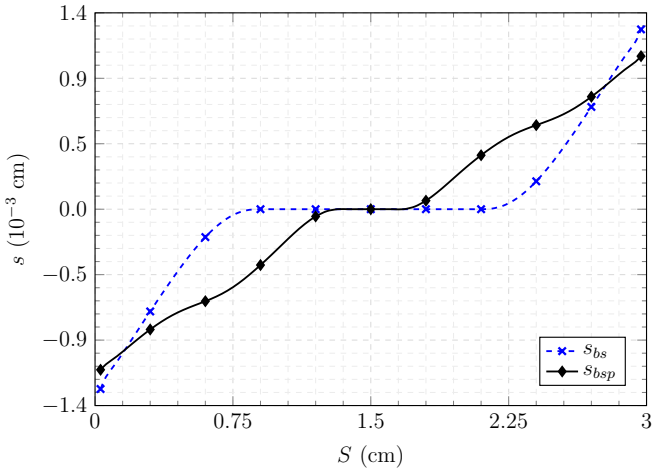

Source: The author.

Figure 58(a) and 58(b) illustrate the fibre displacements (u_E) and the domain

load line displacements (u_D), in x direction, obtained in *bs* and *bsp* scenarios, respectively. One understands better the opposite signs of slips in Fig. 57 by comparing these figures. The slipping ensures that fibre displacements are smaller, in modulus, than domain displacements because the external load is applied on the boundary. The opposite behaviour can be observed when the external load is applied directly on the fibre, such as the pull-out test, in which the fibre displacements are always higher than the domain's (Fig. 50).

Figure 58 – Reinforcements and domain displacements (u_E and u_D, respectively) in x direction, as a function of the fibre length S, considering *bs* (a) and *bsp* (b) scenarios.

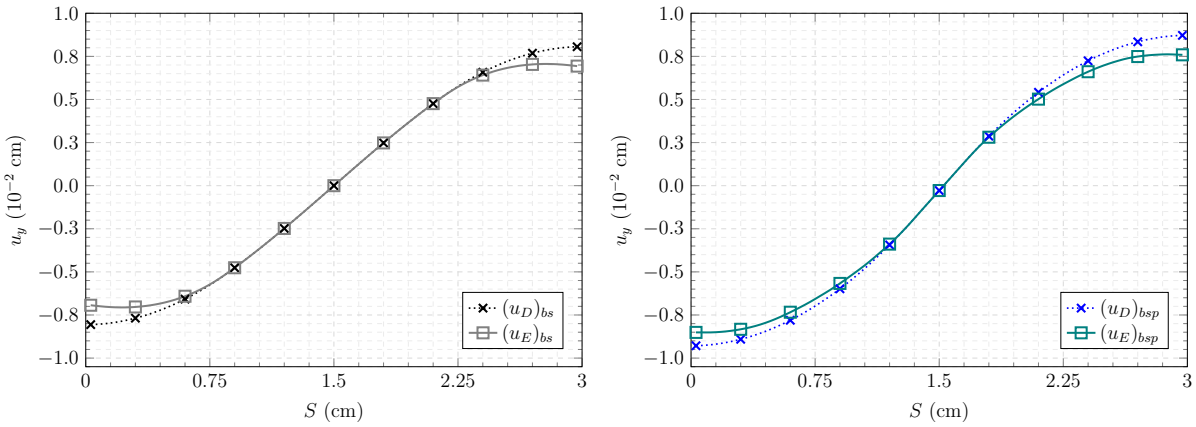

(a) *bs* scenario (b) *bsp* scenario

Source: The author.

Considering the above-mentioned analyses, one concludes that yielding together with slipping lead to the normal forces and the plastic strains attenuation in addition to an increase in slip values. Obviously, when the nonlinear laws follow the parameters presented in this application. This behaviour can be explained by the yielding effect, which intensifies the fibres displacements and causes intense slipping behaviour. On the other hand, the slip limits the adherence force values, which causes the normal force attenuation. Although these results do not have reference values, the presented discussion is consistent and demonstrate coherence of the obtained mechanical responses.

Figure 59 illustrates y direction displacements over the boundary obtained in *bsp* scenario. A magnification factor equals to 2 is considered in the deformed shape. The displacements behaviour is in agreement with the expected for the external loads applied on the structure (Fig. 53).

Figure 59 – Colour map of y direction displacements (in cm) over the boundary, considering *bsp* scenario.

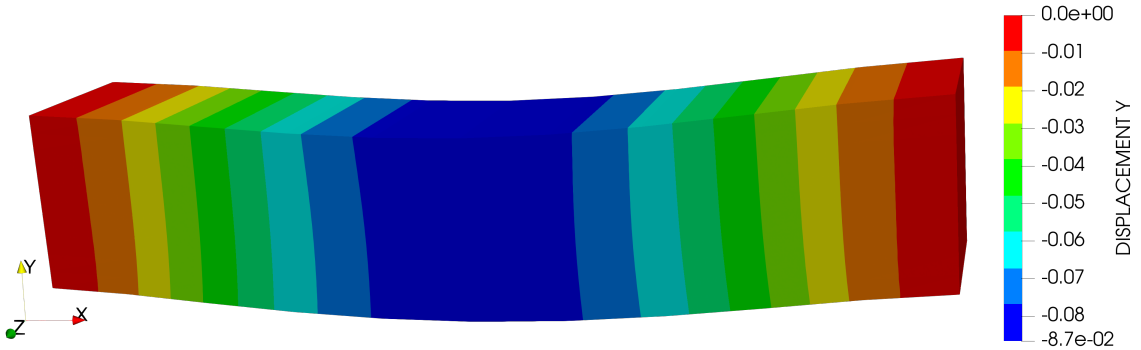

Source: The author.

5

Reinforced time Dependent Formulations

The time dependent behaviour of 3D reinforced and non-reinforced domains is presented herein through the viscoelastic formulations. The rheological models (134) of Kelvin-Voigt or Boltzmann represent the linear viscoelastic behaviour. The BEM formulations consider the rheological model to represent the viscoelasticity without the need for convolutional integration or domain discretization. Coupling viscoelastic formulations are also presented, which are obtained through the 1DBEM/BEM coupling technique.

5.1 Viscoelasticity and BEM: Literature Review

The usual approach for viscoelasticity in elasticity problems is the use of fluency and relaxation functions, which leads to a quasi-static incremental problem. In that case, the time dependent solution is obtained from integral transformations or the correspondence principle (97). Then, the application complex geometries and nonuniform boundary conditions becomes a true challenge. Besides that, the problem becomes too sensible to the time step size. More details about the classical approach can be found in the literature (135, 136, 137).

An alternative to the classical approach is the use of rheological models to represent the viscoelastic behaviour (134). With that, different time-dependent models can be constructed from the basic rheological elements, including linear and nonlinear models. In this context, the use of the BEM for modelling viscoelastic problems via rheological formulations is truly effective. The advantages previously mentioned in this text allow for modelling numerous viscoelastic problems without the need for domain discretization. Among the studies found in the literature with BEM approaches for viscoelastic modelling,

one may highlight: the evaluation of Stress Intensity Factors in viscoelastic polymers via the BEM (138); the use of Laplace transformation to evaluate the crack behaviour within a Kelvin-Voigt rheological model material (139); a BEM energetic approach for viscoelastic media (140) and the mechanical analysis of anisotropic viscoelastic domains with the consideration of initial imperfections (141).

An alternative procedure to handle the rheological models via BEM was presented by Mesquita (142), which proposed a simplification to make the viscous constitutive matrices directly proportional to the elastic constitutive matrix. Applying this strategy along with disregarding the inertia terms, all terms of the time-dependent integral equation become written as a function of the same constitutive matrix. Then, the same discretization used for the elastic problem can be applied straightforwardly to the time-discretized viscoelastic problem. This approach have showed great potential to be the basis of further developments in BEM viscoelastic formulations, being expanded for reinforced (90, 81) and 3D domains (143). Additionally, this approach have been utilised into fracture mechanics problems (54) and viscoplastic anisotropic media (130). Finally, the 2D viscoelastic BEM Lagrangian formulation for reinforced domains have been proposed by this author (66) recently. Thus, the expansion of that formulation for 3D Isogeometric analyses is a subject of this work.

5.2 The rheological models

The viscoelastic materials present a time dependent behaviour called memory or hereditary effects. This means that the mechanical response of such materials depend no only on the applied load intensity, but also on its historic throughout time. The rheological models are an alternative to mathematically represent this phenomenon (144). This approach adopts the following hypothesis: stationary and homogeneous physical properties, in addition to quasi-static behaviour. Besides, different classical formulations can be mentioned to treat the viscoelasticity phenomenon as mentioned in (145, 146), which are also briefly mentioned in (147).

5.2.1 Basic elements of the rheological models

The rheological models are built from the association of basic elements. Each one of the basic elements represents a theoretical mechanical behaviour through simple mathematical relations. Figure 60 illustrates these elements. The parallel with elements of electric circuits (transistors, transformers and capacitors) is clear and valid.

Figure 60(a) exhibits a spring element, which represents the perfectly elastic behaviours. This element responds instantly with strains when subjected to an applied load. The response is directly proportional to a constitutive tensor, similarly to Eq. A.8.

Besides, there are no permanent strains, i.e., the materials returns to its original shape once the load is removed, regardless of its intensity.

Figure 60 – Basic elements representation: (a) spring and (b) dashpot.

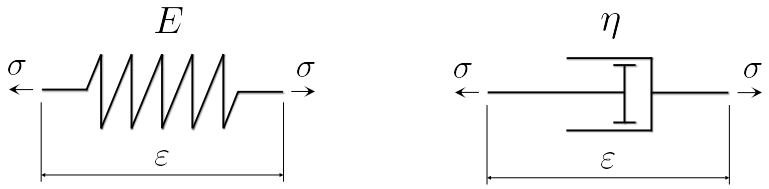

(a) (b)

Source: The author.

The constitutive relation of the spring is similar to the Hooke's law (Eq. A.8) as follows:

$$\sigma_{ij}^{(el)} = D_{ijlm}\varepsilon_{lm}^{(el)} \tag{5.1}$$

in which the index (el) identify the elastic fields related to the spring element.

Figure 60(b) exhibits a dashpot element, which represents the perfectly viscous behaviour. When subjected to an applied load, this element responds with strains rate, which demonstrates the time dependency. The dashpot element is mathematically represented by:

$$\sigma_{ij}^{(v)} = \eta_{ijlm}\dot{\varepsilon}_{lm}^{(v)} \tag{5.2}$$

in which η_{ijlm} is the viscous constitutive tensor, analogously to D_{ijlm} from Eq. 5.1. $\dot{\varepsilon}_{lm}^{v}$ represent the derivative of ε_{lm}^{v} with respect to time. It is worth mentioning that there is no instant response in the dashpot element, since it responses only with a strains rate.

The viscous constitutive tensor is mathematically represented by the following expression:

$$\eta_{ijlm} = \theta_\lambda \lambda \delta_{ij}\delta_{lm} + \theta_\mu \mu \left(\delta_{il}\delta_{jm} + \delta_{im}\delta_{jl}\right) \tag{5.3}$$

where μ and λ are the parameters presented for Eq. A.10. θ_λ and θ_μ are viscous representative parameters (144). A acceptable simplification of these parameters, according to Mesquita (144), is as follows:

$$\theta_\lambda = \theta_\mu = \gamma \tag{5.4}$$

Thus, Eq. 5.3 is rewritten as follows:

$$\eta_{ijkl} = \gamma \left[\lambda \delta_{ij}\delta_{lm} + \mu \left(\delta_{il}\delta_{jm} + \delta_{im}\delta_{jl}\right)\right] = \gamma D_{ijlm} \tag{5.5}$$

in which D_{ijlm} is the elastic constitutive tensor.

Hence, the dashpot relation (Eq. 5.2) can be rewritten as a function of the same constitutive matrix D_{ijlm} of the spring element, as follows:

$$\sigma_{ij}^{(v)} = \gamma D_{ijlm} \dot{\varepsilon}_{lm}^{(v)} \tag{5.6}$$

Likewise the electric circuits, the basic elements presented herein can be arranged in different ways (parallel and series associations) to assemble the rheological models.

5.2.2 Kelvin-Voigt model

The Kelvin-Voigt model (or simply Kelvin model) is composed by a series association of a spring and a dashpot, as illustrated in Fig. 61.

Figure 61 – Association scheme of the Kelvin-Voigt viscoelastic model.

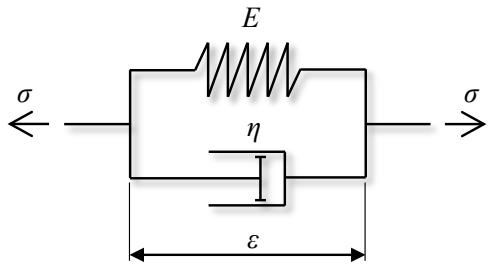

Source: The author.

In the electric circuits analogy, the strain is analogous to the electric potential difference (or voltage). Therefore, both elements in Fig. 61 must be subjected to the same strain ε. The stress σ is analogous to the intensity of current in the electric circuit, thus σ must be divided into the spring and dashpot elements in Fig. 61. With these considerations, one writes:

$$\begin{aligned} \varepsilon_{ij} &= \varepsilon_{ij}^{(el)} = \varepsilon_{ij}^{(v)} \\ \sigma_{ij} &= \sigma_{ij}^{(el)} + \sigma_{ij}^{(v)} \end{aligned} \tag{5.7}$$

Applying Eq. 5.1 and 5.6 into Eq. 5.7, one writes the Kelvin model's relation as follows:

$$\sigma_{ij} = D_{ijlm}\varepsilon_{lm} + \gamma D_{ijlm}\dot{\varepsilon}_{lm} \tag{5.8}$$

in which σ_{ij} and ε_{lm} are the total stresses and strains, respectively. $\dot{\varepsilon}_{lm}$ is the rate of strains, i.e., the strains derivatives with respect to time.

It is worth mentioning that the Kelvin model does not present any immediate strains when subjected to σ_{ij}. This is explained by the series association, which implies that both the sprint and the dashpot present the same ε_{lm}. Thus, the absence of immediate strains in the dashpot impede any immediate response of the spring. This mechanical behaviour is not realistic for a large number of real materials, hence more complex models are necessary.

5.2.3 Boltzmann model

The Boltzmann model is composed by a series association of one spring and one Kelvin-Voigt's scheme, as illustrated in Fig. 62.

Figure 62 – Association scheme of the Boltzmann viscoelastic model.

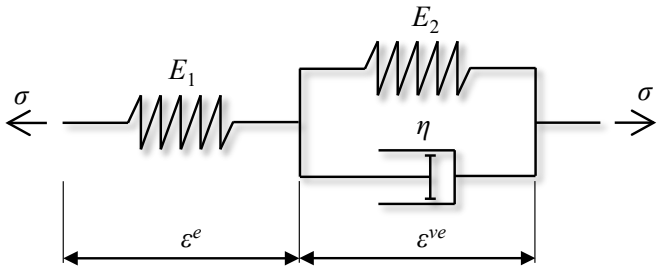

Source: The author.

Stresses and strains in the Boltzmann model are divided into: the purely elastic portions ($\sigma_{ij}^{(e)}$, $\varepsilon_{ij}^{(e)}$) that are related to the spring E_1 and the viscoelastic portions ($\sigma_{ij}^{(ev)}$, $\varepsilon_{ij}^{(ev)}$) that are related to the Kelvin scheme of E_2 and η. One can relate these portions as follows:

$$\begin{aligned} \varepsilon_{ij} &= \varepsilon_{ij}^{(e)} + \varepsilon_{ij}^{(ve)} \\ \sigma_{ij} &= \sigma_{ij}^{(e)} = \sigma_{ij}^{(ve)} \end{aligned} \tag{5.9}$$

Equation 5.8 can be applied to the association of E_2 and η, as follows:

$$\sigma_{ij}^{(ve)} = E_2 \bar{D}_{ijlm} \varepsilon_{lm}{}^{(ve)} + \gamma E_2 \bar{D}_{ijlm} \dot{\varepsilon}_{lm}^{(ve)} \tag{5.10}$$

in which $E_2 \bar{D}_{ijlm} = D_{ijlm}$ for the spring E_2. Using this same concept, Eq. 5.1 can be applied for the spring E_1 as follows:

$$\sigma_{ij}^{(e)} = E_1 \bar{D}_{ijlm} \varepsilon_{lm}^{(e)} \tag{5.11}$$

Thus, applying Eq. 5.10 and the time derivative of Eq. 5.11 into Eq. 5.9, one writes the Boltzmann's relation as follows:

$$\sigma_{ij} = \frac{E_1 E_2}{E_1 + E_2} \bar{D}_{ijlm} \left(\varepsilon_{lm} + \gamma \dot{\varepsilon}_{lm}\right) - \frac{\gamma E_2}{E_1 + E_2} \dot{\sigma}_{ij} \tag{5.12}$$

in which σ_{ij} and ε_{lm} are the total stresses and strains, respectively. $\dot{\sigma}_{ij}$ is the rate of stresses, i.e., the stresses derivative with respect to time.

It is worth mentioning that the Boltzmann model overcomes the mentioned limitations of the Kelvin model, due to properly represent both immediate and time dependent responses. Because of this fact, the Boltzmann model is also called standard solid.

5.3 Viscoelastic BEM formulations

The rheological model's relation must be applied into the BEM formulation in order to produce a viscoelastic formulation. Therefore, each rheological model leads to a different numerical formulation.

5.3.1 Kelvin Voigt's 3D domains formulation

Equation 5.8 must be applied into the boundary relation from Eq. 2.4, instead of the elastic constitutive relation. Thus:

$$\int_\Gamma U^*_{ki} t_i d\Gamma - \int_\Omega E^*_{kij} D_{ijlm} \varepsilon_{lm} d\Omega - \int_\Omega E^*_{kij} \gamma D_{ijlm} \dot{\varepsilon}_{lm} d\Omega + \int_\Omega U^*_{ki} b_i d\Omega = 0 \tag{5.13}$$

Applying Eq. A.24, Eq. A.25 and Eq. A.7 into Eq. 5.13, one writes:

$$\int_\Gamma U^*_{ki} t_i d\Gamma - \int_\Omega P^*_{kij} u_{i,j} d\Omega - \gamma \int_\Omega P^*_{kij} \dot{u}_{i,j} d\Omega + \int_\Omega U^*_{ki} b_i d\Omega = 0 \tag{5.14}$$

in which $\dot{u}_{i,j}$ is the derivative of the term $u_{i,j}$ with respect to time.

Then, integrating the second and third terms by parts and applying Eq. A.23 and A.20, one writes:

$$\int_\Gamma U^*_{ki} t_i d\Gamma - \int_\Gamma T^*_{ki} u_i d\Gamma - \int_\Omega \Delta_k u_i d\Omega - \gamma \int_\Gamma T^*_{ki} \dot{u}_i d\Gamma - \gamma \int_\Omega \Delta_k \dot{u}_i d\Omega + \int_\Omega U^*_{ki} b_i d\Omega = 0 \tag{5.15}$$

The source point is considered to be internal to Ω, thus one may applies the sifting property of the Dirac delta function Δ_k. This process results in the free terms u^s_i and $\dot{u}^s_i$. One may now write the viscoelastic version of the Somigliana's identity as follows:

$$u^s_i + \gamma \dot{u}^s_i + \int_\Gamma T^*_{ki} u_i d\Gamma + \gamma \int_\Gamma T^*_{ki} \dot{u}_i d\Gamma = \int_\Gamma U^*_{ki} t_i d\Gamma + \int_\Omega U^*_{ki} b_i d\Omega \tag{5.16}$$

Equation 5.16 is analogous to the elastic Somigliana's identity (Eq. 2.9). The boundary integral equation is obtained by applying the limiting process (Sec. 2.3). Thus, one obtains the following:

$$c^s_{ki}\left[u^s_i + \gamma \dot{u}^s_i\right] + \int_\Gamma T^*_{ki} u_i d\Gamma + \gamma \int_\Gamma T^*_{ki} \dot{u}_i d\Gamma = \int_\Gamma U^*_{ki} t_i d\Gamma + \int_\Omega U^*_{ki} b_i d\Omega \tag{5.17}$$

in which the free term c^s_{ki} is the same presented for Eq. 2.23.

Equation 5.17 can be rewritten in an algebraic from, following the process described in Ch. 2. With that, both the Lagrangian or NURBS approximations can be applied herein to represent a viscoelastic BEM or IGABEM formulation. Thus:

$$\mathbf{H}\hat{\mathbf{u}} + \gamma \mathbf{H}\dot{\hat{\mathbf{u}}} = \mathbf{G}\hat{\mathbf{t}} + \int_\Omega U^*_{ki} b_i d\Omega \tag{5.18}$$

in which $\dot{\hat{\mathbf{u}}}$ is the derivative of the displacements parameters $\hat{\mathbf{u}}$ with respect to time.

Besides the boundary and domain integrations already treated in Ch. 2 and 3, Eq. 5.18 presents a first order time derivative of the displacements. The implicit version of the Finite Difference Method (backward finite differences) is applied herein to solve the time differential equation. This approach is based on discretising the time differential equation into a finite number of time steps and applying the following approximation:

$$\dot{\hat{\mathbf{u}}}^{t+1} = \frac{\hat{\mathbf{u}}^{t+1} - \hat{\mathbf{u}}^t}{\Delta t} \tag{5.19}$$

in which $t+1$ is the current time step and t is the previous time step. The size of a time step is constant and equals Δt.

Applying Eq. 5.19 into Eq. 5.18, one writes:

$$\left(1 + \frac{\gamma}{\Delta t}\right)\mathbf{H}\hat{\mathbf{u}}^{t+1} = \mathbf{G}\hat{\mathbf{t}}^{t+1} + \frac{\gamma}{\Delta t}\mathbf{H}\hat{\mathbf{u}}^t + \int_\Omega U^*_{ki} b^{t+1}_i d\Omega \tag{5.20}$$

Equation 5.20 then defines the boundary solutions (displacements and tractions) at a given time step $t+1$. Note that this is a time marching process, for which initial conditions (at $t=0$) are required. Besides, the convergence of the Finite Difference Method must be verified regarding the time step size Δt. This equation is in fact well-behaved in relation to Δt and more details about it can be found in the literature (144, 147).

The expression for internal stress can be obtained from Eq. 5.17 by following the process detailed in Ch. 2. Firstly, the derivative of Eq. 5.17 with respect to the source point coordinates are computed. Then, applying Eq. A.7), one writes the following:

$$\varepsilon^s_{ij} + \gamma \dot{\varepsilon}^s_{ij} - \int_\Gamma T^*_{ki,j} u_i d\Gamma - \gamma \int_\Gamma T^*_{ki,j} \dot{u}_i d\Gamma = -\int_\Gamma E^*_{kij} t_i d\Gamma - \int_\Omega E^*_{kij} b_i d\Omega \tag{5.21}$$

Applying Eq. 5.7, Eq. 5.1 and Eq. 5.6 into the first and second terms of Eq. 5.21, one writes:

$$\sigma^s_{jk} + \int_\Gamma S^*_{ijk} u_i d\Gamma + \gamma \int_\Gamma S^*_{ijk} \dot{u}_i d\Gamma = \int_\Gamma D^*_{ijk} t_i d\Gamma + \int_\Omega D^*_{ijk} b_i d\Omega \tag{5.22}$$

in which the integral kernels S^*_{ijk} and D^*_{ijk} are the hypersingular solutions given Eq. 2.19 and 2.18, respectively. σ^s_{jk} represents the total stress at the source point, which is equal to the sum of the elastic and viscous portions in the Kelvin-Voigt model.

Equation 5.22 can be algebraically written as follows:

$$\boldsymbol{\sigma_s} + \mathbf{H}'\hat{\mathbf{u}} + \gamma\mathbf{H}'\dot{\hat{\mathbf{u}}} = \mathbf{G}'\hat{\mathbf{t}} + \int_\Omega D^*_{ijk} b_i d\Omega \tag{5.23}$$

in which the matrixes $\mathbf{H}'$ and $\mathbf{G}'$ are the same presented in Ch. 2 for the TBIE.

Applying the Finite Difference Method, one writes:

$$\boldsymbol{\sigma_s}^{t+1} = \mathbf{G}'\hat{\mathbf{t}}^{t+1} - \mathbf{H}'\hat{\mathbf{u}}^{t+1} - \gamma\mathbf{H}'\dot{\hat{\mathbf{u}}}^{t+1} + \int_\Omega D^*_{ijk} b_i^{t+1} d\Omega \tag{5.24}$$

where $\dot{\mathbf{u}}^{t+1}$ is obtained from Eq. 5.19, since the boundary displacements at $t+1$ and t are both known.

To determine the elastic and viscous portions of $\boldsymbol{\sigma_s}^{t+1}$, one must recall the Kelvin-Voigt model's relations. For that, the time derivative of Eq. 5.1 is written as follows:

$$\dot{\sigma}^{(el)}_{ij} = D_{ijlm}\dot{\varepsilon}^{(el)}_{lm} \tag{5.25}$$

Then, applying Eq. 5.25 and 5.1 into Eq. 5.8, one obtains the following differential equation for stress:

$$\sigma_{ij} = \sigma^{(el)}_{ij} + \gamma\dot{\sigma}^{(el)}_{ij} \tag{5.26}$$

The total stress σ_{ij} is known from Eq. 5.24, thus applying the Finite Differences Method is enough to solve Eq. 5.26 regarding the elastic stress portion, which results in:

$$\boldsymbol{\sigma}^{t+1}_{\boldsymbol{el}} = \frac{\boldsymbol{\sigma_s}^{t+1} + {}^{\gamma}/_{\Delta t}\boldsymbol{\sigma}^{t}_{\boldsymbol{el}}}{1 + {}^{\gamma}/_{\Delta t}} \tag{5.27}$$

in which $\boldsymbol{\sigma}^{t+1}_{\boldsymbol{el}}$ is the elastic portion of $\boldsymbol{\sigma}^{t+1}_{\boldsymbol{s}}$. Finally, the viscous stress portion $\boldsymbol{\sigma}^{t+1}_{\boldsymbol{v}}$ can be find as follows:

$$\boldsymbol{\sigma}^{t+1}_{\boldsymbol{v}} = \boldsymbol{\sigma_s}^{t+1} - \boldsymbol{\sigma}^{t+1}_{\boldsymbol{el}} \tag{5.28}$$

5.3.2 Kelvin Voigt's 1D domains formulation

The 1DBEM viscoelastic formulation is obtained from Eq. 5.22. This expression can be applied to 1D domains, in which the domain integrations become line integrations

along $\bar{x}$ and the boundary integrations become the simple evaluation of the fundamental solutions at the endpoints (1 e n), as follows:

$$u^s + \gamma \dot{u}^s + (uN^*)\Big|_0^L + (\gamma \dot{u} N^*)\Big|_0^L = (Nu^*)\Big|_0^L + \int_0^L pu^* dx \tag{5.29}$$

which replace the elastic formulation presented in Eq. 3.50.

The expression for internal displacements (Eq. 3.57) is rewritten as follows:

$$u_j + \gamma \dot{u}_j - N^*_{j1}u_1 + N^*_{jn}u_n - N^*_{j1}\dot{u}_1 + N^*_{jn}\dot{u}_n = -u^*_{j1}N_1 + u^*_{jn}N_n + q_j \tag{5.30}$$

in which j is a given internal point.

The 1DBEM algebraic system can be rewritten considering Eq. 5.29 and 5.30 as follows:

$$\mathbf{Hu} + \gamma \mathbf{H}\dot{\mathbf{u}} = \mathbf{Gn} + \bar{\mathbf{G}}\mathbf{f} \tag{5.31}$$

in which the matrices $\mathbf{H}$, $\mathbf{G}$ and $\bar{\mathbf{G}}$ are the same presented for Eq. 3.55.

The same procedure presented in Sec. 3.5 is applied into Eq. 5.31. Thus, one writes:

$$\mathbf{K_E u} + \gamma \mathbf{K_E}\dot{\mathbf{u}} = \mathbf{G_E f} \tag{5.32}$$

in which the matrices $\mathbf{K_E}$ and $\mathbf{G_E}$ are given by Eq. 3.60.

The Finite Difference Method as detailed in Sec. 5.3.1 is applied into Eq. 5.32, which results in the following:

$$\left(1 + \frac{\gamma}{\Delta t}\right)\mathbf{K_E u}^{t+1} = \mathbf{G_E f}^{t+1} + \frac{\gamma}{\Delta t}\mathbf{K_E u}^t \tag{5.33}$$

The procedure presented in Sec. 3.5 for the axial forces calculation is also valid herein. However, Eq. 3.62 must be replaced by:

$$\mathbf{n}^{t+1} = \left(1 + \frac{\gamma}{\Delta t}\right)\mathbf{K_E u}^{t+1} - \mathbf{G_E f}^{t+1} - \frac{\gamma}{\Delta t}\mathbf{K_E u}^t \tag{5.34}$$

Besides, the axial internal force is divided into the elastic $N(el)$ and viscous $N(v)$ portions in the Kelvin viscoelastic formulation. In order to find these portions, one writes Eq. 5.26 for axial forces as follows:

$$N(tot) = N(el) + \gamma \dot{N}(el) \tag{5.35}$$

in which $N(tot)$ is the total axial force, resulting from $N(el) + N(v)$. The solution of this expression determines the elastic portion as follows:

$$N^{t+1}(el) = \frac{N^{t+1}(tot) + {}^{\gamma}/_{\Delta t}}{1 + {}^{\gamma}/_{\Delta t}} \tag{5.36}$$

The viscous portion can be obtained by subtracting the elastic portion from the total axial force, similarly to Eq. 5.28.

5.3.3 Boltzmann's 3D domains formulation

To obtain the viscoelastic BEM formulation for Boltzmann, Eq. 5.12 must be applied into Eq. 2.4. A process similar to the one described in Sec. 5.3.1 is followed, as demonstrated in (143, 54), which leads to:

$$\begin{aligned} c_{ki}\left[u_i + \gamma \dot{u}_i\right] + \int_\Gamma T^*_{ki} u_i d\Gamma + \gamma \int_\Gamma T^*_{ki} \dot{u}_i d\Gamma = \left(\frac{E_1 + E_2}{E_2}\right) \int_\Gamma U^*_{ki} t_i d\Gamma + \\ \gamma \int_\Gamma U^*_{ki} \dot{t}_i d\Gamma + \left(\frac{E_1 + E_2}{E_2}\right) \int_\Omega U^*_{ki} b_i d\Omega + \gamma \int_\Omega U^*_{ki} \dot{b}_i d\Omega \end{aligned} \tag{5.37}$$

in which $\dot{t}_i$ and $\dot{b}_i$ are the time derivatives of t_i and b_i, respectively.

The Finite Difference Method is applied into Eq. 5.37, as described in Sec. 5.3.1. In this case, boundary tractions and body forces also have their time derivatives approximated, similarly to Eq. 5.19 for displacements. Equation 5.38 can then be algebraically written, by applying the Lagrangian or NURBS approximations, as described in Ch. 2. Thus:

$$\begin{aligned} \left(1 + \frac{\gamma}{\Delta t}\right) \mathbf{H}\hat{\mathbf{u}}^{t+1} = \left(\frac{\gamma}{\Delta t} + \frac{E_1 + E_2}{E_2}\right) \left(\mathbf{G}\hat{\mathbf{t}}^{t+1} + \int_\Omega U^*_{ki} b_i^{t+1} d\Omega\right) + \\ \frac{\gamma}{\Delta t} \left(\mathbf{H}\hat{\mathbf{u}}^{t} - \mathbf{G}\hat{\mathbf{t}}^{t} - \int_\Omega U^*_{ki} b_i^{t} d\Omega\right) \end{aligned} \tag{5.38}$$

The expression for internal stress ($\boldsymbol{\sigma_s}$) can be obtained through a process similar to the one presented in Sec. 5.3.1. Its algebraic representation is as follows (54):

$$\begin{aligned} \boldsymbol{\sigma}_s^{t+1} = \Bigg[\mathbf{G}'\hat{\mathbf{t}}^{t+1} - \frac{E_2}{E_1 + E_2} \left(\mathbf{H}'\hat{\mathbf{u}}^{t+1} + \gamma \mathbf{H}'\dot{\hat{\mathbf{u}}}^{t+1} - \gamma \mathbf{G}'\dot{\hat{\mathbf{t}}}^{t+1} - \gamma \int_\Omega D^*_{ijk} \dot{b}^{t+1} d\Omega\right) \\ + \int_\Omega D^*_{ijk} b^{t+1} d\Omega + \frac{\gamma}{\Delta t} \frac{E_2}{E_1 + E_2} \boldsymbol{\sigma}_s^t\Bigg] \left(1 + \frac{\gamma}{\Delta t} \frac{E_2}{E_1 + E_2}\right)^{-1} \end{aligned} \tag{5.39}$$

As well as the Kelvin-Voigt formulation, the total stress $\boldsymbol{\sigma_s}$ is divided into the elastic and viscous portions through Eq. 5.27 and 5.28.

5.4 Reinforced viscoelastic formulations

The expressions of the BEM viscoelastic presented in this chapter must be applied into the coupling technique formulation presented in Ch. 3. Thus, different couplings can

be obtained from mixing the different viscoelastic models for fibre and domain. Each one of this couplings may represent a different mechanical behaviour from real-world engineering applications.

5.4.1 Kelvin/Elastic coupling

Elastic 1DBEM fibres reinforce 3D Kelvin-Voigt's domains in this time-dependent coupling model. The coupled formulation requires the expressions of boundary values and internal displacements algebraic representations, which are considered instead of Eq. 3.5 and Eq. 3.6. The viscoelastic BIE is represented by Eq. 5.20, which must consider the fibre's adherence force as the body forces b_i. For this, the integration scheme presented in Sec. 3.3 is considered herein, which provides the numerical evaluation of the domain integral term in Eq. 5.20. Therefore, the algebraic representation of Eq. 5.20 can be rewritten as follows (13):

$$(1+\alpha)\mathbf{H_{CC}}\hat{\mathbf{u}}_\mathbf{C} = \mathbf{G_{CC}}\hat{\mathbf{t}}_\mathbf{C} + \alpha\mathbf{H_{CC}}\hat{\mathbf{u}}_\mathbf{C}^{(-)} + \mathbf{G_{CF}}\mathbf{f_D} \tag{5.40}$$

where $\alpha = \gamma/\Delta t$. The index $^{(-)}$ herein represents the variables evaluated at the previous time step (t), all vectors without it contain information at the current time step $(t+1)$.

The algebraic equation for internal displacements can also be obtained from Eq. 5.20, by applying it for internal points. This equation provides displacements at domain positions coincident with reinforcements nodes. Then:

$$(1+\alpha)\,\mathbf{u_D} + (1+\alpha)\,\mathbf{H_{FC}}\hat{\mathbf{u}}_\mathbf{C} = \mathbf{G_{FC}}\hat{\mathbf{t}}_\mathbf{C} + \mathbf{G_{FF}}\mathbf{f_D} + \alpha\mathbf{H_{FC}}\hat{\mathbf{u}}_\mathbf{C}^{(-)} + \alpha\mathbf{u_D}^{(-)} \tag{5.41}$$

The matrices in Eq. 5.40 and Eq. 5.41 are the same presented in Sec. 3.2.

Equation 3.7 remains valid because the reinforcements are elastic. Therefore, one writes the algebraic representation for the Kelvin/Elastic coupling by considering the relations from Eq. 3.2, Eq. 3.7, Eq. 5.40 and Eq. 5.41 as follows:

$$\begin{bmatrix} (1+\alpha)\,\mathbf{H_{CC}} & \mathbf{0} & -\mathbf{G_{CF}} \\ (1+\alpha)\,\mathbf{H_{FC}} & (1+\alpha)\,\mathbf{I} & -\mathbf{G_{FF}} \\ \mathbf{0} & \mathbf{K_F} & \mathbf{G_F} \end{bmatrix} \begin{Bmatrix} \hat{\mathbf{u}}_\mathbf{C} \\ \mathbf{u_D} \\ \mathbf{f_D} \end{Bmatrix} = \begin{bmatrix} \mathbf{G_{CC}} & \alpha\mathbf{H_{CC}} & \mathbf{0} \\ \mathbf{G_{FC}} & \alpha\mathbf{H_{FC}} & \alpha\mathbf{I} \\ \mathbf{0} & \mathbf{0} & \mathbf{0} \end{bmatrix} \begin{Bmatrix} \hat{\mathbf{t}}_\mathbf{C} \\ \mathbf{u}_\mathbf{C}^{(-)} \\ \mathbf{u}_\mathbf{D}^{(-)} \end{Bmatrix} \tag{5.42}$$

Then, one properly enforces the boundary conditions, in a similar process to the one presented for Eq. 3.9. This system then determines the unknown boundary values $\mathbf{x_C}$ and the unknown reinforcements values $\mathbf{u_D}$, $\mathbf{f_D}$ at the current time step $t+1$. It is worth mentioning that the previous time step information is necessary to solve this system, which characterises it as a time marching process like Eq. 5.20. Hence, initial conditions

must be informed to start the time marching process and the analysis is performed along a discretised time, as usual in time approximated problems.

The expression for internal stress $\boldsymbol{\sigma_s}$ (Eq. 5.24) is then updated to account for the fibre's adherence force in the domain term, as follows:

$$\boldsymbol{\sigma_s} = \mathbf{G'_{SC}}\hat{\mathbf{t}}_\mathbf{C} + \mathbf{G'_{SF}}\mathbf{f_D} - \mathbf{H'_{SC}}\hat{\mathbf{u}}_\mathbf{C} - \gamma\mathbf{H'_{SC}}\dot{\hat{\mathbf{u}}}_\mathbf{C} \tag{5.43}$$

in which the index $\boldsymbol{s}$ represents the source point positioned at an internal point (not coincident with any fibre nodes). The time derivative $\dot{\mathbf{u}}_\mathbf{C}$ is given by Eq. 5.19.

5.4.2 Kelvin/Kelvin coupling

1DBEM fibres following Kelvin-Voigt behaviour reinforce 3D Kelvin-Voigt's domains in this coupling scheme. The 3D integral equations from Sec. 5.4.1 (Eq. 5.40 and Eq. 5.41) remain valid herein. Besides, the reinforcements viscoelastic equation (Eq. 5.33) and the compatibility relations from Eq. 3.2 are considered herein to obtain the following system of equations for this coupling scheme:

$$\begin{bmatrix} (1+\alpha)\,\mathbf{H_{CC}} & \mathbf{0} & -\mathbf{G_{CF}} \\ (1+\alpha)\,\mathbf{H_{FC}} & (1+\alpha)\,\mathbf{I} & -\mathbf{G_{FF}} \\ \mathbf{0} & (1+\alpha)\,\mathbf{K_F} & \mathbf{G_F} \end{bmatrix} \begin{Bmatrix} \hat{\mathbf{u}}_\mathbf{C} \\ \mathbf{u_D} \\ \mathbf{f_D} \end{Bmatrix} = \begin{bmatrix} \mathbf{G_{CC}} & \alpha\mathbf{H_{CC}} & \mathbf{0} \\ \mathbf{G_{FC}} & \alpha\mathbf{H_{FC}} & \alpha\mathbf{I} \\ \mathbf{0} & \mathbf{0} & \alpha\mathbf{K_F} \end{bmatrix} \begin{Bmatrix} \hat{\mathbf{t}}_\mathbf{C} \\ \mathbf{u}_\mathbf{C}^{(-)} \\ \mathbf{u}_\mathbf{D}^{(-)} \end{Bmatrix} \tag{5.44}$$

Equation 5.43 for internal stress remain valid in this coupling scheme, because this expression does no depend on the reinforcements mechanical behavior.

5.4.3 Boltzmann/Elastic coupling

Elastic 1DBEM fibres reinforce 3D Boltzmann's domains in this time-dependent coupling model. The viscoelastic BIE for Boltzmann's represented by Eq. 5.38. The fibres contribution are accounted in the domain integral term through the adherence force, which applies the integration scheme presented in Sec. 3.3. Thus, Eq. 5.38 is rewritten as follows (13):

$$(1+\alpha)\,\mathbf{H_{CC}}\hat{\mathbf{u}}_\mathbf{C} = \left(\alpha + \tfrac{E_1+E_2}{E_2}\right)\left(\mathbf{G_{CC}}\hat{\mathbf{t}}_\mathbf{C} + \mathbf{G_{CF}}\mathbf{f_D}\right) + \alpha\left(\mathbf{H_{CC}}\hat{\mathbf{u}}_\mathbf{C}^{(-)} - \mathbf{G_{CC}}\hat{\mathbf{t}}_\mathbf{C}^{(-)} - \mathbf{G_{CF}}\mathbf{f}_\mathbf{D}^{(-)}\right) \tag{5.45}$$

This expression can be applied to internal points coincident with the reinforcement nodes as follows:

$$\begin{aligned}(1+\alpha)\,\mathbf{u_D} + (1+\alpha)\,\mathbf{H_{FC}}\hat{\mathbf{u}}_\mathbf{C} = \left(\alpha + \tfrac{E_1+E_2}{E_2}\right)\left(\mathbf{G_{FC}}\hat{\mathbf{t}}_\mathbf{C} + \mathbf{G_{FF}}\mathbf{f_D}\right) + \\ \alpha\left(\mathbf{H_{FC}}\hat{\mathbf{u}}_\mathbf{C}^{(-)} + \mathbf{u}_\mathbf{D}^{(-)} - \mathbf{G_{FC}}\hat{\mathbf{t}}_\mathbf{C}^{(-)} - \mathbf{G_{FF}}\mathbf{f}_\mathbf{D}^{(-)}\right)\end{aligned} \tag{5.46}$$

Equation 3.7 remains valid because the reinforcements are elastic. Therefore, one writes the algebraic representation for the Boltzmann/Elastic coupling by considering the relations from Eq. 3.2, Eq. 3.7, Eq. 5.45 and Eq. 5.46 as follows:

$$\begin{bmatrix} (1+\alpha)\,\mathbf{H_{CC}} & \mathbf{0} & -\left(\alpha+\frac{E_1+E_2}{E_2}\right)\mathbf{G_{CF}} \\ (1+\alpha)\,\mathbf{H_{FC}} & (1+\alpha)\,\mathbf{I} & -\left(\alpha+\frac{E_1+E_2}{E_2}\right)\mathbf{G_{FF}} \\ \mathbf{0} & \mathbf{K_F} & \mathbf{G_F} \end{bmatrix} \begin{Bmatrix} \hat{\mathbf{u}}_\mathbf{C} \\ \mathbf{u_D} \\ \mathbf{f_D} \end{Bmatrix} = \\ \begin{bmatrix} \left(\alpha+\frac{E_1+E_2}{E_2}\right)\mathbf{G_{CC}} & \alpha\mathbf{H_{CC}} & \mathbf{0} & -\alpha\mathbf{G_{CC}} & -\alpha\mathbf{G_{CF}} \\ \left(\alpha+\frac{E_1+E_2}{E_2}\right)\mathbf{G_{FC}} & \alpha\mathbf{H_{FC}} & \alpha\mathbf{I} & -\alpha\mathbf{G_{FC}} & -\alpha\mathbf{G_{FF}} \\ \mathbf{0} & \mathbf{0} & \mathbf{0} & \mathbf{0} & \mathbf{0} \end{bmatrix} \begin{Bmatrix} \hat{\mathbf{t}}_\mathbf{C} \\ \hat{\mathbf{u}}_\mathbf{C}^{(-)} \\ \mathbf{u_D}^{(-)} \\ \hat{\mathbf{t}}_\mathbf{C}^{(-)} \\ \mathbf{f_D}^{(-)} \end{Bmatrix} \tag{5.47}$$

The expression for internal stress $\boldsymbol{\sigma_s}$ (Eq. 5.39) is then updated to account for the fibre's adherence force in the domain term, as follows:

$$\boldsymbol{\sigma_s} = \Big[\mathbf{G'_{SC}}\hat{\mathbf{t}}_\mathbf{C} - \frac{E_2}{E_1+E_2}\Big(\mathbf{H'_{SC}}\hat{\mathbf{u}}_\mathbf{C} + \gamma\mathbf{H'_{SC}}\dot{\hat{\mathbf{u}}}_\mathbf{C} - \gamma\mathbf{G'_{SC}}\dot{\hat{\mathbf{t}}}_\mathbf{C} - \gamma\mathbf{G'_{SF}}\dot{\mathbf{f}}_\mathbf{D}\Big) \\ +\gamma\mathbf{G'_{SF}}\mathbf{f_D} + \frac{\gamma}{\Delta t}\frac{E_2}{E_1+E_2}\boldsymbol{\sigma}_s^{(-)}\Big]\left(1+\frac{\gamma}{\Delta t}\frac{E_2}{E_1+E_2}\right)^{-1} \tag{5.48}$$

5.5 Reinforcements elastoplasticity behaviour modelling in Viscoelastic formulations

The elastoplastic formulation presented in Sec. 4.4 can be straightforward applied to any reinforced viscoelastic formulation that consider the reinforcements behaviour time-independent. Thus, both the Kelvin/Elastic and the Boltzmann/Elastic allow it.

In order to apply the elastoplastic formulation, the coupling system (Eq. 5.42 or Eq. 5.47) must be written in terms of incremental values, since the elastoplastic approach is solved by a Newton-Raphson scheme. Therefore, at a given time step t, the incremental values of all variables present in the system are:

$$\begin{aligned} \boldsymbol{\Delta}\hat{\mathbf{p}}_\mathbf{C} &= \hat{\mathbf{p}}_\mathbf{C}^{t} - \hat{\mathbf{p}}_\mathbf{C}^{t-1} & \boldsymbol{\Delta}\hat{\mathbf{x}}_\mathbf{C} &= \hat{\mathbf{x}}_\mathbf{C}^{t} - \hat{\mathbf{x}}_\mathbf{C}^{t-1} \\ \boldsymbol{\Delta}\hat{\mathbf{u}}_\mathbf{C}^{(-)} &= \hat{\mathbf{u}}_\mathbf{C}^{t-1} - \hat{\mathbf{u}}_\mathbf{C}^{t-2} & \boldsymbol{\Delta}\mathbf{u_D} &= \mathbf{u_D}^{t} - \mathbf{u_D}^{t-1} \\ \boldsymbol{\Delta}\mathbf{u_D}^{(-)} &= \mathbf{u_D}^{t-1} - \mathbf{u_D}^{t-2} & \boldsymbol{\Delta}\mathbf{f_D} &= \mathbf{f_D}^{t} - \mathbf{f_D}^{t-1} \end{aligned} \tag{5.49}$$

The current unknown incremental values $\boldsymbol{\Delta}\mathbf{u_C}$, $\boldsymbol{\Delta}\mathbf{u_D}$ and $\boldsymbol{\Delta}\mathbf{p_D}$ are obtained by applying Eq. 5.49 into the coupling system (Eq. 5.42 or Eq. 5.47). Besides, the unbalanced vector $\mathbf{f_{des}}$ in the Kelvin/Elastic coupling can be calculated as follows:

$$\mathbf{f_{des}} = -\begin{bmatrix} -\mathbf{G_{CF}} \\ -\mathbf{G_{FF}} \\ \mathbf{G_E} \end{bmatrix} \{\mathbf{\Delta f_D}^{corr}\} \tag{5.50}$$

In the Boltzmann/Elastic coupling, the unbalanced vector is given by:

$$\mathbf{f_{des}} = -\begin{bmatrix} -\left(\alpha + \frac{E_1+E_2}{E_2}\right)\mathbf{G_{CF}} \\ -\left(\alpha + \frac{E_1+E_2}{E_2}\right)\mathbf{G_{FF}} \\ \mathbf{G_E} \end{bmatrix} \{\mathbf{\Delta f_D}^{corr}\} \tag{5.51}$$

Thus, an iterative nonlinear problem is solved into a unique load step within each time step of the viscoelastic time marching process. Figure 63 illustrates the marching process scheme, in which t_F is the total number of time steps.

Figure 63 – Marching process scheme during the fibre elastoplasticity process in viscoelastic formulations.

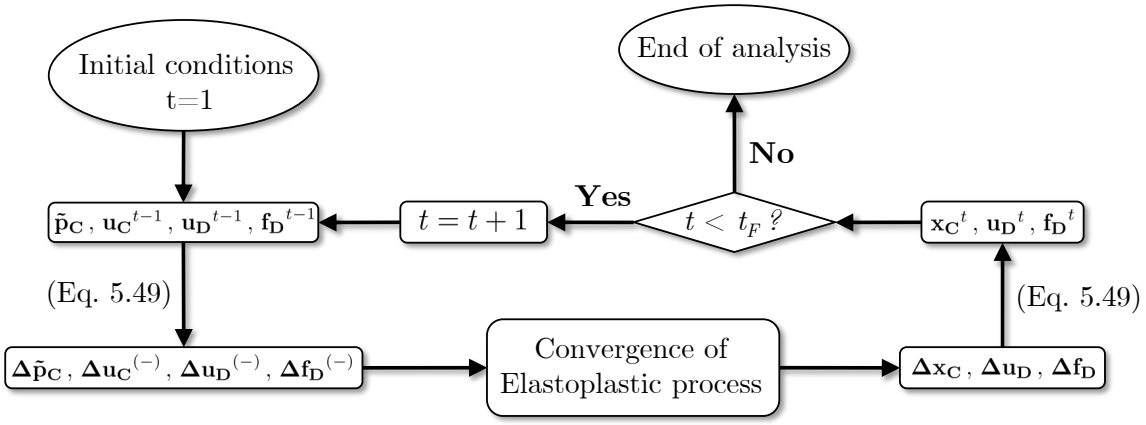

Source: The author.

5.6 Numerical applications of the viscoelastic coupled formulations

This Section presents the numerical applications executed with the proposed viscoelastic formulations. The first application presents a reinforced BEM model, having a pure FEM model from Ansys as reference. The second application validates the nonlinear reinforced viscoelastic IGABEM formulation with pure FEM Ansys model reference results. The third application presents the modelling of a complex 3D model inspired by lifting mechanism structures.

5.6.1 Lagrangian BEM viscoelastic formulation application

This application handles the mechanical analysis of the structure illustrated in Fig. 64. Figure 64(a) illustrates the external geometry and loadings. The structure is reinforced

by two webs of connected fibres, as illustrated in Fig. 64(b). Such reinforcements webs are positioned at domain I, at positions $z = 2.5$ cm and $z = 7.5$ cm. The fibres have been assumed as linear elastic with the following mechanical properties: Young's modulus $E_f = 240$ GPa and cross-section area $A_f = 0.6$ cm^2. Figure 64 illustrates the key points p_i, in which the results will be presented. The time dependent behaviour of the matrix (domains I and II) is governed by the Kelvin-Voigt model with $\gamma_I = 45.454545$ days, $\gamma_{II} = \gamma_I/2$, Young's moduli $E_I = 30$ GPa and $E_{II} = 220$ GPa;

Figure 64 – Nonhomogeneous structure analysed via the Lagrangian viscoelastic BEM. Dimensions in cm.

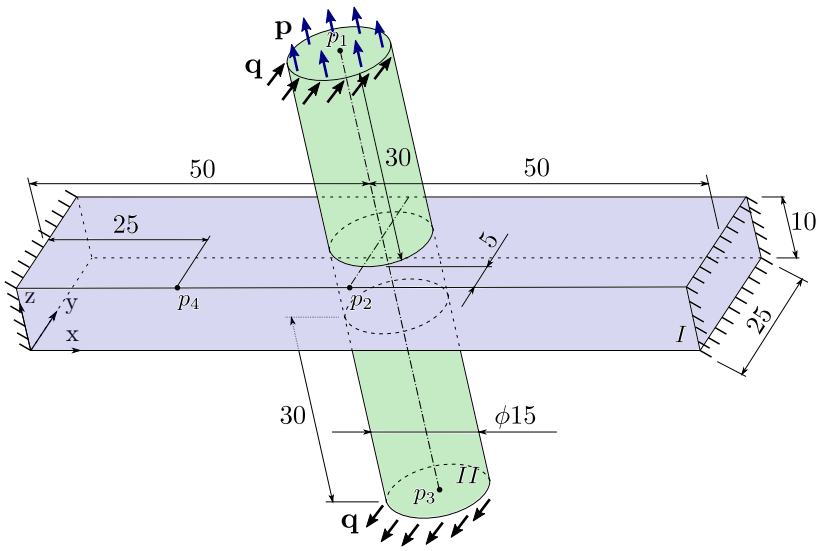

(a) External geometry

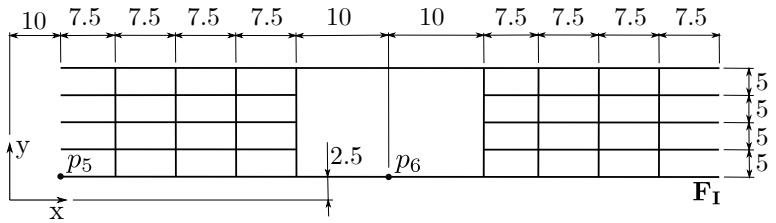

(b) Internal web of fibres

Source: The author.

Only the Lagrangian approximation is applied in this example. The boundary element mesh is composed by 5148 linear quadrilateral elements and 6484 collocation points. Structured mesh discretises the lateral sides of the domain I. The reinforcement's mesh have 352 quadratic elements and 656 nodes. Figure 65 illustrates both boundary and reinforcements mesh in (a) and (b), respectively. An equivalent pure FEM model has been constructed on Ansys, which led to references responses for the scenarios that consider the Kelvin viscoelastic model. The pure FEM model is composed by 82424 solid 20-nodes elements and 1598 link elements, with a total of 153213 nodes. Previous analysis demonstrated mesh convergence for both the pure FEM and 1DBEM/BEM models.

Figure 65 – Boundary mesh (a) and reinforcements mesh (b) of the BEM model for the viscoelastic application.

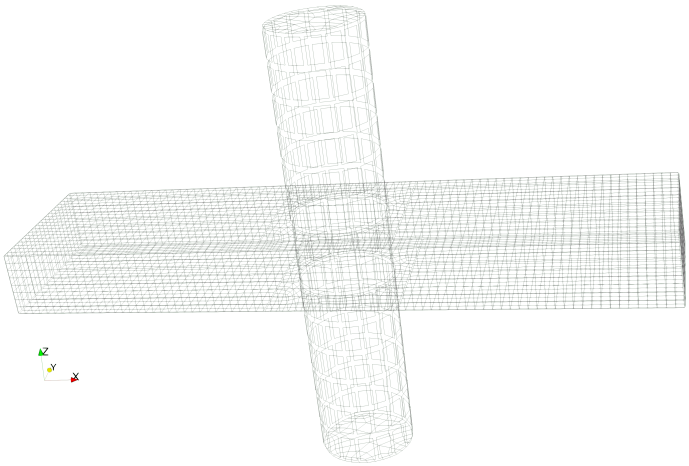

(a)

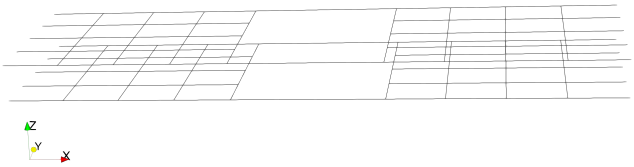

(b)

Source: The author.

The time dependent analysis is set to finish at 200 days with a time step of $\Delta t = 2$ days for both the 1DBEM/BEM and the Ansys analysis. It is worth mentioning that the entire analyses required a computational time of 27 minutes for the 1DBEM/BEM and 33 minutes for the Ansys, approximately.

Figure 66 illustrates the fibres' axial stress results through its variation along the $\mathbf{F_I}$ fibre's length (S_f) at 200 days in (a) and its evolution along time at point p_6 in (b). $\mathbf{F_I}$ is the bottom long fibre illustrated in Fig. 64(b) and p_6 is the maximum stress (in modulus) point among all fibres, also illustrated in the same figure. Both mentioned entities are at the web of fibres at $z = 7.5$ cm.

Figure 66 demonstrates good agreement between the 1DBEM/BEM results ("Kelvin" series) and the reference ("Ansys" series) responses in both (a) and (b). This result demonstrates the accuracy of the proposed formulation. It is worth mentioning the slightly differences among the axial stress values at the fibres ends. Besides, the results have excellent agreement in smooth regions.

The differences of mechanical predictions at the fibre ends have been previously reported in the literature (88, 133, 89, 13). Because of the domain mesh, ANSYS smooths the mechanical predictions at those regions. For sake of clarity, concentrated forces have not been applied at the fibre ends. Thus, the normal force should be nil at those positions.

The 1DBEM/BEM achieves accurately this prediction whereas ANSYS fails on it. This analysis demonstrates that 1DBEM/BEM is superior to the classical pure FEM approach in this particular problem.

Figure 66 – Axial stress results at reinforcements: values over fibre $\mathbf{F_I}$ at time equals to 200 days (a) and evolution along time in point p_6 (b).

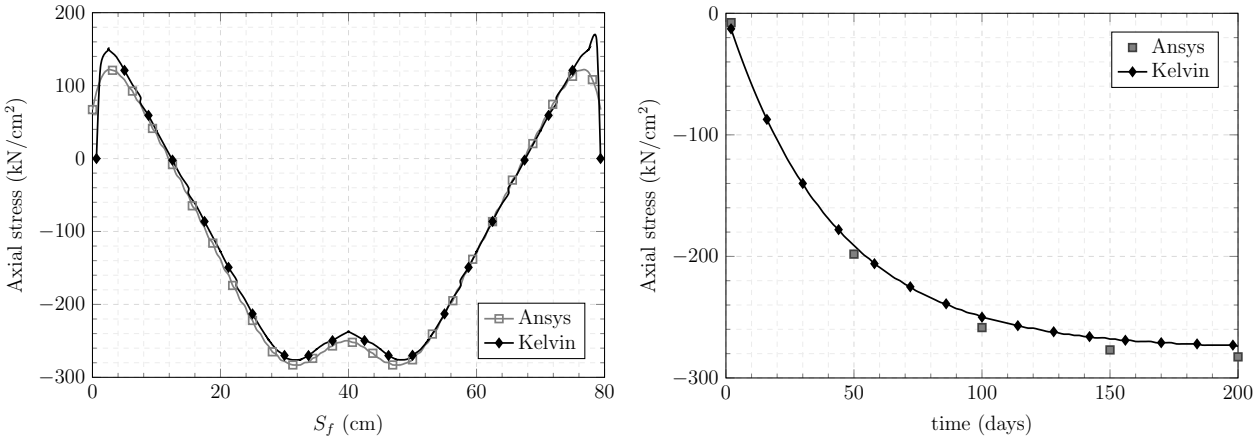

(a) (b)

Source: The author.

Figure 67 illustrates the evolution along time of the boundary displacements (u_X, u_y and u_z) obtained from the 1DBEM/BEM ("Kelvin" series) and the reference ("Ansys" series), at point p_3 in (a) and at point p_4 in (b). This figure illustrates the excellent agreement for boundary displacements, which demonstrates the accuracy of the proposed formulation.

Figure 67 – Boundary displacements evolution along time at points: p_3 (a) and p_4 (b).

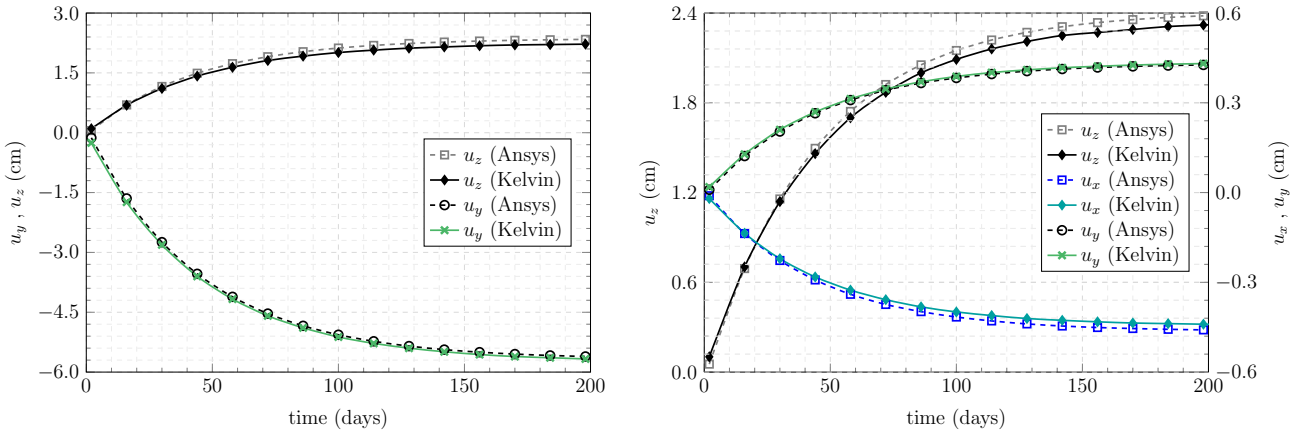

(a) (b)

Source: The author.

Figure 68 illustrates the colour map of displacements along z direction at the final time step obtained via 1DBEM/BEM in (a) and via Ansys in (b). This figure illustrates

the excellent correspondence of the boundary displacement field between the proposed model and the reference. The maximum values have a difference about 1.5%.

The displacements results at the reinforcement's points are in Fig. 69. The results obtained via 1DBEM/BEM ("Kelvin" series) are compared against the Ansys responses. Only the maximum displacements points have been illustrated for each direction: u_x at p_5 in (a), u_y and u_z at p_6 in (b). This figure demonstrates once again good agreement among the responses, which demonstrates the accuracy of the proposed formulation.

Figure 68 – Displacements along z direction at the final time step of the viscoelastic analysis (in cm).

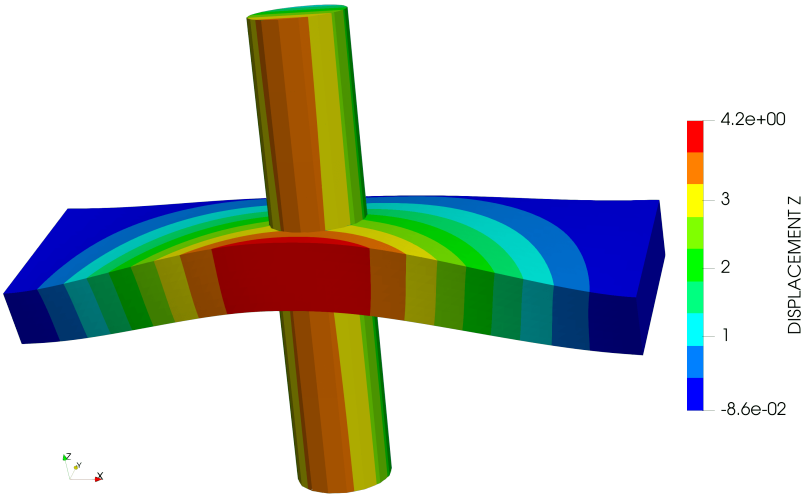

(a) 1DBEM/BEM Kelvin results

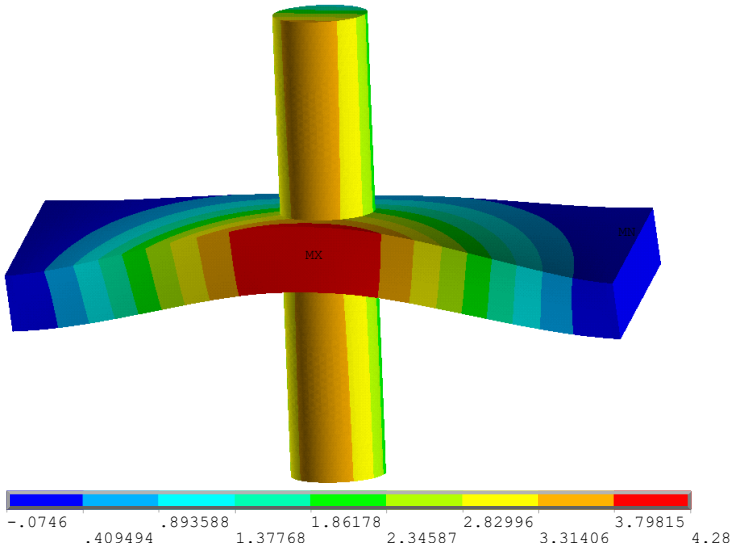

(b) Ansys Kelvin results

Source: The author.

Figure 69 – Reinforcement's displacements evolution along time at points: p_5 (a) and p_6 (b).

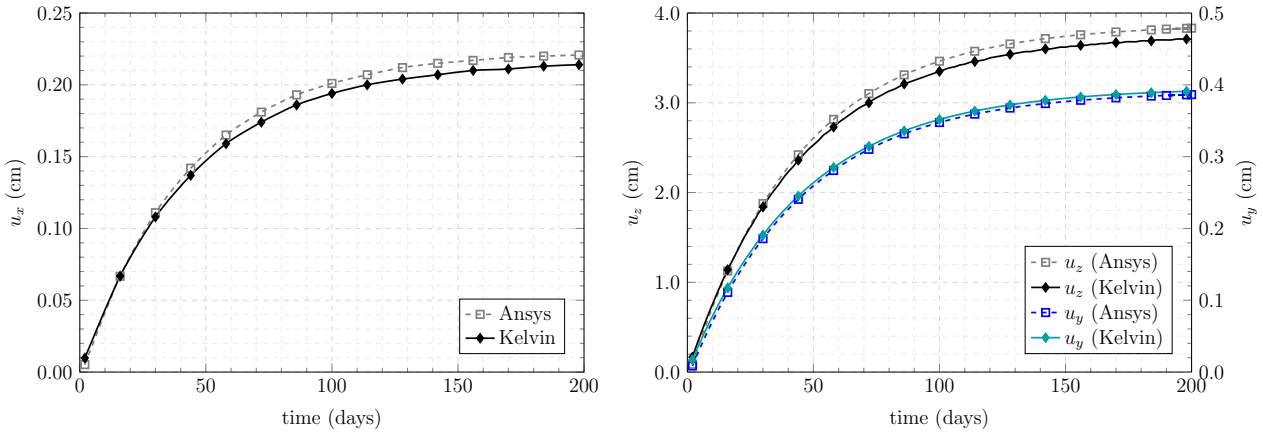

(a) (b)

Source: The author.

5.6.2 Nonlinear viscoelastic application

This application handles the mechanical analysis of the structure illustrated in Fig. 70. Four long fibres reinforce the nonhomogeneous Kelvin-Voigt viscoelastic solid. The fibres cross the interface between material I and II. The fibres account for elastoplastic behaviour, thus, the formulation presented in Sec. 5.5 is applied herein. The material properties of the 3D domains are: Young's modulus $E_I = 600$ kN/cm^2, $E_{II} = 400$ kN/cm^2, Poisson ratios $\nu_I = \nu_{II} = 0.25$ and viscoelastic parameter $\gamma_I = \gamma_{II} = 45.45454545$ days. The fibre properties are: $E_f = 1000$ kN/cm^2, cross-section area $A_f = 0.1$ cm^2, yield stress $\sigma_y = 10$ kN/cm^2 and plastic modulus $K_f^p = 100$ kN/cm^2. The applied load is $\mathbf{p} = 1$ kN/cm^2, which is constant throughout the viscoelastic analysis. This application considers nil initial conditions.

Figure 70 – Structure analysed through the nonlinear viscoelastic formulation: geometry (dimensions in cm) and loads.

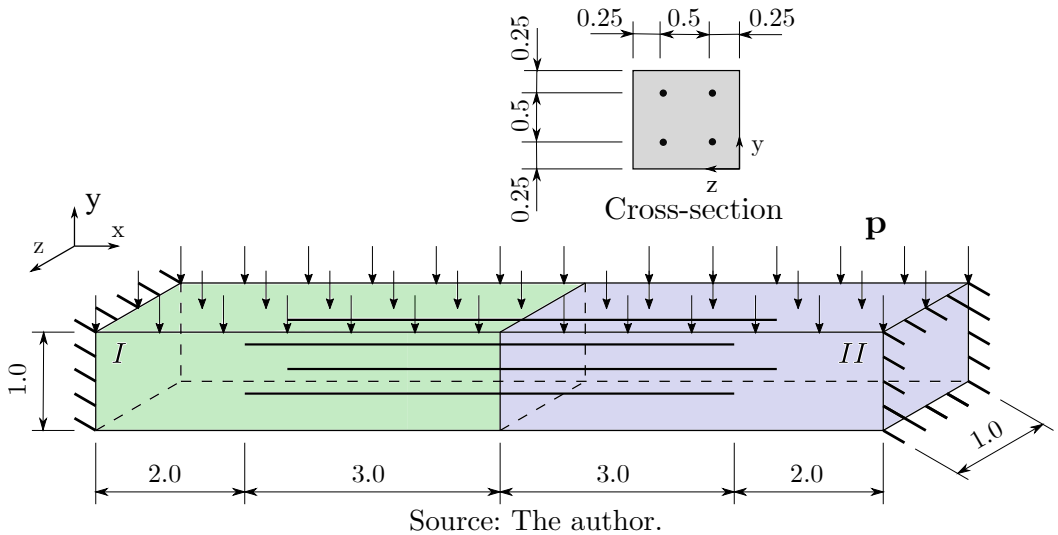

Source: The author.

The viscoelastic analysis is performed within 200 time steps of $\Delta t = 2$ days each, which lead to a total of 400 days. The nonlinear analysis of each time step considers a tolerance for convergence of 10^{-6}. The IGABEM model is composed by 12 bi-quadratic NURBS surfaces ($p = q = 2$). The NURBS surfaces have 16 control points in the solid axial direction (global x) and 5 in the transverse direction (global y and z). The mechanical model results in 780 collocation points. The sub-region interface is composed by a pair of NURBS with coincident position of collocation and control points. The reinforcements mesh is composed by 160 quadratic elements and 328 nodes (40 elements in each long fibre). The crossings between fibres and boundary interfaces enforce the Connection Element presented in Sec. 3.6. Only the Isogeometric approximation is used in this example.

A pure FEM model constructed on *ANSYS*® software is the reference in this application. This model is composed by 40000 solid quadratic elements and 480 link linear elements (trusses), considering the symmetry property of the problem along z direction. *ANSYS*® can represent the Kelvin-Voigt response by considering a dumping behaviour directly proportional to the stiffness with a factor equals to γ. The time step size is $\Delta t = 2$ and the analysis finishes at 200 days. Mesh convergence has been achieved herein, regarding displacements at the boundary and both displacements and stresses at the reinforcements.

Figura 71 illustrates normal stresses and plastic strains at 400 days as a function of the lower-right fibre (positioned at $y = 0.\ 25$, $z = 0.\ 25$ cm) length (S). This figure compares the results obtained by the proposed model (IGABEM) and the reference responses (Ansys).

Figure 71 – Normal stress σ_N and plastic strain ε_{pl} at 400 days along the lower-right fibre length S.

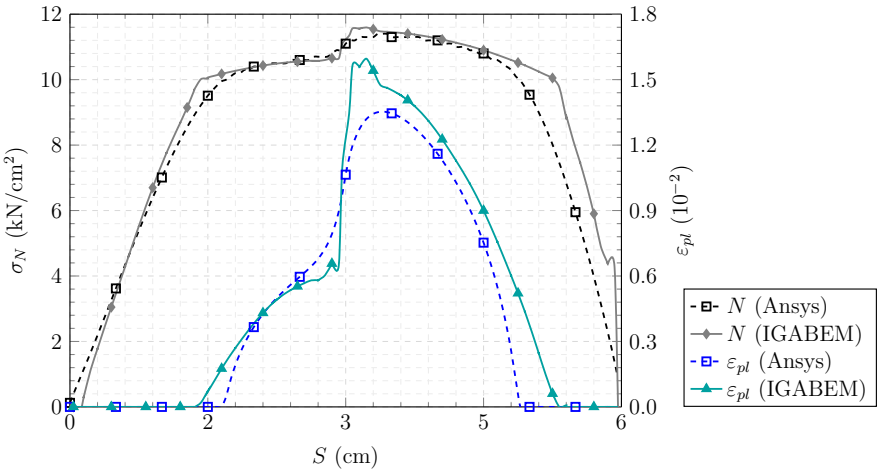

Source: The author.

Figura 71 demonstrates good agreement among the responses. Some minor differences can be observed, although it can be explained by the oscillations in force results, which are prominent in mesh domain methods.

Four points (p_1, p_2, p_3 and p_4) illustrate the evolution of mechanical responses along time. Figura 72 illustrates the points' positions. p_1, p_2, p_3 and p_4 are lower-right fibre points, in which p_3 is the centre point (on the sub-regions interface), p_1 is positioned in the fibre's region within I and p_2 is positioned in the region within II. p_4 is a internal point at the sub-region I.

Figure 72 – Selected points p_i in the structure for the analysis of mechanical results along time.

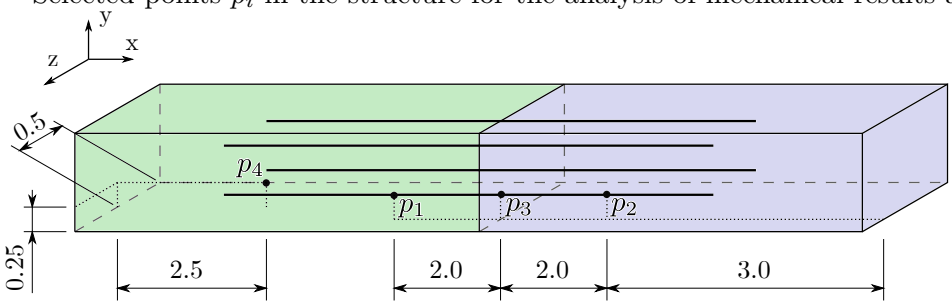

Source: The author.

Figures 73(a) and 73(b) illustrate the normal force N and plastic strain ε_{pl} evolution along time at p_1 and p_2 points, respectively. These figures show a good agreement between the proposed model results (IGABEM) and the reference (Ansys) in both points. Furthermore, one clearly observes the hardening behaviour in the N evolution at the time corresponding to the plastic strain evolution start. This behaviour can be explained by the reinforcements material constitutive law, which exhibits an isotropic hardening after the elastic limit.

Figure 73 – Evolution of normal force N and plastic strain ε_{pl} along time at p_1 (a) and p_2 (b).

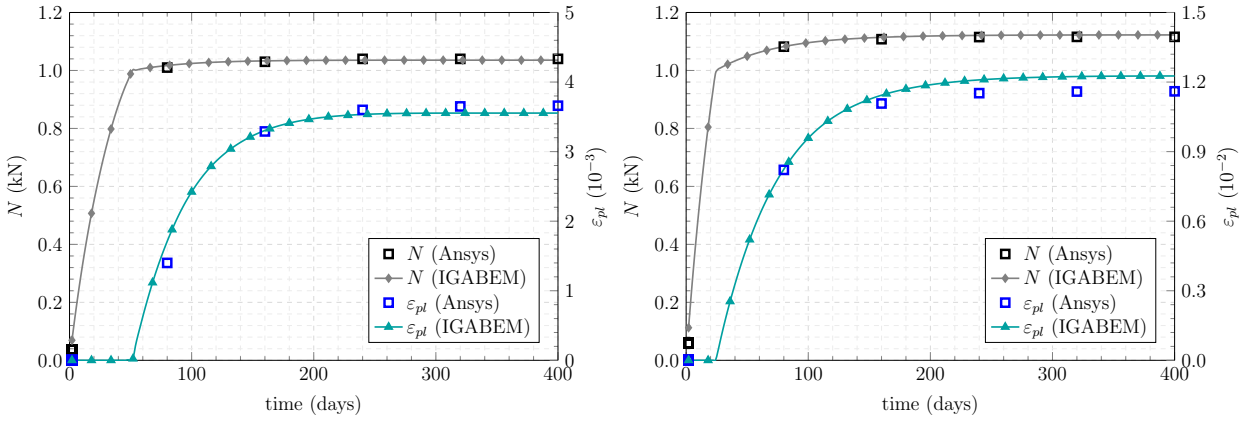

(a) (b)

Figure 74 exhibits the displacements results (in y and z directions) at p_3, which corresponds to the fibres maximum displacements point. One observes excellent agreement of these results regarding the reference. The displacements follow the characteristic Kelvin-Voigt behaviour, despite their pure elastic and time independent mechanical behaviour. This response has been observed because the fibre mechanical response depends directly on the matrix response, since all the external loads are applied at the structural boundary.

Figure 75 illustrates the displacements results (in x and y directions) at the internal point p_4. The analysis of this figure enables similar conclusions as performed for the responses in Fig. 74. Then, it illustrates the excellent accuracy and performance of IGABEM approach.

Figure 74 – Displacements in y and z directions at p_3 along time.

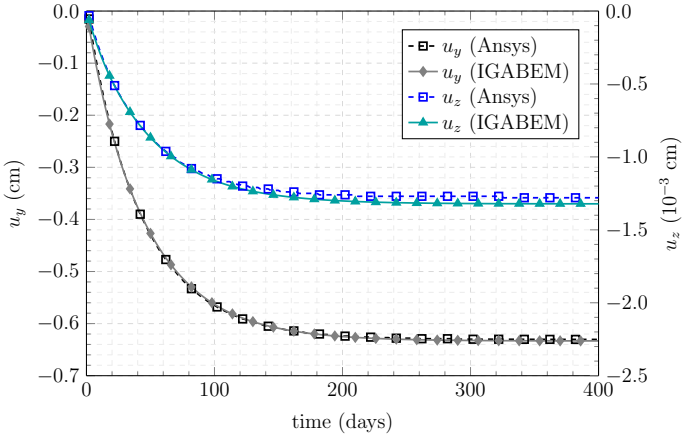

Source: The author.

Figure 75 – Displacements in x and y directions at p_4 along time.

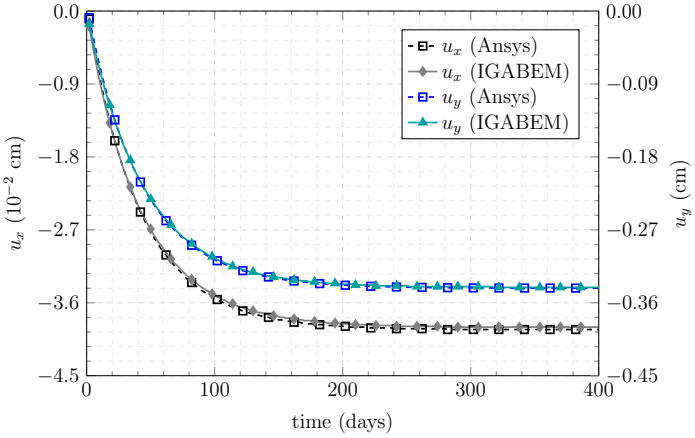

Source: The author.

Figura 76 exhibits the colour map of displacements at 400 days over the boundary. This figure illustrates the results from the proposed model (a) and the reference responses (b) through the magnitude of the displacements vector $\{u_x\,, u_y\,, u_z\}^\intercal$. Besides, the structure deformed shape considers real scale. Figura 76 demonstrates the accuracy of the proposed model. The displacements field distribution over the boundary is accurate considering the reference and the maximum difference is lower than 0.7%.

It is worth emphasising the computational efficiency of the proposed formulation. The number of degrees of freedom is considerably low (4308) and the computational time consuming is about 2 minutes. Considering the complexity of the problem (nonlinear and time discretised) and the accuracy of the obtained results, the computational performance can be considered excellent.

Figure 76 – Magnitude of displacements (in cm) at 400 days over the boundary results.

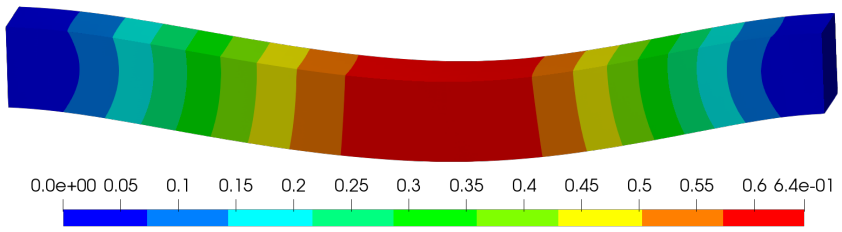

(a) IGABEM

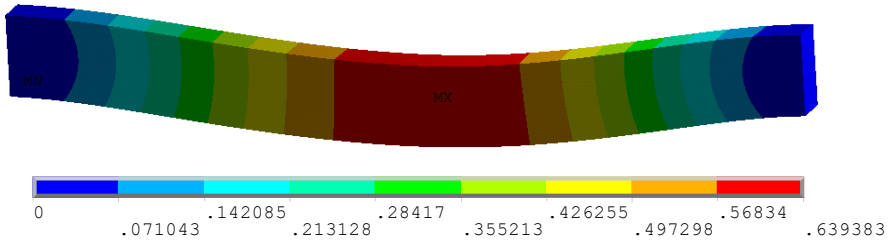

(b) Reference (Ansys)

Source: The author.

5.6.3 IGABEM viscoelastic formulation application

This application handles the mechanical analysis of the structure illustrated in Fig. 77. The 3D geometry has been inspired in lifting mechanism structures and it is composed by a hook (sub-domain II) and a pad eye (sub-domain I). Long fibres reinforce the sub-domain I as illustrated in Fig. 78. All reinforcing bars have circular cross-sections of radius equal to 0. 3 cm (grey coloured fibres in Fig. 78) or 0. 6 cm (black coloured fibres). This application considers nil initial conditions. The applied loads are $\mathbf{q_x} = 2$ kN/cm^2 and $\mathbf{q_z} = 2$ kN/cm^2.

This application considers five distinct scenarios, which cover the coupling of different constitutive laws (models) of matrix and fibres as presented in Secs. 5.4.1, 5.4.2 and 5.4.3. Tabela 1 details such scenarios. The viscoelastic parameter γ equals 45. 45454545 days, all Young's moduli are written in GPa and the fibres Young's modulus is $E_f = 200$ GPa in all scenarios.

Scenario	**Domains Models**	**Sub-region I**			**Sub-region II**			**Fibres**	
		E_I	γ_I	$(E_B)_I$	E_{II}	γ_{II}	$(E_B)_{II}$	Model	γ_f
Elastic	Elastic	40	-	-	220	-	-	Elastic	-
ke	Kelvin	40	γ	-	220	γ	-	Elastic	-
kv_1	Kelvin	40	γ	-	220	γ	-	Kelvin	γ
kv_2	Kelvin	40	γ	-	220	γ	-	Kelvin	2γ
be_1	Boltzmann	120	γ	60	371. 25	γ	540	Elastic	-
be_2	Boltzmann	72	γ	90	300	γ	825	Elastic	-

Table 1 – Different scenarios considered for the viscoelastic analyses.

Figure 77 – Structure analysed in Application 5: isometric view and detailed view of each sub-region I and II. Dimensions in cm.

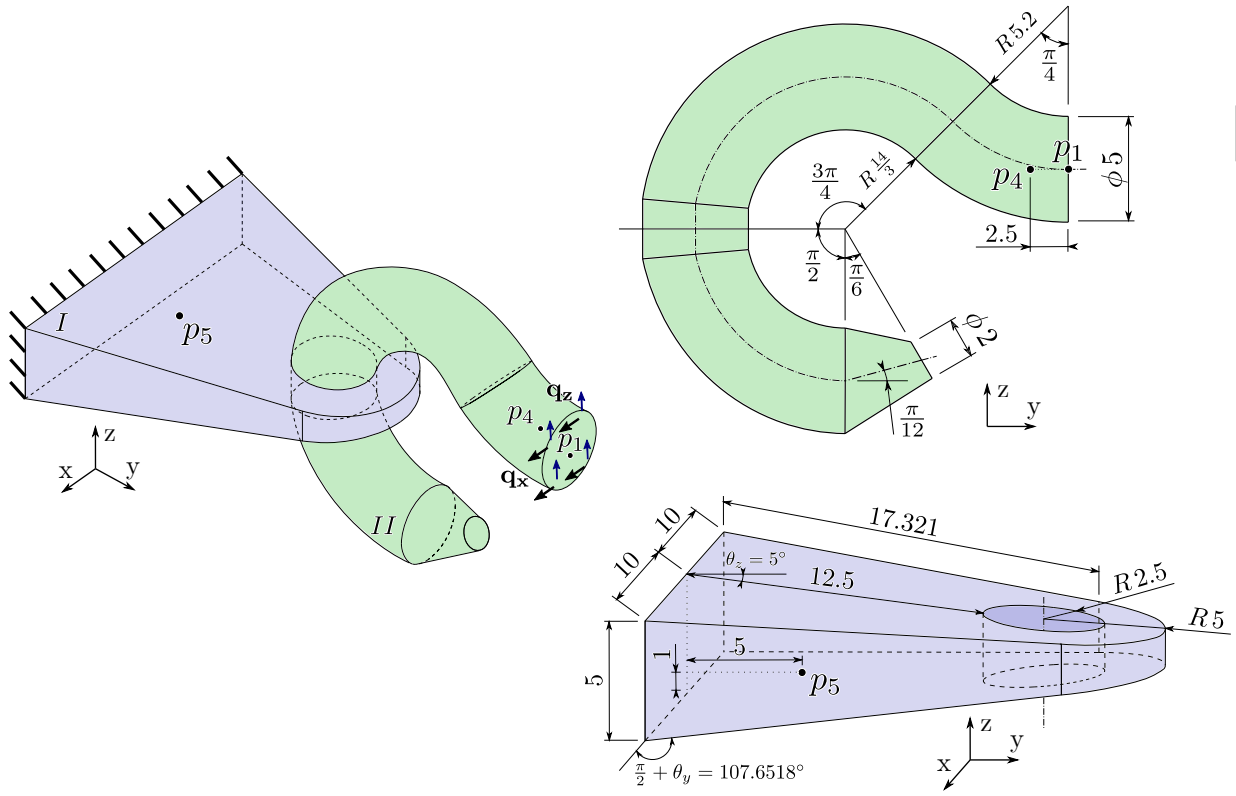

Source: The author.

All scenarios presented upon Tabela 1 have the same global stiffness. To achieve this condition, the resulting stiffness in Boltzmann models (Young's modulus in series with Boltzmann modulus) should be equivalent to the Young's modulus in Kelvin-Voigt models for both sub-regions. Thus, the mechanical response at the viscoelastic analysis end should be the same in all scenarios.

Only the IGABEM formulation is applied for this example. The isogeometric model is composed by 45 regular NURBS surfaces with bi-quadratic basis functions. The geometrically exact model has 429 collocation points. However, this model has been refined through knots insertion for obtaining convergence of the mechanical fields representation. This technique adds knots and control points, without changing the NURBS surfaces geometry (16). The knots insertion is uniform over all surfaces leading to the four different meshes:

- M0: 429 collocation points in the IGABEM model and 216 reinforcement elements (452 nodes) over the fibres, with approximate length equals to 1. 2 cm each one;
- M1: 989 collocation points in the IGABEM model and 324 reinforcement elements (668 nodes) over the fibres, with approximate length equals to 0. 8 cm each one;
- M2: 3157 collocation points in the IGABEM model and 652 reinforcement elements

Figure 78 – Detailed views of the reinforcing long fibres within sub-region I, considering symmetry in x direction. Dimensions in cm.

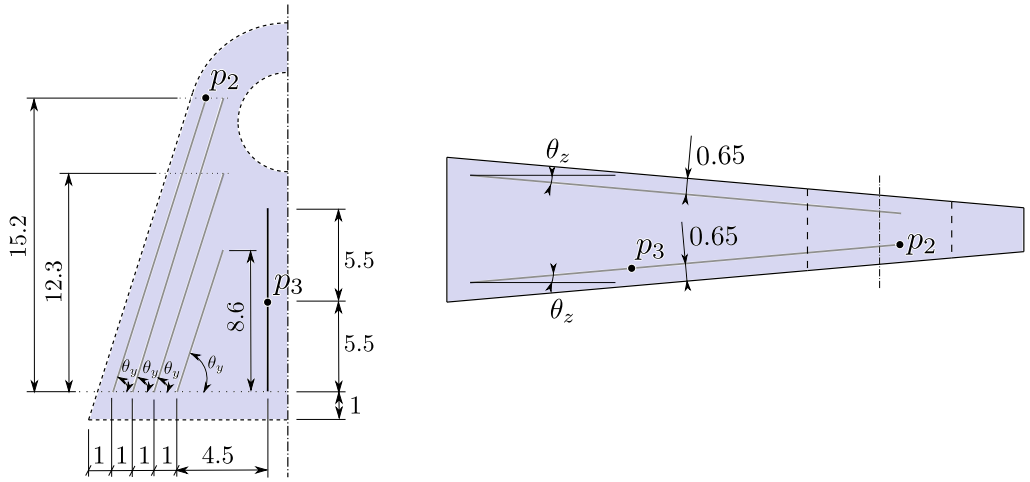

Source: The author.

(1324 nodes) over the fibres, with approximate length equals to 0. 4 cm each one;

- M3: 11165 collocation points in the IGABEM model and 1300 reinforcement elements (2620 nodes) over the fibres, with approximate length equals to 0. 2 cm each one.

in which the reinforcements mesh has been refined simultaneously. All reinforcement elements are quadratic.

Figure 79(a) exhibits the convergence of the displacements magnitude at p_1 (point over the boundary of II) and p_2 (point over the fibres). Figure 79(b) shows the convergence of normal force N at p_3 (over the fibres). These analyses consider the Elastic scenario, therefore the results are time independent. All p_i positions can be found in Figs. 77 and 78.

Figure 79 – Mesh convergence results regarding displacements magnitude at p_1 and p_2 (a) and fibre normal force N (b), as a function of the total amount of nodes in the mesh n_p.

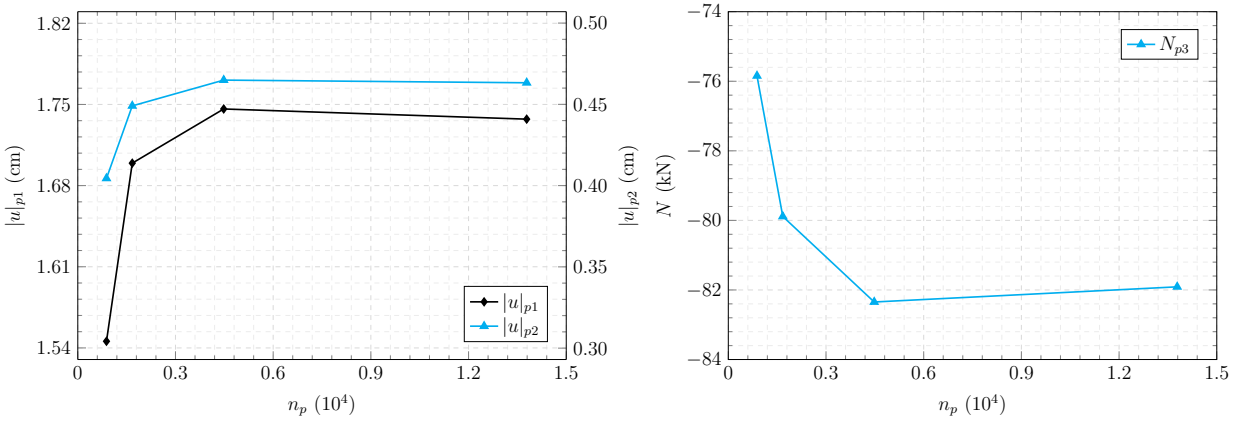

(a) (b)

Source: The author.

Mesh M2 handles the mechanical analysis of this problem because of the convergence

results. The difference considering the most refined mesh is 0. 51% in displacements and 0. 53% in fibre normal forces. Figure 80 illustrates M0 and M2 meshes.

Figure 80 – Collocation point meshes: obtained directly from CAD geometric model (a) and refined for the mechanical fields representation with knot insertion (b).

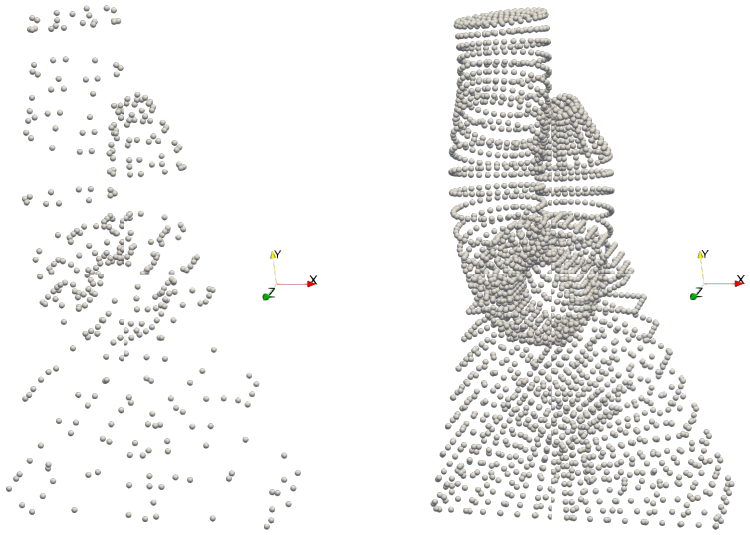

(a) M0 (b) M2

Source: The author.

The time dependent analyses are performed with M2 mesh, considering 150 time steps of $\Delta t = 2$ days and a total analysis time of 300 days. The time increment value Δt leads to convergent responses. The internal point p_4 and the fibre point p_2 illustrate the displacement results along time, considering the five scenarios. Figura 81 illustrates the displacements magnitude at p_4 in (a) and p_2 in (b).

Figure 81 – Displacements magnitude $|u|$ in cm at p_4 (a) and p_2 (b) along time, considering all different scenarios.

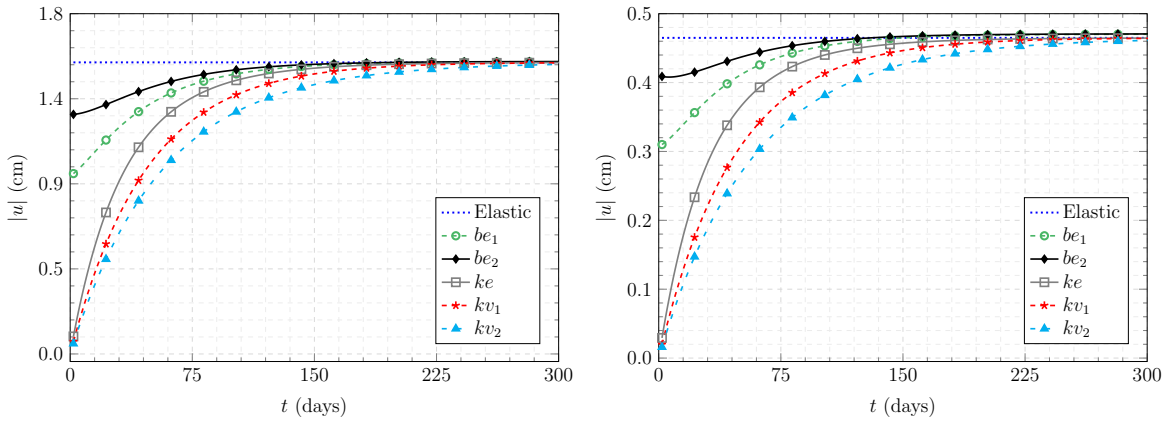

(a) (b)

Source: The author.

Figure 81 illustrates the comparison of the different scenarios responses. All displacements have an asymptotic behaviour, which tends to the elastic response at the

time analysis end. This behaviour is expected in the rheological models because the dashpot element influence tends to zero along time and all scenarios have equal global stiffness. On the other hand, one observes the difference between Boltzmann and Kelvin scenarios, consisting of the immediate response, as expected (54). Besides, the increase in Boltzmann modulus from be_1 to be_2 results in more pronounced immediate displacements. Regarding Kelvin scenarios, one observes the initial displacements velocity following the order $ke > kv_1 > kv_2$, as a result of the reinforcements time dependency, which follows an inverse order ($kv_2 > kv_1 > ke$). Thus, the initial displacements velocity is inversely proportional to the time dependent mechanical behaviour of reinforcements.

The internal point p_3 and the long fibre centre point p_5 illustrate the stress results. These points enable the analysis of stress transfer between fibre and matrix along time. Stress results at p_5 account for von Mises stress (σ_{VM}) in its total (tot), elastic (el) and viscous (v) portions. Normal force (N) results at p_3 also present elastic (el) and viscous (v) portions when viscoelastic behaviour is accounted in the fibres. Figura 82 exhibits these results considering ke scenario, whereas Figura 83 illustrates the kv_1 scenario results and Figura 84 accounts for kv_2 scenario.

Figure 82 – von Mises stress σ_{VM} at the internal point p_5 (a) and normal forces N at p_3 along time, considering ke scenario. (el) refers to the elastic portion, (v) refers to the viscous portion, (tot) is the total value and "Elastic" is the result obtained by the linear time-independent model.

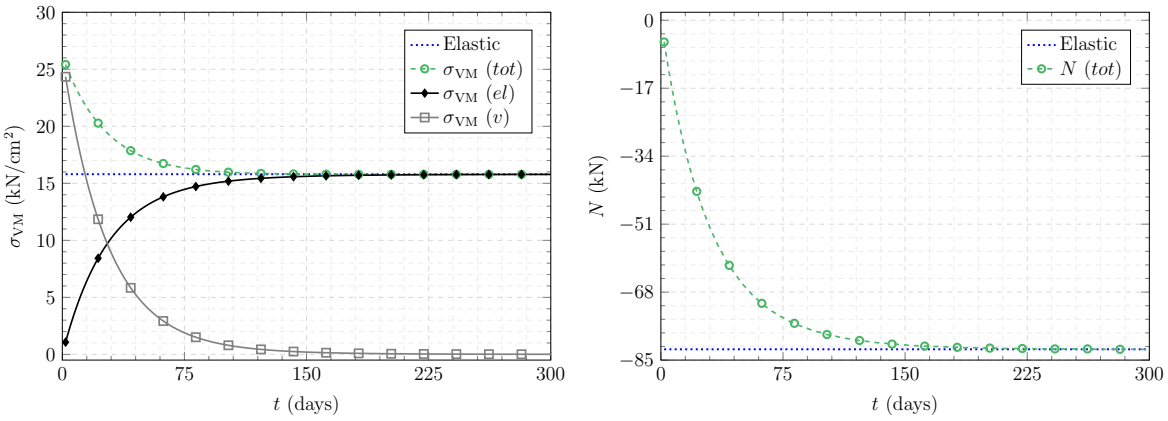

(a) (b)

Source: The author.

One observes the domain total stress results (σ_{VM} (tot)) decreasing along time in Figura 82 whereas the total fibre normal force N (tot) increases in modulus. Thus, the stress transfer occurs from domain to fibres, which is a characteristic of Kelvin-Voigt domains reinforced by elastic fibres, as well as ke scenario. This behaviour can be explained by the lack of viscous response in the reinforcements, in which the N (tot) follows the evolution of the Kelvin-Voigt elastic portion. This situation leads to the relaxation in the domain (matrix) regions near the fibres, which is usually observed in many reinforced

materials.

Figure 83 – von Mises stress σ_{VM} at p_5 (a) and normal forces N at p_3 along time, considering kv_1 scenario. (el) refers to the elastic portion, (v) refers to the viscous portion, (tot) is the total value and "Elastic" is the result obtained by the linear time-independent model.

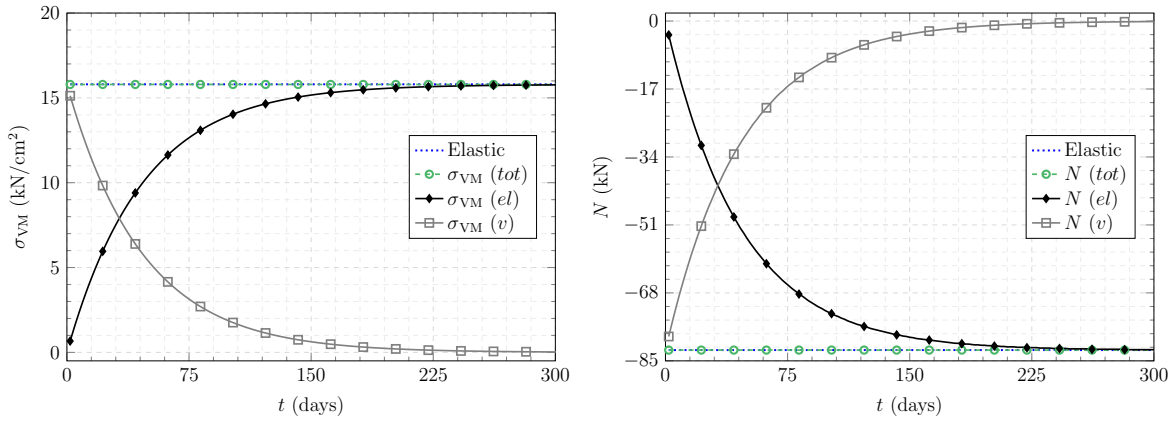

(a) (b)

Source: The author.

Figure 84 – von Mises stress σ_{VM} at p_5 (a) and normal forces N in p_3 along time, considering kv_2 scenario. (el) refers to the elastic portion, (v) refers to the viscous portion, (tot) is the total value and "Elastic" is the result obtained by the linear time-independent model.

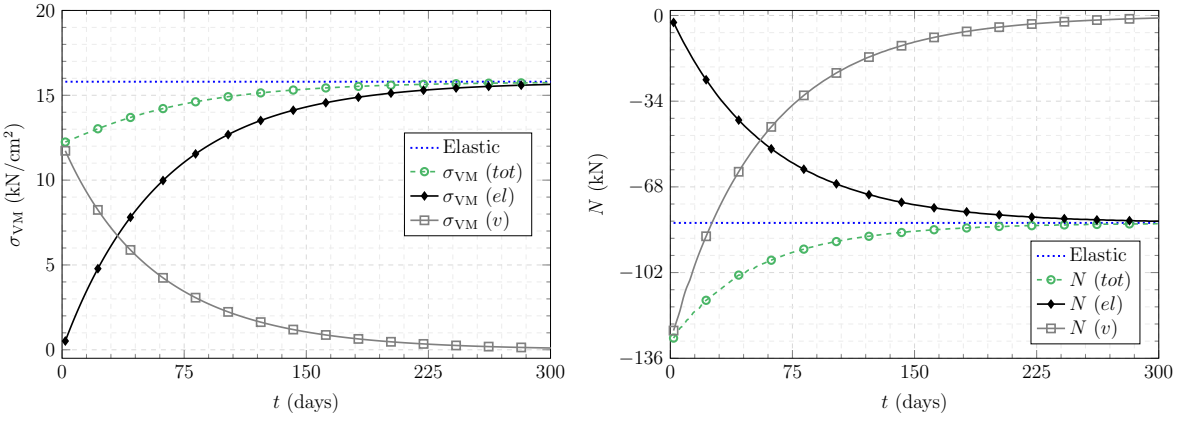

(a) (b)

Source: The author.

The relaxation behaviour is not observed in Figura 83 because both materials (domain and fibres) present the same time dependent behaviour in kv_1 scenario. This scenario results in constant total stresses in both domain and fibres. Besides, the reinforcements results are also divided into elastic and viscous portions as well as the domain stress.

One observes the opposite behaviour of Fig. 82 in Fig. 84. The relaxation occurs in the fibre and stiffening is observed in the domain. The higher fibres viscoelastic parameter ($\gamma_f = 2\gamma$) in kv_2 scenario explain this behaviour. Then, one observes higher contribution of

the viscous portion in the fibres response and stress transfer from fibre to domain (opposite of *ke* scenario).

Besides, Figs. 82, 83 and 84 demonstrated that all mechanical time dependent results tend to the elastic response along time, as expected. These figures demonstrate the robustness of the proposed time dependent formulations, which allow for representing several mechanical behaviours and different constitutive laws for both matrix and reinforcements.

Figures 85, 86 and 87 illustrate the colour map of displacement over the boundary obtained after 300 days in x, y and z directions, respectively. These results are equal at the analysis end for all scenarios, as above-mentioned. The structure deformed shape considers a magnification factor equals 5.

Figure 85 – Colour map of displacements (in cm) along x direction (u_x) over the boundary obtained at the end of the viscoelastic analysis.

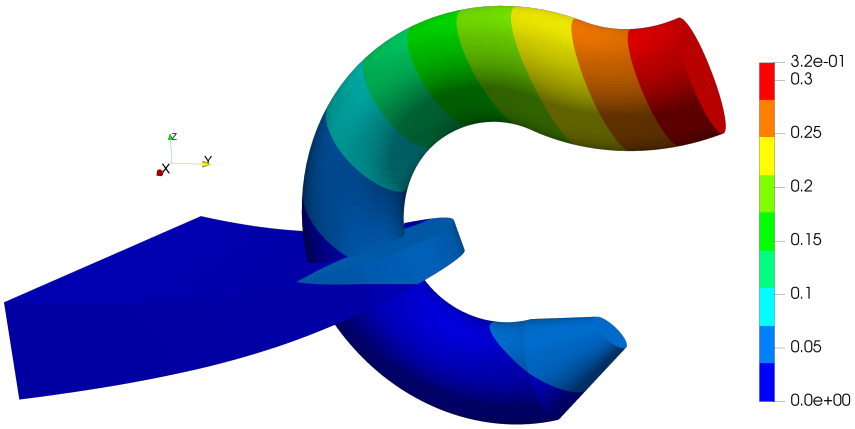

Source: The author.

Figure 86 – Colour map of displacements (in cm) along y direction (u_y) over the boundary obtained at the end of the viscoelastic analysis.

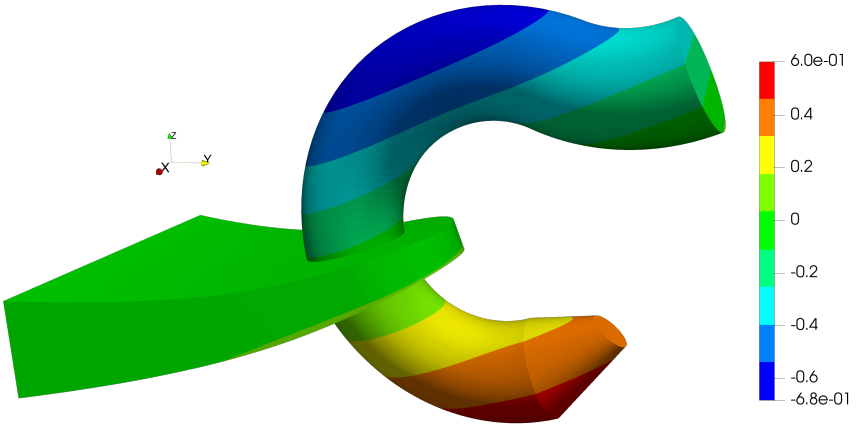

Source: The author.

One observes the coherence of the obtained results in Figs. 85, 86 and 87, considering the applied loads over the structure (Figura 77). All obtained displacements are nil over

Figure 87 – Colour map of displacements (in cm) along z direction (u_z) over the boundary obtained at the end of the viscoelastic analysis.

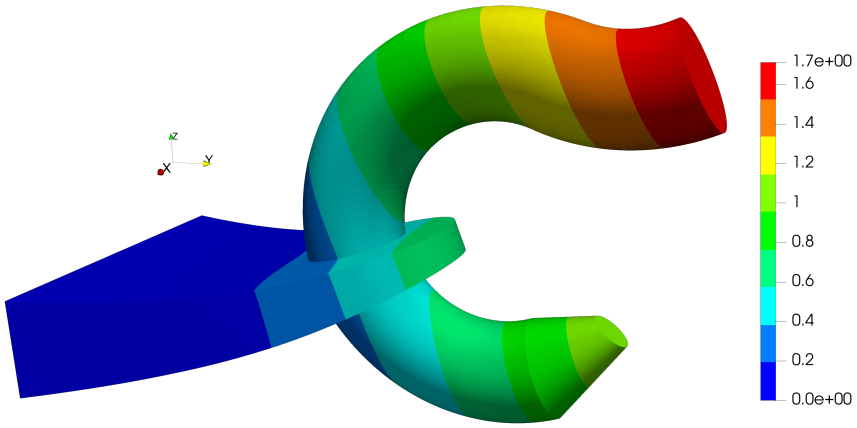

Source: The author.

the fixed surface. The circumferential surface in which $\mathbf{q_x}$ and $\mathbf{q_z}$ are applied exhibited the u_x and u_z maximum values. Besides, these values follow the correct orientation of the applied loads.

Figures 88 and 89 illustrate the colour maps of fibres displacements magnitudes and normal forces obtained after 300 days, respectively. The structure deformed shape considers a magnification factor of 5.

Figure 88 – Colour map of displacements magnitude (in cm) over the fibres obtained at the end of the viscoelastic analysis.

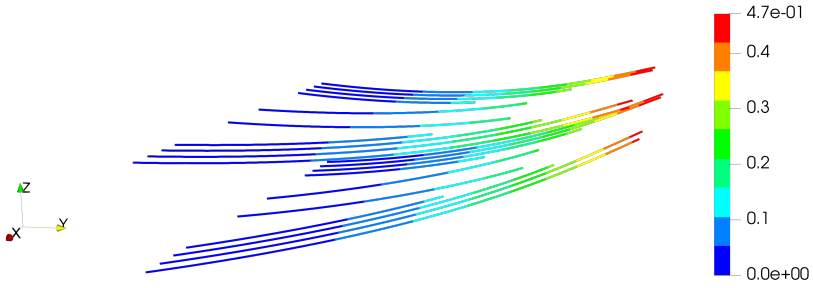

Source: The author.

Figures 88 and 89 also exhibit coherent results. Fibre displacements are in agreement with the boundary displacements over material I, in which the fibres are embedded. Furthermore, the upper layer of fibres shows compression, whereas the lower layer shows tension. The predominant bending stress in the fibres region explains this behaviour, which is consistent with the applied load (Fig. 77).

The above-presented discussions indicate that all performed mechanical analyses led to coherent results and in agreement with the expected behaviours. Besides, it is worth mentioning that the computational time consuming was approximately 13 minutes in the elastic scenario and 20 minutes in the time dependent scenarios. These performances

demonstrate the computational efficiency of the proposed formulations.

Figure 89 – Colour map of normal force (in kN) over the fibres obtained at the end of the viscoelastic analysis.

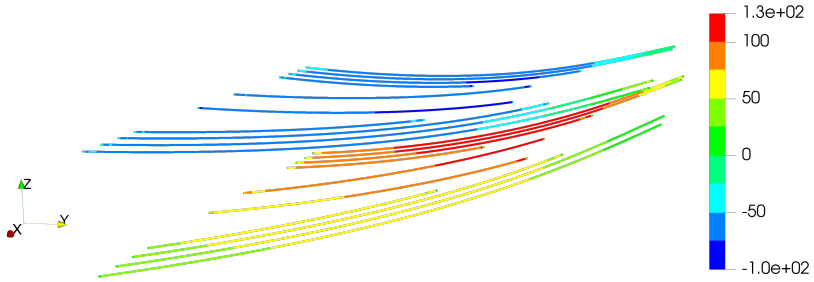

Source: The author.

6

Nonlinear fracture mechanics via the IGABEM

In this study, cracked 3D solids are represented by the nonlinear fracture mechanics via the IGABEM. Nonlinear cracked are modelled at sub-regions interfaces of the IGABEM as cohesive fractures, via different cohesive laws. Additionally, the viscous behaviour of the cohesive crack according to different loading rates is studied. This chapter presents the literature review on the topic, the developed formulations and numerical applications.

6.1 Fracture mechanics for quasi-brittle materials

]The mechanical failure of quasi-brittle materials has been characterised by the nonlinear dissipation phenomena at the so-called fracture process zone (FPZ). This zone is small in comparison with the crack length in purely brittle materials, which lead to the linear elastic fracture mechanics (LEFM). Therefore, in LEFM, these nonlinear phenomena can be disregarded. However, the FPZ is not small enough in quasi-brittle materials, which triggers nonlinear effects that must be accounted for the accurate mechanical modelling (148).

In this context, there are two mechanics of energy dissipation at the FPZ: the energy necessary to form new crack faces (analogous to LEFM) and the energy necessary to beat the material's residual resistance. Two different approaches may model such phenomenon: the equivalent elastic crack and the fictitious crack.

The equivalent elastic crack applies Griffith energy criteria and the entire crack energy is used to form new crack faces. Therefore, the second dissipation mechanics is neglected and the crack propagation may follow LEFM models. The equivalent elastic crack's length is defined by material parameters (149, 150). On the other hand, the fictitious

crack approach considers a major role of the energy portion related to the material's residual resistance (151, 152).

This study applies a fictitious crack approach based on the model proposed by Hillerborg, Modéer and Petersson (2). In this approach, the FPZ is represented by a fictitious crack ahead of the real crack, under the influence of cohesive forces, as illustrated in Fig. 90. Such forces as represented as a function of the Crack Opening Displacement (COD) and material's parameters, such as fracture energy G_σ and traction strength f_T. The relation between these physical quantities is called cohesive law. The fictitious crack growth initiates at the critical COD point (COD_c) and goes on until the observed cohesive force matches the f_T.

Figure 90 – Illustration of the fictitious crack model proposed by (2).

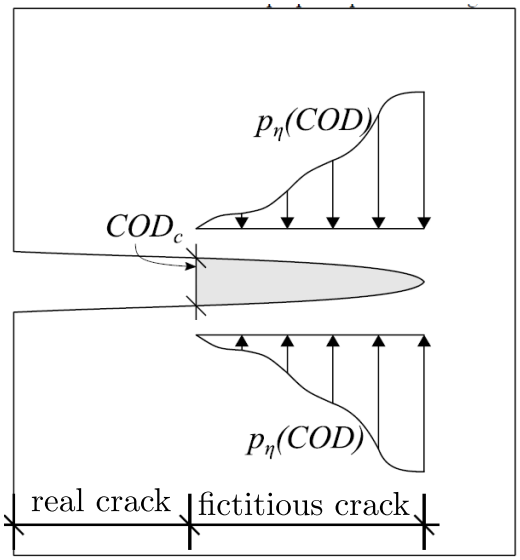

Source: The author.

It is worth mentioning that the fictitious crack model leads to non-singularities at the crack tip (as opposed to the LEFM). The energy responsible for removing cohesive forces from the fictitious crack can be calculated as follows:

$$G_\sigma = \int_0^{COD_c} p_\eta(COD) dCOD \tag{6.1}$$

in which $p_\eta(COD)$ is the cohesive law. This function may be written in different forms to represent different mechanical behaviours observed in real-life materials. This study deals with three cohesive laws: linear, bilinear and exponential.

It is worth mentioning that the adherence force's axial component is preponderant in the crack growth process, since the required energy to propagate in mode II is proven to be 20 - 25 times higher in comparison to the mode I (153). Then, the variation of tangential cohesive forces can be neglected. Hence, this work considers the tangential crack forces to be constant until the COD achieves the critical value COD_c.

6.1.1 The linear cohesive law

The linear cohesive law is the simplest model. It considers a linear variation of the cohesive forces along the COD, achieving zero at the COD_c as illus ted in Fig. 91. The area bellow the curve matches G_σ and the cohesive law can be written as:

$$p_\eta(COD) = \begin{cases} f_T(1 - \dfrac{COD}{COD_c}) & \text{for } 0 \leq COD \leq COD_c \\ 0 & \text{for } COD > COD_c \end{cases} \tag{6.2}$$

Figure 91 – Cohesive linear law

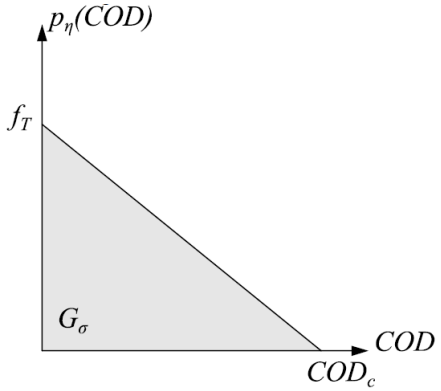

Source: Rocha, 2020 (63)

The critical value COD_c can be determined from the area bellow the curve and it is as follows:

$$COD_c = \frac{2G_\sigma}{f_T} \tag{6.3}$$

6.1.2 The bilinear cohesive law

The bilinear cohesive law can be understood as a piecewise linear function, which has a change in inclination at the crack opening value COD^*, f_T^* as illustrated in Fig. 92.

Considering the area bellow the curve as equal G_σ, one can easily find the parameter values:

$$\begin{aligned} f_T^* &= \frac{f_T}{3} \\ COD^* &= 0.8\frac{G_\sigma}{f_T} \\ COD_c &= 3.6\frac{G_\sigma}{f_T} \end{aligned} \tag{6.4}$$

Then, the expression for the bilinear law is as follows:

Figure 92 – Cohesive bilinear law

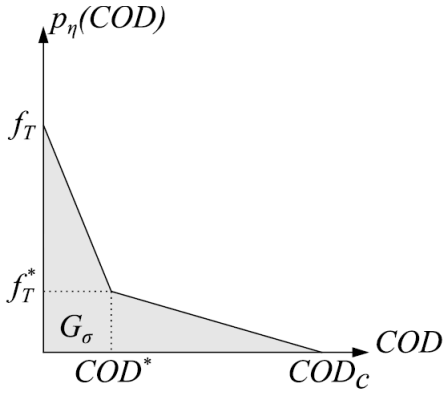

Source: Rocha, 2020 (63)

$$p_\eta(COD) = \begin{cases} f_T - \left(\frac{f_T - f_T^*}{COD^*}\right) COD & \text{for } 0 \leq COD \leq COD^* \\ \frac{f_T^* COD}{COD^* - COD_c} + f_T^* \left(1 - \frac{COD^*}{COD^* - COD_c}\right) & \text{for } COD^* \leq COD \leq COD_c \\ 0 & \text{for } COD > COD_c \end{cases} \quad (6.5)$$

6.1.3 The exponential cohesive law

The exponential cohesive law can considers a nonlinear exponential relation between COD and adherence force (as illustrated in Fig. 93) and can be written as follows:

$$p_\eta(COD) = f_T e^{-\frac{f_T}{G_\sigma} COD} \quad (6.6)$$

Figure 93 – Exponential bilinear law

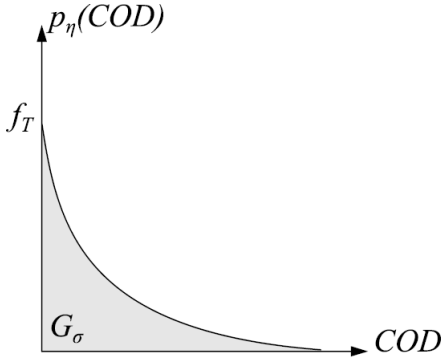

Source: Rocha, 2020 (63)

It is worth pointing that the simplification applied for tangential cohesive forces above-mentioned cannot be adequately considered with the tangential law, since it does not presents a value of COD_c. In such case, the tangential forces are assumed to be null when $p_\eta(COD)$ achieves 1% of f_T.

6.2 IGABEM formulation for the nonlinear crack growth

The fictitious crack approach of Hillerborg, Modéer and Petersson (2) is applied herein in the context of the 3D IGABEM coupled with the sub-region technique. In such case, the crack propagation patch follows the sub-region interface NURBS surfaces. Then, the propagation patch must be previously known in order to correctly build the geometrical model, which is relatively common in the context of laboratory tests.

As presented in Sec. 2.7, the IGABEM algebraic equation must be splitted into the sub-regions k_1 and k_2:

$$\begin{bmatrix} \mathbf{H}^B_{k_1} & \mathbf{H}^I_{k_1} & \mathbf{0} \\ \mathbf{0} & \mathbf{H}^I_{k_2} & \mathbf{H}^B_{k_2} \end{bmatrix} \begin{Bmatrix} \hat{\mathbf{u}}^B_{k_1} \\ \hat{\mathbf{u}}^I_{k_1} \\ \hat{\mathbf{u}}^B_{k_2} \end{Bmatrix} = \begin{bmatrix} \mathbf{G}^B_{k_1} & \mathbf{G}^I_{k_1} & \mathbf{0} \\ \mathbf{0} & \mathbf{G}^I_{k_2} & \mathbf{G}^B_{k_2} \end{bmatrix} \begin{Bmatrix} \hat{\mathbf{t}}^B_{k_1} \\ \hat{\mathbf{t}}^I_{k_1} \\ \hat{\mathbf{t}}^B_{k_2} \end{Bmatrix} + \mathfrak{b}_{k_1} + \mathfrak{b}_{k_2} \tag{6.7}$$

As long as k_1 and k_2 have the same mechanical properties, the matrices from Eq. 6.7 can be grouped into: external boundary terms (B) and crack faces terms ($+$ and $-$ for each face, respectively). Then:

$$\begin{bmatrix} \mathbf{H}^B & \mathbf{H}^+ & \mathbf{H}^- \end{bmatrix} \begin{Bmatrix} \hat{\mathbf{u}}^B \\ \hat{\mathbf{u}}^+ \\ \hat{\mathbf{u}}^- \end{Bmatrix} = \begin{bmatrix} \mathbf{G}^B & \mathbf{G}^+ & \mathbf{G}^- \end{bmatrix} \begin{Bmatrix} \hat{\mathbf{t}}^B \\ \hat{\mathbf{t}}^+ \\ \hat{\mathbf{t}}^- \end{Bmatrix} \tag{6.8}$$

which represents the cracked problem formulation.

6.2.1 Nonlinear problem solving: the constant operator

In order to solve the nonlinear problem, a Newthon-Raphson technique is applied herein. The total external load is divided into load steps and each load step starts with the consideration of a linear behaviour (elastic prediction). This is the first iteration, in which the following is valid:

$$\begin{aligned} \hat{\mathbf{u}}^+ &= \hat{\mathbf{u}}^- \\ \hat{\mathbf{t}}^+ &= -\hat{\mathbf{t}}^- \end{aligned} \tag{6.9}$$

Besides, the prescribed displacements and tractions of the load step are considered as $\Delta\hat{\mathbf{u}}^B_{\text{APP}}$ and $\Delta\hat{\mathbf{t}}^B_{\text{APP}}$ in the vectors $\hat{\mathbf{u}}^B$ and $\hat{\mathbf{t}}^B$. Then, the elastic prediction is as follows:

$$\begin{bmatrix} \mathbf{H}^B & -\mathbf{G}^B & (\mathbf{H}^+ + \mathbf{H}^-) & -(\mathbf{G}^+ - \mathbf{G}^-) \end{bmatrix} \begin{Bmatrix} \hat{\mathbf{u}}^B \\ \hat{\mathbf{t}}^B \\ \hat{\mathbf{u}}^+ \\ \hat{\mathbf{t}}^+ \end{Bmatrix} = \begin{bmatrix} -\bar{\mathbf{H}}^B & \bar{\mathbf{G}}^B \end{bmatrix} \begin{Bmatrix} \Delta\hat{\mathbf{u}}^B_{\text{APP}} \\ \Delta\hat{\mathbf{t}}^B_{\text{APP}} \end{Bmatrix} \tag{6.10}$$

With that, displacements and tractions at the collocation points in the crack faces can be calculated. Then, the values are rotated to a local coordinate system (η,l_1,l_2) as follows:

$$\begin{aligned} \begin{Bmatrix} u_{\eta}^{+} \\ u_{l_1}^{+} \\ u_{l_2}^{+} \end{Bmatrix} &= \mathbf{R}^{+}\mathbf{u}^{+} \quad \text{and} \quad \begin{Bmatrix} u_{\eta}^{-} \\ u_{l_1}^{-} \\ u_{l_2}^{-} \end{Bmatrix} = \mathbf{R}^{-}\mathbf{u}^{-} \\ \begin{Bmatrix} t_{\eta}^{+} \\ t_{l_1}^{+} \\ t_{l_2}^{+} \end{Bmatrix} &= \mathbf{R}^{+}\mathbf{t}^{+} \quad \text{and} \quad \begin{Bmatrix} t_{\eta}^{-} \\ t_{l_1}^{-} \\ t_{l_2}^{-} \end{Bmatrix} = \mathbf{R}^{-}\mathbf{t}^{-} \end{aligned} \tag{6.11}$$

In the local coordinate system, the Crack opening displacement (COD) can be calculated as follows:

$$\text{COD} = -u_{\eta}^{-} - u_{\eta}^{+} \tag{6.12}$$

At each collocation point, the unbalanced t_{exc} is found as follows:

$$t_{\text{exc}} = p_{\eta} - p_{\eta}(\text{COD}) \tag{6.13}$$

in which $t_{\eta}(\text{COD})$ is obtained from Eq. 6.2, Eq. 6.5 or Eq. 6.6, depending on the cohesive law adopted (linear, bilinear or exponential, respectively).

The k collocation points in which $||t_{exc}^{k}|| \geq 0$ are identified. These unbalanced forces must be reapplied in the system in the form of traction parameters at the control points. For that, the inverse mapping of displacements is applied:

$$\hat{\mathbf{t}}_{inc(i,j,e)}^{e} = \left(R_{ij,pq}^{e}(\xi^{k},\eta^{k})\right)^{-1} (\mathbf{R})^{-1} \begin{Bmatrix} t_{exc}^{k} \\ 0 \\ 0 \end{Bmatrix} \tag{6.14}$$

where e is the NURBS surface that contains the collocation point k, which has the parametric coordinates ξ^{k},η^{k}. $R_{ij,pq}$ are the NURBS Rational Basis functions from Eq. 2.57. It is important to note that the number of unbalanced collocation points is not equal to the number of unbalanced control points, since a single value $||t_{\text{exc}}^{k}|| \geq 0$ leads to several $\hat{\mathbf{t}}_{inc(i,j,e)}^{e} \neq 0$. In fact, it is possible to obtain local-support NURBS, in which each collocation points is mapped only by the control points parameters respective of its own knot span. That is obtained by using knot vectors with multiplicity equals $p+1$, being p the NURBS degree. Hence, the reapplication process is performed by knot span, as illustrated in Fig. 94.

The control points with calculated $\hat{\mathbf{t}}_{inc(i,j,e)}^{e}$ from Eq. 6.14 are then identified by $\hat{\mathbf{t}}_{\text{exc}}^{k}$, whereas the remaining control points at the crack faces are represented by the index

Figure 94 – Illustration of the reapplication process of a single t^k_{exc} to the control points of a selected knot span.

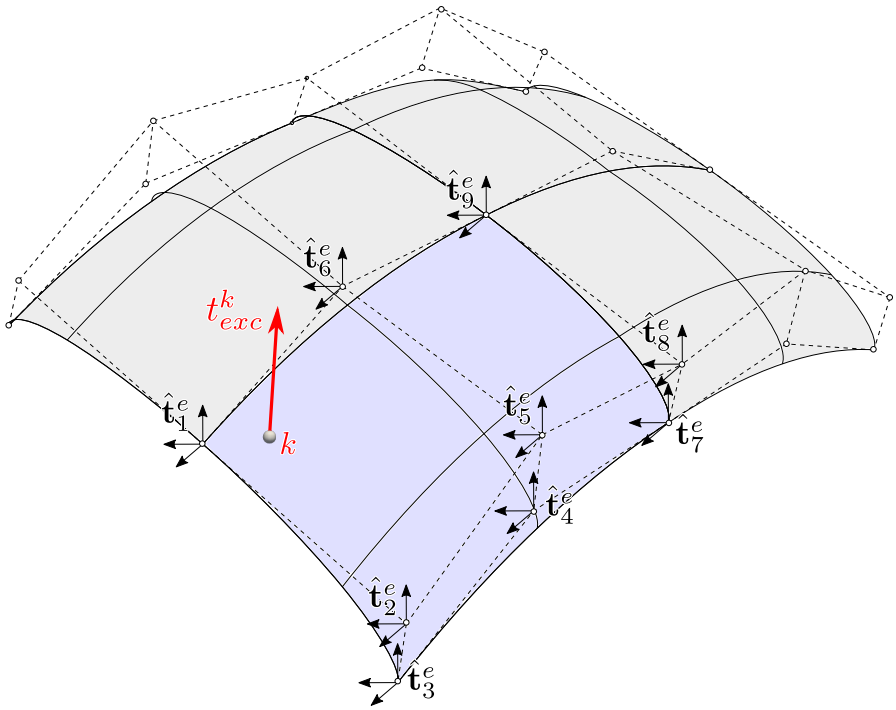

Source: The author.

j. The compatibility relations from Eq. 6.9 remain valid only for j control points. At the control points k, both $\hat{\mathbf{u}}^+_k$ and $\hat{\mathbf{u}}^-_k$ are unknown and $\hat{\mathbf{t}}^+_k = -\hat{\mathbf{t}}^-_k = \hat{\mathbf{t}}^k_{\text{exc}}$.

Then, the reapplication of forces considers the following algebraic system:

$$\begin{bmatrix} \mathbf{H}^B & -\mathbf{G}^B & (\mathbf{H}^+_j + \mathbf{H}^-_j) & -(\mathbf{G}^+_j - \mathbf{G}^-_j) & \mathbf{H}^+_k & \mathbf{H}^-_k \end{bmatrix} \begin{Bmatrix} \hat{\mathbf{u}}^B \\ \hat{\mathbf{t}}^B \\ \hat{\mathbf{u}}^+_j \\ \hat{\mathbf{t}}^+_j \\ \hat{\mathbf{u}}^+_k \\ \hat{\mathbf{u}}^-_k \end{Bmatrix} = \begin{bmatrix} (\mathbf{G}^+_k - \mathbf{G}^-_k) \end{bmatrix} \left\{ \hat{\mathbf{t}}^k_{\text{exc}} \right\} \tag{6.15}$$

After the reapplication, Eq. 6.11 to Eq. 6.14 are applied once again. The tolerance for convergence is verified with the Euclidean norm of the vector $\mathbf{t}_{\text{exc}}$, which contains the unbalanced tractions (Eq. 6.13) at all collocation points of the crack surface. This approach, called Constant operator, is considered a modified Newthon-Raphson formulation, since is does not update the matrices contribution due to the linear degradation. As previously-mentioned for the nonlinear reinforced formulations, such technique may be advantageous for BEM since the integration process to update BEM's matrices is highly computationally demanding.

6.2.2 Numerical application of the cohesive formulation: Cube under tension

This first application of the cohesive approach aims to validate the implementations. For that, a simple parallelepiped structure under tension is analysed, as illustrated in Fig. 95. Such structure is clamped at its left end and subjected to a prescribed displacement at its right end. The notch is symmetrically positioned at the half span, as illustrated by the shaded area in this figure. The material properties are as follows: Young modulus of 30 MPa, null Poisson ratio , fracture energy $G_f = 0.015$ kNm, tensile material strength $f_T = 3$ MPa, applied displacement $\bar{u}_{\text{APP}} = 0.015$ m. The geometric parameters illustrated in Fig. 95 are as follows: $a = 2$ cm, $b = c = 1$ cm.

Figure 95 – Structure analysed in the first application of the cohesive fracture modelling.

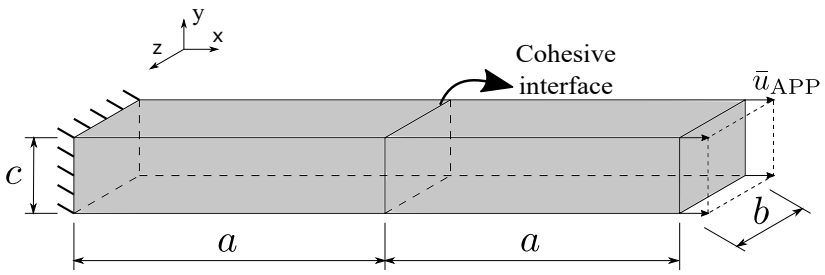

Source: The author.

The nonlinear problem has been solved through 100 load steps and tolerance for convergence equal to 10^{-3}. Moreover, 12 regular NURBS of linear order ($p = q = 1$) discretise the solid, resulting in a model with 48 collocation points.

Figure 96 illustrates the results obtained for tractions at the crack interface versus the applied displacement. It is possible to observe that such results replicate the behaviour of the cohesive laws (Figs. 91, 92 and 93). Such similarity is expected due to the problem's simplicity of geometry and load (uniaxial traction with nill Poisson ratio). Therefore, the observed results validate the correct implementation of the proposed cohesive laws.

Furthermore, Fig. 97 illustrates the number of iterations necessary to achieve convergence along the load steps process. One observes the expected behaviour for a Constant Operator approach: the regions in which the inclination of the cohesive curve is higher require more iterations to achieve convergence for the same tolerance. Besides, the linear and bilinear laws achieve a point in which only 1 iteration is necessary, since such laws have fully horizontal curves after $COD > COD_c$. Such behaviour is not observed for the exponential law, because it doesn't have a defined COD_c point.

Figure 96 – Tractions at the cohesive interface as a function of the applied displacements

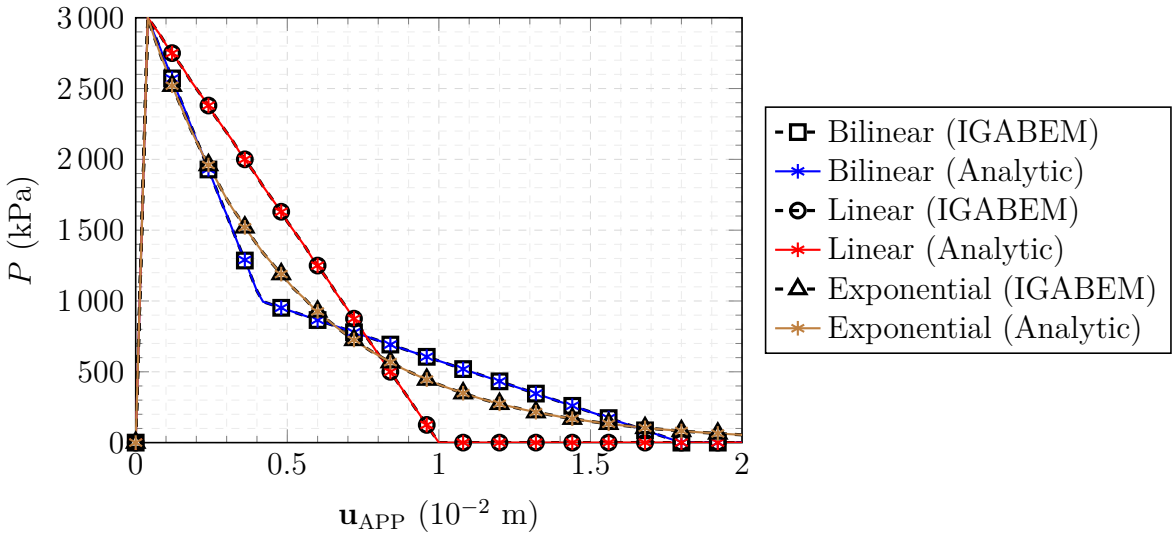

Source: The author.

Figure 97 – Number of iterations to achieve convergence per load step

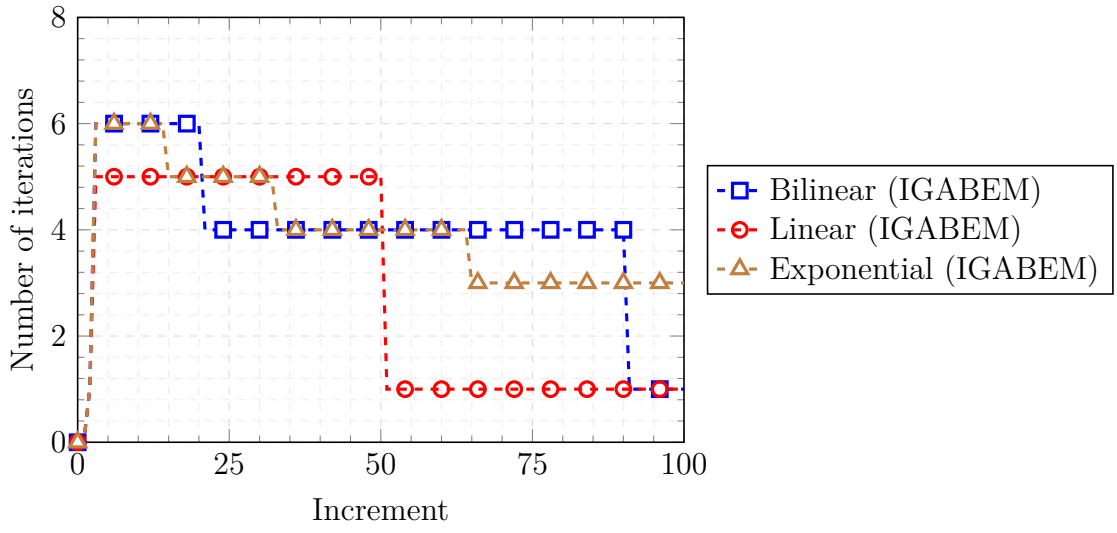

Source: The author.

6.2.3 *Numerical application of the cohesive formulation 2: Three-point bending of concrete specimen*

This application handles the nonlinear fracture modelling of a concrete specimen tested at three-point bending. Reference results and parameters can be found in the literature (154). Fig. 98 illustrates the structure considered for the numerical model. The geometrical parameters are as follows: $a = b = 20$ cm, $l = 40$ cm, $sup = 1.0$ cm and a notch height $nh = 5$ cm. The material properties are as follows: Young modulus of 30 MPa, Poisson ratio $\nu = 0.15$, fracture energy $G_f = 75$ N/m, tensile material strength $f_T = 3$ MPa.

Figure 98 – Structure analysed in the second application of the viscous-cohesive model.

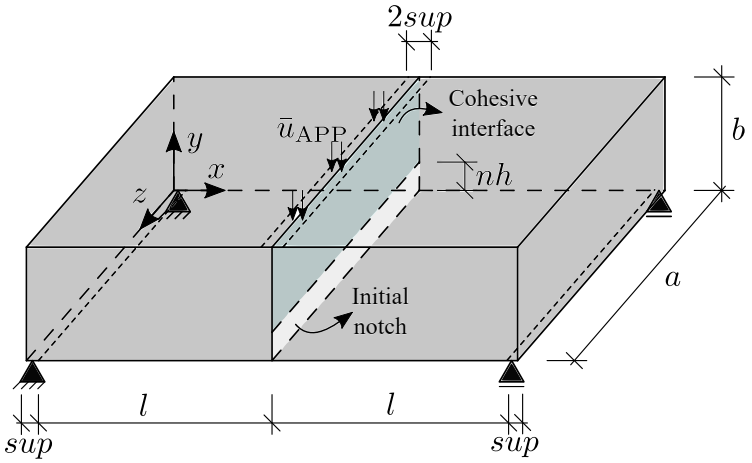

Source: The author.

The nonlinear problem has been solved through 24 load steps and tolerance for convergence equal to 10^{-3}. Moreover, 12 regular NURBS of linear order ($p = q = 1$) discretise the solid, resulting in a model with 48 collocation points.

The structure analysed in this application is discretised into 18 NURBS surfaces of second-order ($p = q = 2$). Knot insertion process has been applied to refine the surfaces by adding control points, resulting in a model with 5311 collocation points, as illustrated in Fig. 99. Mesh convergence has been verified using the reference solution's linear portion.

Figure 99 – Mesh of collocation points applied in the mechanical analysis of the second application of the cohesive model.

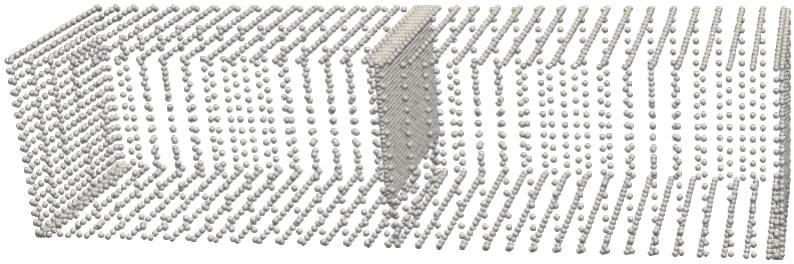

Source: The author.

Fig. 100 illustrates the results obtained via the three different cohesive laws (linear, bilinear and exponential) in comparison with the reference results. It is worth mentioning that the tractions are normalised by the beam's thickness in this graph, in order to make the comparison with the 2D reference (154) valid. One observes a good fit of the numerical results of the proposed models. In fact, both the peak load and the post-peak behaviours were successfully represented by the models, specially with the linear law, which presents the best fit.

Figure 100 – Normalised tractions at the cohesive interface as a function of the applied displacements

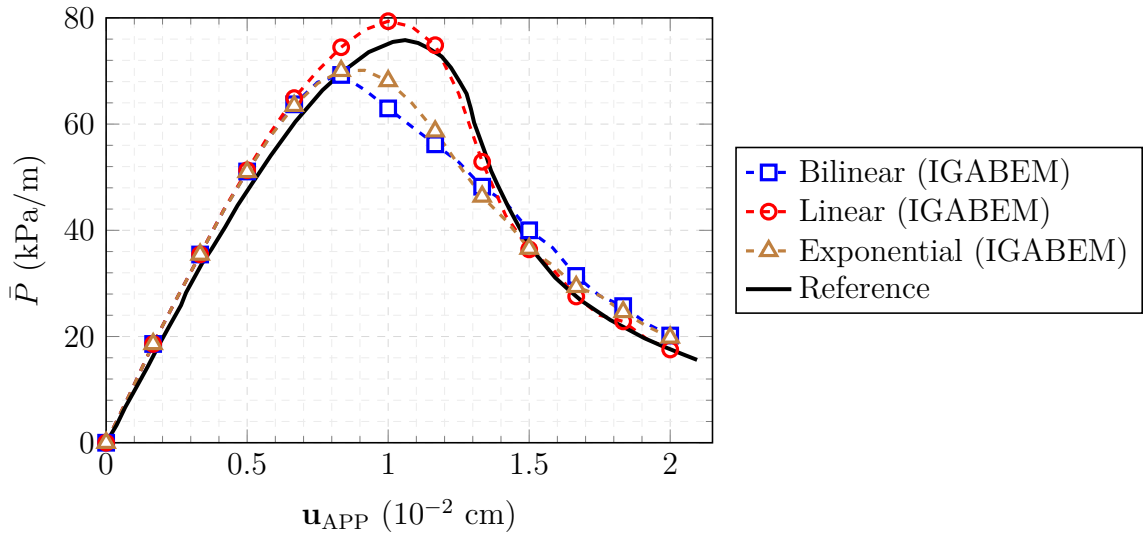

Source: The author.

Furthermore, Fig. 101 shows the number of iterations necessary to achieve convergence per load step, using the three different cohesive laws. Differently from Fig. 97, this example does not achieve a point in which load steps can converge in only one load step. This happens because this cohesive propagation is not constant along the crack face, thus there is always some point of the crack face in a different region of the cohesive law.

Figure 101 – Number of iterations to achieve convergence per load step

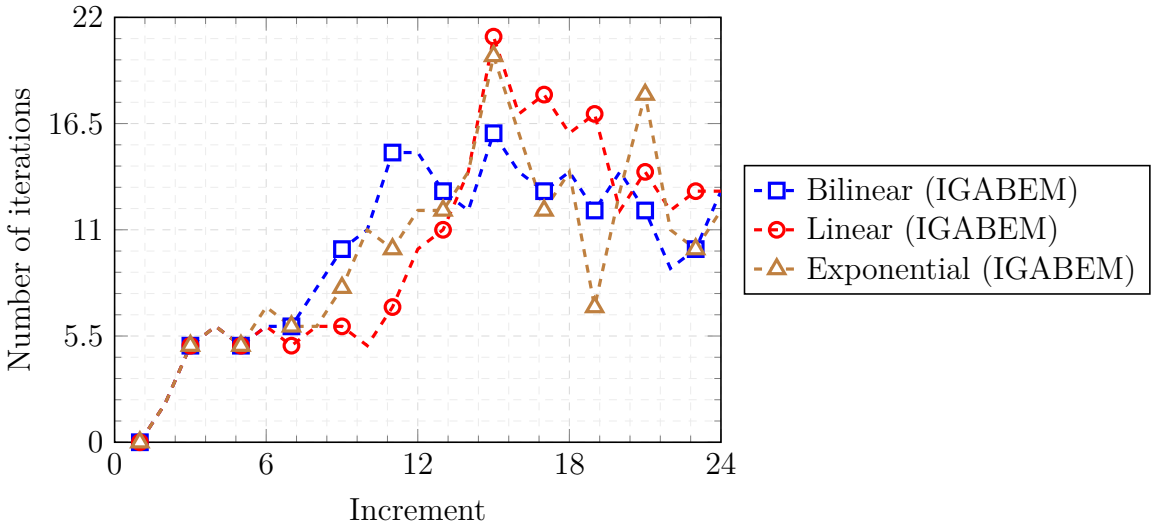

Source: The author.

6.3 Cohesive Crack Propagation Accounting for Loading Rates

The fracture mechanics formulations above-presented consider that the FPZ's resistance material behaviour is constant. However, several materials show that such behaviour is considerable dependent on the loading rate (155, 156). Experimental results can be seen in Fig. 102, which shows how the resistant load (peak load) and the apparent fracture energy monotonically increase with the loading rate increase whereas the displacement value associated to the peak load remains virtually the same.

Figure 102 – Load *vs* displacement curves for High-Strength Concrete at different load rates

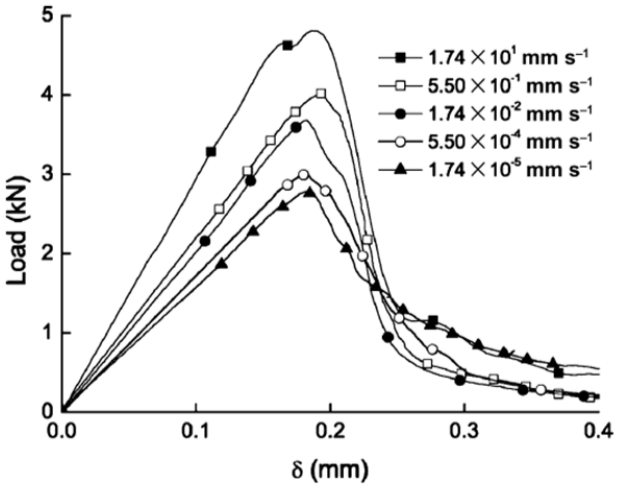

Source: (156)

The physical micro-mechanisms governing the cohesive fracture under loading rate and/or load duration processes have not been fully understood. Nevertheless, experimental evidences suggest that the micro cracking delay at high strain rates characterises such failure (157), which has been named as the first stage. Afterwards, the second stage starts, which is composed by multiple micro crack propagation at the FPZ (158). It is worth mentioning that the discrete crack propagation in quasi-brittle materials is the result of micro voids connection and micro crack propagation at the FPZ. Thus, the reduction of micro cracking with the strain rate increase leads to the reduction of the macro nonlinear behaviour and the increase of the material tensile strength. Because the micro cracks do not have sufficient time for searching the minimum energy path, they have been forced to propagate along the shortest path with higher resistance. Therefore, it suggests that fracture energy and the peak load increase as a function of the loading rate (156).

6.3.1 Viscous cohesive model

(159) proposed modifications in the classical cohesive laws (linear, bilinear and exponential) to properly represent the viscous behaviours, which is dependent on the load

rates. Such modifications have been motivated by the experimental relations provided by the references (160, 155). The present study is pioneer to apply such modified viscous-cohesive laws for fracture mechanics problems within a IGABEM framework. In order to do that, the Constant Operator above-presented can be maintained, whereas the cohesive law relations (Eqs. 6.2, 6.5 and 6.6) are replaced by the viscous-cohesive laws.

The cohesive law account for loading rates influence is proposed as follows:

$$p_\eta(COD) = \Psi(C\dot{O}D)\, f(COD, G(C\dot{O}D)) \tag{6.16}$$

where $C\dot{O}D$ is the time-derivative of the crack opening displacement. $G(C\dot{O}D)$ represents the fracture energy influenced by the time variance of the COD. $\Psi(C\dot{O}D)$ refers to the cohesive law modified by the rate dependent fracture energy and $f(COD, G(C\dot{O}D))$ is the time dependent function, which can be written as:

$$\Psi(C\dot{O}D) = 1 + \left(\frac{C\dot{O}D}{C\dot{O}D_0}\right)^n \tag{6.17}$$

in which COD_0 indicates a normalisation parameter for COD and n is the exponent of rate dependence.

Besides, the function $G(C\dot{O}D)$ is written as:

$$G(C\dot{O}D) = \begin{cases} 1 + \left(\dfrac{C\dot{O}D}{C\dot{O}D_w}\right)^{n_w} & \text{for } C\dot{O}D \leq C\dot{O}D_w \\ 0 & \text{for } C\dot{O}D > C\dot{O}D_w \end{cases} \tag{6.18}$$

in which COD_w is the fracture opening rate at which the material tends to the brittle behaviour and n_w is a dimensionless index for governing the evolution from quasi-brittle to brittle behaviour. Both these parameters represent the mechanical behaviour and can be obtained experimentally.

It is worth stressing that Eq. 6.16 addresses the failure mechanisms during crack propagation. (161) presents an extensive experimental analysis of macro and micro-cracking propagation at different loading rates. From the microscopic analysis at the FPZ, they observed that cracks propagate at the weakest part of the cement past, i.e., the inter-facial transition zone, under static and quasi-static loading conditions. Then, the major crack appears because the interconnection of small cracks at the FPZ. However, at high loading rates, cracks have less time for searching the weakest parts. Consequently, fails through the aggregate have been observed. Moreover, a large amount of micro-cracks around the major crack is observed. The observations of (161) can be correlated to Eq. 6.16. The distribution of small cracks at the inter-facial transition zone provides a reduced value of f_T and an extended cohesive behaviour, with a higher value of COD_c, under static and

quasi-static loading rate. On the other hand, under higher loading rate, the major crack path through the aggregate provides a higher value of f_T and a smaller value of COD_c because of the reduction of neighbouring cracks.

6.3.2 Updated linear, bilinear and exponential laws

In order to obtain the updated cohesive laws accounting for the viscous behaviour, the time dependent expression for crack energy Eq. 6.18 must be considered in the formulation of the law (Sections 6.1.1, 6.1.2 and 6.1.2).

Then, the linear viscous-cohesive law can be written as:

$$p_\eta(COD) = \begin{cases} f_T \left(1 - \dfrac{COD}{COD_c^{up}}\right) & \text{for } 0 \leq COD \leq COD_c^{up} \\ 0 & \text{for } COD > COD_c^{up} \end{cases} \tag{6.19}$$

in which $COD_c^{up} = G(C\dot{O}D)\, COD$.

The bilinear viscous-cohesive law is written as follows:

$$p_\eta(COD) = \begin{cases} f_T - \left(\frac{f_T - f_T^*}{COD^*}\right) \frac{COD}{G(C\dot{O}D)} & \text{for } 0 \leq COD \leq COD_{up}^* \\ \frac{f_T}{COD^* - COD_c^{up}} \frac{COD}{G(C\dot{O}D)} + f_T^* \left(1 - \frac{COD_{up}^*}{COD_{up}^* - COD_c^{up}}\right) & \text{for } COD_{up}^* \leq COD \leq COD_c^{up} \\ 0 & \text{for } COD > COD_c^{up} \end{cases} \tag{6.20}$$

where $COD_{up}^* = COD^*\, G(C\dot{O}D)$.

Finally, the updated exponential law is as follows:

$$p_\eta(COD) = f_T \exp\left\{-f_T \frac{COD}{G(C\dot{O}D)}\right\} \tag{6.21}$$

6.3.3 Numerical application of rate dependent cohesive behaviour: Cube under tension

The first application for the improved nonlinear load rate dependent formulation is the fracture analysis of a parallelepiped structure under tension, as illustrated in Fig. 95. Such structure is clamped at its left end and subjected to a prescribed displacement at its right end. The notch is symmetrically positioned at the half span, as illustrated by the shaded area in this figure.

The material properties are as follows: Young modulus of 30 MPa, null Poisson ratio , fracture energy $G_f = 0.015$ kNm, tensile material strength $f_T = 3$ MPa, applied displacement $\bar{u}_{\text{APP}} = 0.015$ m, normalisation parameter tensile $C\dot{O}D_0 = 0.284$ m/s, exponent

of rate dependency $n = 0.27$, normalisation parameter threshold opening $C\dot{O}D_w = 0.1$ m/s and exponent of rate dependency for threshold opening $n_w = 0.25$. Such material parameters have been adopted from literature reference (156). The geometric parameters illustrated in Fig. 95 are as follows: $a = 40$ cm, $b = c = 20$ cm. The nonlinear problem has been solved through 60 load steps and tolerance for convergence equal to 10^{-3}. Moreover, 12 regular NURBS of linear order ($p = q = 1$) discretise the solid, resulting in a model with 48 collocation points.

Three different loading rates have been applied in this analysis, which are equal to: 10^{-3}, 10^{-5} and 10^{-7} m/s. In addition, the linear, bi-linear and exponential cohesive laws represent the nonlinear fracture behaviour in the problem.

Fig. 103 illustrates the tractions vs applied displacement curves for the three cohesive laws. As expected, the loading rate increase leads to the apparent increase on the material tensile strength. Similar behaviour has been observed for the apparent fracture energy. Thus, the higher values of external loads trigger the fracture process when high loading rates are applied. Moreover, the threshold opening displacement reduce as the load rate increase. This is a major feature of this approach, which represent the physical phenomenon experimentally observed. Then, the material tends to the brittle behaviour as the loading rate increase.

It is worth mentioning that the resulting curves of tractions vs COD are analogous to the behaviour observed in Fig. 103, due to the simple geometry of the problem.

Finally, one can also observe that the critical load value is the same for all the three laws, once the loading rate is the same in Fig. 103. Moreover, the differences among the mechanical behaviour are attributed to the cohesive law description. Nevertheless, the mechanical behaviour for each curve follows the assumption of each cohesive law, which indicates the implementation accuracy.

6.3.4 Numerical application of rate dependent cohesive behaviour 2: Three-point bending of concrete specimen with different loading rates

This application deals with the viscous-cohesive fracture of a concrete specimen tested at three-point bending. Experimental reference results and parameters can be found in the literature (159). Fig. 98 illustrates the structure considered for the numerical model. The geometrical parameters are as follows: $a = b = 100$ mm, $l = 182.5$ mm, $sup = 2.5$ cm and a notch height $nh = 23$ mm. The material properties are as follows: Young modulus of 18.666 MPa, Poisson ratio $\nu = 0.15$, fracture energy $G_f = 219.6$ J/m^2, tensile material strength $f_T = 1.904$ MPa, normalisation parameter tensile $C\dot{O}D_0 = 1.119$ mm/s, exponent of rate dependency $n = 0.429$, normalisation parameter threshold opening $C\dot{O}D_w = 0.529$ mm/s and exponent of rate dependency for threshold opening $n_w = 0.322$. Such parameters

Figure 103 – Reactive tractions at crack face versus applied displacement obtained by different viscous-cohesive laws.

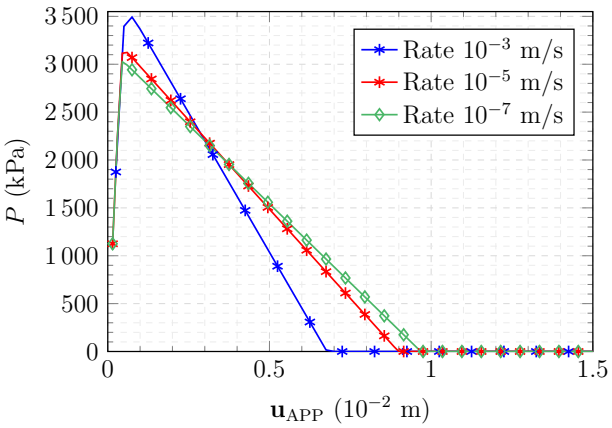

(a) Linear viscous-cohesive law

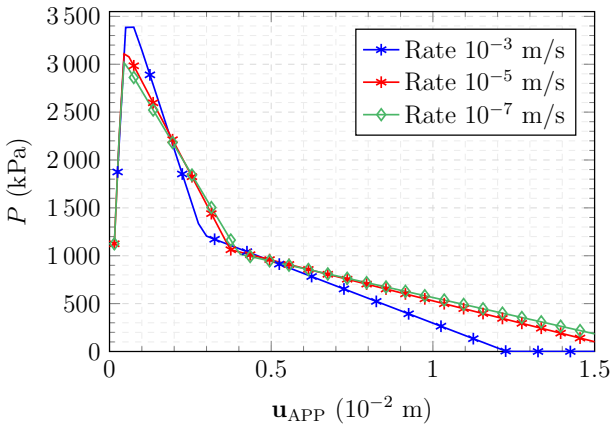

(b) Bilinear viscous-cohesive law

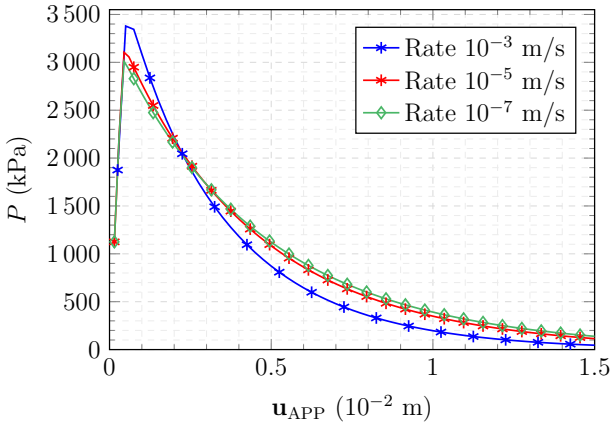

(c) Exponential viscous-cohesive law

were obtained via inverse analysis considering the viscous-cohesive law and the laboratory results (159).

The applied displacement is $\bar{u}_{\text{APP}} = 0.35$ mm into 30 load steps in the nonlinear analysis. The tolerance for convergence is 10^{-3}. Three different loading rates have been applied in this analysis, which are equal to: $8.33 \cdot 10^{-4}$, $8.33 \cdot 10^{-3}$ and $8.33 \cdot 10^{-2}$ mm/s. In addition, the linear, bi-linear and exponential cohesive laws represent the nonlinear fracture behaviour in the problem.

The structure analysed in this application is discretised into 18 NURBS surfaces of second-order ($p = q = 2$). Knot insertion process has been applied to refine the surfaces by adding control points, resulting in a model with 4303 collocation points, as illustrated in Fig. 104. Mesh convergence has been verified using the reference solution's linear portion.

Firstly, the results obtained via the three different viscous-cohesive laws are compared with the experimental envelope in Fig. 105. A loading rate of $8.33 \cdot 10^{-4}$ is considered herein. One observes that the bilinear law provides a better fit with the experimental

Figure 104 – Mesh of collocation points applied in the mechanical analysis of the second application of the viscous-cohesive model.

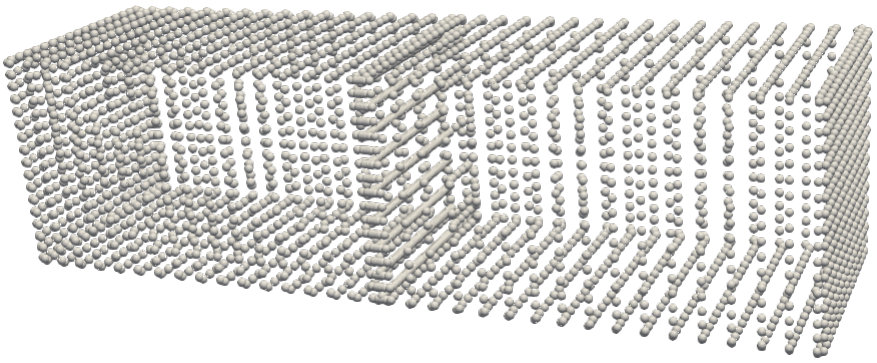

Source: The author.

results. It is worth mentioning that such results for different loading rates show similar behaviour and lead to the same conclusion. Therefore, the bilinear law will be considered for the further analyses.

Figure 105 – Applied force versus CMOD obtained using different cohesive laws with the same parameters.

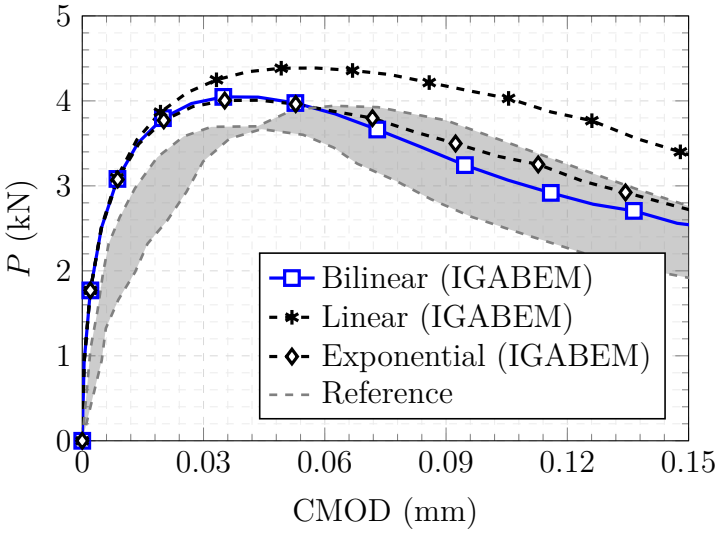

Source: The author.

Fig. 106 shows the comparison between the experimental envelope and the fitted numerical curves at the simulated loading rates using the bilinear viscous-cohesive law. One observes a good fit between then numerical results and the experimental data. Fig 106(d) exhibits a comparison between the numerical curves with different load rates, which shows an initial stiffness increase and an increase in the peak load curve with the load rate. Beyond the peak, curves show close adherence between load values.

Fig. 107 illustrates the behaviour of the adjusted viscous-cohesive law chosen for conventional concrete (bilinear) in comparison with the trilinear curve fitted in the

Figure 106 – Applied force versus CMOD for comparing the obtained numerical results with the conventional concrete experimental envelope.

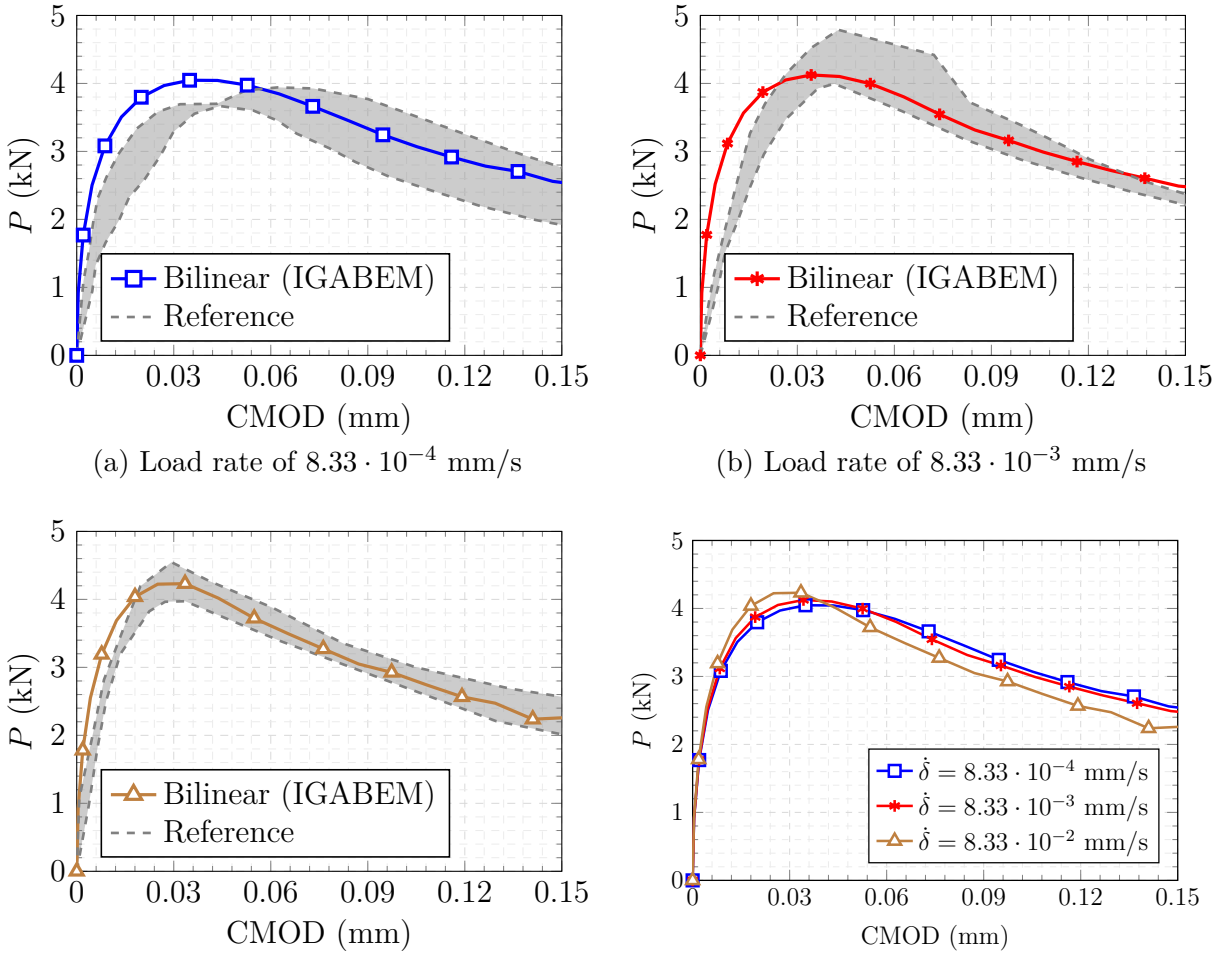

(a) Load rate of $8.33 \cdot 10^{-4}$ mm/s

(b) Load rate of $8.33 \cdot 10^{-3}$ mm/s

(c) Load rate of $8.33 \cdot 10^{-2}$ mm/s

(d) Numerical results of all load rates

Source: The author.

reference (159). One observes that, as the loading rate increases, the tensile strength also increases and the critical crack opening decreases for both models. There is a good fit between the proposed model and the reference model. However, the proposed model has showed (in Fig. 106) a fit with the experimental values as good as the reference model, but having a lower number of parameters (since the curve presents only two piecewise regions, against three).

The results presented herein conclude that the proposed viscous-cohesive model is adequate for modelling conventional concrete at low loading rates.

Figure 107 – Viscous cohesive curve applied for conventional concrete.

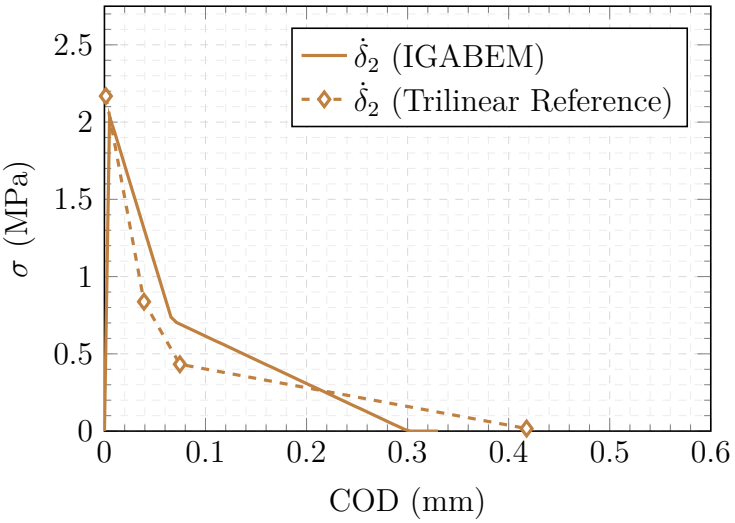

Source: The author.

7

ADAPTIVITY

Mesh Adaptive strategies are proposed in this work for either the 3D IGABEM and the reinforced formulation 1DBEM/IGABEM. The mesh Adaptive analysis may provide the adequate refinement necessary to accurately represent the displacements and tractions fields (within a stipulated error tolerance) in a mechanical analysis based on the isogeometric models provided from CAD. Although these models are geometrically exact, more refinement is usually necessary for the mechanical analysis. Therefore, the Adaptivity analyses favours the straightforward process connection between the mechanical analysis and the geometry design. This chapter presents the formulation developed for the Adaptivity strategies proposed herein, as well as numerical examples comparing the convergence achieved via the Adaptivity against the homogeneous refinement of all NURBS surfaces.

7.1 Literature review

It is well-known that Adaptive mesh strategies are composed by three phases: the error estimator, the Adaptive tactics and the mesh refinement process (162). In most cases the critical part is the error estimation, specially when the analysis must not rely on exact solutions for all problems. In that case, a posteriori error estimators stand out, since they provide reliable estimates for the exact error without having reference or exact solutions. This concept is already well-developed in the context of the FEM (163). However, the particularities of the BEM, such as the lack of domain discretization, presents further challenges for the development of accurate and robust a posteriori error estimators. In this context, it is usual for the error estimator to rely on exact solutions or more refined meshes (164, 165) and modified collocation strategies (166, 167).

An elegant approach for a posteriori point-wise error estimation in the BEM is

based on the hypersingular integral equation (TBIE), which allows for the error evaluation solely at the boundary without the need for domain discretization. Such approach is known as the hypersingular residual (18) and relies on evaluating the residual of the BEM DBIE equation considering the hypersingular integral equation (TBIE). This approach has been further studied in the literature (168, 169, 170) and Liang et al. (171) demonstrated that a error estimator calculated from the absolute difference between the DBIE and the TBIE solutions is equivalent to the hypersingular residual demonstrated by Paulino (18). This error estimator is adopted herein as a basis for the mesh Adaptive strategies.

In the context of the Adaptive tactics, Zienkiewicz's work (17) has become a classical reference and its strategy has been the basis for several applications among FEM and BEM formulations (170). Effective Adaptive schemes are usually based on mesh optimality criteria of equal distribution of global error and equal distribution of specific error over the approximation elements (172). In this work, the Adaptive tactic is based on the above-presented studies.

The mesh refinement process is the last step for developing a complete mesh Adaptive scheme. The refinement process for polynomial elements in BEM formulations is well-developed in the literature (171, 173, 165). Nevertheless, in the context of IGA frameworks, the oriented locally refinement of NURBS requires several specific solutions. Most of them are based on the use of different B-splines formulations (such as hierarchical or T-constructions) or splitting the NURBS surfaces or even modifying the tensor-product that defines a NURBS surface (174, 175, 176). This work applies the knot insertion process (16) to produce refined knot vectors for regular NURBS surfaces that leads to both more refined approximation spaces and the increase of the amount of collocation points. For 2D IGABEM problems, the knot insertion may easily produce locally refined NURBS lines (177), however it does not allow for the local refinement of surfaces (175) in the 3D IGABEM. Therefore, this work proposes the uniform refinement of each NURBS surfaces in a process similar to the strategy proposed by Nguyen et al. (178) for 2D isogeometric approaches of the FEM and XFEM.

Finally, it is worth mentioning that mesh Adaptivity schemes for coupled BEM formulations for fibre-reinforced problems are not found in the literature yet. In fact, Adaptive FEM-BEM coupling formulations have been presented for transmission and interface problems (179, 180) and electromagnetism (181). Thus, this work proposes a innovative error estimator for the coupling 1DBEM/BEM, which allows the development of a mesh Adaptive scheme for Reinforced IGABEM formulations.

7.2 Hypersingular Error estimator

This study presents two types of Hypersingular error estimator applied to the IGABEM. This first approach is called the Displacements based error estimator and follows what exists in the literature (18, 171). Then, a derived approach based on strains is developed and presented in Sec. 7.2.2.

7.2.1 Displacements based error estimator

The hypersingular error in based on solving the same model with two different linear systems of equations (18). These two systems consist of applying, respectively, the DIE or the TIE for all of the collocation points of the model. Equation 2.74 can algebraically represent both systems, therefore:

$$\mathbf{H}\hat{\mathbf{u}}_{\mathbf{S}} = \mathbf{G}\hat{\mathbf{t}}_{\mathbf{S}} + \mathfrak{b}_{\mathbf{S}} \tag{7.1}$$

$$\mathbf{H}'\hat{\mathbf{u}}_{\mathbf{H}} = \mathbf{G}'\hat{\mathbf{t}}_{\mathbf{H}} + \mathfrak{b}_{\mathbf{H}} \tag{7.2}$$

in which the indexes **S** e **H** represent the values related to the DIE (singular) and the TIE (hypersingular) systems, respectively. Applying the boundary conditions in those expressions, one writes:

$$\mathbf{A}\hat{\mathbf{x}}_{\mathbf{S}} = \mathbf{B}\hat{\mathbf{p}} + \mathfrak{b}_{\mathbf{S}} \tag{7.3}$$

$$\mathbf{A}'\hat{\mathbf{x}}_{\mathbf{H}} = \mathbf{B}'\hat{\mathbf{p}} + \mathfrak{b}_{\mathbf{H}} \tag{7.4}$$

where $\hat{\mathbf{p}}$ are the prescribed boundary conditions. These expressions result in the unknown values at the boundary $\hat{\mathbf{x}}_{\mathbf{S}}$ and $\hat{\mathbf{x}}_{\mathbf{H}}$.

The traditional hypersingular error estimator can be represented by the difference between the DIE and the TIE solutions, as demonstrated in (171). This error estimator is named herein as displacements based error estimator, which is as follows:

$$\mathfrak{e} = \mathbf{x}_{\mathbf{S}} - \mathbf{x}_{\mathbf{H}} \tag{7.5}$$

in which $\mathfrak{e}$ is the error estimator.

7.2.2 Strains based error estimator

This work proposes a alternative hypersingular error estimator, which is based on the difference between the strains at the boundary (ε_{ij}), obtained from $\mathbf{x}_{\mathbf{S}}$ and $\mathbf{x}_{\mathbf{S}}$.

In order to calculate the strains at the boundary from a given boundary solution $\hat{\mathbf{x}}$, one applies the indirect approach demonstrated by Aliabadi (58) for 3D problems. In

this approach, the strains ε_{ij} and tractions σ_{ij} at a given point are calculated from the global displacements u_i and tractions t_i values at this point.

A local coordinates system is defined, considering the NURBS parametric coordinates directions (η_1, η_2) as the local directions $(\tilde{x}_1, \tilde{x}_2)$ in the plane of the NURBS surface. The third direction $\hat{x}_3$ is defined along the outward normal vector to the surface. The rotation matrix from the global x_i to the local $\tilde{x}_i$ system is $\mathbb{R}_{ij}$.

There are two vectors $h_i(\eta_1,\eta_2)$ and $g_i(\eta_1,\eta_2)$ that are tangent to the NURBS surfaces at the current point. These vectors are defined along the parametric directions (η_1, η_2) respectively, and are calculated as follows:

$$\begin{aligned} h_i(\eta_1,\eta_2) &= \frac{\partial x_i}{\partial \eta_1}(\eta_1,\eta_2) = \sum_{\alpha=1}^{m} \frac{\partial N_\alpha(\eta_1,\eta_2)}{\partial \eta_1} \hat{X}_i^\alpha \\ g_i(\eta_1,\eta_2) &= \frac{\partial x_i}{\partial \eta_2}(\eta_1,\eta_2) = \sum_{\alpha=1}^{m} \frac{\partial N_\alpha(\eta_1,\eta_2)}{\partial \eta_2} \hat{X}_i^\alpha \end{aligned} \tag{7.6}$$

in which m is the number of control points in the current NURBS surface. $\hat{X}_i^\alpha$ is the global coordinate in the x_i direction of the control point α. N_α are the interpolation functions related to the control point α. The outward normal vector is then defined as the cross product $d_i(\eta_1,\eta_2) = h_i(\eta_1,\eta_2) \times g_i(\eta_1,\eta_2)$.

The tangent vectors from Eq. 7.6 and the outward normal vector determine the rotation matrix components $\mathbb{R}_{ij}$ as follows:

$$\begin{aligned} \mathbb{R}_{1i} &= \frac{h_i}{h} \qquad i = 1,2,3 \\ \mathbb{R}_{2i} &= \frac{g_i}{g} \qquad i = 1,2,3 \\ \mathbb{R}_{3i} &= \frac{1}{d}\left[h\, g_i - h_i\, g_i \frac{h_i}{h}\right] \qquad i = 1,2,3 \end{aligned} \tag{7.7}$$

where $d = \sqrt{d_i d_i}$, $h = \sqrt{h_i h_i}$ and $g = \sqrt{g_i g_i}$.

The parametric directions η_1 and η_2 may not be orthogonal in the real space. Hence, the angle θ between this directions must be taken into account, as:

$$\theta = \cos^{-1}\left(\mathbb{R}_{1i}\, \mathbb{R}_{2i}\right) \tag{7.8}$$

Then, the stresses in the normal plane $\tilde{x}_3$ are directly calculated from the traction values, as follows:

$$\tilde{\sigma}_{3j} = \tilde{t}_i \qquad i = 1,2,3 \tag{7.9}$$

in which $\tilde{t}_i = \mathbb{R}_{ij}\, t_j$.

The strains in the plane $(\tilde{x}_1, \tilde{x}_2)$ are calculated from the global displacements and the rotation matrix.

$$\begin{aligned}
\tilde{\varepsilon}_{11} &= \sum_{\alpha=1}^{m} \hat{u}_j^{\alpha}\, \mathbb{E}_j^{11\alpha}(\eta_1,\eta_2) \qquad j=1,2,3 \\
\tilde{\varepsilon}_{22} &= \sum_{\alpha=1}^{m} \hat{u}_j^{\alpha}\, \mathbb{E}_j^{22\alpha}(\eta_1,\eta_2) \qquad j=1,2,3 \\
\tilde{\varepsilon}_{12} &= \sum_{\alpha=1}^{m} \hat{u}_j^{\alpha}\, \mathbb{E}_j^{12\alpha}(\eta_1,\eta_2) \qquad j=1,2,3
\end{aligned} \tag{7.10}$$

where $\hat{u}_j^{\alpha}$ is the displacement parameter along the direction j at the control point α. $\mathbb{E}_j^{11\alpha}$, $\mathbb{E}_j^{22\alpha}$ and $\mathbb{E}_j^{12\alpha}$ are as follows:

$$\begin{aligned}
\mathbb{E}_j^{11\alpha}(\eta_1,\eta_2) &= \frac{\partial N_\alpha(\eta_1,\eta_2)}{\partial \eta_1}\frac{\mathbb{R}_{1j}}{h} \\
\mathbb{E}_j^{22\alpha}(\eta_1,\eta_2) &= \mathbb{R}_{2j}\left[\frac{\partial N_\alpha(\eta_1,\eta_2)}{\partial \eta_1}\frac{-\cot\theta}{h} + \frac{\partial N_\alpha(\eta_1,\eta_2)}{\partial \eta_2}\frac{1}{g\,\sin\theta}\right] \\
\mathbb{E}_j^{12\alpha}(\eta_1,\eta_2) &= \mathbb{R}_{2j}\left[\frac{\partial N_\alpha(\eta_1,\eta_2)}{\partial \eta_1}\frac{1}{h}\right] + \mathbb{R}_{1j}\left[-\frac{\partial N_\alpha(\eta_1,\eta_2)}{\partial \eta_1}\frac{\cot\theta}{h} + \frac{\partial N_\alpha(\eta_1,\eta_2)}{\partial \eta_2}\frac{1}{g\,\sin\theta}\right]
\end{aligned} \tag{7.11}$$

Hooke's law (Eq. A.10) applied in the local system allows finding all of the remaining stress and strain components from the values obtained in Eq. 7.9 and Eq. 7.10. Thus, the global strain components ε_{ij} are obtained from the following systems transformation:

$$\varepsilon_{ij} = \mathbb{R}_{ki}\,\mathbb{R}_{nj}\,\tilde{\varepsilon}_{kn} \tag{7.12}$$

Therefore, the strains based error estimator $\mathfrak{e}$ is writen as follows:

$$\mathfrak{e} = \varepsilon_{ij}^{\mathbf{S}} - \varepsilon_{ij}^{\mathbf{H}} = \begin{Bmatrix} \varepsilon_{11}^{\mathbf{S}} - \varepsilon_{11}^{\mathbf{H}} \\ \varepsilon_{22}^{\mathbf{S}} - \varepsilon_{22}^{\mathbf{H}} \\ \varepsilon_{33}^{\mathbf{S}} - \varepsilon_{33}^{\mathbf{H}} \\ \varepsilon_{12}^{\mathbf{S}} - \varepsilon_{12}^{\mathbf{H}} \\ \varepsilon_{13}^{\mathbf{S}} - \varepsilon_{13}^{\mathbf{H}} \\ \varepsilon_{23}^{\mathbf{S}} - \varepsilon_{23}^{\mathbf{H}} \end{Bmatrix} \tag{7.13}$$

where $\varepsilon_{ij}^{\mathbf{S}}$ and $\varepsilon_{ij}^{\mathbf{H}}$ are the global values of strains obtained from the above-presented procedure applied respectively for the singular and the hypersingular solutions.

7.3 Adaptive scheme

In order to obtain a more stable adaptive scheme, it is worth splitting the total error $\mathfrak{e}$ into two portions: $\mathfrak{e}_u$ and $\mathfrak{e}_t$. $\mathfrak{e}_u$ is the error present at surfaces in which displacements

are approximated and tractions are prescribed, whereas $\mathfrak{e}_t$ is present at surfaces in which tractions are approximated and displacements are prescribed. This separation is important because the solution of the BEM systems are composed by two different mechanical fields (displacements and tractions), which might have very distinct orders of magnitude. Then, one writes:

$$\mathfrak{e} = \begin{Bmatrix} \mathfrak{e}_u \\ \mathfrak{e}_t \end{Bmatrix} \tag{7.14}$$

Thus, the L2 norms of the error at each NURBS surface i are as follows:

$$||e_u||_i^2 = \int_{S_i} (\mathfrak{e}_u)^2 dS \quad \text{and} \quad ||e_t||_i^2 = \int_{S_i} (\mathfrak{e}_t)^2 dS \tag{7.15}$$

in which S_i is the area of the NURBS surface i. The total error norms are given by considering all of the NURBS surfaces n_{surf} in the model, as follows:

$$||e_u||^2 = \sum_{i=1}^{n_{surf}} ||e_u||_i^2 \quad \text{e} \quad ||e_t||^2 = \sum_{i=1}^{n_{surf}} ||e_t||_i^2 \tag{7.16}$$

The definition of average error in the Adaptivity context is based on imposing a global condition together with a local condition for the error norms. The global condition is as follows:

$$||e_u|| \leq \bar{\eta}_u ||u|| \quad \text{e} \quad ||e_t|| \leq \bar{\eta}_t ||t|| \tag{7.17}$$

in which $\bar{\eta}_u$ and $\bar{\eta}_t$ are, respectively, the desired error percentages for displacements and tractions, which are pre-established for the convergence analysis.

The local condition is as follows:

$$||e_u||_i \leq ||e_u||_i^{req} \quad \text{e} \quad ||e_t||_i \leq ||e_t||_i^{req} \tag{7.18}$$

where the index req refers to the required local error values that attend the prescribed $\bar{\eta}_u$ and $\bar{\eta}_t$. The L2 norms $||u||$ and $||t||$ refer to the "theoretically exact" results of displacements and tractions respectively, which can be represented by:

$$||u|| = \left(||\hat{u}||^2 + ||e_u||^2\right)^{1/2} \quad \text{e} \quad ||t|| = \left(||\hat{t}||^2 + ||e_t||^2\right)^{1/2} \tag{7.19}$$

in which $||\hat{u}||^2$ e $||\hat{t}||^2$ are the L2 norms of the approximated solutions $\hat{\mathbf{u}}$ and $\hat{\mathbf{t}}$.

The req error portions from Eq. 7.18 are defined by the mesh optimality criterion based on the equal distribution of the error (172). This criterion is mathematically represented by the following:

$$||e_u||_i^{req} = \frac{||e_u||}{\sqrt{m_u}} \quad \text{e} \quad ||e_t||_i^{req} = \frac{||e_t||}{\sqrt{m_t}} \tag{7.20}$$

in which m_u and m_t are the number of elements composing the errors $\mathfrak{e}_u$ and $\mathfrak{e}_t$, respectively.

The refinement parameters ξ proposed by Zienkiewicz (17) is defined for both the global and local conditions (Eq. 7.17 and 7.18). For this, those expressions are written as a ratio considering the current and the desired error values, as follows:

$$\xi_{glob}^u = \frac{||e_u||}{\bar{\eta}_u||u||} \quad \text{and} \quad \xi_{glob}^t = \frac{||e_t||}{\bar{\eta}_t||t||} \tag{7.21a}$$

$$\xi_{loc}^u = \frac{||e_u||_i}{||e_u||_i^{req}} \quad \text{and} \quad \xi_{loc}^t = \frac{||e_t||_i}{||e_t||_i^{req}} \tag{7.21b}$$

Then, one defines a single parameter that simultaneously attend the global and the local conditions, by $\xi = \xi_{glob} \cdot \xi_{loc}$. Hence, applying Eq. 7.21a, 7.21b, 7.20 and 7.19, one writes:

$$\xi_i^u = \frac{||e_u||_i}{\bar{\eta}_u\sqrt{\dfrac{||\hat{u}||^2 + ||e_u||^2}{m_u}}} \tag{7.22a}$$

$$\xi_i^t = \frac{||e_t||_i}{\bar{\eta}_t\sqrt{\dfrac{||\hat{t}||^2 + ||e_t||^2}{m_t}}} \tag{7.22b}$$

It is worth mentioning that the denominator in Eq. 7.22 coincide with $\bar{e}_m$ from (17), but Eq. 7.22 specifically splits the error into the portions calculated from displacements and from tractions. This splitting is also important in of obtaining the relative errors, since each one should be divided only by the tractions or the displacements approximated.

Therefore, $\xi_i > 1$ defines the required refinement in each NURBS surfaces. The new refinement is based on the parameter h_i, which represents the average size of an element. Hence, h_i has a dimension of length (cm, for instance) and is calculated as follows:

$$h_i = \sqrt{\frac{A_i}{n_{elem}^i}} \tag{7.23}$$

where A_i is the total area of the surface i. n_{elem}^i is the number of knot spans in the surface i, which is given by $n_{elem}^i = (m-p)(n-q)$. Thus, the updated h_i^{up} is as follows:

$$h_i^{up} = \frac{h_i}{(\xi_i)^{1/p}} \quad , \quad \text{se} \quad \xi_i > 1 \tag{7.24}$$

in which p is a convergence parameter, which can be adopted as the mesh order of approximation (17). For IGA models, p is adopted as the higher value between p and q. The ξ_i considered herein is the higher value between ξ_i^u and ξ_i^t from Eq. 7.22.

The resulting h_i^{up} determines the number of knots to be inserted on each NURBS surface. This number is chosen so that the resulting knot spans have a real dimension as close to h_i^{up} as possible.

7.4 NURBS refinement process: knot insertion

The knot insertion process allows increasing the NURBS mesh density in a procedure analogous to the h-refinement of the isoparametric approaches. With that, the approximation is improved by having more knot spans and control points, without modifying the NURBS geometry. Therefore, one achieves a more refined mesh with a geometry model as exact as the original one. More details about this formulation can be found in the literature (16).

Let $\Xi = \{\xi_1,...,\xi_{n+p+1}\}$ and $\mathfrak{N} = \{\eta_1,...,\eta_{m+q+1}\}$ be the knot vectors of a NURBS surface in the parametric directions u and v, respectively. One may insert an addition knot in any of u or v in a analogous procedure. Let $\bar{\xi} \in [\xi_1, \xi_{n+p+1}[$ be the knot inserted into the u direction. One defines the coordinate $\mathbf{Q}_i = \{x_1^i w_i, x_2^i w_i, x_3^i w_i, w_i\}$ based on the current control points positions x_j^i and weights w_i.

Inserting $\bar{\xi}$ generates an updated $\bar{\mathbf{Q}}_i$ as follows:

$$\bar{\mathbf{Q}}_i = \alpha_i \mathbf{Q_i} + (1 - \alpha_i)\mathbf{Q}_{i-1} \tag{7.25}$$

in which:

$$\alpha_i = \begin{cases} 1 & i \leq k - p \\ \dfrac{\bar{\xi} - \xi_i}{\xi_{i+p} - \xi_i} & k - p + 1 \leq i \leq k \\ 0 & i \geq k + 1 \end{cases} \tag{7.26}$$

where k denotes the knot span in which $\bar{\xi}$ is inserted, i.e., the smallest interval $\bar{\xi} \in [\xi_k, \xi_{k+1}[$. p is the NURBS order in the u direction.

$\bar{\mathbf{Q}}_i$ from Eq. 7.25 determines the new control points positions $\bar{x}_j^i$ and weights $\bar{w}_i$ by the following:

$$\bar{\mathbf{Q}}_i = \left\{\bar{x}_1^i \bar{w}_i,\, \bar{x}_2^i \bar{w}_i,\, \bar{x}_3^i \bar{w}_i,\, \bar{w}_i\right\} \tag{7.27}$$

One may insert a knot $\bar{\eta}$ into the other NURBS parametric direction v by simply reapplying this procedure considering the knot vector $\mathfrak{N}$. Figure 108 illustrates the knot insertion in a given NURBS surface (a) on both directions u (b) and v (c).

Figure 108 – Example of NURBS refinement by knot insertion on both directions u and v.

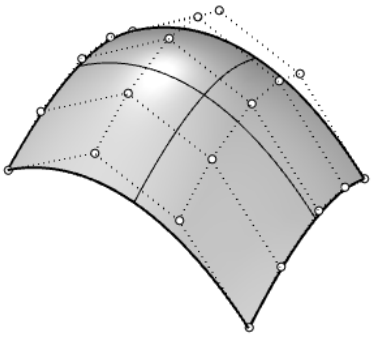

(a) Original surface

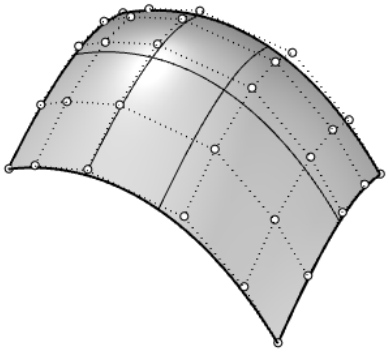

(b) Knot insertion in u direction

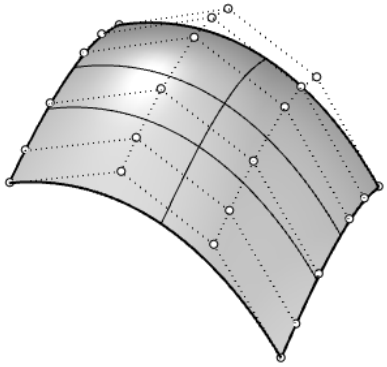

(c) Knot insertion in v direction

The knot insertion process is adequate to produce NURBS surfaces uniformly refined. Figure 108 demonstrates that inserting a knot in one parametric direction creates not only a new cell but a new row of cells in the respective new knot span. Therefore, the NURBS is not refined by region but by rows and columns of cells. With that, it is not possible to create a NURBS surface locally refined by this process only.

The literature presents some alternatives to produce locally refined NURBS surfaces, which often use different B-splines formulations (such as hierarchical or T-constructions) or propose splitting the NURBS surfaces or the tensor-product between $\boldsymbol{\Xi}$ and $\mathfrak{N}$ (174, 175, 176). In order to maintain the regular NURBS surfaces formulation of this study, the NURBS refinement is performed uniformly by the knot insertion process. The inserted knots $\bar{\xi}$ and $\bar{\eta}$ are calculated to obtain a uniform subdivision of the exiting knot spans in $\boldsymbol{\Xi}$ and $\mathfrak{N}$. In the adaptive scheme, Eq. 7.24 defines the required number of knots inserted into each NURBS surfaces.

7.5 Adaptive scheme for reinforced cracked solids

In order to properly access a adaptive scheme for reinforced cracked solids, the Dual BEM strategy must be coupled with the 1DBEM/IGABEM technique. The Dual BEM strategy (14) enables the representation of physical discontinuities (cracks) by discretising

both faces (denoted by Γ_f^* and Γ_f^-) with coincident NURBS surfaces, as presented in Sec. 2.8. Then, Eq. 2.84 replaces Eq. 3.5 into the 1DBEM/IGABEM coupling formulation, as follows:

$$\mathbf{H_{CC}u_C} = \mathbf{G_{CC}p_C} + \mathbf{G_{CF}f_D} \tag{7.28}$$

which is applied to the 1DBEM/IGABEM formulation, by defining the following vector and matrices grouping:

$$\mathbf{H_{CC}} = \begin{bmatrix} \mathbf{H} \\ \mathbf{H}^+ \\ \mathbf{H}^- \end{bmatrix} \quad , \quad \mathbf{u_C} = \begin{Bmatrix} \hat{\mathbf{u}} \\ \hat{\mathbf{u}}^+ \\ \hat{\mathbf{u}}^- \end{Bmatrix} \quad , \quad \mathbf{G_{CC}} = \begin{bmatrix} \mathbf{G} \\ \mathbf{G}^+ \\ \mathbf{G}^- \end{bmatrix} \quad , \quad \mathbf{p_C} = \begin{Bmatrix} \hat{\mathbf{t}} \\ \hat{\mathbf{t}}^+ \\ \hat{\mathbf{t}}^- \end{Bmatrix} \tag{7.29}$$

Thus, the Dual BEM can be adequately represented in the 1DBEM/IGABEM traditional system of algebraic equations, as follows:

$$\begin{bmatrix} \mathbf{H_{CC}} & \mathbf{0} & -\mathbf{G_{CF}} \\ \mathbf{H_{FC}} & \mathbf{I} & -\mathbf{G_{FF}} \\ \mathbf{0} & \mathbf{K_F} & \mathbf{G_F} \end{bmatrix} \begin{Bmatrix} \hat{\mathbf{u}}_\mathbf{C} \\ \mathbf{u_F} \\ \mathbf{p_F} \end{Bmatrix} = \begin{bmatrix} \mathbf{G_{CC}} \\ \mathbf{G_{FC}} \\ \mathbf{0} \end{bmatrix} \left\{ \hat{\mathbf{t}}_\mathbf{C} \right\} \tag{7.30}$$

The application of the displacements and strains based error estimators for this formulation requires some careful considerations. Such error estimators provide point-wise error values at the boundary Then, the TBIE can be applied for boundary points in Eq. 7.30 by replacing its first line. It is worth mentioning that, for the crack face, this procedure means exchange the crack face that receives the TBIE and the one that receives the DBIE.

However, the same technique cannot be applied to assess the errors at the reinforcements, since the equivalent TBIE (or hypersingular form) for the 1DBEM is simply an equilibrium relation. Thus, such expression cannot be coupled in the algebraic system of equations (Eq. 7.30), since it does not address properly the fibres' displacements.

Therefore, the present study proposes the use of FEM/IGABEM coupling technique to provide an adequate point-wise a posteriori error estimate at the reinforcements. Then, FEM truss elements model the reinforcements in the FEM/IGABEM approach, which replaces the use of the hypersingular form in the error estimates along the reinforcements. Thus, Eq. 7.1 may be replaced by the following:

$$\begin{bmatrix} \mathbf{H_{CC}} & \mathbf{0} & -\mathbf{G_{CF}} \\ \mathbf{H_{FC}} & \mathbf{I} & -\mathbf{G_{FF}} \\ \mathbf{0} & \mathbf{K}_{\text{1DBEM}} & \mathbf{G}_{\text{1DBEM}} \end{bmatrix} \begin{Bmatrix} \hat{\mathbf{u}}_\mathbf{S} \\ (\mathbf{u_F})_\mathbf{S} \\ (\mathbf{f_F})_\mathbf{S} \end{Bmatrix} = \begin{bmatrix} \mathbf{G_{CC}} \\ \mathbf{G_{FC}} \\ \mathbf{0} \end{bmatrix} \left\{ \hat{\mathbf{t}}_\mathbf{S} \right\} \tag{7.31}$$

$$\begin{bmatrix} \mathbf{H'_{CC}} & \mathbf{0} & -\mathbf{G'_{CF}} \\ \mathbf{H_{FC}} & \mathbf{I} & -\mathbf{G_{FF}} \\ \mathbf{0} & \mathbf{K}_{\text{FEM}} & \mathbf{G}_{\text{FEM}} \end{bmatrix} \begin{Bmatrix} \hat{\mathbf{u}}_\mathbf{H} \\ (\mathbf{u_F})_\mathbf{H} \\ (\mathbf{f_F})_\mathbf{H} \end{Bmatrix} = \begin{bmatrix} \mathbf{G'_{CC}} \\ \mathbf{G_{FC}} \\ \mathbf{0} \end{bmatrix} \left\{ \hat{\mathbf{t}}_\mathbf{H} \right\} \tag{7.32}$$

where $\mathbf{K}_{\text{1DBEM}}$ and $\mathbf{G}_{\text{1DBEM}}$ are the 1DBEM influence matrices (182). $\mathbf{K}_{\text{FEM}}$ and $\mathbf{G}_{\text{FEM}}$ are the classical stiffness matrix and lumping matrix, respectively, from the truss FEM formulation. The subscripts **S** and **H** indicate the singular and hypersingular solutions, which have been used to evaluate the error estimator. The FEM matrices are as follows:

$$(\mathbf{K}_{\text{FEM}})_{ij} = \int_0^L EA\,\phi_{i,\bar{x}}(\bar{x})\phi_{j,\bar{x}}(\bar{x})d\bar{x} \tag{7.33a}$$

$$(\mathbf{G}_{\text{FEM}})_{ij} = \int_0^L \phi_i(\bar{x})\phi_j(\bar{x})d\bar{x} \tag{7.33b}$$

It is worth mentioning that the second expression of the linear system (Eq. 7.31 and Eq. 7.32) remains unmodified for both the singular and the hypersingular systems. This expression is a displacements integral equation for internal nodes, for which the equivalent hypersingular form would provide stresses instead of displacements. Besides, this equation handles the displacements compatibility between the domain points and fibres points. Therefore, it can be kept unmodified.

The above-presented procedures for the adaptive strategy can be applied taking into account the reinforcement elements. Particularly, the adaptive scheme for the reinforcements leads to a resulting h_i^{up} (from Eq. 7.24) value for each reinforcement element i. Then, the subdivision process of these elements is trivial, since each 1D element is sub-divided into integer number of sub-elements, which result elements size as close to h_i^{up} as possible.

7.5.1 Numerical Applications for convergence analysis

This section presents the analysis of five different numerical applications. Such examples validate the proposed error estimators and adaptive strategies by comparing the mechanical results with reference models and analysing the convergence versus globally refinement process.

7.5.2 Application 1: Homogeneous fixed beam

This application handles the mesh convergence analysis of the structure illustrated in Fig. 109. The solid is under a continuous distribuited load of 1 kN/cm^2, as illustrated in Fig. 109(a). The material and geometrical properties are: Young's modulus of 500 kN/cm^2, nil Poisson's ratio, solid's length in the axial direction equals 5 cm and squared cross-section of 1x1 cm. The exact geometric model is composed by 6 bi-quadratic regular NURBS surfaces and a total of 54 collocation points, as illustrated in Fig. 109(b).

A tolerance $\bar{\eta}_u = 10^{-2}$ is considered for the faces in which tractions are prescribed, otherwise the tolerance is $\bar{\eta}_t = 3 \cdot 10^{-2}$. The adopted ratio $\bar{\eta}_t/\bar{\eta}_u$ is determined by the initial normalised errors $||e_u||$ and $||e_t||$ obtained in the geometrical model illustrated in Fig. 109(a).

Figure 109 – Structure analysed in Application 1.

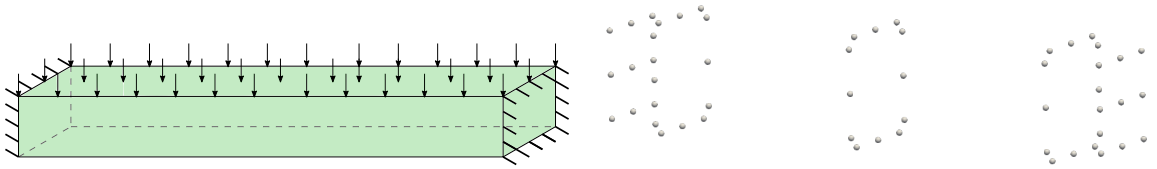

(a) Mechanical model (b) Geometric model

Source: The author.

Figure 110 illustrates the comparison between the proposed Adaptive refinement and a homogeneous refinement, concerning the total global errors $||e_G||$. The homogeneous refinement establishes that all NURBS surfaces are equally refined in both directions at all iterations, regardless of the obtained error values.

Figure 110 – Convergence of Application 1.

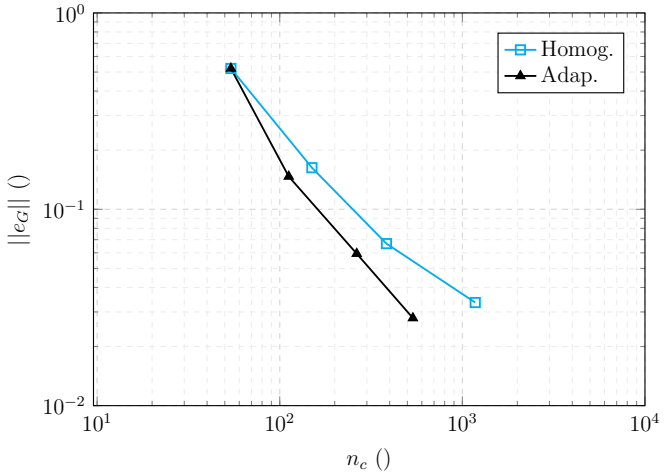

Source: The author.

The final meshes obtained by the Adaptive refinement and by the homogeneous refinement are illustrated in Fig. 111(b) and Fig. 111(a). The final meshes contain, respectively, 536 and 1176 collocation points.

Figure 111 – Final control points meshes obtained in Application 1

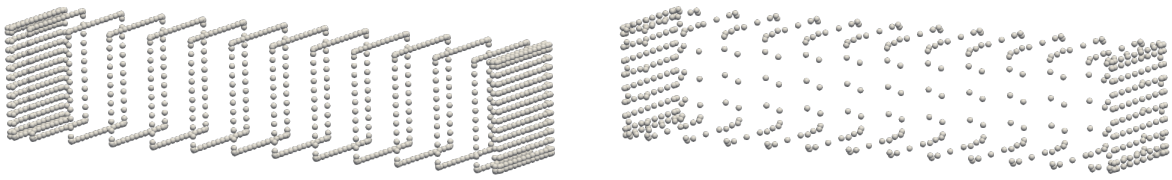

(a) Homogeneous refinement (b) Adaptive refinement

Source: The author.

One observes that the Adaptive refinement achieved a final mesh with less than half collocation points in relation to the homogeneous' final mesh. In addition, the obtained

final error is slightly smaller (0.0084 against 0.0105, respectively). Therefore, the proposed Adaptive scheme was significantly more efficient than a homogeneous refinement, leading to a more accurate model with fewer degrees of freedom.

A pure FEM model was constructed in Ansys to attest the accuracy of the obtained results, since this application handles a simple geometry. The FEM model is composed by 27152 nodes and considers the geometry's symmetry property along the transverse direction (orthogonal to the applied load orientation). Mesh convergence has been verified, regarding displacements and strains at the boundary.

Figure 112 illustrates the comparison between the displacement modulus obtained by the final mesh from the Adaptive scheme, the reference Ansys model and the initial mesh. Figure 113 illustrates similar comparison, considering the strains L2 norm.

One observes good agreement between the results obtained by the final mesh from the Adaptive scheme (Fig. 112(a), Fig. 113(a)) and the reference (Fig. 112(b), Fig. 113(b)). In addition to the accuracy in the mechanical fields distribution, one also notices a maximum difference between these results equal to 0.38% and 4% in displacements and strains, respectively. On the other hand, the initial mesh results (Fig. 112(c), Fig. 113(c)) were less precise, with a significant 34% difference in displacements regarding the reference. Besides, its strains distribution field is clearly poor and inaccurate. In spite of being geometrically exact, it is evident that the initial mesh is not adequate to be used in the mechanical analysis.

Figure 112 – Displacement modulus obtained by the final mesh of the Adaptive scheme (a), by the reference Ansys model (b) and by the initial mesh (c).

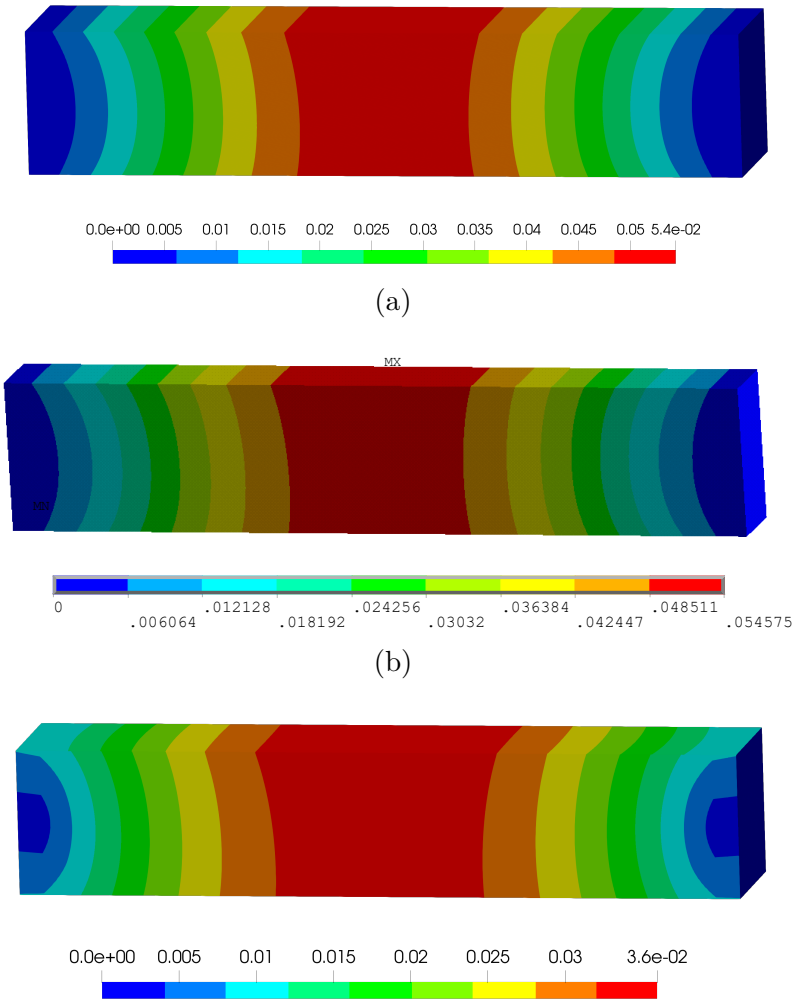

Source: The author.

The final $||e_G||$ obtained via the Adaptive scheme is 0.84%, as above-mentioned. Whereas the maximum difference observed between the displacement results in Fig. 112 is 0.38%. Despite these values not being coincident, the error estimator accomplished its objective. The most important aspect of the error estimator is not its accuracy in value, but its ability to foresee the required refinement on each surface. Thus, the adopted error estimator efficiently led to the accurate results observed in Fig. 112 and Fig. 113, with a more efficient mesh than the one obtained through the homogeneous refinement.

Figure 113 – Strains L2 norm obtained by the final mesh of the Adaptive scheme (a), by the reference Ansys model (b) and by the initial mesh (c).

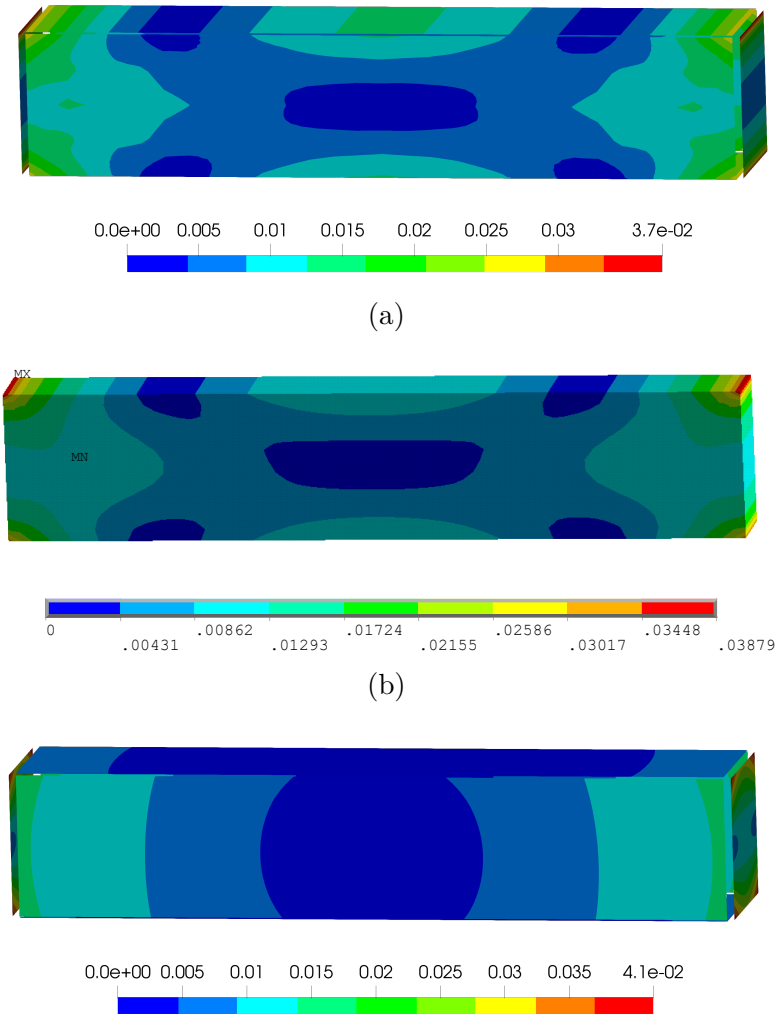

Source: The author.

7.5.3 Application 2: Nonhomogeneous 3D structure

This application handles the Adaptivity analysis of the nonhomogeneous structure illustrated in Fig. 114(a). The domain II of the solid model represents a thick-walled tube and domain I represents a support, which is fixed in its bottom face. The material properties of I are: Young's modulus $E_I = 200$ GPa and Poisson's ratio $\nu_I = 0.2$. The material properties of II are: Young's modulus $E_{II} = 220$ GPa and Poisson's ratio $\nu_{II} = 0.3$. The applied load is $\mathbf{q} = 10$ kN/cm^2.

Figure 114(b) illustrates the exact geometric model, which is composed by 32 6 bi-quadratic regular NURBS surfaces and a total of 140 collocation points. This model considers the symmetry property of the structure in the direction x.

Figure 115 illustrates the convergence analysis of this example. A tolerance of

Figure 114 – Structure analysed in Application 2.

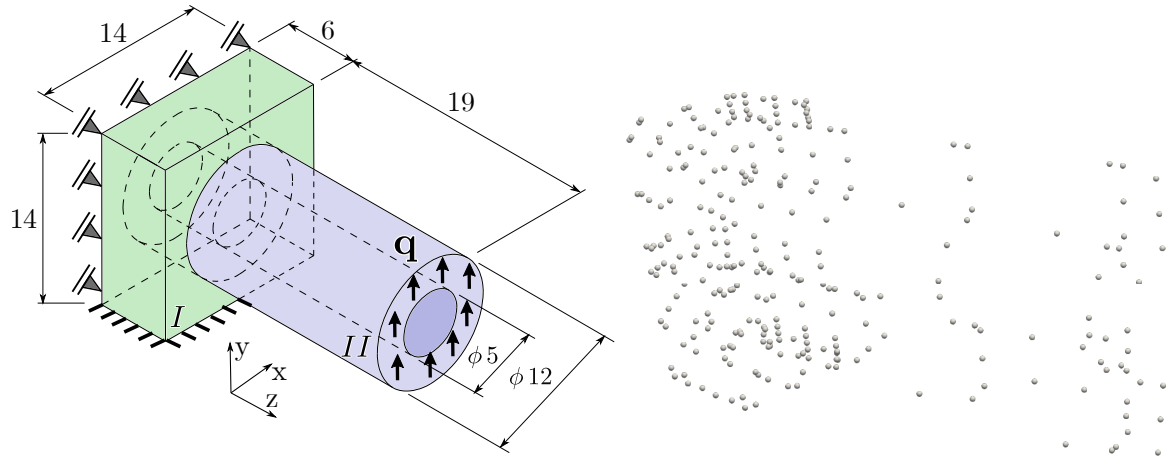

(a) Mechanical model (b) Geometric model with symmetry (collocation points)

Source: The author.

$\bar{\eta}_u = 0.05$ is considered for the faces in which displacements are unknown, otherwise one considers $\bar{\eta}_t = 0.03$. The adopted ratio $\bar{\eta}_t/\bar{\eta}_u$ is determined by the ratio between the initial normalised errors $||e_u||$ and $||e_t||$. Figure 115(a) illustrates the results obtained by considering the proposed error estimator based on strains. Figure 115(b) illustrates the results obtained by considering the hypersingular error estimator based on displacements.

Figure 115 – Convergence graphs of Application 2 considering two different error estimators.

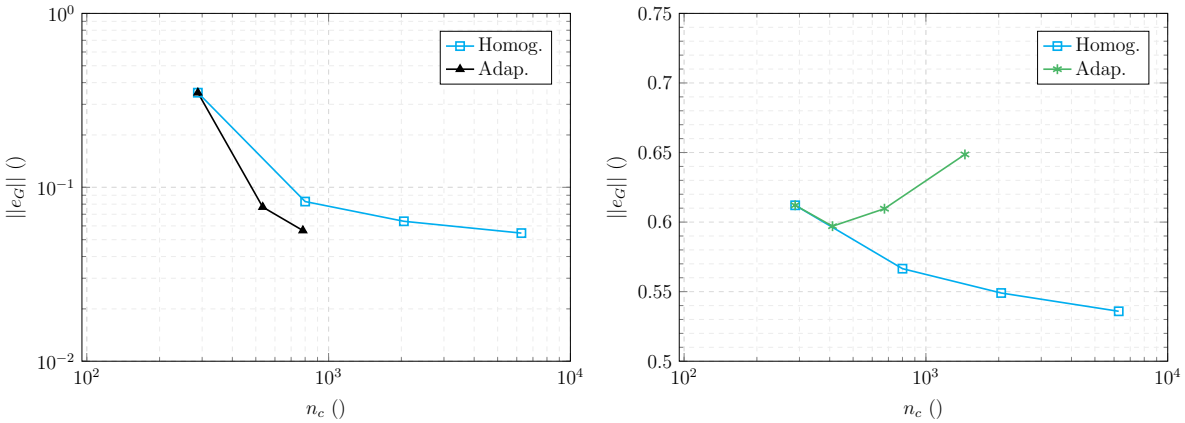

(a) Error estimator based on strains (b) Error estimator based on displacements

Source: The author.

A point p_1 and a line L_1 are selected at the boundary of the structure to illustrated the obtained mechanical fields results. Figure 116 exhibits the position of those. Figure 117 shows the modulus of the displacements at p_1 throughout the Adaptive and homogeneous refinement processes. One observes that the Adaptive refinement with the strains error estimator results follow the homogeneous refinement results, however it presents fewer

collocation points in all iterations. The Adaptive refinement with the displacements error estimator, on the other hand, produces results that does not agree with the homogeneous refinement nor converge with it in all iterations.

Figure 116 – Position of L_1 and p_1 at the boundary of the structure.

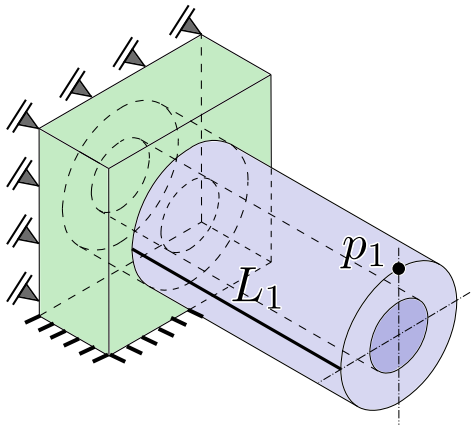

Source: The author.

Figure 117 – Displacement modulus at p_1 throughout the Adaptive and homogeneous refinement processes.

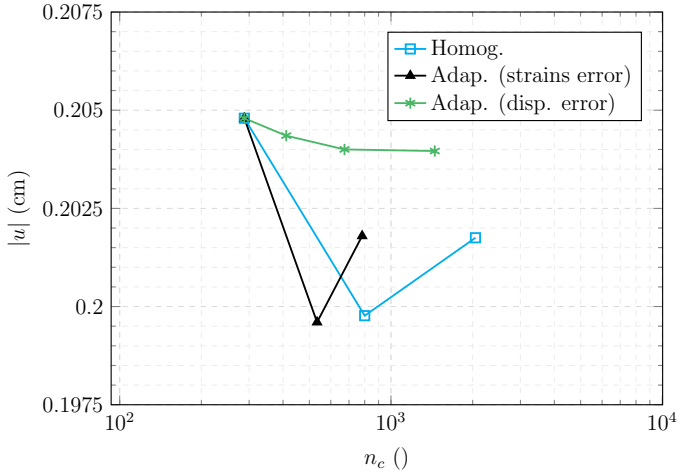

Source: The author.

Figure 118 – Final control points meshes obtained in Application 2.

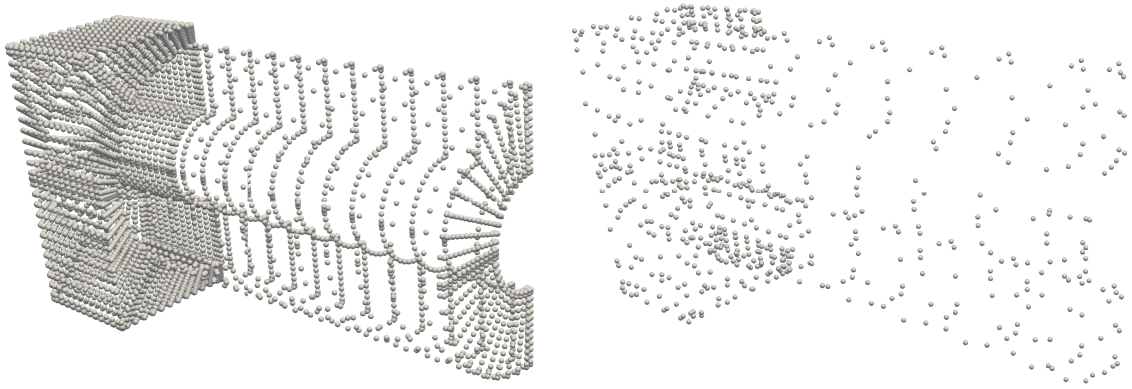

(a) Homogeneous refinement

(b) Adaptive refinement with the error estimator based on strains

(c) Adaptive refinement with the error estimator based on displacements

Source: The author.

For the next results analyses, the final homogeneous mesh (illustrated in Fig. 118(a)) is considered as a reference, since it is the most refined available and shows the minimum error values (Fig. 115(a)). In addition, the following three meshes M0, M1 and M2 are further analysed:

- M0: initial mesh, illustrated in Fig. 114(b);
- M1: Final mesh obtained in the Adaptive refinement with the error estimator based on strains, illustrated in Fig. 118(b);
- M2: Final mesh obtained in the Adaptive refinement with the error estimator based on displacements, illustrated in Fig. 118(c).

Figure 119 illustrates the displacement modulus difference observed between each one of M0, M1 and M2 meshes in relation to the above-mentioned reference mesh. This graph is a function of the line L_1 length S_l, which is illustrated in Fig. 114(a). The colour map of these differences over the external boundaries is also illustrated in Fig. 120.

Figure 119 – Difference in displacement modulus along L_1 obtained by meshes M0, M1 and M2 in relation to the homogeneous reference mesh.

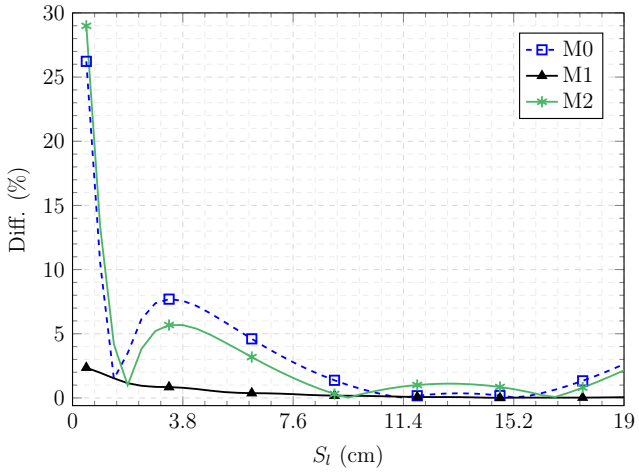

Source: The author.

One observes in Fig. 119 and 120 that M1 definitely produces the results closer to the reference results among the three analysed meshes.

Figure 121 illustrates the colour map of the displacement modulus obtained by M1 and the final homogeneous mesh. These figures illustrates the deformed structure with a scale factor equals 10. One observes a excellent agreement between these results, although M1 is composed by significantly fewer collocation points.

Figure 121 – Colour map of displacement modulus obtained by M1 (a) and the final homogeneous mesh (b).

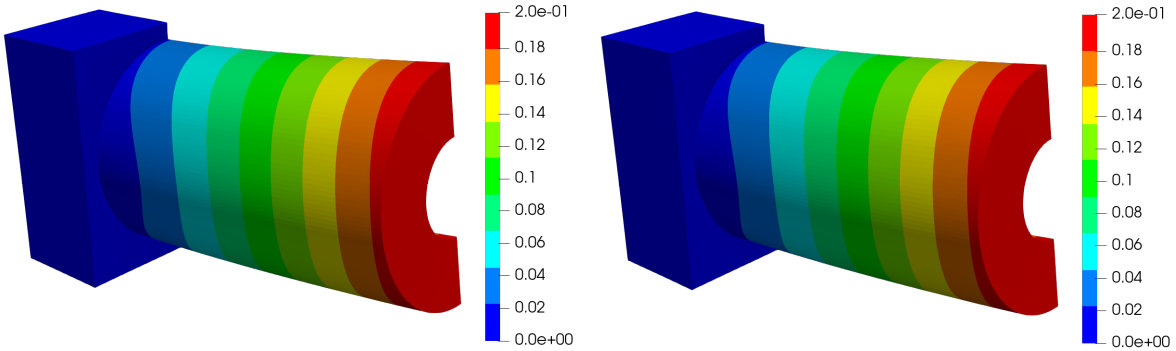

(a) (b)

Source: The author.

7.5.4 *Application 3: Reinforced Quarter Cylinder*

This application handles the mesh convergence analysis of the reinforced structure illustrated in Fig. 122, which exhibits the mechanical model and its dimensions. The prescribed displacements are $\bar{\mathbf{u}}_\mathbf{y} = \bar{\mathbf{u}}_\mathbf{x} = 0.5$ cm. The solid presents a Young's modulus of

Figure 120 – Colour map of displacement modulus difference obtained by meshes M0, M1 and M2 in relation to the homogeneous reference mesh.

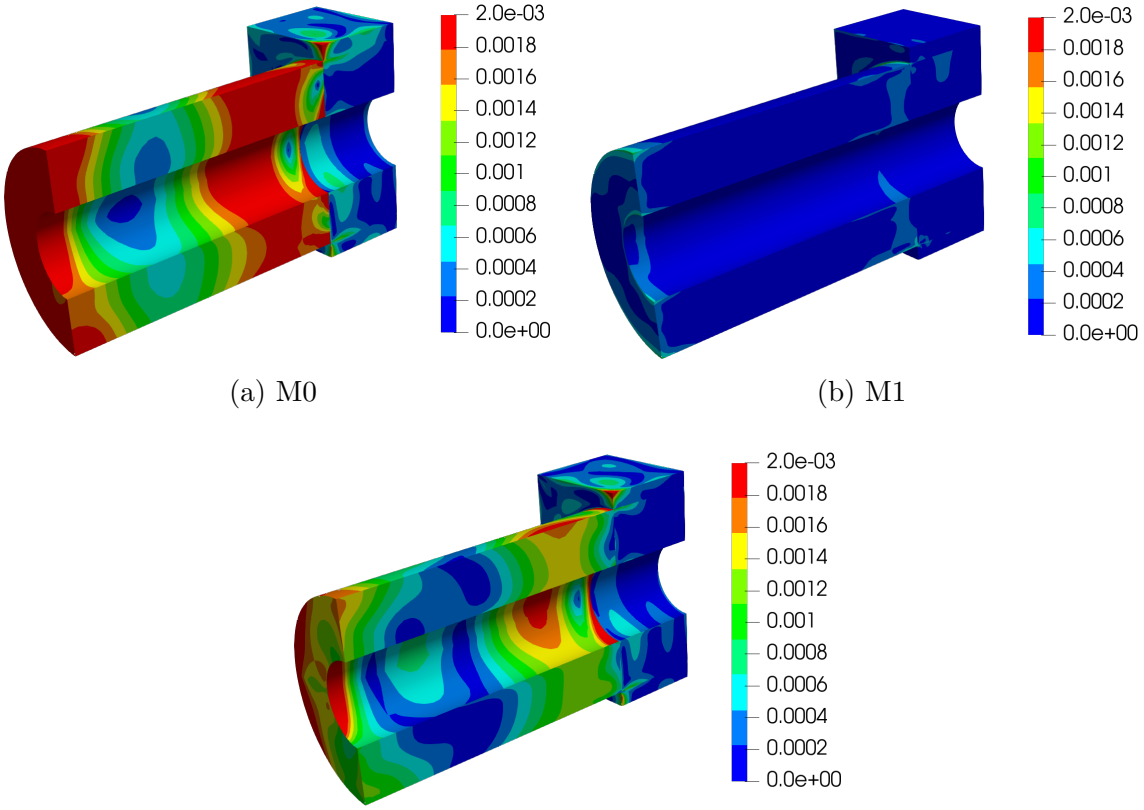

(a) M0 (b) M1

(c) M2

Source: The author.

100 kN/cm^2 and nill Poisson ratio. The reinforcements have a Young's modulus of 200 kN/cm^2 and a circular transverse section with radius equal 0.2 cm.

Figure 123 illustrates the initial mesh. The boundary isogeometric mesh (Fig. 123(a)) is composed by 6 bi-quadratic regular NURBS surfaces and a total of 54 collocation points. 4 quadratic elements discretize each one of the long reinforcing fibres, which leads to a total of 54 nodes as illustrated in Fig. 123(b).

The Adaptive refinement analysis of this example applies both the proposed strains based error estimator and the displacements based error estimator. For the first case, a tolerance of $\bar{\eta}_u = 0.015$ is considered for the surfaces in which tractions are prescribed (nill or not), otherwise the tolerance is $\bar{\eta}_t = 0.025$. For the second case, the tolerances are $\bar{\eta}_u = 0.015$ and $\bar{\eta}_t = 0.075$. In both cases, the tolerance for the reinforcements error is $\bar{\eta}_R = 0.015$. The adopted ratios $\bar{\eta}_t/\bar{\eta}_u$ are determined by the observed error values $||e_u||$ and $||e_t||$ obtained with the homogeneous refinement process.

Figure 124 illustrates the comparison between the proposed Adaptive refinement and a homogeneous refinement, regarding the convergence of the total global errors $||e_G||$. The analyses considering the error estimator based on strains and based on displacements

Figure 122 – Reinforced structure analysed in Application 3.

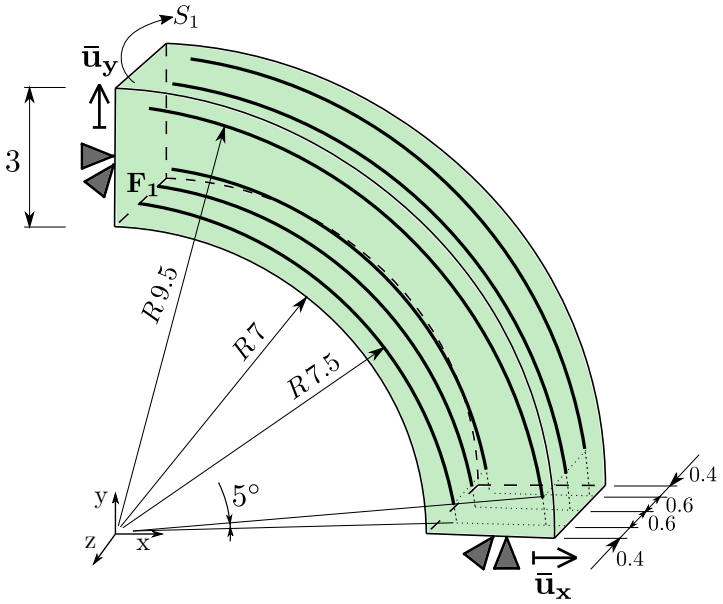

Source: The author.

Figure 123 – Geometric initial models of Application 3.

(a) Boundary model (b) Fibres model

Source: The author.

are illustrated in (a) and (b), respectively. As previously mentioned in the firs application, the homogeneous refinement establishes that all NURBS surfaces are equally refined at all iterations and consequently does not depend on the error estimator considered.

Figure 124(a) shows the convergence of the processes considering the strains based error estimator. The final mesh obtained by the Adaptive refinement contains 150 reinforcements nodes and 546 collocation points at the boundary, with a total of 696 collocation points. The final mesh obtained by the homogeneous refinement is composed by 1176 collocation points at the boundary and 390 reinforcements nodes, which leads to a total of 1566 collocation points. The final values of $||e_G||$ are 0.027 and 0.0268, respectively.

Figure 124(b) shows the convergence of the processes considering the displacements based error estimator. In this case, the Adaptive refinement does not achieve convergence, in

Figure 124 – Convergence graphs of Application 3 considering two different error estimators.

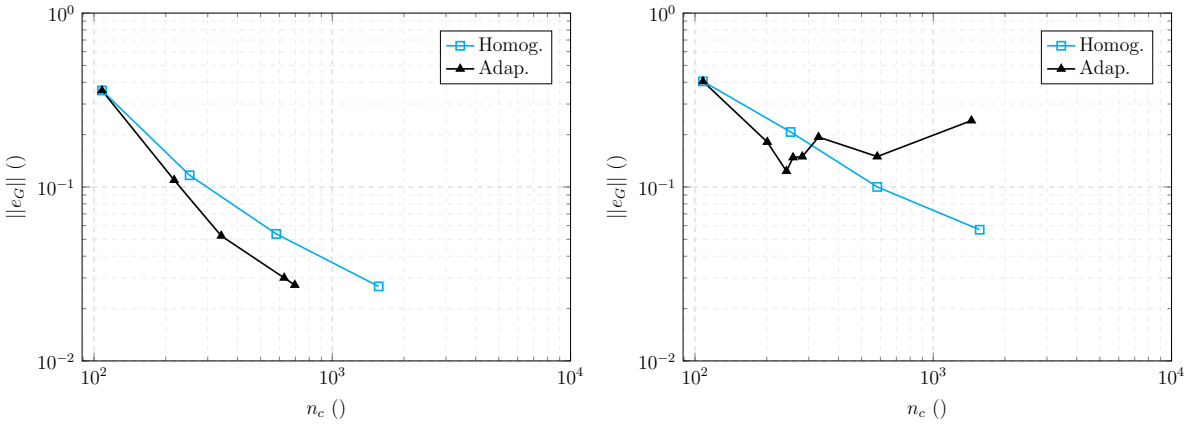

(a) Error estimator based on strains (b) Error estimator based on displacements

Source: The author.

fact the total error value increases in some iterations. Therefore, the iterative process stops at the eighth iteration due to computational limitations, even though the the prescribed tolerances are not achieved. The homogeneous refinement produces the same 4 iterations illustrated in Fig. 124(a), which is also not enough to get the prescribed tolerances (only $\bar{\eta}_t$ was achieved).

It is worth comparing the homogeneous refinement processes illustrated in Fig. 124(a) and Fig. 124(b). Despite the homogeneous meshes be the same regardless of the chosen error estimator, Fig. 124(a) exhibits a smaller final $||e_G||$ value after the four iterations (2.682% against 5.68%). Since the strains based error estimator has already been evaluated by the previous applications, there is a chance that the displacements based error estimator is over-estimating the error values at some surfaces. This fact could also explain why the Adaptive process does not find convergence when this error estimator is considered.

In this regard, Fig. 125 illustrates each one of the portions of the error ($||e_t||$ in tractions, $||e_u||$ in displacements and $||e_R||$ at the reinforcements). Whereas Fig. 125(a) demonstrates a balance between the error portions when the strains based error estimator is used, Fig. 125(b) shows that the $||e_t||$ portion is preponderant when the displacements based error estimator is considered.

Figure 125 – Convergence of each portion of the error in the Adaptive refinement, considering the two different error estimators.

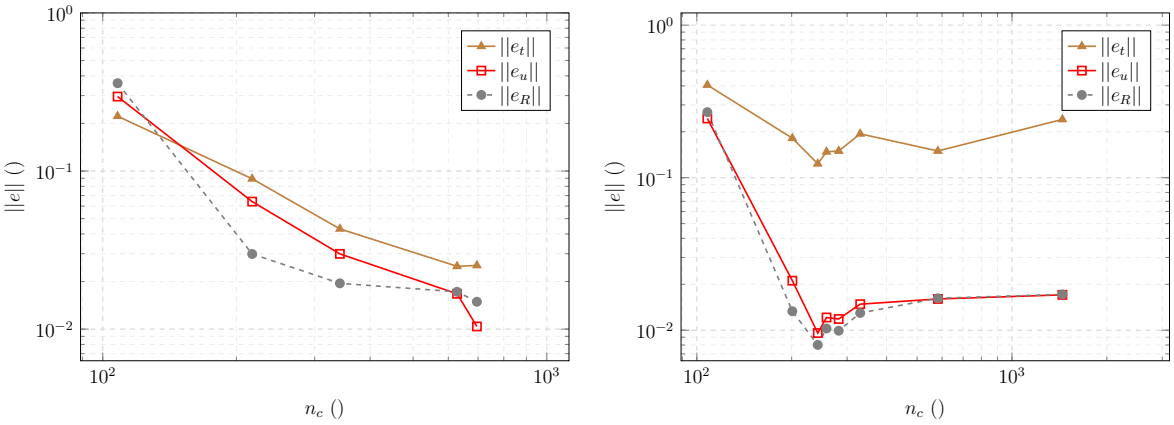

(a) Error estimator based on strains (b) Error estimator based on displacements

Source: The author.

To illustrate the results of the refinement processes, the following meshes are considered for the next analyses:

- M0: initial mesh, illustrated in Fig. 123;
- M1: Final mesh obtained in the Adaptive refinement with the error estimator based on strains;
- M2: Final mesh obtained in the Adaptive refinement with the error estimator based on displacements;
- M3: Final mesh obtained in the homogeneous refinement after 4 iterations, which does not depend on the error estimator considered.

Figure 126 illustrates the final reinforcement meshes obtained with the homogeneous refinement (a), the Adaptive refinement with the strains based error estimator (b) and the Adaptive refinement with the displacements based error estimator (c). Figure 127 exhibits the final boundary meshes considering the same three cases.

Regarding the reinforcements, Fig. 126(b) demonstrates that M1 was able to produce more refinement near the long fibres ends. This behaviour is explained by the oscillation results observed at these regions, as previously mentioned in this study. This oscillations decrease in most refined meshes, which was properly identified by the Adaptive refinement considering the strains based error estimator. On the other hand, the displacements based error estimator was not able to identify this necessity, which led to the homogeneously refined reinforcement mesh M2 observed in Fig. 126(c). As showed by Fig. 125, M2 did not produce error values as good as M1.

Figure 126 – Final reinforcements meshes obtained in Application 3.

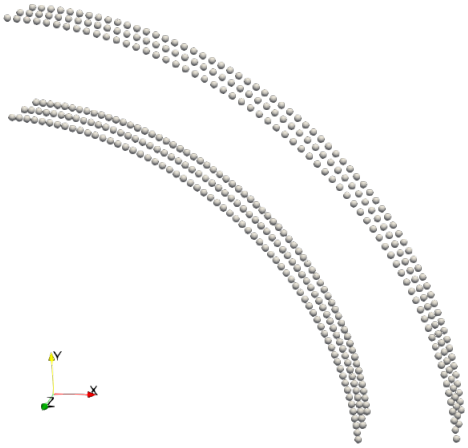

(a) Homogeneous refinement (M3)

(b) Adaptive refinement with the strains based error estimator (M1)

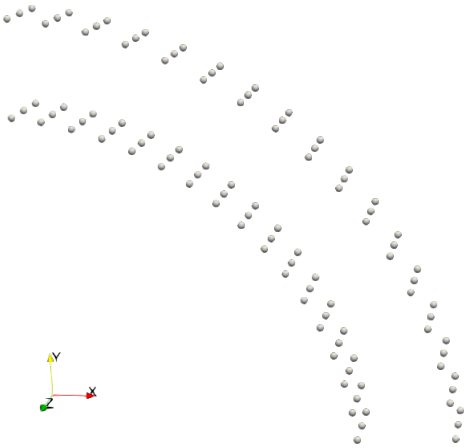

(c) Adaptive refinement with the displacements based error estimator (M2)

Source: The author.

Figures 127(b) and 127(a) demonstrate that the Adaptive process with the strains based error led to more efficient refinement. Especially considering that the final error values $||e_G||$ are basically the same in M1 and M3. In addition, Fig. 127(c) shows the difficulties of the Adaptive refinement based on the displacements error estimator. Even though a significantly higher tolerance was set to tractions, the higher estimated values of $||e_t||$ observed in Fig. 125(b) led to a extremely thin and unnecessary refinement of the fixed surfaces. In fact, more refinement was necessary at the other surfaces, as illustrated by the meshes M1 and M3, which have lower values of error. Therefore, it is clear that $||e_t||$ is overestimated in relation to $||e_u||$ and $||e_R||$ by the displacements based error, which have disturbed the Adaptive refinement process.

Figure 128 illustrates the axial stress distribution throughout fibre $\mathbf{F_1}$ (illustrated in Fig. 122) as a function of its length S_f, obtained with M0, M1, M2 and M3. Only half of the fibre's length is illustrated in this graph, since the mechanical results are symmetric.

Figure 127 – Final boundary meshes obtained in Application 3.

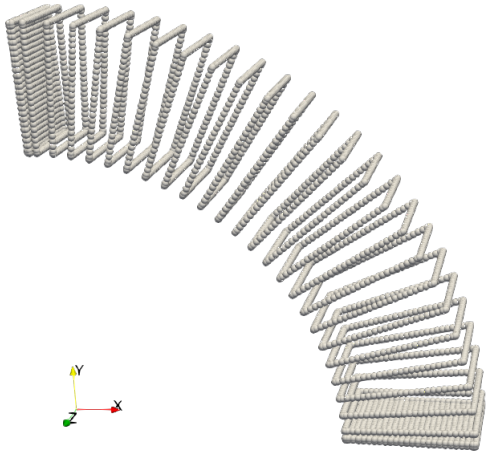

(a) Homogeneous refinement (M3)

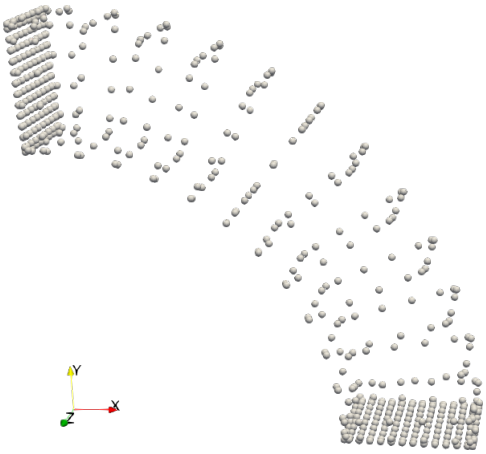

(b) Adaptive refinement with the strains based error estimator (M1)

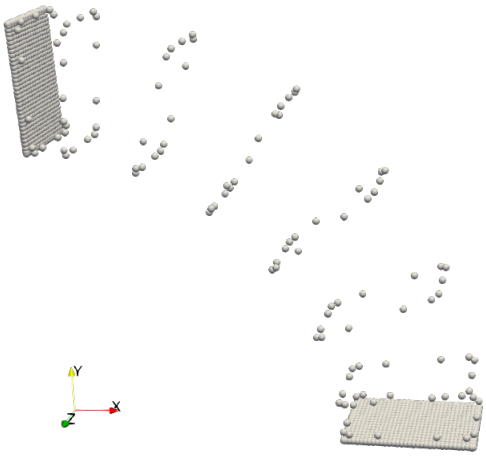

(c) Adaptive refinement with the displacements based error estimator (M2)

Source: The author.

One observes a good agreement between the results of M1 and M3, in which the oscillations are limited to a very small region near the long fibre ends. The M2 results were slightly better than the initial mesh M0, but the oscillations still cover a significant length of the fibre.

Figure 129 exhibits the tractions modulus distribution over the surface S_1, which is the surface that $\bar{\mathbf{u}}_\mathbf{y}$ is applied over (illustrated in Fig. 122). The results obtained by the four meshes M0, M1, M2 and M3 are illustrated. Once again, one observes a good agreement between the responses obtained by M1 and M3, wheres the initial mesh results (M0) are considerably different. This analysis consolidate the conclusions above-mentioned for Fig. 128. On the other hand, M2 shows traction results in disagreement with M1 and M3, despite having the surface S_1 much more refined in relation to the other meshes. Considering the good agreement between M1 and M3 in spite of their different number of collocation points, one can conclude that M2 results are not accurate.

Figure 128 – Axial stress along fibre $\mathbf{F_1}$ obtained by initial mesh and the final meshes from the Adaptive and homogeneous reinforcements.

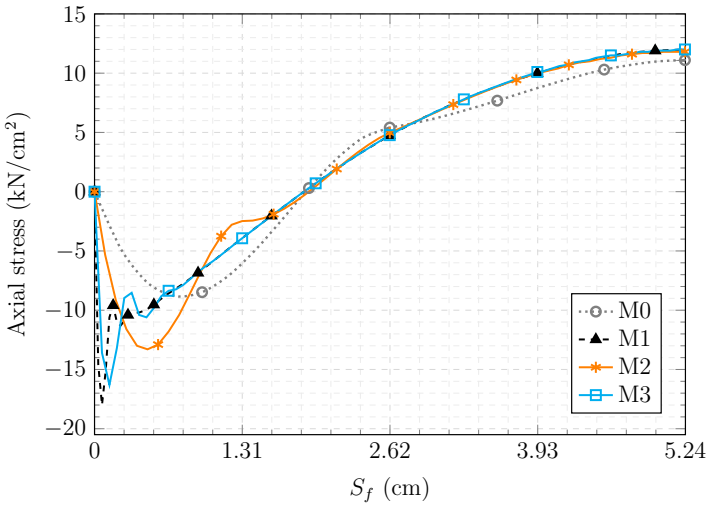

Source: The author.

7.5.5 *Application 4: Reinforced Cylinder with hole*

This application handles the mesh convergence analysis of the reinforced structure illustrated in Fig. 130, which exhibits the mechanical model and its dimensions. This structure consists of a solid cylinder with a central squared hole and reinforced by four long fibers positioned in the plane $z = 0$. The applied loads are $\mathbf{q_x} = 5$ kN/cm^2 and $\mathbf{q_y} = 0.5$ kN/cm^2. The solid presents a Young's modulus of 3000 kN/cm^2 and Poisson ratio $\nu = 0.2$. The reinforcements have a Young's modulus of 22000 kN/cm^2 and a circular transverse section with radius equal 0.3 cm.

Figure 131 illustrates the initial mesh. The boundary isogeometric mesh (Fig. 131(a)) is composed by 18 bi-quadratic regular NURBS surfaces and a total of 88 collocation points. 3 quadratic elements discretize each one of the long reinforcing fibres, which leads to a total of 28 nodes as illustrated in Fig. 131(b).

The Adaptive refinement analysis of this example applies the proposed strains based error estimator with a tolerance of $\bar{\eta}_u = 0.01$ for the surfaces in which tractions are prescribed (nill or not), otherwise $\bar{\eta}_t = 0.06$. The tolerance for the reinforcement errors is $\bar{\eta}_R = 0.01$. The adopted ratio $\bar{\eta}_t/\bar{\eta}_u$ is determined by the observed error values $||e_u||$ and $||e_t||$ in the the homogeneous refinement process.

Figure 132 illustrates the comparison between the proposed Adaptive refinement and a homogeneous refinement, regarding the convergence of the total global error values $||e_G||$. As previously mentioned in the first application, the homogeneous refinement establishes that all NURBS surfaces are equally refined at all iterations and consequently does not depend on the error estimator considered. This figure demonstrates that the

Figure 129 – Distribution of the tractions modulus over surface S_1 obtained by initial mesh and the final meshes from the Adaptive and homogeneous reinforcements.

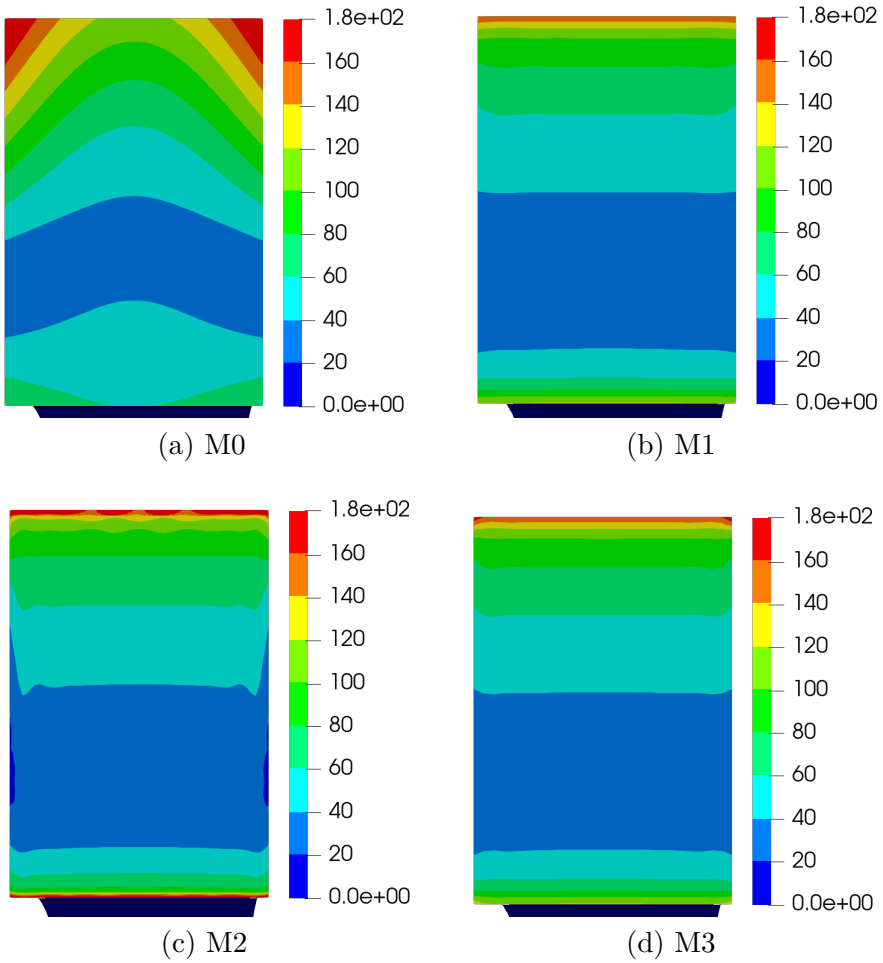

(a) M0 (b) M1

(c) M2 (d) M3

Source: The author.

Adaptive refinement is able to find a more efficient mesh for error values below 5%. In fact, the final error value in the Adaptive process is 3,77% with a total of 1761 collocation points, whereas the final error in the homogeneous refinement is 5,12% with 3528 collocation points.

Figure 133 illustrates the final reinforced meshes obtained in the homogeneous refinement process (a) and the Adaptive process (b). Firstly, one observes that the homogeneous process requires a much higher number of fibre's collocation points in order to achieve the prescribed tolerance. In addition, the Adaptive refinement of the fibres is a result of the applied loads, which produces a bending and tension behavior, together with the central hole's influence. So, the external fibres are more refined near the fixed surface, as a result of the bending behavior. Whereas the internal fibres are more refined near the central region, which is close to the squared hole present in the solid. Therefore, one concludes that the reinforcements were more significantly refined at the regions in which more stress is concentrated. At these regions, the fibres results tend to show the oscillation behavior, which truly explains a more required refinement.

Figure 130 – Reinforced structure analysed in Application 4.

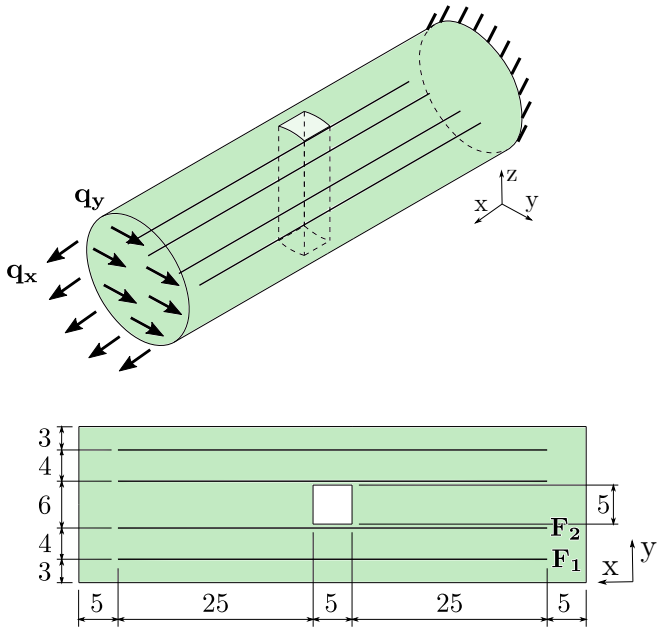

Source: The author.

Figure 131 – Geometric initial models of Application 4.

(a) Boundary model

(b) Fibres model

Source: The author.

Figure 134 illustrates the final boundary meshes obtained in the homogeneous refinement process (a) and the Adaptive process (b). As previously mentioned, the Adaptive process has achieved a mesh with half of the collocation points of the homogeneous mesh and a lower error value. This figure illustrates the efficiency of the Adaptive refinement, which was able to produce thinner refinement near the squared hole. This region presents stresses concentration that explains the required more refinement.

The final meshes produced by the homogeneous refinement and the Adaptive

Figure 132 – Convergence graph of Application 4

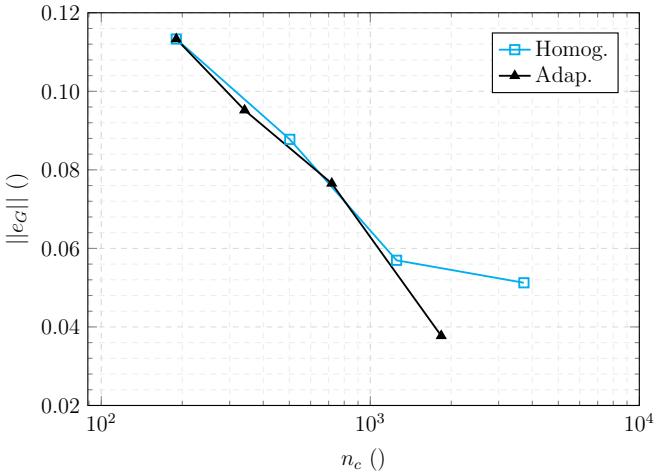

Source: The author.

Figure 133 – Final reinforcements meshes obtained in Application 4.

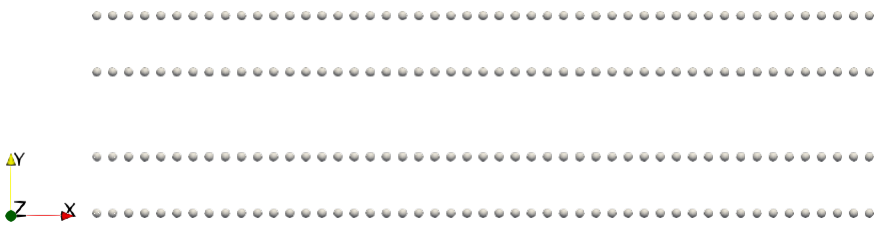

(a) Homogeneous refinement

(b) Adaptive refinement

Source: The author.

refinement are considered in the following figures by the names “Homog.” and “Adap.”, respectively. Figure 135 illustrates the final axial stress results along the fibres $\mathbf{F_1}$ and $\mathbf{F_2}$ lengths (S_f), obtained by the two mentioned meshes in addition to the initial mesh. One observes a good agreement between the refined meshes, although the Adaptive one has much less collocation points. On the other hand, the initial mesh presents significant oscillations throughout its entire length and was not able to accurately represents the expected mechanical behaviour. Furthermore, Fig. 135(b) exhibits a peak of axial stress in the central region, which is close to the solid’s squared hole. It is worth stressing that the Adaptive refinement was able to correctly represents this peak and minimise the oscillations related to it without need a mesh as refined as the homogeneous one.

Figure 134 – Final boundary meshes obtained in Application 4.

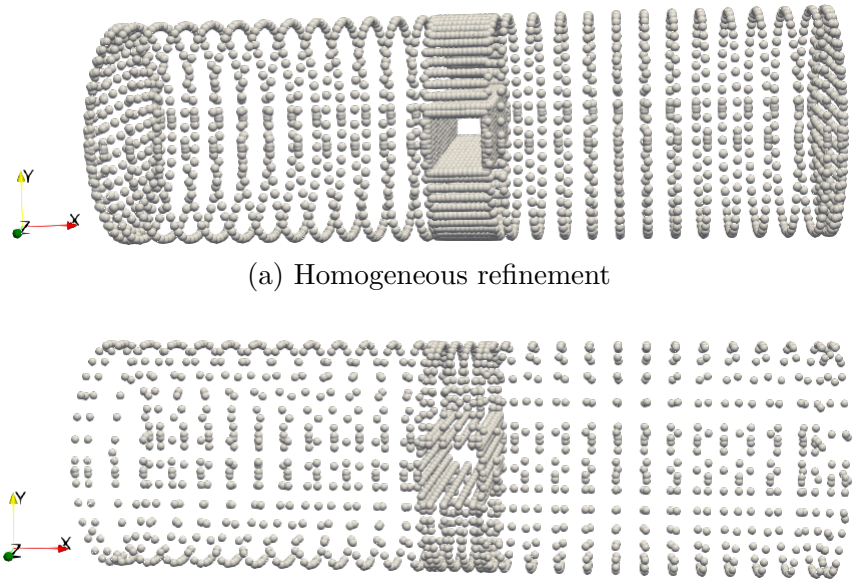

(a) Homogeneous refinement

(b) Adaptive refinement

Source: The author.

Figure 135 – Axial stress along fibres obtained by initial mesh and the final meshes from the Adaptive and homogeneous reinforcements.

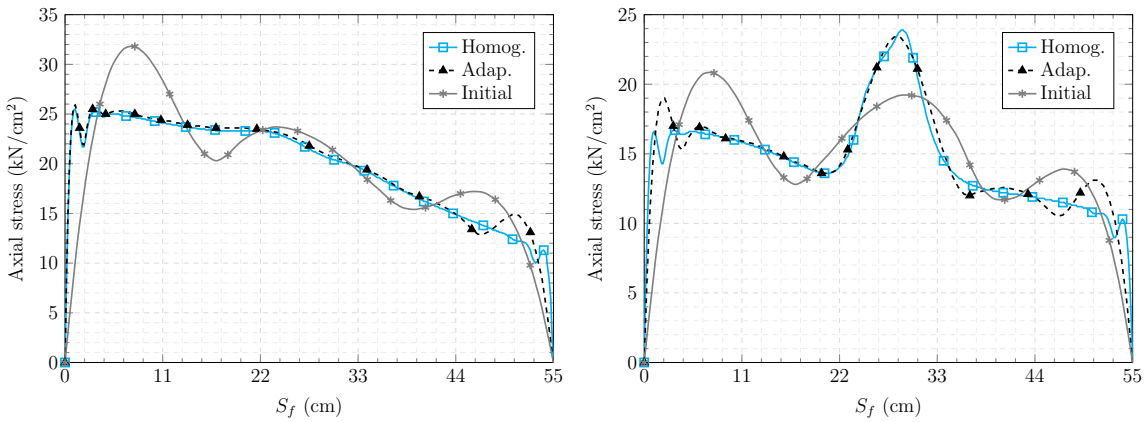

(a) $\mathbf{F_1}$ (b) $\mathbf{F_2}$

Source: The author.

Figure 136 shows the displacement modulus along the fibres $\mathbf{F_1}$ and $\mathbf{F_2}$ lengths (S_f), obtained by the three meshes. In this case, all of the three results are in agreement, even though the initial mesh results were definitely not precise in Fig. 135. Therefore, one concludes that the analysis of only displacements is not enough to truly evaluates the accuracy of the results obtained by a given mesh.

Figure 136 – Displacements modulus along fibres obtained by initial mesh and the final meshes from the Adaptive and homogeneous reinforcements.

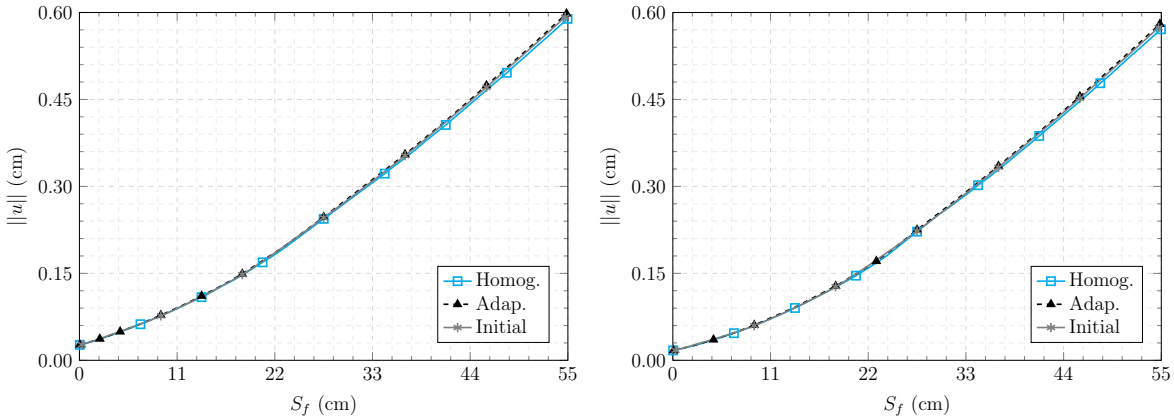

(a) $\mathbf{F_1}$ (b) $\mathbf{F_2}$

Source: The author.

Figure 137 illustrates the colour map of displacements modulus obtained by the final meshes from the Adaptive and the homogeneous refinement processes. A scale factor equals 10 is considered for the structure's deformed shape. This figure exhibits excellent agreement between the results obtained by these meshes. Thus, one demonstrates the accuracy of the Adaptive final mesh, even with less collocation points than the homogeneous final mesh.

7.5.5.1 Exemple 5: Convergence analysis of reinforced single-edge notched body

This application presents the adaptivity analysis of a single-edge notched body, which is reinforced by four long fibres, as illustrated in Fig. 138. The Dual BEM technique (14) has been utilised herein for the mechanical fields representation in the 3D IGABEM formulation. Two long fibres cross the crack surfaces, which can be represented by the fibre connection element technique, as previously proposed by the authors in the literature (132). The physical properties of the solid are: $h = 10$ cm, $b = 5$ cm, $a = 2.5$ cm, $\sigma = 1$ kN/cm^2, Young's modulus of 1000 kN/cm^2 and Poisson ratio of 0.2. The fibres have circular cross-section with radius of 0.2 cm and Young's modulus of 500 kN/cm^2.

This application considers two initial meshes A and B, which represent the exact structure geometry. Both models represent the external boundary through 14 bi-quadratic NURBS surfaces, whereas 2 bi-quadratic NURBS represent the crack faces in A and 2 NURBS of $p = q = 4$ in B. Then, A results in 80 collocation points and B results in 116. Figures 139(a) and 139(b) illustrate the meshes A and B, respectively. Both models account for the same initial reinforcements mesh with 4 quadratic 1DBEM element representing each long fibre, as illustrated in Fig. 139(c).

Figure 137 – Colour map of displacement modulus obtained with the final meshes from the following refinement schemes.

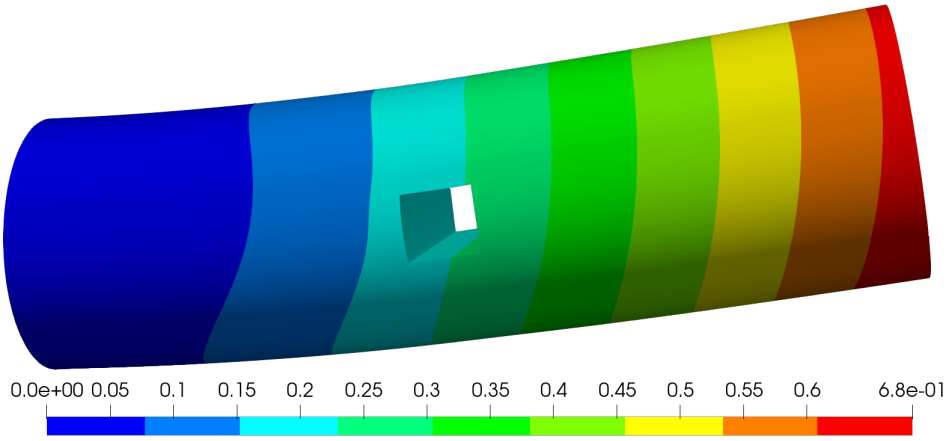

(a) Homogeneous refinement

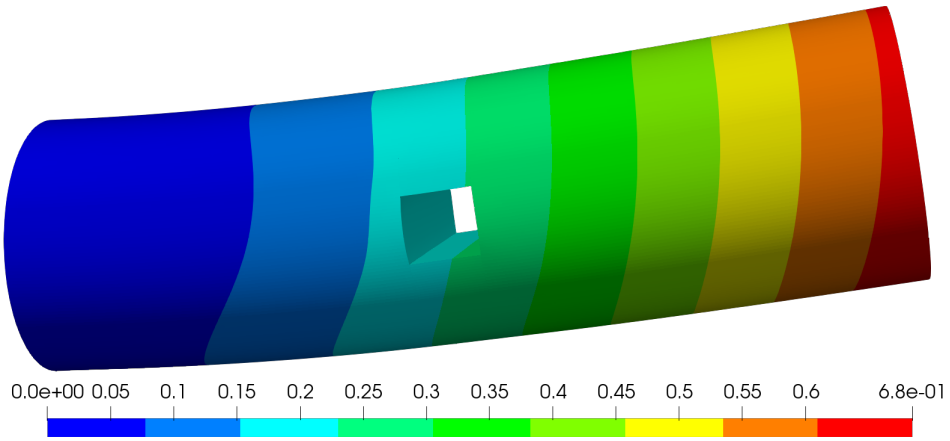

(b) Adaptive refinement

Source: The author.

The tolerance for convergence is $\bar{\eta}_u = \bar{\eta}_t = \bar{\eta}_R = 0.01$ for all surfaces. The adaptivity analysis applies only the proposed strains based error estimator because this estimator has demonstrated superior efficiency in previous applications. Figure 140 illustrates the performance comparison between the proposed refinement strategy and the globally homogeneous refinement regarding the convergence of the total global errors $||e_G||$, obtained by models A and B, respectively. The proposed strategy led to significantly better convergence rates in both models A and B.

Figure 141 illustrates the final boundary collocation points positions obtained in the globally homogeneous and in the adaptive mesh refinement for models A and B. It is worth mentioning that the collocation points illustrated in Fig. 141(c) and 141(d) only differ at the crack faces. Besides, the adaptive refinement identified the critical regions in the body, i.e., with high mechanical fields gradients. Particularly, the lateral boundaries surrounding the supports and the crack, which exhibit the highest error values. Consequently, such

Figure 138 – Reinforced cracked solid analysed in Application 5.

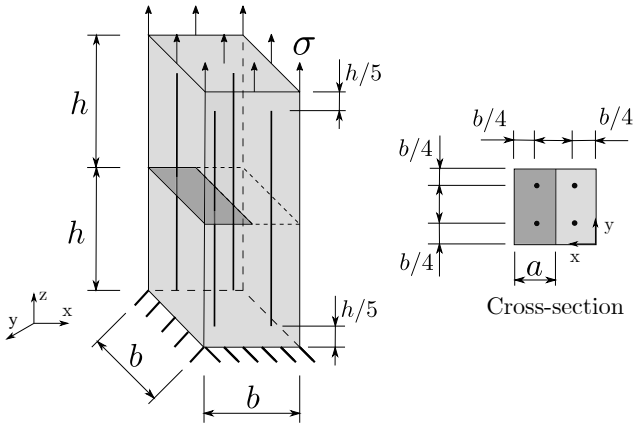

Source: The author.

Figure 139 – Geometric initial models of Application 5.

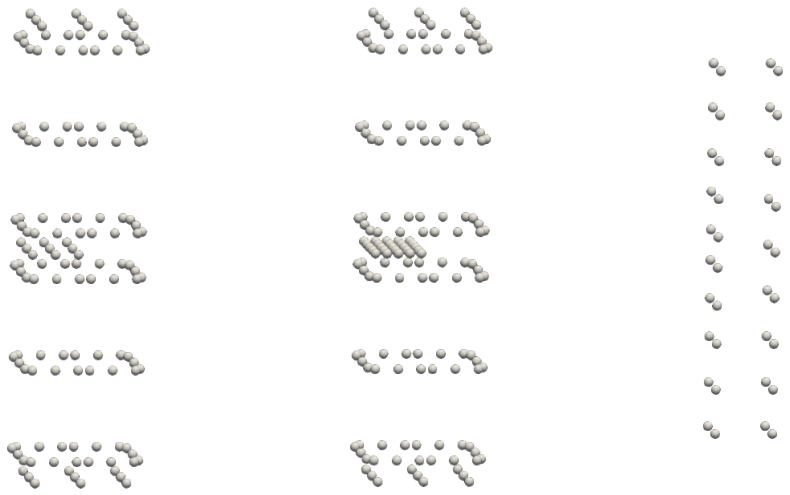

(a) Boundary model A (b) Boundary model B (c) Reinforcements mesh

Source: The author.

boundaries require finer mesh refinement because of the stress concentration, which makes the globally homogeneous refinement less effective.

Figure 140 – Convergence graphs obtained in Application 5 considering two initial boundary meshes.

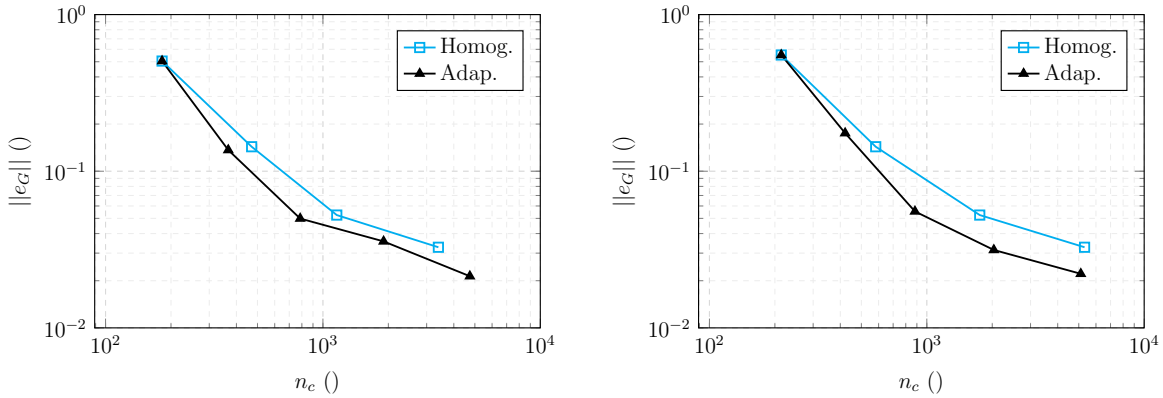

(a) Model A (b) Model B

Source: The author.

Figure 141 – Final boundary meshes obtained in Application 5.

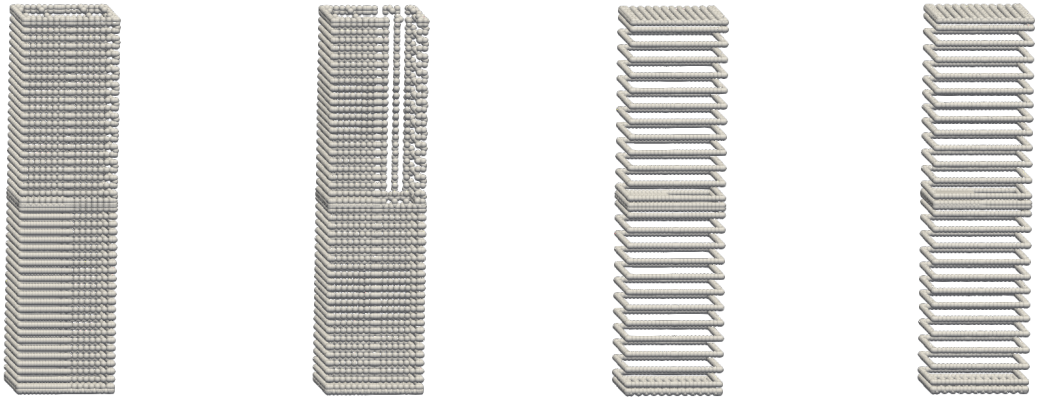

(a) Model A: Adaptive refinement (b) Model B: Adaptive refinement (c) Model A: Homogeneous refinement (d) Model B: Adaptive refinement

Source: The author.

Figure 142 illustrates the final reinforcements meshes. It is worth stressing that the final meshes achieved by the homogeneous process are identical in scenarios A and B, as observed in Fig. 142(c). Besides, both A and B models led to similar evolution behaviour with the adaptive refinement. Firstly, the bottom region of all fibres are more refined because of the presence of a clamped surface at the solid's bottom. Secondly, the fibres crossing the crack faces have the intersection regions represented by finer meshes, since that region presents a huge stress concentration. Therefore, this refinement type is required for accurately representing the stress gradient.

Figure 143 illustrates the z displacement at the crack surfaces obtained by the models considered herein. Because of the circular fibre's cross-section, the displacements around the fibre position behave axisymmetrically, similarly to Fig. 143(d). However, both the homogeneous and the proposed refinement results obtained by model A do not lead to

Figure 142 – Final reinforcements meshes obtained in Application 5.

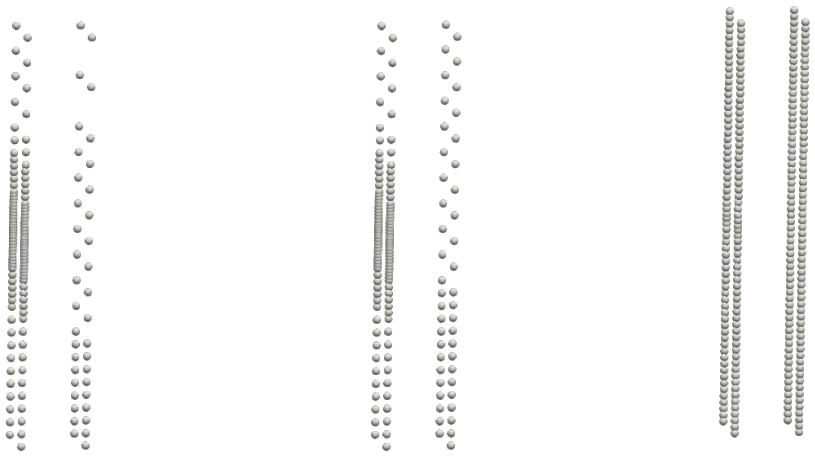

(a) Model A: Adaptive refinement (b) Model B: Adaptive refinement (c) Homogeneous refinement (A and B)

Source: The author.

such expected behaviour. On the other hand, the proposed process with model B (Fig. 143(b)) achieved the expected mechanical behaviour with fewer collocation points than the globally homogeneous process. In this regard, the complex distribution of mechanical fields at the crack faces has been properly represented by fourth-degree NURBS functions, whereas the h-refinement of bi-quadratic functions does not adequately represent the same evolution of the mechanical fields description neither with adaptive nor homogeneous mesh refinement.

Figure 143 – Colour map of z displacements obtained at the crack faces in Application 5. Scale factor equals 50.

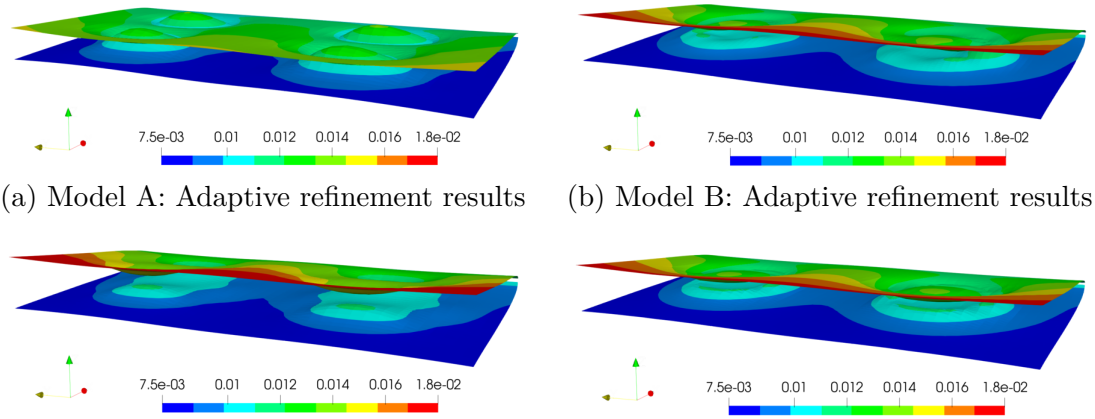

(a) Model A: Adaptive refinement results (b) Model B: Adaptive refinement results

(c) Model A: Homogeneous refinement results (d) Model B: Homogeneous refinement results

Source: The author.

Figure 144 illustrates the displacements responses obtained at the boundary by

model B. The adaptive and the homogeneous refinement results are in (a) and (b), respectively. The results presented in this figure show the good agreement between the predictions of models A and B. Besides, such results fills the expected mechanical behaviour in this application.

Figure 144 – Colour map of displacements modulus obtained with model B in Application 5.

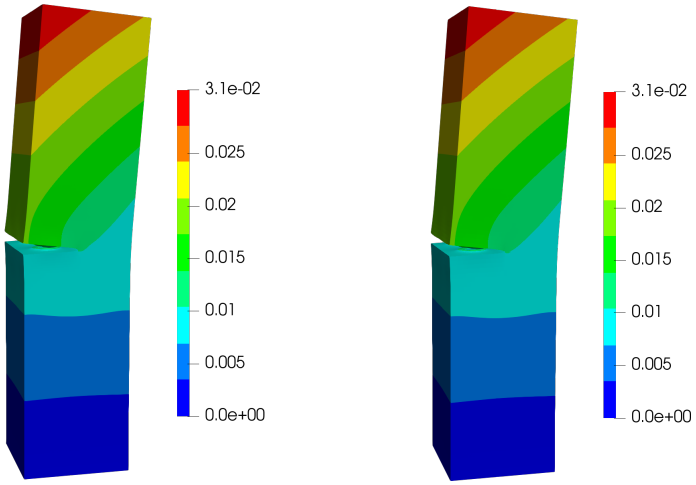

(a) Adaptive refinement results (b) Homogeneous refinement results

Source: The author.

8

Concluding remarks

In this thesis, several innovative IGABEM formulations have been developed for the mechanical analysis of a wide variety of engineering problems in three-dimensional domains reinforced by fibres. Linear and non-linear problems have been treated by accounting for the reinforcement's nonlinearities (elastoplasticity and bond-slip). Time dependent problems have also been addressed by the viscoelastic modelling of both domain and crack cohesive interfaces. Besides, fracture mechanics problems have been assessed by a innovative Cohesive reinforced IGABEM. Finally, studies of adaptive mesh convergence have expanded the fully integration between CAD pre-processors and IGABEM sofrware.

In Chapter 3, the innovative reinforced coupling formulation 1DBEM/IGABEM for three-dimensional fibre-reinforced bodies have been presented. Different from the 2D coupling, in 3D domains the load line integration requires a special integration scheme over a cylindrical shell. It is worth mentioning the extension of the coupling formulation for 3D domains enables the proper representation of complex reinforced structural systems, which are intrinsically 3D. In this chapter, the authors dealt with crossing between fibres and 3D boundaries by developing the connection element. This approach resulted in continuous stress and displacements fields, which effectively overcomes a limitation in usual coupling approaches without the need for remeshing the NURBS surfaces or modifying the IGABEM formulation. The connection element also originally allowed the modelling of fibres crossing crack faces, as presented in the Reinforced single-edge notched body application example.

Chapter 4 presented the nonlinear reinforced formulations, accounting for the elastoplasticity and bond-slip behaviour of the reinforcements. The bi linear isotropic hardening approach has been utilised into the elastoplastic formulation. The secant Newton-Raphson scheme solves the nonlinear problem, which avoids updating the involved matrices. Because the matrices involved in the formulation are non-symmetric and fully-populated, this procedure is advantageous. This formulation enables the representation of yielding

phenomenon along the reinforcements, which has major importance in structural problems. The bond-slip formulation enables the numerical representation of slip behaviour between fibre and matrix. The pull-out test Application demonstrates the robustness and accuracy of the proposed formulation. The proper representation of this application by a 3D BEM or IGABEM formulations is another improvement in the current state of art made in this thesis. Additionally, the performance when both nonlinearities evolve simultaneously have been proven, which lead to an original nonlinear IGABEM formulation. The application in Sec. 4.6.1 demonstrated that the IGABEM formulation enables accurate results and requires less collocation points than the conventional Lagrangian formulation when modelling such type of problem. Besides, isogeometric models lead to minor geometric errors for a vast number of complex shapes, which make it appropriate for representing complex 3D problems.

In Chapter 5, the time dependent section presented viscoelastic approaches accounting for different fibre and matrix constitutive laws with Kelvin-Voigt and Boltzmann rheological models, which is another contribution in the context of 3D IGABEM. The numerical applications of this chapter demonstrate the accuracy of the proposed formulation for linear or elastoplastic fibres embedded into viscoelastic 3D domains, in which significant reduction over the number of degrees of freedom can be observed when comparing the BEM or IGABEM formulations to the equivalent pure FEM models used as reference. Additionally, the proposed formulation has proven to be able to represent different mechanical behaviours, such as relaxation or stiffening. Those can be properly represented by the correct choice of the sub-structures time dependent behaviour between matrix and reinforcement. Besides, this chapter illustrates the robustness of the proposed formulations for complex nontrivial 3D geometry modelling. In these applications, the computational analysis time was presented and it shows excellent performance.

Chapter 6 expanded the existing cohesive fracture mechanics approach for three-dimensional IGABEM formulations. The constant operator technique has been utilised herein, since it does not require the re-evaluation of IGABEM matrices between iterations. Previous experience with the nonlinear reinforced IGABEM formulations showed that this type of approach is advantageous regarding performance. An innovative IGABEM cohesive approach to account for load rate influence has been presented by the viscous cohesive model at crack interfaces. Numerical applications demonstrated the accuracy of the proposed cohesive formulations, including to represent experimental results.

Chapter 7 presented a deep study about the reinforced IGABEM formulation conversion, which led to contributions to the state of art of mesh adaptivity strategies for IGABEM. A modified hypersingular error estimator was proposed without the need to analytical solutions or domain discretization to evaluate approximation errors. The proposed error estimator based on strains favours the adequate assessment of the mesh

refinement required among the NURBS surfaces because it is not affected by the different magnitude orders of the boundary solutions and allows for the adequate error evaluation at all boundaries (including clamped surfaces). Additionally, an adaptivity strategy was proposed for reinforced IGABEM formulations by estimating the error at the fibres via the comparison between FEM and 1DBEM. Such approach was able to identify the refinement required at the most critical fibre's regions (near stress concentrations and endpoints), minimising the mechanical fields oscillations usually observed at these regions with fewer degrees of freedom than the globally homogeneous mesh refinement. The simplicity and effectiveness of the NURBS surfaces refinement strategy is an important advantage of the proposed approach because it does not require changing the regular NURBS surfaces formulation. Besides, all numerical applications had good convergence rates within the proposed strain based error estimator, being better than the globally homogeneous mesh refinement. The proposed formulation is effective and contributes to the straightforward connection between IGABEM and CAD software.

Finally, several contributions in the field of three-dimensional IGABEM formulations have been made, highlighting the non-homogeneous reinforced domains modelling, fracture mechanics, nonlinear formulations and adaptive mesh refinement. Besides, three papers were published (132, 182, 183) with the advances made in this thesis.

8.1 Recommendations for future work

The reinforced formulations presented herein have been quite comprehensive, however there are still some opportunities to advance in this field. One possible way is to improve the reinforcement modelling, accounting for different mechanical solicitations besides the axial force. With that, the formulation could be more suitable to represent reinforcements with a higher ratio between cross-section area and matrix. Additionally, it is possible to develop the tangent approach to solve the linear problems involving elasto-plasticity and bond-slip. This advance would require updating the coupling formulation between iterations to represent the mechanical degradation, which would lead to fewer iterations to achieve convergence. However, this is still a challenge for performance, since updating the IGABEM matrices is quite time consuming.

In the field of fracture mechanics of reinforced domains, there are several opportunities of future studies based on the work presented herein. The coupling of the nonlinear behaviour of both reinforcements and viscous-cohesive crack in the 3D body may lead to a extremely complete model in terms of fracture mechanics for reinforced bodies. Both formulations were presented herein, which makes this work an excellent reference for this field. Additionally, an outstanding contribution this field would be the proposition of crack propagation schemes in the IGABEM framework. It is noticeable that the global aspect of

NURBS interpolation jeopardises the remeshing. Therefore, special approaches, such as enrichment strategies or trimmed curves, are a promising manner to tackle this limitation of IGABEM.

The adaptive strategy formulation presented also has an appealing possible extension. That would be the consideration of locally refinement at NURBS surfaces. With that, one could achieve even better convergence rates, since it would take better advantage of the error estimator information. Nonetheless, the locally refinement of NURBS surfaces requires alternative Isogeometric formulations, such as hierarchical or T-construction B-splines. Furthermore, adaptive strategies with different refinement approaches besides the h-refinement applied herein could lead to good results. In this field, it is worth mentioning the importance of the proposed error estimators presented herein for future works reference.

References

1 KRAHL, P. A.; GIDRÃO, G. d. M. S.; CARRAZEDO, R. Cyclic behavior of UHPFRC under compression. **Cement and Concrete Composites**, Elsevier, v. 104, p. 103363, 2019.

2 HILLERBORG, A.; MODÉER, M.; PETERSSON, P.-E. Analysis of crack formation and crack growth in concrete by means of fracture mechanics and finite elements. **Cement and concrete research**, Elsevier, v. 6, n. 6, p. 773–781, 1976.

3 GOULD, L. S. **Sophisticated software for solid gear design**. 2015. Disponível em: https://www.mmsonline.com/articles/sophisticated-software-for-solid-gear-design. Acesso em: 25 Dez. 2022.

4 PEURIFOY, R. L. Formwork for concrete structures. In: **Engineering, Materials Science**. [S.l.: s.n.], 1964.

5 FOSTER, S. J.; AGARWAL, A.; AMIN, A. Design of steel fiber reinforced concrete beams for shear using inverse analysis for determination of residual tensile strength. **Structural Concrete**, Wiley Online Library, v. 19, n. 1, p. 129–140, 2018.

6 CHU, J. **Carbon nanotube "Stitches" strengthen composites**. 2016. Disponível em:https://news.mit.edu/2016/carbon-nanotube-stitches-strengthen-composites-0803. Acesso em: 25 Dez. 2022.

7 MORGAN, E. F.; BOUXSEIN, M. L. Use of finite element analysis to assess bone strength. **IBMS BoneKEy**, Nature Publishing Group, v. 2, p. 8, 2005.

8 COTTRELL, J. A.; HUGHES, T. J.; BAZILEVS, Y. **Isogeometric analysis: toward integration of CAD and FEA**. Singapore: John Wiley & Sons, 2009.

9 ZIENKIEWICZ, O.; KELLY, D.; BETTESS, P. The coupling of the finite element method and boundary solution procedures. **International journal for numerical methods in engineering**, Wiley Online Library, v. 11, n. 2, p. 355–375, 1977.

10 BETAWI, A.; ZAMAN, M. **Bulkhead**. 2010. Disponível em: http://katakamal.blogspot.com/2010/10/bulkhead.html. Acesso em: 07 Jan. 2020.

11 AERONAVES. **Formação RSB – Aeroporto**. 2016. Disponível em: http://rsbals.weebly.com/aeronaves.html. Acesso em: 07 jan. 2020.

12 ARMENTANI, E.; CITARELLA, R. DBEM and FEM analysis on non-linear multiple crack propagation in an aeronautic doubler-skin assembly. **International Journal of Fatigue**, Elsevier, v. 28, n. 5-6, p. 598–608, 2006.

13 NETO, A. R.; LEONEL, E. D. The mechanical modelling of nonhomogeneous reinforced structural systems by a coupled BEM formulation. **Engineering Analysis with Boundary Elements**, v. 109, p. 1 – 18, 2019. ISSN 0955-7997.

14 HONG, H.-K.; CHEN, J.-T. Derivations of integral equations of elasticity. **Journal of Engineering Mechanics**, American Society of Civil Engineers, v. 114, n. 6, p. 1028–1044, 1988.

15 PERSKY, R. **Python IGES Geometry Library**. 2013. Disponível em: https://readthedocs.org/projects/pyiges/. Acesso em 15 Nov., 2020.

16 PIEGL, L.; TILLER, W. **The NURBS book**. Berlin, Germany: Springer Science & Business Media, 1996.

17 ZIENKIEWICZ, O. C.; ZHU, J. Z. A simple error estimator and adaptive procedure for practical engineerng analysis. **International journal for numerical methods in engineering**, Wiley Online Library, v. 24, n. 2, p. 337–357, 1987.

18 PAULINO, G. H.; GRAY, L.; ZARIKIAN, V. Hypersingular residuals—a new approach for error estimation in the boundary element method. **International Journal for Numerical Methods in Engineering**, Wiley Online Library, v. 39, n. 12, p. 2005–2029, 1996.

19 ABEL, N. H. **Oeuvres complètes de Niels Henrik Abel: Nouvelle édition**. Cambridge: Cambridge University Press, 2012. v. 2. (Cambridge Library Collection - Mathematics, v. 2).

20 HELMHOLTZ, H. von. Theorie der luftschwingungen in rohren mit offenen enden. **Journal für die reine und angewandte Physik**, Leipzig, v. 1, p. 1–72, 1860.

21 MAXWELL, J. C. L. On the calculation of the equilibrium and stiffness of frames. **The London, Edinburgh, and Dublin Philosophical Magazine and Journal of Science**, Taylor and Francis, v. 27, n. 182, p. 294–299, 1864.

22 BETTI, E. Teoria della elasticita'. **Il Nuovo Cimento (1869-1876)**, v. 7, n. 1, p. 69–97, 1872. ISSN 1827-6121.

23 THOMSON, W. Note on the integration of the equations of equilibrium of an elastic solid. In: _____. **Mathematical and Physical Papers**. Cambridge: Cambridge University Press, 2011. (Cambridge Library Collection - Physical Sciences, v. 1), p. 97–99.

24 SOMIGLIANA, C. Sopra l'equilibrio di un corpo elastico isotropo. **Il Nuovo Cimento (1877-1894)**, v. 17, n. 1, p. 140–148, 1885. ISSN 1827-6121.

25 FRIEDMAN, M. B.; SHAW, R. Diffraction of pulses by cylindrical obstacles of arbitrary cross section. **Journal of Applied Mechanics**, v. 29, n. 1, p. 40–46, 03 1962. ISSN 0021-8936.

26 CHEN, L. H.; SCHWEIKERT, D. G. Sound radiation from an arbitrary body. **The Journal of the Acoustical Society of America**, v. 35, n. 10, p. 1626–1632, 1963.

27 MUSKHELISHVILI, N. I. **Some Basic Problems of the Mathematical Theory of Elasticity**. Heidelberg: Springer Netherlands, 1977. ISBN 9789001607012.

28 KUPRADZE, V. **Potential Methods in the Theory of Elasticity**. [S.l.]: Israel Program for Scientific Translations, 1965.

29 BOGOMOLNY, A. Fundamental solutions method for elliptic boundary value problems. **SIAM Journal on Numerical Analysis**, SIAM, v. 22, n. 4, p. 644–669, 1985.

30 RIZZO, F. J. An integral equation approach to boundary value problems of classical elastostatics. **Quarterly of applied mathematics**, v. 25, n. 1, p. 83–95, 1967.

31 RIZZO, F.; SHIPPY, D. A formulation and solution procedure for the general non-homogeneous elastic inclusion problem. **International Journal of Solids and Structures**, v. 4, n. 12, p. 1161 – 1179, 1968. ISSN 0020-7683.

32 RIZZO, F. J.; SHIPPY, D. J. A method for stress determination in plane anisotropic bodies. **J. Compos. Mater**, v. 4, p. 36–61, 1970.

33 CRUSE, T. A.; SWEDLOW, J. **Interactive program for analysis and design problems in advanced composites technology**. Pittsburgh, Pennyskvania, 1971.

34 BREBBIA, C. Weighted residual classification of approximate methods. **Applied Mathematical Modelling**, Elsevier, v. 2, n. 3, p. 160–164, 1978.

35 BREBBIA, C.; DOMINGUEZ, J. Boundary element methods for potential problems. **Applied Mathematical Modelling**, Elsevier, v. 1, n. 7, p. 372–378, 1977.

36 BANERJEE, P. K.; BUTTERFIELD, R. Boundary element methods in geomechanics. **Finite elements in geomechanics**, John Wiley & Sons, New York, p. 529–570, 1977.

37 DOMINGUEZ, J. **Stress analysis around anchor plates: a boundary element method application**. 1977. PhD Thesis — Universidad de Sevilla, 1977.

38 BREBBIA, C.; DOMINGUEZ, J. **Boundary Elements: An Introductory Course**. [S.l.]: Sydney Grammar School Press, 1994. ISBN 9781853123498.

39 SWOBODA, G.; MERTZ, W.; BEER, G. Rheological analysis of tunnel excavations by means of coupled finite element (FEM)–boundary element (BEM) analysis. **International journal for numerical and analytical methods in geomechanics**, Wiley Online Library, v. 11, n. 2, p. 115–129, 1987.

40 SINGH, R.; SHARMA, K.; VARADARAJAN, A. Elasto-plastic analysis of tunnel excavation in layered rock medium by coupled febem. **Numerical Methods in Geomechanics**, p. 941–950, 1988.

41 CODA, H. B.; VENTURINI, W. S. On the coupling of 3D BEM and FEM frame model applied to elastodynamic analysis. **International Journal of Solids and Structures**, Elsevier, v. 36, n. 31-32, p. 4789–4804, 1999.

42 GRIFFITH, A. A. Vi. the phenomena of rupture and flow in solids. **Philosophical transactions of the royal society of london. Series A, containing papers of a mathematical or physical character**, The royal society London, v. 221, n. 582-593, p. 163–198, 1921.

43 WESTERGAARD, H. M. Bearing pressures and cracks. **Journal of Applied Mechanics**, v. 6, p. A49–53, 1939.

44 IRWIN, G. R. Analysis of stresses and strains near the end of a crack traversing a plate. **Journal of Applied Mechanics-Transactions of the ASME**, E24, p. 351–369, 1957.

45 SNEDDON, I. N. The distribution of stress in the neighbourhood of a crack in an elastic solid. **Proceedings of the Royal Society of London. Series A. Mathematical and Physical Sciences**, The Royal Society London, v. 187, n. 1009, p. 229–260, 1946.

46 CRUSE, T. A.; VANBUREN, W. Three-dimensional elastic stress analysis of a fracture specimen with an edge crack. **International Journal of Fracture Mechanics**, Springer, v. 7, n. 1, p. 1–15, 1971.

47 SNYDER, M. D.; CRUSE, T. A. Boundary-integral equation analysis of cracked anisotropic plates. **International Journal of Fracture**, Springer, v. 11, n. 2, p. 315–328, 1975.

48 WATSON, J. Hermitian cubic and singular elements for plane strain. **Developments in boundary element methods**, Elsevier London, v. 4, p. 1–28, 1986.

49 GRAY, L.; MARTHA, L. F.; INGRAFFEA, A. Hypersingular integrals in boundary element fracture analysis. **International Journal for Numerical Methods in Engineering**, Wiley Online Library, v. 29, n. 6, p. 1135–1158, 1990.

50 PORTELA, A.; ALIABADI, M.; ROOKE, D. Dual boundary element metho: Effective implementation for crack problems. **International Journal for Numerical Methods in Engineering**, v. 33, p. 1269 – 1287, 04 1992.

51 MI, Y.; ALIABADI, M. Dual boundary element method for three-dimensional fracture mechanics analysis. **Engineering analysis with boundary elements**, Elsevier, v. 10, n. 2, p. 161–171, 1992.

52 LEONEL, E. D.; VENTURINI, W. S. Dual boundary element formulation applied to analysis of multi-fractured domains. **Engineering Analysis with Boundary Elements**, Elsevier, v. 34, n. 12, p. 1092–1099, 2010.

53 LEONEL, E. D.; VENTURINI, W. S. Non-linear boundary element formulation with tangent operator to analyse crack propagation in quasi-brittle materials. **Engineering analysis with boundary elements**, Elsevier, v. 34, n. 2, p. 122–129, 2010.

54 OLIVEIRA, H. L.; LEONEL, E. D. A BEM formulation applied in the mechanical material modelling of viscoelastic cracked structures. **International Journal of Advanced Structural Engineering**, Springer, v. 9, n. 1, p. 1–12, 2017.

55 CORDEIRO, S. G. F.; LEONEL, E. D. Cohesive crack propagation modelling in wood structures using BEM and the tangent operator technique. **Engineering Analysis with Boundary Elements**, Elsevier, v. 64, p. 111–121, 2016.

56 BREBBIA, C. A. **The boundary element method for engineers**. [S.l.]: John Wiley & Sons, Incorporated, 1978. ISBN 9780470264386.

57 BREBBIA, C. A. Weighted residual classification of approximate methods. **Applied Mathematical Modelling**, v. 2, n. 3, p. 160 – 164, 1978. ISSN 0307-904X.

58 ALIABADI, M. H. **The Boundary Element Method**: Applications in solids and structures. Chichester: John Wiley and Sons, 2002. v. 2. 580 p.

59 GUIGGIANI, M.; GIGANTE, A. A General Algorithm for Multidimensional Cauchy Principal Value Integrals in the Boundary Element Method. **Journal of Applied Mechanics**, v. 57, n. 4, p. 906–915, 1990.

60 GUIGGIANI, M.; KRISHNASAMY, G.; RUDOLPHI, T. J.; RIZZO, F. J. A General Algorithm for the Numerical Solution of Hypersingular Boundary Integral Equations. **Journal of Applied Mechanics**, v. 59, n. 3, p. 604–614, 09 1992. ISSN 0021-8936.

61 CRUSE, T. A.; PRATT; CONN., W. A. G. E. H. **Mathematical Foundations of the Boundary-Integral Equation Method in Solid Mechanics**. [S.l.]: Defense Technical Information Center, 1977. 120 p.

62 CORDEIRO, S. G. F. **Contribuições às análises de fratura e fadiga de componentes tridimensionais pelo método dos elementos de contorno dual**. 2008. 320 p. Tese (Doutorado) — Escola de Engenharia de São Carlos, Universidade de São Paulo, São Carlos, 2008.

63 ROCHA, M. **Análise da fratura em corpos tridimensionais com base em formulações enriquecidas do Método dos Elementos de Contorno**. 2020. 130 p. Dissertação (Mestrado) — Departamento de Engenharia de Estruturas, Escola de Engenharia de São Carlos, Universidade de São Paulo, São Carlos, 2020.

64 LEONEL, E. D. **Modelos não lineares do Método dos Elementos de Contorno para análise de problemas de fratura e aplicação de modelos de confiabilidade em estruturas submetidas à fadiga**. 2009. 406 p. Tese (Doutorado) — Escola de Engenharia de São Carlos, Universidade de São Paulo, São Carlos, 2009.

65 ANDRADE, H. C. **Análise da propagação de fissuras em estruturas bidimensionais não- homogêneas via Método dos Elementos de Contorno**. 2017. 241 p. Dissertação (Mestrado) — Departamento de Engenharia de Estruturas, Escola de Engenharia de São Carlos, Universidade de São Paulo, São Carlos, 2017.

66 NETO, A. R. **Modelos numéricos baseados no Método dos Elementos de Contorno para a análise mecânica de domínios viscoelásticos enrijecidos com comportamento não-linear**. 2019. 183 p. Dissertação (Mestrado) — Departamento de Engenharia de Estruturas, Escola de Engenharia de São Carlos, Universidade de São Paulo, São Carlos, 2019.

67 CORDEIRO, S. G. F.; LEONEL, E. D. Mechanical modelling of three-dimensional cracked structural components using the isogeometric dual boundary element method. **Applied Mathematical Modelling**, Elsevier, v. 63, p. 415–444, 2018.

68 COX, M. G. The numerical evaluation of b-splines. **IMA Journal of Applied Mathematics**, Oxford University Press, v. 10, n. 2, p. 134–149, 1972.

69 de Boor, C. On calculating with b-splines. **Journal of Approximation Theory**, v. 6, n. 1, p. 50 – 62, 1972. ISSN 0021-9045.

70 HUGHES, T. J.; COTTRELL, J. A.; BAZILEVS, Y. Isogeometric analysis: CAD, finite elements, nurbs, exact geometry and mesh refinement. **Computer methods in applied mechanics and engineering**, Elsevier, v. 194, n. 39-41, p. 4135–4195, 2005.

71 PENG, X.; ATROSHCHENKO, E.; KERFRIDEN, P.; BORDAS, S. P. A. Isogeometric boundary element methods for three dimensional static fracture and fatigue crack growth. **Computer Methods in Applied Mechanics and Engineering**, Elsevier, v. 316, p. 151–185, 2017.

72 GREVILLE, T. Numerical procedures for interpolation by spline functions. **Journal of the Society for Industrial and Applied Mathematics, Series B: Numerical Analysis**, SIAM, v. 1, n. 1, p. 53–68, 1964.

73 TADA, H.; PARIS, P.; IRWIN, G. The analysis of cracks handbook. **New York: ASME Press**, v. 2, p. 1, 2000.

74 ATLURI, S.; GRANNELL, J. J. **Boundary element methods (BEM) and combination of BEM-FEM**. Georgia: Georgia Institute of Technology, 1978.

75 BEER, G.; WATSON, J. O. **Introduction to finite and boundary element methods for engineers**. New York: Wiley, 1992.

76 STAMOS, A. A.; BESKOS, D. E. Dynamic analysis of large 3-d underground structures by the bem. **Earthquake engineering & structural dynamics**, Wiley Online Library, v. 24, n. 6, p. 917–934, 1995.

77 GANGULY, S.; LAYTON, J. B.; BALAKRISHNA, C. Symmetric coupling of multi-zone curved galerkin boundary elements with finite elements in elasticity. **International Journal for Numerical Methods in Engineering**, Wiley Online Library, v. 48, n. 5, p. 633–654, 2000.

78 ELLEITHY, W. M.; TANAKA, M.; GUZIK, A. Interface relaxation FEM–BEM coupling method for elasto-plastic analysis. **Engineering Analysis with Boundary Elements**, Elsevier, v. 28, n. 7, p. 849–857, 2004.

79 BIA, R. A.; OSTROWSKI, Z.; KASSAB, A. J.; YIN, Q.; SCIUBBA, E. et al. Coupling BEM, FEM and analytic solutions in steady-state potential problems. **Engineering analysis with boundary elements**, Elsevier, v. 26, n. 7, p. 597–611, 2002.

80 AOUR, B.; RAHMANI, O.; NAIT-ABDELAZIZ, M. A coupled FEM/BEM approach and its accuracy for solving crack problems in fracture mechanics. **International Journal of Solids and Structures**, Elsevier, v. 44, n. 7-8, p. 2523–2539, 2007.

81 TROYANI, N.; PÉREZ, A. A comparison of a finite element only scheme and a BEM/FEM method to compute the elastic-viscoelastic response in composite media. **Finite Elements in Analysis and Design**, Elsevier, v. 88, p. 42–54, 2014.

82 FERNANDES, G. R.; PITUBA, J. J. C.; NETO, E. A. de S. FEM/BEM formulation for multi-scale analysis of stretched plates. **Engineering Analysis with Boundary Elements**, Elsevier, v. 54, p. 47–59, 2015.

83 RIZOS, D.; WANG, Z. Coupled BEM–FEM solutions for direct time domain soil–structure interaction analysis. **Engineering Analysis with Boundary Elements**, Elsevier, v. 26, n. 10, p. 877–888, 2002.

84 RIBEIRO, D. B.; PAIVA, J. B. de. An alternative BE–FE formulation for a raft resting on a finite soil layer. **Engineering Analysis with Boundary Elements**, Elsevier, v. 50, p. 352–359, 2015.

85 CITARELLA, R.; CRICRÌ, G. Three-dimensional BEM and FEM submodelling in a cracked FML full scale aeronautic panel. **Applied Composite Materials**, Springer, v. 21, n. 3, p. 557–577, 2014.

86 CITARELLA, R.; GIANNELLA, V.; VIVO, E.; MAZZEO, M. FEM–DBEM approach for crack propagation in a low pressure aeroengine turbine vane segment. **Theoretical and Applied Fracture Mechanics**, Elsevier, v. 86, p. 143–152, 2016.

87 GIANNELLA, V.; PERRELLA, M.; CITARELLA, R. Efficient FEM-DBEM coupled approach for crack propagation simulations. **Theoretical and Applied Fracture Mechanics**, Elsevier, v. 91, p. 76–85, 2017.

88 CODA, H. B.; VENTURINI, W. S.; ALIABADI, M. H. A general 3D BEM/FEM coupling applied to elastodynamic continua/frame structures interaction analysis. **International Journal for Numerical Methods in Engineering**, v. 46, n. 5, p. 695–712, 1999.

89 LEITE, L. G.; CODA, H. B.; VENTURINI, W. S. Two-dimensional solids reinforced by thin bars using the boundary element method. **Engineering Analysis with Boundary Elements**, v. 27, n. 3, p. 193 – 201, 2003. ISSN 0955-7997.

90 MESQUITA, A. D.; CODA, H. B. A two-dimensional BEM/FEM coupling applied to viscoelastic analysis of composite domains. **International journal for numerical methods in engineering**, Wiley Online Library, v. 57, n. 2, p. 251–270, 2003.

91 MESQUITA, A. D.; CODA, H. B. New methodology for the treatment of two dimensional viscoelastic coupling problems. **Computer methods in applied mechanics and engineering**, Elsevier, v. 192, n. 16-18, p. 1911–1927, 2003.

92 BOTTA, A. S.; VENTURINI, W. S. Reinforced 2D domain analysis using BEM and regularized BEM/FEM combination. **CMES: Computer Modeling in Engineering & Sciences**, v. 8, n. 1, p. 15–28, 2005.

93 BANERJEE, P. K.; BUTTERFIELD, R. **Boundary element methods in engineering science**. London: McGraw-Hill, 1981. v. 17.

94 ANTES, H. Fundamental solution and integral equations for timoshenko beams. **Computers & structures**, Elsevier, v. 81, n. 6, p. 383–396, 2003.

95 CRUZ, J. M. F. **Contribuição à análise estática e dinâmica de pórticos pelo Método dos Elementos de Contorno**. 2012. 391 p. Tese (Doutorado) — Universidade Federal da Paraíba, João Pessoa, 2012.

96 FERRO, N. C. P. **Uma combinação MEC/MEF para análise de interação solo-estrutura**. 1999. 193 p. Tese (Doutorado) — Escola de Engenharia de São Carlos, Universidade de São Paulo, São Carlos, 1999.

97 RIZZO, F. J.; SHIPPY, D. J. An application of the correspondence principle of linear viscoelasticity theory. **SIAM Journal on Applied Mathematics**, SIAM, v. 21, n. 2, p. 321–330, 1971.

98 KASSIMALI, A. **Matrix Analysis of Structures**. 2. ed. Stamford: Cengage Learning, 2012.

99 WEAVER, W.; GERE, J. M. **Matrix analysis framed structures**. New York: Springer science & business media, 2012.

100 BUFFON, L. P. **Formulações do Método dos Elementos de Contorno para a análise mecânica de domínios planos não-homogêneos enrijecidos**. 2018. 143 p. Tese (Doutorado) — Escola de Engenharia de São Carlos, Universidade de São Paulo, São Carlos, 2018.

101 KRAHL, P. A.; CARRAZEDO, R.; DEBS, M. K. E. Mechanical damage evolution in UHPFRC: experimental and numerical investigation. **Engineering Structures**, Elsevier, v. 170, p. 63–77, 2018.

102 KRAHL, P. A. **Lateral stability of ultra-high performance fiber-reinforced concrete beams with emphasis in transitory phases**. 2018. 191 p. Tese (Doutorado) — School of Engineering of São Carlos, University of São Paulo, São Carlos, 2018.

103 GETTU, R.; GARDNER, D. R.; SALDIVAR, H.; BARRAGÁN, B. Study of the distribution and orientation of fibers in sfrc specimens. **Materials and Structures**, Springer, v. 38, n. 1, p. 31–37, 2005.

104 YOO, D.-Y.; BANTHIA, N.; KANG, S.-T.; YOON, Y.-S. Effect of fiber orientation on the rate-dependent flexural behavior of ultra-high-performance fiber-reinforced concrete. **Composite Structures**, Elsevier, v. 157, p. 62–70, 2016.

105 WATSTEIN, D. Bond stress in concrete pullout specimens. **ACI Journal Proceedings**, v. 38, p. 37–52, 1941.

106 BRESLER, B.; BERTERO, V. Behavior of reinforced concrete under repeated load. **Journal of the Structural Division**, 1968.

107 DUCATTI, V. A. **Concreto de elevado desempenho: estudo da aderência com a armadura**. 1993. 295 p. Tese (Doutorado) — Escola Politécnica, Universidade de São Paulo, São Paulo, 1993.

108 ZULINI, I. **Efeito do confinamento na aderência entre barras de aço e concreto de alta resistência à compressão**. 2019. 137 p. Dissertação (Mestrado) — Departamento de Engenharia de Estruturas, Escola de Engenharia de São Carlos, Universidade de São Paulo, São Carlos, 2019.

109 RILEM-FIP-CEB. Bond test for reinforcing steel. 1. beam test (7-ii-28 d). 2. pull-out test (7-ii-128). tentative recommendations. **RILEM Journal Materials and Structures**, v. 6, n. 32, 1973.

110 ALMEIDA FILHO, F. M. **Contribuição ao estudo da aderência entre barras de aço e concreto auto-adensáveis.** 1993. 291 p. Tese (Doutorado) — Escola de Engenharia de São Carlos, Universidade de São Paulo, São Carlos, 1993.

111 FUSCO, P. B. **Técnica de armar as estruturas de concreto**. São Paulo, SP: Pini, 1995.

112 LEONHARDT, F.; MÖNNING, E. Construções de concreto-volume 3: princípios básicos sobre a armação de estruturas de concreto armado. **Rio de Janeiro: Interciência**, p. 171–174, 1978.

113 CEB-FIP. Bulletin d'information n. 195/197. **Comité Euro-International du Béton - FIP Model Code**, Paris, 1990.

114 HUANG, Z.; ENGSTRÖM, B.; MAGNUSSON, J. Experimental investigation of the bond and anchorage behaviour of deformed bars in high strength concrete. **Chalmers University of Technology, Division of Concrete Structures, Report**, v. 95, n. 4, p. 32, 1996.

115 HARAJLI, M. H.; SALLOUKH, K. Effect of fibers on development/splice strength of reinforcing bars in tension. **Materials Journal**, v. 94, n. 4, p. 317–324, 1997.

116 NGO, D.; SCORDELIS, A. C. Finite element analysis of reinforced concrete beams. **ACI Journal Proceedings**, v. 64, n. 3, p. 152–163, 1967.

117 NILSON, A. H. Nonlinear analysis of reinforced concrete by the finite element method. **ACI Journal Proceedings**, v. 65, n. 9, p. 757–766, 1968.

118 YANKELEVSKY, D. Z. A two-phase one dimensional model for steel-concrete interaction. **Computers & structures**, Elsevier, v. 65, n. 6, p. 781–794, 1997.

119 SPACONE, E.; LIMKATANYU, S. Responses of reinforced concrete members including bond-slip effects. **Structural Journal**, v. 97, n. 6, p. 831–839, 2000.

120 BOTTA, A. S. **Método dos elementos de contorno para análise de corpos danificados com ênfase no fenômeno da localização de deformações**. 2003. 185 p. Tese (Doutorado) — Escola de Engenharia de São Carlos, Universidade de São Paulo, São Carlos, 2003.

121 TRESCA, H. **Mémoire sur l'écoulement des corps solides soumis à de fortes pressions**. [S.l.]: Gauthier-Villars, 1864.

122 TOLLMIEN, W.; SCHLICHTING, H.; GORTLER, H.; RIEGELS, F. W. Spannungsverteilung in plastischen korpern. In: _____. **Riegels F.W. (eds) Ludwig Prandtl Gesammelte Abhandlungen**. Berlin, Heidelberg: Springer, 1961.

123 MELAN, E. Zur plastizität des räumlichen kontinuums. **Archive of Applied Mechanics**, Springer, v. 9, n. 2, p. 116–126, 1938.

124 PRAGER, W. Recent developments in the mathematical theory of plasticity. **Journal of applied physics**, AIP, v. 20, n. 3, p. 235–241, 1949.

125 CHEN, W. F.; HAN, D. J. **Plasticity for structural engineers**. New York: J. Ross Publishing, 2007.

126 PROENÇA, S. P. B. **Análise não-linear de estruturas**: Notas de aula. Escola de Engenharia de São Carlos, Universidade de São Paulo, São Carlos, 2019.

127 SWEDLOW, J. L.; CRUSE, T. A. Formulation of boundary integral equations for three-dimensional elasto-plastic flow. **International Journal of Solids and Structures**, Elsevier, v. 7, n. 12, p. 1673–1683, 1971.

128 BUI, H. D. Some remarks about the formulation of three-dimensional thermoelastoplastic problems by integral equations. **International Journal of Solids and Structures**, Elsevier, v. 14, n. 11, p. 935–939, 1978.

129 TELLES, J. C. F.; BREBBIA, C. A. The boundary element method in plasticity. **Applied Mathematical Modelling**, Elsevier, v. 5, n. 4, p. 275–281, 1981.

130 VANALLI, L. **O MEC e o MEF aplicados à análise de problemas viscoplásticos em meios anisotrópicos e compostos**. 2004. 194 p. Tese (Doutorado) — Escola de Engenharia de São Carlos, Universidade de São Paulo, São Carlos, 2004.

131 LEONEL, E. D. **Notas de aula para a disciplina introdução à mecânica da fratura**. Escola de Engenharia de São Carlos, Universidade de São Paulo, São Carlos, 2018.

132 NETO, A. R.; LEONEL, E. D. Three dimensional nonlinear BEM formulations for the mechanical analysis of nonhomogeneous reinforced structural systems. **Engineering Analysis with Boundary Elements**, v. 123, p. 200 – 219, 2021. ISSN 0955-7997.

133 ROCHA, F. C.; VENTURINI, W. S.; CODA, H. B. Sliding frame-solid interaction using BEM/FEM coupling. **Latin American Journal of Solids and Structures**, scielo, v. 11, p. 1376 – 1399, 2014. ISSN 1679-7825.

134 TSCHOEGL, N. W. **The phenomenological theory of linear viscoelastic behavior: an introduction**. New York: Springer Science & Business Media, 2012.

135 TELLES, J. C. F.; BREBBIA, C. A. Elastic/viscoplastic problems using boundary elements. **International Journal of Mechanical Sciences**, Elsevier, v. 24, n. 10, p. 605–618, 1982.

136 VENTURINI, W. S. **Application of the boundary element formulation to solve geomechanical problems**. 1982. PhD Thesis — University of Southampton, 1982.

137 CHABOCHE, J. L.; LEMAITRE, J. **Mechanics of solid materials**. Cambridge: Cambridge University Press Cambridge, 1990. 556 p.

138 SYNGELLAKIS, S.; WU, J. Evaluation of polymer fracture parameters by the boundary element method. **Engineering Fracture Mechanics**, Elsevier, v. 75, n. 5, p. 1251–1265, 2008.

139 SLADEK, J.; SUMEC, J.; SLADEK, V. Viscoelastic crack analysis by the boundary integral equation method. **Ingenieur-Archiv**, Springer, v. 54, n. 4, p. 275–282, 1984.

140 LEE, S. S.; KIM, Y. J. Time-domain boundary element analysis of cracked linear viscoelastic solids. **Engineering fracture mechanics**, Elsevier, v. 51, n. 4, p. 585–590, 1995.

141 CHEN, Y.; HWU, C. Boundary element analysis for viscoelastic solids containing interfaces/holes/cracks/inclusions. **Engineering analysis with boundary elements**, Elsevier, v. 35, n. 8, p. 1010–1018, 2011.

142 MESQUITA, A. D.; CODA, H. B. An alternative time integration procedure for boltzmann viscoelasticity: a bem approach. **Computers & Structures**, Elsevier, v. 79, n. 16, p. 1487–1496, 2001.

143 MESQUITA, A. D.; CODA, H. B. A simple kelvin and boltzmann viscoelastic analysis of three-dimensional solids by the boundary element method. **Engineering analysis with boundary elements**, Elsevier, v. 27, n. 9, p. 885–895, 2003.

144 MESQUITA, A. D. **Novas metodologias e formulações para o tratamento de problemas inelásticos com acoplamento progressivo MEC/MEF**. 2002. 291 p. Tese (Doutorado) — Escola de Engenharia de São Carlos, Universidade de São Paulo, São Carlos, 2002.

145 GURTIN, M. E.; STERNBERG, E. On the linear theory of viscoelasticity. **Archive for Rational Mechanics and Analysis**, v. 11, p. 291–356, 1962. ISSN 1432-0673.

146 CHRISTENSEN, R. **Theory of Viscoelasticity (Second Edition)**. Second edition. New York: Academic Press, 1982.

147 OLIVEIRA, H. L. **Modelos numéricos aplicados à análise viscoelástica linear e à otimização topológica probabilística de estruturas bidimensionais: uma abordagem pelo Método dos Elementos de Contorno**. 2017. 199 p. Tese (Doutorado) — Escola de Engenharia de São Carlos, Universidade de São Paulo, São Carlos, 2017.

148 PLANAS, J.; ELICES, M. Nonlinear fracture of cohesive materials. **International Journal of Fracture**, v. 51, p. 139–157, 1991.

149 JENQ, Y.; SHAH, S. P. Two parameter fracture model for concrete. **Journal of engineering mechanics**, American Society of Civil Engineers, v. 111, n. 10, p. 1227–1241, 1985.

150 BA<ZANT, Z. P.; KAZEMI, M. et al. Determination of fracture energy, process zone longth and brittleness number from size effect, with application to rock and conerete. **International Journal of fracture**, v. 44, n. 2, p. 111–131, 1990.

151 DUGDALE, D. S. Yielding of steel sheets containing slits. **Journal of the Mechanics and Physics of Solids**, Elsevier, v. 8, n. 2, p. 100–104, 1960.

152 BARENBLATT, G. I. The mathematical theory of equilibrium cracks in brittle fracture. In: **Advances in applied mechanics**. [S.l.]: Elsevier, 1962. v. 7, p. 55–129.

153 REINHARDT, H. W.; XU, S. A practical testing approach to determine mode ii fracture energy giif for concrete. **International Journal of Fracture**, Springer, v. 105, n. 2, p. 107–125, 2000.

154 SALEH, A.; ALIABADI, M. Crack growth analysis in concrete using boundary element method. **Engineering fracture mechanics**, Elsevier, v. 51, n. 4, p. 533–545, 1995.

155 WITTMANN, F.; ROELFSTRA, P.; MIHASHI, H.; HUANG, Y.-Y.; ZHANG, X.-H.; NOMURA, N. Influence of age of loading, water-cement ratio and rate of loading on fracture energy of concrete. **Materials and structures**, Springer, v. 20, n. 2, p. 103–110, 1987.

156 RUIZ, G.; ZHANG, X.; YU, R.; PORRAS, R.; POVEDA, E.; VISO, J. D. Effect of loading rate on fracture energy of high-strength concrete. **Strain**, Wiley Online Library, v. 47, n. 6, p. 518–524, 2011.

157 REINHARDT, H.; WEERHEIJM, J. Tensile fracture of concrete at high loading rates taking account of inertia and crack velocity effects. **International Journal of Fracture**, Springer, v. 51, n. 1, p. 31–42, 1991.

158 BRARA, A.; KLEPACZKO, J. R. Fracture energy of concrete at high loading rates in tension. **International Journal of Impact Engineering**, Elsevier, v. 34, n. 3, p. 424–435, 2007.

159 SANTOS, F. L. G. dos et al. A viscous-cohesive model for concrete fracture in quasi-static loading rate. **Engineering Fracture Mechanics**, Elsevier, v. 228, p. 106893, 2020.

160 RÜSCH, H. Researches toward a general flexural theory for structural concrete. **Journal of the American Concrete Institute**, v. 57, n. 1, p. 1–28, 1960.

161 VEGT, I.; BREUGEL, V.; WEERHEIJM, J. Failure mechanisms of concrete under impact loading. **Fracture Mechanics of Concrete and Concrete Structures, FraMCoS-6**, v. 1, p. 579–587, 2007.

162 KITA, E.; KAMIYA, N. Recent studies on adaptive boundary element methods. **Advances in Engineering Software**, Elsevier, v. 19, n. 1, p. 21–32, 1994.

163 AINSWORTH, M.; ODEN, J. T. **A posteriori error estimation in finite element analysis**. [S.l.]: John Wiley & Sons, 2011. v. 37.

164 KELLY, D.; MILLS, R.; REIZES, J.; MILLER, A. A posteriori estimates of the solution error caused by discretization in the finite element, finite difference and boundary element methods. **International journal for numerical methods in engineering**, Wiley Online Library, v. 24, n. 10, p. 1921–1939, 1987.

165 AURADA, M.; FERRAZ-LEITE, S.; PRAETORIUS, D. Estimator reduction and convergence of adaptive BEM. **Applied Numerical Mathematics**, Elsevier, v. 62, n. 6, p. 787–801, 2012.

166 KAWAGUCHI, K.; KAMIYA, N. An adaptive bem by sample point error analysis. **Engineering analysis with boundary elements**, Elsevier, v. 9, n. 3, p. 255–262, 1992.

167 GUIGGIANI, M. Error indicators for adaptive mesh refinement in the boundary element method—a new approach. **International journal for numerical methods in engineering**, Wiley Online Library, v. 29, n. 6, p. 1247–1269, 1990.

168 MENON, G.; PAULINO, G. H.; MUKHERJEE, S. Analysis of hypersingular residual error estimates in boundary element methods for potential problems. **Computer methods in applied mechanics and engineering**, Elsevier, v. 173, n. 3-4, p. 449–473, 1999.

169 CHATI, M. K.; PAULINO, G. H.; MUKHERJEE, S. The meshless standard and hypersingular boundary node methods—applications to error estimation and adaptivity in three-dimensional problems. **International Journal for Numerical Methods in Engineering**, Wiley Online Library, v. 50, n. 9, p. 2233–2269, 2001.

170 FEISCHL, M.; FüHRER, T.; HEUER, N.; KARKULIK, M.; PRAETORIUS, D. Adaptive boundary element methods. **Archives of Computational Methods in Engineering**, Springer Science and Business Media LLC, v. 22, n. 3, p. 309–389, Jun 2014. ISSN 1886-1784.

171 LIANG, M.-T.; CHEN, J.-T.; YANG, S. Error estimation for boundary element method. **Engineering analysis with boundary elements**, Elsevier, v. 23, n. 3, p. 257–265, 1999.

172 OÑATE, E.; BUGEDA, G. A study of mesh optimality criteria in adaptive finite element analysis. **Engineering Computations: Int J for Computer-Aided Engineering**, Emerald Group Publishing Limited, v. 10, n. 4, p. 307–321, 1993.

173 LIAPIS, S. An adaptive boundary element method for the solution of potential flow problems. **Engineering analysis with boundary elements**, Elsevier, v. 18, n. 1, p. 29–37, 1996.

174 ZIMMERMANN, C.; SAUER, R. A. Adaptive local surface refinement based on lr nurbs and its application to contact. **Computational Mechanics**, Springer, v. 60, n. 6, p. 1011–1031, 2017.

175 DODGSON, N. A.; KOSINKA, J. Can local nurbs refinement be achieved by modifying only the user interface? **Computer-Aided Design**, Elsevier, v. 71, p. 28–38, 2016.

176 KAGAN, P.; FISCHER, A.; BAR-YOSEPH, P. Z. Mechanically based models: Adaptive refinement for b-spline finite element. **International Journal for Numerical Methods in Engineering**, Wiley Online Library, v. 57, n. 8, p. 1145–1175, 2003.

177 GANTNER, G.; PRAETORIUS, D.; SCHIMANKO, S. Adaptive isogeometric boundary element methods with local smoothness control. **Mathematical Models and Methods in Applied Sciences**, World Scientific, v. 30, n. 02, p. 261–307, 2020.

178 NGUYEN, V. P.; ANITESCU, C.; BORDAS, S. P.; RABCZUK, T. Isogeometric analysis: an overview and computer implementation aspects. **Mathematics and Computers in Simulation**, Elsevier, v. 117, p. 89–116, 2015.

179 CARSTENSEN, C.; FUNKEN, S. A.; STEPHAN, E. P. On the adaptive coupling of FEM and BEM in 2–d–elasticity. **Numerische Mathematik**, Springer, v. 77, n. 2, p. 187–221, 1997.

180 AURADA, M.; FEISCHL, M.; FÜHRER, T.; KARKULIK, M.; MELENK, J. M.; PRAETORIUS, D. Classical FEM-BEM coupling methods: nonlinearities, well-posedness, and adaptivity. **Computational Mechanics**, Springer, v. 51, n. 4, p. 399–419, 2013.

181 LEYDECKER, F.; MAISCHAK, M.; STEPHAN, E. P.; TELTSCHER, M. Adaptive fe–be coupling for an electromagnetic problem in r3 — a residual error estimator. **Mathematical Methods in the Applied Sciences**, v. 33, n. 18, p. 2162–2186, 2010.

182 NETO, A. R.; LEONEL, E. D. Nonlinear IGABEM formulations for the mechanical modelling of 3d reinforced structures. **Applied Mathematical Modelling**, v. 102, p. 62–100, 2022. ISSN 0307-904X.

183 NETO, A. R.; LEONEL, E. D. One step forward towards the full integration of BEM and CAD software: An effective adaptive approach. **Engineering Analysis with Boundary Elements**, v. 143, p. 457–482, 2022. ISSN 0955-7997.

184 TIMOSHENKO, S.; GOODIER, J.; GOODIER, J. **Theory of Elasticity**. [S.l.]: McGraw-Hill, 1951. (Engineering societies monographs).

185 CHOU, P.; PAGANO, N. **Elasticity: Tensor, Dyadic, and Engineering Approaches**. [S.l.]: Dover Publications, 1992. (Dover Civil and Mechanical Engineering Series). ISBN 9780486669588.

186 VALLIAPPAN, S. **Continuum Mechanics Fundamentals**. [S.l.]: A.A. Balkema, 1981. (Balkema academic and technical publications).

APPENDIX A

FUNDAMENTALS OF ELASTICITY

This appendix presents the most relevant concepts of the theory of elasticity for the development of the BEM formulations handled in this study. References are provided as a source for more detailed explanations, such as the following classical works: (184), (185) and (186).

A.1 Cauchy stress

The classical theory of elasticity considers as a hypothesis the solid homogeneity, in which internal restoring interactions are present in all points of the solid (theory of continuity). These internal interactions result from body forces and surface forces. It is worth remarking that dynamic effects are neglected in this study.

Let Ω denotes an elastic domain in equilibrium condition, as illustrated in Figura 145. External forces F_i are applied at the boundary of Ω, which results in internal restoring forces at all body's points. One can divide Ω into two portions A and B by a cross section that contains the P point and has a normal vector pointed in the x_j direction. Considering A, there is a resulting force at the cross section that balances all external forces F_i applied over A. Let ΔF_i be the resulting force over a small area ΔA_j in the cross section, then the Cauchy stress σ_{ij} can be defined as follows:

$$\sigma_{ij} = \lim_{\Delta A \to 0} \frac{\Delta F_i}{\Delta A_j} = \frac{\partial F_i}{\partial A_j} \tag{A.1}$$

In three-dimensional problems, one can perform three perpendicular cuts as illustrated in Figura 145, whereas each one results in σ_{ij} for $i = 1,2,3$. Thus, one writes the Cauchy stress tensor composed by 9 components for each point P, as illustrated in Figura 146.

Nevertheless, the Cauchy theorem can be demonstrated by writing the local equilibrium relations over the orthogonal axis of a infinitesimal element (Figura 146). Thus:

$$\sigma_{ij} = \sigma_{ji} \tag{A.2}$$

Figure 145 – Representation of a continuous body.

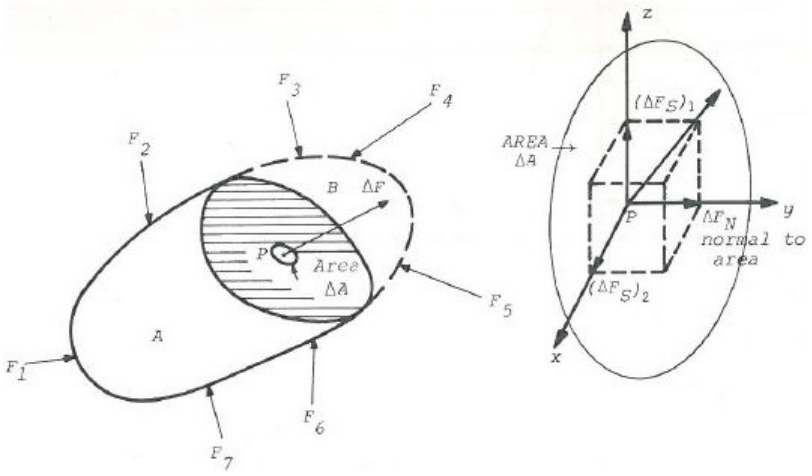

Source: (186), adapted.

Figure 146 – Stress state at a given point

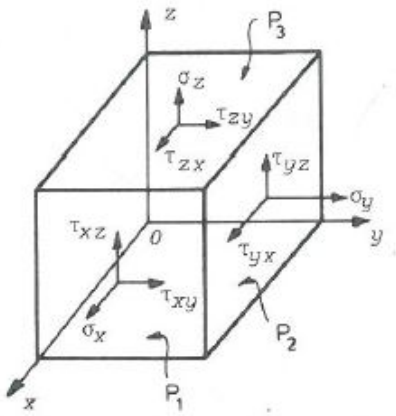

Source: (186), adapted.

in which the stresses σ_{ij} where $i \neq j$ are named as the shear stresses.

The tractions at any point of Ω can be defined from the Cauchy stress tensor. For this, For that, one must write the local equilibrium of the infinitesimal element (Figura 147) considering cuts in the orthogonal directions. Thus:

$$t_i = \sigma_{ij}\eta_j \tag{A.3}$$

in which η_j is the vector normal to the cut plan.

When body forces b_i are considered in the infinitesimal element (Figura 146), the stresses σ_{ij} must be in static equilibrium with the applied b_i. Thus, one writes:

$$\sigma_{ij,j} + b_i = 0 \tag{A.4}$$

Figure 147 – Representation of cut in infinitesimal

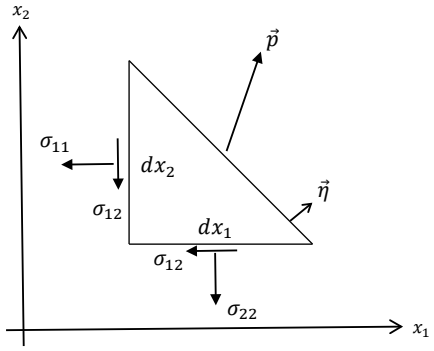

Source: The author.

It is worth remarking that Eq. A.4 represents the longitudinal equilibrium (of forces) and Eq. A.3 represents the rotational equilibrium (of moments). Equation A.4 is also the governing equation of the elastic boundary value problem (BVP).

A.2 Strains

When external loads are applied into a solid, the energy is transferred to the material and dissipated through its shape change. This is the origin of the strains, which represent the measure of the body's shape change at each material point. The strains are energetic conjugates of the stresses, which means that they depend on the adopted stress measure. For the Cauchy stress, linear strains must be considered. The linear strain is based on the body's initial configuration, therefore the hypothesis of small displacements and deformations must be taken into account. With that, the difference between initial and final (deformed) shapes can be neglected.

The longitudinal strain can be defined from the length variation in a infinitesimal element (Figura 148) subjected to a displacements field u_i, as follows:

$$\varepsilon_{11} = \frac{\Delta L}{L} = \frac{dx_1 + u_1 + {}^{\partial u_1}/_{\partial x_1} dx_1 - u_1 - dx_1}{dx_1} = \frac{\partial u_1}{\partial x_1} = u_{1,1} \tag{A.5}$$

The shear strain is defined by the angular variation of the infinitesimal element vertices:

$$\gamma_{12} = \frac{\pi}{2} - \theta = \alpha_1 + \alpha_2 \cong \frac{{}^{\partial u_1}/_{\partial x_2} dx_2}{dx_2} + \frac{{}^{\partial u_2}/_{\partial x_1} dx_1}{dx_1} = \frac{\partial u_1}{\partial x_2} + \frac{\partial u_2}{\partial x_1} = u_{1,2} + u_{2,1} \tag{A.6}$$

Strains from different directions can be obtained in an analogous process, which results in 9 components. As well as the the shear stresses, the shear strains are also symmetric. The cartesian components of the strain tensor for linear and small deformations are given as follows:

Figure 148 – Strains in infinitesimal element. 2D representation

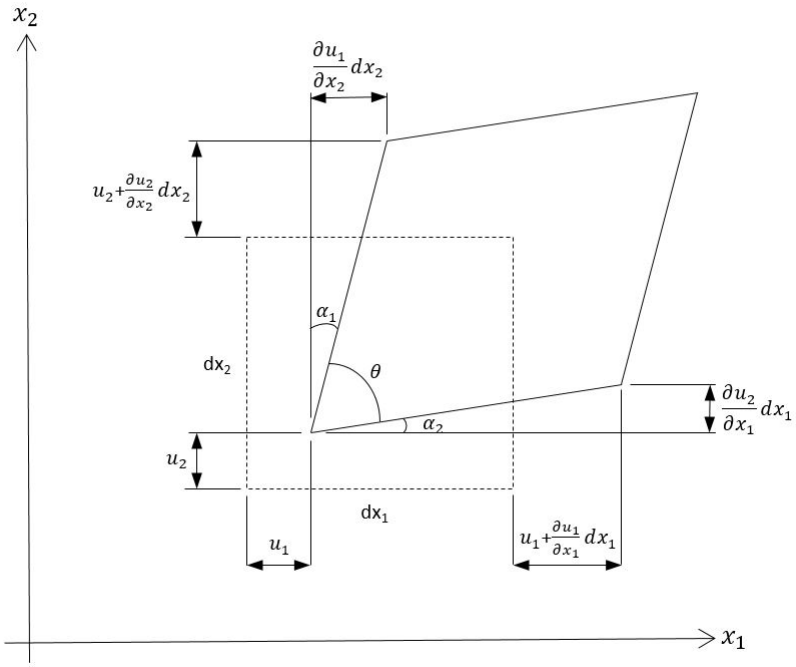

Source: The author.

$$\varepsilon_{ij} = \frac{1}{2}\left(u_{i,j} + u_{j,i}\right) \tag{A.7}$$

A.3 Stress-strain relation

As previously mentioned, stress and strain are material responses resulting from the load application over Ω. Therefore, they are related by a constitutive connection, which depends on the material behavior. For isotropic linear elastic materials, this relation is known as Hooke's law. In this scenario, the material is considered perfectly elastic (no residual deformations after unloading) and isotropic, which means that physical properties are the same regardless of direction.

The generalized Hooke's law is written as:

$$\sigma_{ij} = D_{ijkl}\varepsilon_{kl} \tag{A.8}$$

where D_{ijkl} is the fourth order constitutive tensor. This relation can also be expressed in a inverse form:

$$\varepsilon_{ij} = C_{ijkl}\sigma_{kl} \tag{A.9}$$

For a generic situation, the tensors D_{ijkl} and C_{ijkl} have 81 components each. However, symmetry can demonstrate that only 21 are indeed independent. In addition, for

isotropic materials, all components can be written in term of only two properties: Young's modulus (E) and Poisson Ratio (ν). Then, Eq. A.8 can be rewritten as follows:

$$\sigma_{ij} = 2\mu\varepsilon_{ij} + \lambda\varepsilon_{kk}\delta_{ij} \tag{A.10}$$

in which δ_{ij} is the Kronecker delta function, μ is the shear modulus and λ is the Lamé parameter. Those variables can be written as:

$$\mu = \frac{E}{2(1+v)} \tag{A.11}$$

$$\lambda = \frac{vE}{(1+v)(1-2v)} \tag{A.12}$$

Equation A.9 can also be written in an inverse form:

$$\varepsilon_{ij} = \frac{1}{2\mu}\sigma_{ij} - \frac{v}{E}\sigma_{kk}\delta_{ij} \tag{A.13}$$

A.4 Elasticity problems solution techniques

One can represent the elasticity problems by mathematical models described by the equilibrium equation (Eq: A.4), compatibity of displacements (Eq. A.7) and constitutive relation (Eq. A.8). The result is a system of differential equations, which represents the BVP in static elastic problems. Figure 149 illustrates a two-dimensional BVP.

Figure 149 – Boundary conditions for a general BVP

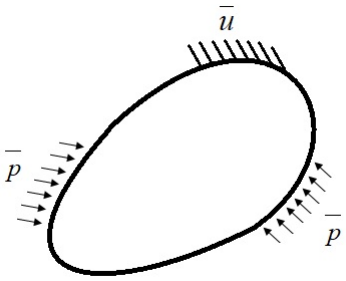

Source: The author.

Boundary conditions are necessary to solve the BVP, in addition to the equations above-mentioned. Dirichlet boundary conditions represent the application of prescribed displacement, whereas Neumann boundary conditions consider applied tractions. The BVPs usually have both conditions.

There are at least two approaches to solve the BVP, which consider the introduction of new function that satisfies the governing differential equations. One of them is named as displacements technique and is usually applied for predominantly Dirichlet problems or

infinite domains. This approach leads to the fundamental solution of Kelvin, which is used in BEM isotropic formulations.

The displacements technique is based on rearrange the differential equations in order to obtain a single displacements function as a solution. Hooke's law (Eq. A.10), the Cauchy formula for tractions (Eq. A.3) and the strains relation (Eq. A.7) are applied into Eq. A.4, which leads to the Navier-Cauchy equation:

$$\mu\left(u_{i,ij}+u_{j,ii}\right)+\lambda u_{i,ij}+b_j=0 \tag{A.14}$$

The Navier-Cauchy solution can be obtained by applying displacements functions that satisfy Eq. A.14 in a process similar to the Airy functions. An adequate function is achieved from the Galerkin vector:

$$u_i=G_{i,mm}-\frac{1}{2(1-\nu)}G_{m,im} \tag{A.15}$$

One can demonstrate that the Galerkin vector is a solution for Eq. A.14 if G satisfies the following:

$$G_{i,mmjj}+\frac{b_i}{\mu}=0 \tag{A.16}$$

The second approach to solve the BVP is the stress technique, which is usually applied for predominantly Neumann problems. In this technique, all equations must be written in terms of a single stress solution. This process results in the following relation, which is known as Beltrami-Michell equation.

$$\sigma_{jk,ii}+\frac{1}{1+\nu}\sigma_{zz,jk}=\frac{-\nu}{1-\nu}\delta_{jk}b_{l,l}-\left(b_{j,k}+b_{j,k}\right) \tag{A.17}$$

This relation, together with the equilibrium equations result in the necessary equation to apply the stress technique. This study deals only with the displacements technique, therefore no further details are presented about Eq. A.17.

A.5 Kelvin's fundamental solutions

The BEM formulation requires the fundamental problem, which is based on a hypothetical BVP with known responses. This BVP is composed by a infinite domain in which a unitary concentrated force is applied. Its solution can be determined by the above-presented displacements technique, therefore the displacement and traction fields are known as fundamental solutions. For a isotropic elastic case, the fundamental solutions were presented by Lord Kelvin in 1882 (23) and have been known as Kelvin' fundamental solutions.

The unitary concentrated force is applied at a given point called "source point" and denoted by **s**. This force can be applied following the 3 orthogonal directions x_i, as illustrated in Fig. 150. Hence, the fundamental problem is the result of the superposition of the (a), (b) and (c) problems. The applied force is mathematically described by the Dirac Delta function ($\Delta(\mathbf{x}^f - \mathbf{x}^s)$). The fundamental solutions are calculated at a given point called "field point" and denoted by **f**.

Figure 150 – Illustration of fundamental problem 3D

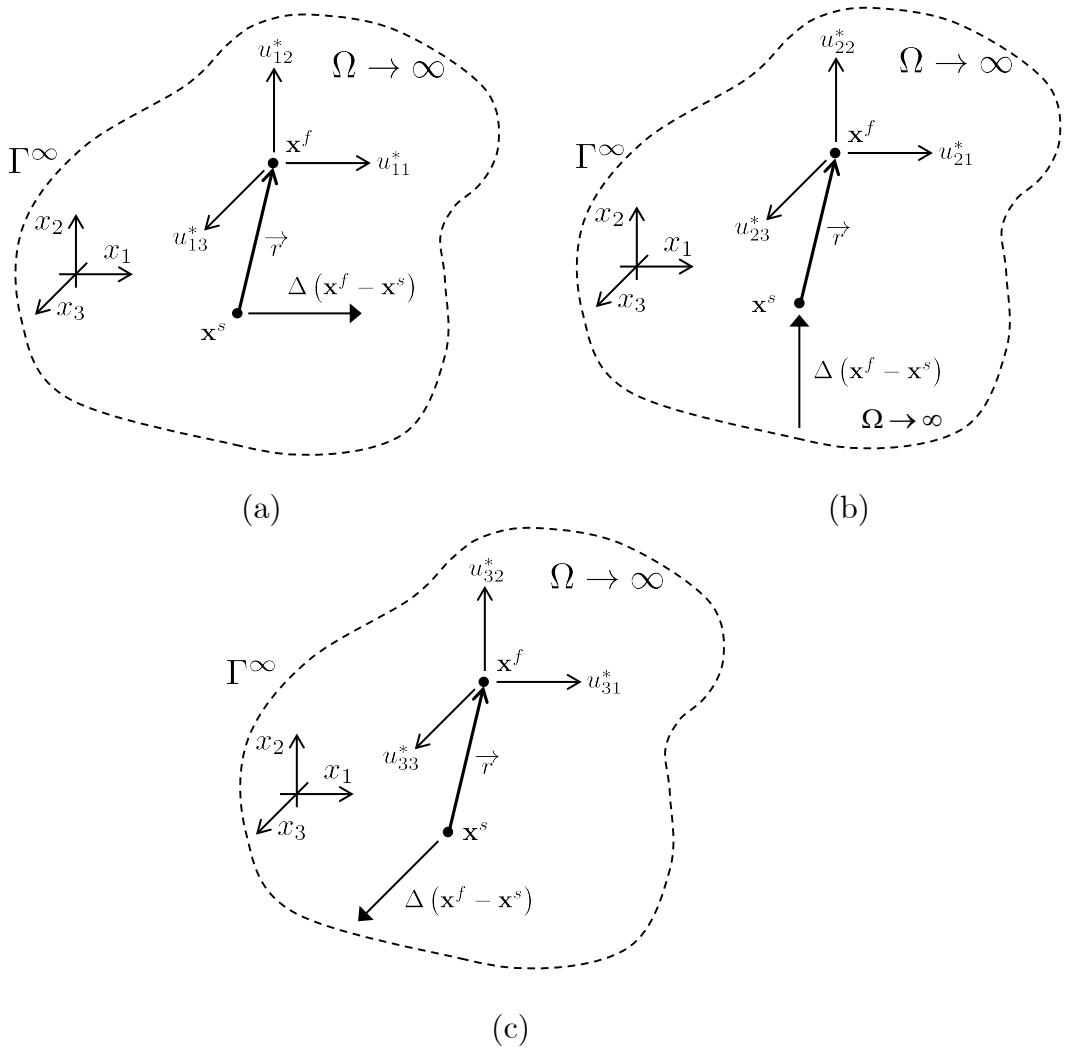

Source: The author.

The equilibrium relation (Eq. A.4) can be evaluated for the three problems (a), (b) and (c). A single relation can describe the equilibrium of all problems as follows:

$$\sigma^*_{kij,j} + b^*_{ki} = 0 \tag{A.18}$$

in which k is the orientation of the applied force in the fundamental problem. The symbol $*$ identifies the fields of the fundamental problem.

The body forces are described by the Dirac delta function, as follows:

$$b^*_{ki} = \Delta(\mathbf{x}^f - \mathbf{x}^s)\delta_{ki} \tag{A.19}$$

where δ_{ki} is the Kronecker delta function.

Applying Eq. A.19 into Eq. A.18, the following equilibrium equation is obtained for the fundamental problem:

$$\sigma^*_{kij,j} = -\Delta(\mathbf{x}^f - \mathbf{x}^s)\delta_{ki} \tag{A.20}$$

It is worth remarking that all fundamental fields have an additional index k, which represents the orientation e_k of the applied force $\Delta(\mathbf{x}^f - \mathbf{x}^s)$. Considering the superposition principle, the value of displacements and tractions at any domain point are given by:

$$u^*_i = \sum_{k=1}^{3} u^*_{ki} \qquad \text{and} \qquad t^*_i = \sum_{k=1}^{3} t^*_{ki} \tag{A.21}$$

which can be written in the indicial notation as follows:

$$\begin{aligned} u^*_i &= u^*_{ki} e_k \\ p^*_i &= p^*_{ki} e_k \end{aligned} \tag{A.22}$$

The most relevant relations from the theory of elasticity can also be applied to the fundamental problem. The Cauchy formula, the stress-strain relation and the displacements compatibility equation can be written, respectively, as follows:

$$\sigma^*_{kij}\eta_j = t^*_{ki} \tag{A.23}$$

$$\sigma^*_{kij} = D_{ijlm}\varepsilon^*_{klm} \tag{A.24}$$

$$\varepsilon^*_{kij} = \frac{u^*_{ki,j} + u^*_{kj,i}}{2} \tag{A.25}$$

The stress-strain relation (Eq. A.24) can incorporate the linear isotropic constitutive tensor, which leads to:

$$\sigma^*_{kij} = 2\mu\left(\varepsilon^*_{kij} + \frac{\nu}{1-2\nu}\varepsilon^*_{kmm}\delta_{ij}\right) \tag{A.26}$$

The fundamental problem solution considers the above-mentioned displacements technique. Then, Eq. A.20 is applied into the Galerkin vector (Eq. A.16), which can be rewritten as:

$$G_{ki,mmjj} + \frac{\Delta(\mathbf{x}^f - \mathbf{x}^s)\delta_{ki}}{\mu} = 0 \tag{A.27}$$

Equation A.27 can be further simplified as follows:

$$\nabla^2 F_{ki} + \frac{1}{\mu}\Delta(x^f - x^s)\delta_{ki} = 0 \tag{A.28}$$

in which $F_{ki} = \nabla^2 G_{ki}$ and ∇^2 is the Laplace operator.

Therefore, Equation A.28 solution can be easily found and is given by:

$$F_{ki} = \frac{1}{4\pi\mu r}\delta_{ki} \tag{A.29}$$

consequently:

$$G_{ki} = \frac{r}{8\pi\mu}\delta_{ki} \tag{A.30}$$

Equation A.15 must be rewritten in order to satisfy the superposition principle of the fundamental problem, as follows:

$$u^*_{ki} = G^*_{ki,mm} - \frac{1}{2(1-\nu)}G^*_{km,im} \tag{A.31}$$

Equation A.30 can now be applied into Eq. A.31, which results in the following displacements fundamental solution U^*_{ki}. More details about this passage can be found in (58).

$$U^*_{ki} = \frac{1}{16\pi\mu(1-\nu)r}\left[(3-4\nu)\delta_{ki} + r_{,k}r_{,i}\right] \tag{A.32}$$

which represents the displacements at the field point $\mathbf{x}^f$ along the direction i, referent to the unitary fundamental force applied at the source point $\mathbf{x}^s$ along the direction k. r is the modulus of the distance vector between the source and field points. Besides, $r_{,i}$ are the directional derivatives of this vector in relation to the field point coordinates. This vector is mathematically described as follows:

$$r_i = x^f_i - x^s_i \tag{A.33}$$

$$r = \sqrt{\sum_{k=1}^{3}\left[\left(x^f_k - x^s_k\right)^2\right]} \tag{A.34}$$

$$r_{,i} = \frac{x^f_i - x^s_i}{r} \tag{A.35}$$

Furthermore, the fundamental solutions of stresses, strains and tractions can be obtained. The first derivatives of the fundamental displacements (Eq. (A.32)) are calculated and applied into Eq. A.25, which results in the fundamental strains E^*_{kij}:

$$E^*_{kij} = -\frac{1}{16\pi\mu(1-\nu)r^2}\left[(1-2\nu)\left(r_{,j}\delta_{ki} + r_{,k}\delta_{ji}\right) + 3r_{,k}r_{,i}r_{,j} - r_{,i}\delta_{kj}\right] \tag{A.36}$$

Equation A.26 is applied into Eq. A.36 to obtain the fundamental solution of stresses P^*_{kij}:

$$P^*_{kij} = -\frac{1}{8\pi(1-\nu)r^2}\left[(1-2\nu)\left(r_{,j}\delta_{ki} + r_{,k}\delta_{ji} - r_{,i}\delta_{kj}\right) + 3r_{,k}r_{,i}r_{,j}\right] \tag{A.37}$$

From Eq. A.37 and Eq. A.23, one can obtain the fundamental solution of tractions T^*_{ki}:

$$T^*_{ki} = -\frac{1}{8\pi(1-\nu)r^2}\left[\frac{\partial r}{\partial \eta}\left[(1-2\nu)\delta_{ki} + 3r_{,k}r_{,i}\right] - (1-2\nu)\left(\eta_i r_{,k} - \eta_k r_{,i}\right)\right] \tag{A.38}$$

where η is the boundary normal vector pointing to the external region in relation to the domain.

In addition, the r derivatives in relation to η are written as follows:

$$\frac{\partial r}{\partial \eta} = r_{,m}\eta_{,m} \tag{A.39}$$

Equations A.32 and A.38 are the fundamental solutions applied into the BEM singular formulation. These expressions must be integrated over the boundary and, consequently, are usually called integral kernels. Moreover, the BEM hypersingular formulation presents two additional fundamental solutions D^*_{kij} and S^*_{kij}, which can be calculated from the above-mentioned singular solutions. This process is presented in the Chapter 2.